REGULATION OF SISTER-CHROMATID COHESION

APPROVED BY SUPERVISORY COMMITTEE

Hongtao Yu, Ph.D. (Mentor)

Sandeep Burma, Ph.D. (Chair)

Joshua Mendell, M.D., Ph.D.

Benjamin Tu, Ph.D.

DEDICATION

I would like to express my deepest gratitude to my mentor Dr. Hongtao Yu for his support, encouragement, guidance throughout my graduate study. Thank you for sharing your knowledge and providing me opportunities to mature as a scientist.

I would like to thank my thesis committee members: Dr. Sandeep Burma, Dr. Joshua Mendell and Dr. Benjamin Tu for their critical and invaluable suggestions. Also, I want to thank Dr. Ryan Potts and Dr. Michael White for their support and time although they left UTSW before I graduate.

I would like to acknowledge the former and current members of the Yu lab, not only for the experimental guidance and assistance but also for the emotional support. I have been enjoying a lot with them in a collaborative and pleasant environment.

Of course this acknowledgment would not be complete without thanking my parents and my husband. Thank you for always providing encouragement when I needed it most.

REGULATION OF SISTER-CHROMATID COHESION

by

GE ZHENG

DISSERTATION

Presented to the Faculty of the Graduate School of Biomedical Sciences

The University of Texas Southwestern Medical Center at Dallas

In Partial Fulfillment of the Requirements

For the Degree of

DOCTOR OF PHILOSOPHY

The University of Texas Southwestern Medical Center at Dallas

Dallas, Texas

December, 2017

REGULATION OF SISTER-CHROMATID COHESION

Publication No._____

GE ZHENG, Ph.D.

The University of Texas Southwestern Medical Center at Dallas, 2017

Supervising Professor: HONGTAO YU, Ph.D.

Orderly execution of two critical events during the cell cycle--DNA replication and chromosome segregation--ensures the stable transmission of genetic materials. The cohesin complex physically connects sister chromatids during DNA replication in a process termed sister-chromatid cohesion. Timely establishment and dissolution of sister-chromatid cohesion is a prerequisite for accurate chromosome segregation, and is tight regulated by the cell cycle machinery and cohesin-associated proteins. Errors in this process can lead to aneuploidy and promote tumorigenesis. Research in this dissertation has provided several key insights into the regulation of sister-chromatid cohesion during the mitotic cell cycle.

First, we report the crystal structure and functional characterization of human Wapl, a key negative regulator of cohesin that promotes cohesin release from chromatin. Our results indicate that Wapl-mediated cohesin release from chromatin requires extensive physical contacts between Wapl and multiple cohesin subunits.

Second, we have determined the crystal structure of human SA2-Scc1 cohesin subcomplex, which is the interaction hub for cohesin regulators. Further biochemical and functional analyses reveal the direct competition between Wapl and the cohesion protector Sgo1 for binding to a conserved site on SA2-Scc1. Our results implicate a role for this direct antagonism in centromeric cohesion protection.

Third, we report the crystal structure of human Pds5B bound to a conserved peptide motif found in both Wapl and Sororin. Further biochemical and functional studies suggest that Pds5 has both positive and negative roles in cohesion regulation and establish the molecular basis for how Wapl and the cohesin-stabilizing factor Sororin antagonistically influence cohesin dynamics on chromosomes. The structure reveals inositol hexakisphosphate (IP6) as an unexpected cofactor of Pds5. The IP6-binding segment of Pds5B engages the N-terminal region of Scc1 and inhibits the binding of Scc1 to Smc3. Our results suggest a direct role of Pds5 in cohesin release from chromosomes by stabilizing a transient, open state of cohesin during its ATPase cycle.

Finally, we show that cohesin loading onto chromosomes requires the phosphorylation of MCM2-7 by Cdc7-Dbf4 kinase (DDK) during early S phase, when a mega-complex composed of MCM2-7, Scc2/4 and cohesin is formed. At active replication forks, inactivation of multiple replisome components impairs cohesin loading, weakens MCM-Scc2/4-cohesin interaction and leads to cohesion defects. By contrast, interfering Okazaki fragment processing and nucleosome assembly during DNA replication do not impact interphase cohesion, suggesting that cohesion

establishment occurs before Okazaki fragment maturation and histone deposition. Our results demonstrate that DNA replication-coupled cohesin loading is required for the establishment of sister-chromatid cohesion.

In conclusion, combining structural, biochemical and cellular approaches, our studies advance the molecular understanding of spatial and temporal regulation of the establishment and dissolution of sister-chromatid cohesion.

TABLE OF CONTENTS

PRIOR PUBLICATIONS

Zheng G, Kanchwala M, Xing C, Yu H. MCM-dependent cohesin loading promotes sister-chromatid cohesion establishment during DNA replication. *Manuscript in preparation*.

Soardi FC[*], Machado-Silva A[*], Linhares ND[*], Zheng G[*], Qu Q, Pena HB, Martins TMM, Vieira HGS, Pereira NB, Melo-Minardi RC, Gomes CC, Gomez RS, Gomes DA, Pires DEV, Ascher DB, Yu H[#] & Pena SDJ[#]. Familial STAG2 germline mutation defines a new human cohesinopathy. *npj Genomic Medicine*. 2017; 2 (1), 7.

Zheng G, Ouyang Z, Yu H. Biochemical and Functional Assays of Human Cohesin-Releasing Factor Wapl. *Methods Mol Biol*. 2017;1515:37-53.

Ouyang Z[*], Zheng G[*], Tomchick DR, Luo X, Yu H. Structural Basis and IP_6 Requirement for Pds5-Dependent Cohesin Dynamics. *Mol Cell*. 2016 Apr 21;62(2):248-59.

Zheng G, Yu H. Regulation of sister chromatid cohesion during the mitotic cell cycle. *Sci China Life Sci*. 2015 Nov;58(11):1089-98.

Hara K[*], Zheng G[*], Qu Q, Liu H, Ouyang Z, Chen Z, Tomchick DR, Yu H. Structure of cohesin subcomplex pinpoints direct shugoshin-Wapl antagonism in centromeric cohesion. *Nat Struct Mol Biol*. 2014 Oct;21(10):864-70.

Ouyang Z[*], Zheng G[*], Song J, Borek DM, Otwinowski Z, Brautigam CA, Tomchick DR, Rankin S, Yu H. Structure of the human cohesin inhibitor Wapl. *Proc Natl Acad Sci U S A*. 2013 Jul 9;110(28):11355-60.

LIST OF FIGURES

LIST OF TABLES

LIST OF DEFINITIONS

APC/C – anaphase-promoting complex/cyclosome

Cdc – cell division cycle

Cdk1 – cyclin-dependent kinase 1

Cdt1 – chromatin licensing and DNA replication factor 1

CHAF1 – chromatin assembly factor 1

Chl1 – chromosome loss protein 1, yeast homologue of DDX11

CMG – Cdc45-MCM-GINS

CSM3 – chromosome segregation in meiosis protein 3, yeast homologue of Tipin

CTCF – CCCTC-binding factor

Ctf4 – chromosome transmission fidelity protein 4, yeast homologue of WDHD1

DAPI – 4',6-diamidino-2-phenylindole

DDK – DBF4- or DRF1-dependent kinase

DDX11 – DEAD/H-Box helicase 11

DSB – double strand break

dsDNA – double-stranded DNA

Eco1/Ctf7 – establishment of cohesion protein 1/ chromosome transmission fidelity protein 7

Esco1/2 – establishment of sister chromatid cohesion N-Acetyltransferase 1/2

FISH – fluorescence in situ hybridization

FRAP – fluorescence recovery after photobleaching

GINS – go, ichi, nii, and san (Japanese numbers 5, 1, 2, 3) containing Sld5, Psf1, Psf2, and Psf3

HDAC8 – histone deacetylase 8

HID – helical insert domain

HD – head domain

HR – homologous recombination

IP_6 – inositol hexakisphosphate

ITC – isothermal titration calorimetry

KD – dissociation constant

MALS – multi-angle light scattering

MCM – mini-chromosome maintenance complex

MES – 2- (N-morpholino) ethanesulfonic acid

MPM – mitotic protein monoclonal

MRX – Mre11-Rad50-Xrs2, yeast homologue of MRN

MRN – Mre11-Rad50-Nbs1

NHD – N-terminal helical domain

NMR – nuclear magnetic resonance

ORC – origin recognition complex

PCNA – proliferating cell nuclear antigen

Pds5 – precocious dissociation of sisters protein 5

PI – propidium iodide

Plk1 – polo-like kinase 1

Pol II – RNA polymerase II

PP2A – serine/threonine protein phosphatase 2A

pre-RC – pre-replication complex

Rec8 – meiotic recombination protein 8

RNAi – RNA interference

RPA – replication protein A

SA1/2 – stromal antigen 1/2

Scc1/2/4 – sister chromatid cohesion protein 1/2/4

SEC – size exclusion chromatography

Sgo1 – shugoshin 1

Smc – structural maintenance of chromosomes

ssDNA – single-stranded DNA

TAD – topologically associating domain

Tipin – Timeless-interacting protein

Tof1 – topoisomerase I interacting factor, yeast homologue of Timeless

TPR – tetratricopeptide repeat

Wapl – wings apart-like protein

WDHD1 – WD repeat and HMG-box DNA binding protein 1

WHD – winged-helix domain

YSR – tyrosine-serine-arginine

CHAPTER I: INTRODUCTION

During the cell cycle, DNA undergoes replication during S phase to generate two identical copies of each chromosome, called sister chromatids. During mitosis, sister chromatids are separated and partitioned evenly to the two daughter cells to maintain genomic stability. Cells receive too many or too few chromosomes become aneuploid. Aneuploidy can drive tumorigenesis in a context-dependent manner (Schvartzman et al., 2010; Solomon et al., 2011). Sister chromatids are physically tethered to each other through the process of sister-chromatid cohesion, as well as DNA catenation, from S phase till metaphase. Sister-chromatid cohesion is mediated by the highly conserved ring-shaped cohesin complex, which topologically entraps chromosomes (Haarhuis et al., 2014; Nasmyth, 2011). Sister-chromatid cohesion prevents premature sister-chromatid separation and ensures accurate chromosome segregation.

Cohesion establishment, maintenance, and removal at different cell cycle phases require a series of coordinated interactions between cohesin and its regulators (Figure 1-1). Cohesin is loaded onto DNA by the cohesin loader complex Scc2–Scc4 in telophase and early G1 (Ciosk et al., 2000; Tonkin et al., 2004; Watrin et al., 2006). At this stage, the chromatin-bound cohesin is highly dynamic, and can be released from chromosomes by the cohesin-releasing factor Wapl, with the help of the scaffold protein Pds5 (Chan et al., 2012; Gandhi et al., 2006; Kueng et al., 2006; Sutani et al., 2009). During S phase, the replicated sister chromatids are tethered by cohesin to establish sister-chromatid cohesion. Cohesion establishment requires the acetylation of two adjacent, evolutionarily conserved lysines on Smc3 by the acetyltransferase Eco1 (Esco1/2 in vertebrates) (Hou and Zou, 2005; Ivanov et al., 2002; Rolef Ben-Shahar et al., 2008;

Rowland et al., 2009; Unal et al., 2008; Zhang et al., 2008a), and in metazoans, the subsequent recruitment of Sororin to cohesin through Pds5 (Lafont et al., 2010; Nishiyama et al., 2010; Rankin et al., 2005; Schmitz et al., 2007). Smc3 acetylation and Sororin antagonize the cohesin-releasing activity of Wapl–Pds5, thereby stabilizing cohesin on chromosomes (Nishiyama et al., 2010; Rowland et al., 2009). Finally, in mitosis, cohesin is released from chromosomes in a stepwise manner in vertebrates (Waizenegger et al., 2000). In early mitosis, Pds5-bound Sororin is phosphorylated by mitotic kinases and dissociates from cohesin (Dreier et al., 2011; Nishiyama et al., 2010; Nishiyama et al., 2013; Zhang et al., 2011). Sororin dissociation allows Wapl to gain access to Pds5 and cohesin, releasing cohesin from chromosome arms. At centromeres, however, a pool of cohesin is shielded from Wapl by the Sgo1–PP2A complex through multiple mechanisms (Hara et al., 2014; Kitajima et al., 2004; Kitajima et al., 2006; Liu et al., 2013b; Riedel et al., 2006; Tang et al., 2006; Tang et al., 2004b). After all sister kinetochores properly attach to microtubules from the opposite spindle poles, Sgo1 redistributes from centromeres to kinetochores (Lee et al., 2008; Liu et al., 2013a), leaving centromeric cohesin unprotected. The unprotected cohesin is cleaved and removed by the protease separase, which becomes active when its inhibitory chaperone securin and cyclin B1 are degraded at the metaphase-anaphase transition (Hauf et al., 2001; Uhlmann et al., 2000). The two separated sets of sister chromatids are equally partitioned to produce two genetically identical daughter cells.

In addition to sister-chromatid cohesion, cohesin performs critical functions in other fundamental chromatin-based processes, including transcription, chromatin compaction, and DNA repair (Remeseiro et al., 2013; Wu and Yu, 2012). Mutations in cohesin and its regulators lead to human diseases termed cohesinopathies, which are characterized by a wide range of

developmental defects, including growth defects, mental retardation, facial anomalies, and other systemic abnormalities (Bose and Gerton, 2010; Mannini et al., 2013; Musio et al., 2006; Tonkin et al., 2004). The pathogenesis of such developmental diseases has been linked to the altered functions of cohesin in transcription regulation during embryogenesis.

ARCHITECTURE OF THE COHESIN COMPLEX

Originally discovered through genetic screens in yeast (Guacci et al., 1997; Michaelis et al., 1997), cohesin components were later found to be highly conserved in all eukaryotes (Losada et al., 1998; Losada et al., 2000; Sumara et al., 2000). In human somatic cells, the cohesin complex consists of four core subunits: Smc1, Smc3, Scc1, and either SA1 or SA2. Smc1 and Smc3 are ATPases related to ABC transporters, and belong to the structural maintenance of chromosomes (Smc) protein family. The ATPase domain of Smc1 or Smc3 is split into two halves by a long coiled coil domain (Figure 1-2). A hinge domain is located at the midpoint of the coiled coil. The coiled coil folds back intramolecularly, allowing the two ATPase halves to form a single globular ATPase head. The ATPase domains of Smc1 and Smc3 bind to two ATP molecules at the interface. Based on the structural and biophysical analyses of the ABC transporters (Chen, 2013; Deshpande et al., 2016; Lammens et al., 2011), ATP hydrolysis and nucleotide release are expected to drive apart the two ATPase domains of cohesin. The hinge domains of Smc1 and Smc3 mediate their heterodimerization.

The ATPase heads of Smc1 and Smc3 are connected by sister chromatid cohesion protein 1 (Scc1), a member of the kleisin protein family, forming a tripartite ring. Recent structural and biochemical studies have revealed that this Smc1–Smc3–Scc1 tripartite ring is asymmetric (Figure 1-2) (Gligoris et al., 2014; Huis in 't Veld et al., 2014). The C-terminal region of Scc1 had been shown previously to form a winged-helix domain (WHD) that interacts directly with the Smc1 ATPase head (Haering et al., 2004). By contrast, the N-terminal region of Scc1 folds

into two helices, which form a four-helix bundle with the coiled-coil region adjacent to the Smc3 ATPase head (Gligoris et al., 2014).

The central region of Scc1 associates with either SA1 or SA2 in vertebrates, two homologues of yeast Scc3. Recently, the crystal structures of human SA2 bound to the central region of Scc1 and free yeast Scc3 were determined (Hara et al., 2014; Roig et al., 2014). These structures showed that SA2/Scc3 is a HEAT repeat-containing protein shaped like a dragon (Figure 1-2). The central region of Scc1 folds into several short helices and binds to SA2 through an extensive binding interface, with many residues at the interface being highly conserved (Hara et al., 2014). In addition to strengthening the tripartite ring of cohesin, SA2 serves as a binding platform for multiple cohesin regulators, including Wapl and Sgo1.

In vitro reconstitution and single-molecule studies have convincingly demonstrated that cohesin can topologically entrap DNA inside its ring structure (Davidson et al., 2016; Kanke et al., 2016; Murayama and Uhlmann, 2014; Stigler et al., 2016). Crosslinking experiments using yeast mini-chromosomes suggest that cohesin mediates cohesion by topologically embracing both sister chromatids as a single ring (Haering et al., 2008; Ivanov and Nasmyth, 2005). The cohesin ring has a diameter of about 30-40 nm when it is fully open (Huis in 't Veld et al., 2014). However, the functional pore of cohesin cannot be larger than about 19 nm when cohesin associates with chromatin (Stigler et al., 2016). The DNA-binding proteins and nucleosomes can significantly hinder the translocation of cohesin along DNA. Both the loading of cohesin onto DNA and its release from DNA thus require the opening of the ring. There are three possible gates in the entire ring: the Smc1–Smc3 hinge, the Smc1–Scc1 gate, and the Smc3–Scc1 gate (Figure 1-2). The crystal structures of all three gates have been determined. Evidence in both

yeast and human cells suggests that cohesin loading onto chromatin involves the opening of the Smc1–Smc3 hinge (Buheitel and Stemmann, 2013; Gruber et al., 2006). Thus, the Smc1–Smc3 hinge has been proposed to be the DNA entry gate of cohesin. Recent findings suggest the Smc3-Scc1 interface as an alternative DNA entry gate (Murayama and Uhlmann, 2015). However, this new model needs to be reconciled with the sufficient cohesin loading for the establishment of sister-chromatid cohesion when Smc3 and Scc1 are covalently fused.

Several lines of recent evidence suggest that the Smc3–Scc1 gate is the DNA exit gate of cohesin. In yeast, fusion of Smc3 to the N-terminal region of Scc1 protects cohesin from its releasing activity in interphase (Chan et al., 2012). In human cells, artificially tethering Smc3 to Scc1 results in persisting cohesin on chromosome arms in prophase and prometaphase (Buheitel and Stemmann, 2013), suggesting that the Smc3–Scc1 fusion blocks the action of Wapl-dependent cohesin release in the prophase pathway. Additionally, mutations that destabilize the Smc3–Scc1 interface abolish the stable interaction between cohesin and chromatin, and disrupt sister-chromatid cohesion in human cells (Huis in 't Veld et al., 2014). Furthermore, recent studies in yeast provide direct evidence that the engineered N-terminal fragment of Scc1 is release from Smc3 in a Wapl-Pds5-dependent manner (Beckouet et al., 2016; Murayama and Uhlmann, 2015). Therefore, the Smc3–Scc1 interface is the conserved DNA exit gate of cohesin. Why DNA enters and exits cohesin through two different gates remains a mystery.

All members in the Smc protein family contribute to the organization of chromosomes and maintenance of genome integrity. In addition to the Smc1–Smc3 heterodimer in cohesin, the Smc2–Smc4 heterodimer is a part of the condensin complex that mediates chromosome condensation while the Smc5–Smc6 complex has multiple functions in DNA damage repair

(Hirano, 2006; Wu and Yu, 2012). The extrusion of DNA by Smc proteins has recently been proposed to mediate the formation of topologically associated domains (TADs) (Fudenberg et al., 2016; Sanborn et al., 2015), which are important structural and functional features of human interphase chromosomes. Consistent with this DNA loop extrusion model, crystallographic and in vivo cross-linking studies on prokaryotic Smc proteins suggested that Smc proteins have two distinct conformations: the rod-shaped Smc dimer in the absence of ATP and ring-shaped Smc dimer in the presence of ATP (Soh et al., 2015). Recurrent switching between these two conformations has been proposed to drive the chromosomal loading of Smc proteins and possibly the formation of DNA loops.

COHESIN-ASSOCIATED REGULATORS

Being the core subunits of the cohesin complex, Smc1, Smc3, Scc1, and SA1/2 are essential for sister-chromatid cohesion. Apart from the four core subunits, several additional proteins are identified as cohesin-associated regulators that interact with cohesin transiently and often in a cell cycle-regulated manner. These regulators include the Scc2-Scc4 complex, Pds5, Wapl, Sgo1, and in metazoans, Sororin, many of which interact with the Scc1–SA1/2 heterodimer in cohesin. These regulatory proteins determine the mode and dynamics of cohesin association with chromosomes.

The precocious dissociation of sisters protein 5 (Pds5) is a highly conserved, large HEAT repeat-containing protein that folds into a hook-like structure (Hartman et al., 2000; Lee et al., 2016; Muir et al., 2016; Ouyang et al., 2016; Panizza et al., 2000). Recent structural studies have shown that Pds5 directly interacts with the N-terminal region of Scc1, which is close to the Smc3-Scc1 interface (Lee et al., 2016; Muir et al., 2016; Ouyang et al., 2016). In one study of human Pds5B structure, inositol hexakisphosphate (IP_6) was identified as a structural cofactor of Pds5, which is required for the structural integrity of Pds5 and Pds5-cohesin interaction both *in vitro* and in human cells (Ouyang et al., 2016). In vertebrates, there are two Pds5 homologues, Pds5A and Pds5B (Losada et al., 2005). Pds5 performs both positive and negative functions in sister-chromatid cohesion in multiple organisms, possibly through recruiting both positive regulators (such as Eco1 and Sororin) and negative regulators (such as Wapl) to cohesin. Indeed, a conserved site on Pds5 has been identified to bind mutually exclusively to Wapl or Sororin (Ouyang et al., 2016). In the budding yeast, Pds5 is essential for cell viability and for cohesion

establishment and maintenance (Chan et al., 2013; Hartman et al., 2000; Panizza et al., 2000). In both budding and fission yeast, Pds5 also interacts with Wapl to mediate cohesin release from chromosomes, and as such, suppressor mutations in Pds5 bypass the requirement for Eco1-mediated Smc3 acetylation during cohesion establishment (Rowland et al., 2009; Sutani et al., 2009; Tanaka et al., 2001). In *Xenopus* egg extracts, Pds5 collaborates with Wapl to facilitate the release of cohesin from chromatin and promotes sister-chromatid resolution during early mitosis (Shintomi and Hirano, 2009). Pds5A- and Pds5B-deficient mice have developmental abnormalities (Carretero et al., 2013; Zhang et al., 2007), and both Pds5A and Pds5B are shown to contribute to sister-chromatid cohesion in mouse cells (Carretero et al., 2013). In human cells, Pds5 is required for Smc3 acetylation and subsequent Sororin association with cohesin (Minamino et al., 2015; Ouyang et al., 2016), suggesting that it should be required for cohesion establishment. However, few or no cohesion defects were observed in Pds5A and Pds5B-depleted human cells (Losada et al., 2005; Minamino et al., 2015; Ouyang et al., 2016), possibly due to incomplete depletion and the dual roles of Pds5 in both cohesion establishment and resolution.

The wings apart-like protein (Wapl) protein was initially identified as an important regulator of heterochromatin organization and chromosome segregation in *Drosophila* (Verni et al., 2000), and was subsequently shown to be conserved from yeast to man, with high homology in the C-terminal domain (Kueng et al., 2006). Crystal structures of human and fungal Wapl proteins reveal that the C-terminal domain of Wapl consists of HEAT repeats, which form functionally important surfaces for cohesin binding (Chatterjee et al., 2013; Ouyang et al., 2013). The N-terminal region of Wapl appears to be flexible and provides additional interactions with

both cohesin and Pds5 (Ouyang et al., 2013). Wapl is a key negative regulator of cohesin, and promotes cohesin release from chromatin, presumably through opening the DNA exit gate at the Smc3–Scc1 interface (Beckouet et al., 2016; Huis in 't Veld et al., 2014; Murayama and Uhlmann, 2015). In all organisms, Wapl inactivation largely bypasses the requirement for positive cohesion factors, including Eco1, Sororin, and Sgo1, in cohesion (Gandhi et al., 2006; Kueng et al., 2006; Nishiyama et al., 2010; Rowland et al., 2009). In interphase cells, Wapl is associated with cohesin through the scaffold protein Pds5, and mediates the dynamic association of cohesin with chromatin (Chan et al., 2012; Kueng et al., 2006). Ablation of Wapl in mouse cells leads to the clustering of cohesin and causes improper chromatin compaction that impedes transcription (Tedeschi et al., 2013). In early mitosis, Wapl triggers cohesin release from chromosome arms. This activity of Wapl promotes sister-chromatid decatenation, spares cohesin from further cleavage by separase, and preserves intact cohesin for the next cell cycle (Haarhuis et al., 2013; Tedeschi et al., 2013).

Sororin was initially discovered as a substrate of the anaphase-promoting complex or cyclosome (APC/C), a multi-subunit ubiquitin ligase complex (Rankin et al., 2005). As a positive regulator of cohesin, Sororin is required for the establishment and maintenance of sister-chromatid cohesion (Rankin et al., 2005; Schmitz et al., 2007). During DNA replication, Sororin is recruited to cohesin through Pds5 in a process that requires Smc3 acetylation, and antagonizes the function of Wapl to stabilize cohesin on chromosomes (Nishiyama et al., 2010). So far, Sororin homologues have only been found in metazoans, not in yeast. The N-terminal flexible region of Wapl proteins in metazoans is much longer than that in yeast. Recently, a conserved tyrosine-serine-arginine (YSR) motif was identified and mapped in Sororin and the N-terminal

region of Wapl (Ouyang et al., 2016). The YSR motifs of Sororin and Wapl bind to the same conserved site on Pds5 and compete for Pds5 binding (Ouyang et al., 2016). This explains how Sororin and Wapl antagonistically regulate cohesin dynamics and sister-chromatid cohesion during cell cycle. The co-emergence of Sororin and the longer N-terminal region of Wapl during evolution offers an additional layer of regulation in sister-chromatid cohesion in higher eukaryotes.

COHESIN LOADING ONTO DNA

Cohesin is loaded onto DNA soon after chromosome segregation and prior to DNA replication. This process is mediated by the cohesin loading complex Scc2–Scc4 (Ciosk et al., 2000; Tonkin et al., 2004; Watrin et al., 2006). Mutations in Scc2 (also known as NIPBL) in humans cause a severe developmental disorder called Cornelia de Lange Syndrome (CdLS), which is a form of cohesinopathy (Krantz et al., 2004; Tonkin et al., 2004). Scc2 contains an N-terminal disordered region that binds to Scc4 and a C-terminal HEAT repeat domain (Chao et al., 2015; Hinshaw et al., 2015). The crystal structures of yeast Scc4 in complex with Scc2-N revealed that the TPR repeats of Scc4 adopts a barrel shape and encapsulates the N-terminal region of Scc2 inside the barrel, thus protecting this flexible region of Scc2 (Chao et al., 2015; Hinshaw et al., 2015). Recently, two research groups determined the crystal structure of conserved C-terminal region of Scc2 (Chao et al., 2017; Kikuchi et al., 2016). The helical repeats of Scc2-C fold into a hook-shaped structure, which is reminiscent of the structures of Scc3 (SA1 or SA2 in vertebrates) and Pds5. Crosslinking and mass spectrometry suggest that Scc2-Scc4 complex makes extensive contacts with cohesin (Chao et al., 2017). Specifically, the conserved C-terminal region of Scc2 has been shown to compete with Pds5 for the same binding site at the N-terminal region of Scc1 (Kikuchi et al., 2016). Many cohesinopathy mutations target conserved residues in the C-terminal region of Scc2 and diminish Scc2 binding to Scc1 (Kikuchi et al., 2016).

In the Scc2-Scc4 complex, Scc4 is required for stabilizing Scc2 and targeting Scc2 to defined chromosome loci (Hinshaw et al., 2015), and Scc2 is critical for catalyzing cohesin

loading (Murayama and Uhlmann, 2014). Using purified fission yeast cohesin and the Scc2–Scc4 loader complex, Murayama and Uhlmann reconstituted topological cohesin loading onto DNA *in vitro* (Murayama and Uhlmann, 2014). They showed that cohesin loading required ATP hydrolysis, and that Scc2 stimulated the ATPase activity of Smc1–Smc3. As mentioned above, the Smc1–Smc3 hinge is the proposed DNA entry gate and has to be opened during cohesin loading by Scc2–Scc4. The ATPase heads of Smc1 and Smc3 are located at the opposite end of the ring structure (Figure 1-2). An interesting question is how ATP hydrolysis at one end of the ring opens the hinge region at the other end.

In addition to simply depositing cohesin onto DNA, the Scc2–Scc4 complex ensures that cohesin is loaded at the proper chromosomal location. In mammalian cells, Scc2 (NIPBL) has been shown to form a complex with cohesin and the mediator complex to load cohesin at gene promoters (Kagey et al., 2010). In budding yeast, the chromatin-remodeling complex at promoters of actively transcribing genes recruits the Scc2–Scc4 complex to the nucleosome-free regions, which loads cohesin to maintain proper DNA morphology in these regions (Huang et al., 2004). Furthermore, as mentioned above, a conserved patch on the surface of yeast Scc4 is critical for the recruitment of the Scc2–Scc4 complex to centromeres to build cohesion (Hinshaw et al., 2015), although the centromere receptor of Scc4 has not been identified. In *Xenopus* egg extracts, the pre-replication complex (pre-RC) and the Cdc7–Drf1 kinase (DDK) recruit Scc2–Scc4 to origins of replication to promote cohesin loading (Gillespie and Hirano, 2004; Takahashi et al., 2008; Takahashi et al., 2004).

Instead of staying at sites where they are originally loaded by the loader complex, cohesin rings are ultimately positioned to sites of convergent transcription in yeast and at CCCTC-

binding factor (CTCF) sites in mammalian cells (Lengronne et al., 2004; Merkenschlager and Odom, 2013; Rubio et al., 2008; Wendt et al., 2008). CTCF recognizes DNA sequences containing CCCTC repeats with its zinc finger domains, and plays important roles in the regulation of chromatin architecture and gene transcription (Merkenschlager and Odom, 2013; Rao et al., 2014; Vietri Rudan et al., 2015). CTCF has been proposed to cooperate with cohesin to induce the formation of chromatin loops exclusively at the convergent CTCF sites with specific orientations (de Wit et al., 2015). Recent Hi-C analysis demonstrated that the Scc2-Scc4 complex promotes the extension of chromatin loops and the formation of TADs, while Wapl restricts the loop extension and prevents looping between incorrectly oriented CTCF sites (Haarhuis et al., 2017). In addition, transcriptional machinery actively pushes cohesin rings along chromosomes in budding yeast and mouse fibroblasts (Busslinger et al., 2017; Lengronne et al., 2004), until cohesin encounters CTCF. These results explain how cohesin is translocated from the original Scc2–Scc4 loading sites to CTCF sites. However, the accumulation of cohesin at CTCF sites is not required for sister-chromatid cohesion, as depletion of CTCF does not cause cohesion defects (Wendt et al., 2008). This CTCF-dependent enrichment of cohesin at defined genomic loci has a specific role in transcription. The mechanism underlying cohesin enrichment at CTCF sites is unclear, but may be a result of a direct interaction between CTCF and the cohesin core subunit SA1/2 (Xiao et al., 2011).

ESTABLISHMENT OF SISTER-CHROMATID COHESION

Fluorescent recovery after photobleaching (FRAP) experiments have shown that cohesin loaded onto DNA in telophase and early G1 turns over rapidly on chromatin in a Wapl–Pds5-dependent manner (Chan et al., 2012; Gerlich et al., 2006; Kueng et al., 2006). At least a pool of cohesin interacts with chromatin much more stably after DNA replication (Gerlich et al., 2006). This stably bound cohesin pool is believed to be cohesive and to generate sister-chromatid cohesion.

A critical factor required for cohesion establishment is the acetyltransferase Eco1/Ctf7 that acetylates Smc3 (Ivanov et al., 2002; Rolef Ben-Shahar et al., 2008; Skibbens et al., 1999; Toth et al., 1999; Unal et al., 2008; Zhang et al., 2008a). In vertebrates, there are two Eco1 orthologs, Esco1 and Esco2, both of which are capable of acetylating Smc3 and contribute to sister-chromatid cohesion (Hou and Zou, 2005; Zhang et al., 2008a). Smc3 acetylation at two conserved lysines is required for cohesion establishment in yeast and in vertebrates, because acetylation-mimicking Smc3 mutations bypass the requirement of Eco1 in cohesion (Rolef Ben-Shahar et al., 2008; Wu et al., 2012; Zhang et al., 2008a). In yeast, mutations in Wapl, Pds5, and Scc3 bypass the requirement for Eco1 and rescue the lethality of *eco1* mutants (Rolef Ben-Shahar et al., 2008; Rowland et al., 2009). Thus, acetylation of Smc3 likely counteracts the cohesin-releasing activities of Wapl, Pds5, and Scc3, thereby stabilizing cohesin on chromosomes to establish cohesion. In human cells, Sororin is additionally recruited to the acetylated cohesin and further shields cohesin from Wapl (Nishiyama et al., 2010). Sororin-bound cohesin is more stably associated with chromatin, and is believed to mediate sister-

chromatid cohesion. As mentioned previously, Sororin homologues have so far only been found in vertebrates and in Drosophila, but not in yeast. Recent findings have shown that the N-terminal acetyltransferase Naa50/San is required for the recruitment of Sororin to cohesin in metazoans (Rong et al., 2016). The physiological substrate of Naa50 in cohesion is unknown, but it can acetylate the N-terminal a-amino group of Scc1. It is possible that this co-translational modification is required for sister-chromatid cohesion (Ribeiro et al., 2016; Rong et al., 2016).

Because the two acetylated lysine residues are located close to the active site of the Smc3 ATPase domain, it is conceivable that Smc3 acetylation may block the releasing activities by inhibiting the ATPase activity of cohesin (Gligoris et al., 2014). On the other hand, Esco1-dependent acetylation or the acetylation-mimicking mutation of purified recombinant human cohesin does not reduce its ATPase activity (Ladurner et al., 2014). Instead, Smc3 acetylation is strictly dependent on the ATPase activity of cohesin, and is coupled to the loading of cohesin onto DNA by the Scc2–Scc4 complex (Ladurner et al., 2014). What is the molecular basis of cohesin acetylation in stabilizing cohesin on chromosome to enable sister-chromatid cohesion? Recent findings showed that cohesin topologically bound to DNA has higher ATPase activity (Murayama and Uhlmann, 2015). Acetylation-mimicking Smc3 mutations prevent the stimulation of ATPase activity by DNA (Murayama and Uhlmann, 2015), which is a prerequisite for Wapl-Pds5-dependent cohesin release from chromosomes (Camdere et al., 2015; Elbatsh et al., 2016; Yu, 2016). These results raise the possibility that DNA entrapped inside the Smc1-Smc3 closure might direct contact the two lysine residues on Smc3 to stimulate the ATPase activity of cohesin. Smc3 acetylation neutralizes the positive charge of the lysine residues, weakens DNA binding, inhibits DNA-dependent ATP hydrolysis, and prevents the subsequent

cohesin release by Wapl-Pds5 (Murayama and Uhlmann, 2015; Ouyang and Yu, 2017; Yu, 2016).

The finding that cohesin acetylation is coupled to its loading suggests that this modification is unlikely to be the sole regulated step in cohesion establishment during S phase. Indeed, cohesin acetylation can occur efficiently before and after DNA replication in *Xenopus* egg extracts (Song et al., 2012). In human cells, Esco1 has been shown to constitutively co-localize with and mediate the acetylation of cohesin at CTCF sites throughout the cell cycle (Minamino et al., 2015; Rahman et al., 2015). This replication-independent cohesin acetylation mediates gene silencing (Rahman et al., 2015). Thus, Smc3 acetylation is necessary but not sufficient for cohesion establishment.

It is possible that only Smc3 acetylation coupled to DNA replication can establish sister-chromatid cohesion (Figure 1-3). Consistent with this hypothesis, Eco1 is recruited to the replication fork through an interaction with PCNA in yeast, and the Eco1–PCNA interaction has been reported to be critical for sister-chromatid cohesion (Moldovan et al., 2006). Similarly, the interaction between Esco2 and PCNA has been proposed to be required for cohesion establishment in *Xenopus* egg extracts (Song et al., 2012). In addition to PCNA, a large number of proteins with known roles in DNA replication are required for sister-chromatid cohesion (Borges et al., 2013; Peters and Nishiyama, 2012; Sherwood et al., 2010). It remains unclear, however, how cohesion establishment is coupled to DNA replication.

COHESIN RELEASE FROM CHROMOSOMES

Timely dissolution of sister-chromatid cohesion in mitosis is critical for accurate chromosome segregation. If cohesion dissolution occurs too early, sister chromatids separate prematurely, and cells undergo spindle checkpoint-dependent arrest in mitosis (Tang et al., 2004b). If cohesion removal happens too late, incomplete sister-chromatid separation leads to lagging chromosomes and aneuploidy in daughter cells. Therefore, cohesive cohesin stably bound to chromatin has to be released in a highly regulated manner. As mentioned previously, cohesin is released from chromosomes in two steps during mitosis in vertebrates (Figure 1-1). In the first step, Wapl removes the majority of cohesin from chromosome arms in the prophase pathway, but spares a small pool of cohesin at centromeres. In the second step, the centromeric cohesin is cleaved by the protease separase.

When cells entering mitosis, mitotic kinases are activated, and phosphorylate cohesin and its associated regulators (Hegemann et al., 2011). Phosphorylation of SA2 by Plk1 and phosphorylation of Sororin by Cdk1 and Aurora B have been shown to be required for efficient cohesin release by Wapl (Dreier et al., 2011; Hauf et al., 2005; Liu et al., 2013b; Nishiyama et al., 2010; Nishiyama et al., 2013). While it is unclear how SA2 phosphorylation stimulates Wapl-dependent release, phosphorylation of Sororin disrupts its interaction with Pds5 and cohesin (Nishiyama et al., 2010). Sororin dissociation allows Wapl to gain access to Pds5 and to remove cohesin from chromosomes presumably through opening the Smc3–Scc1 interface.

Because DNA is entrapped inside the Smc1-Smc3 closure as revealed in the presence of ATPγS in vitro (Murayama and Uhlmann, 2015), cohesin release requires the sequential

disengagement of Smc ATPase domains and the opening of Smc3-Scc1 interface by Wapl-Pds5. In a recent study, a point mutation in Smc1 at the apical site of the ATPase domain, but not an Smc3 mutation at the basal site, was shown to inhibit the opening of the Smc3-Scc1 interface, whereas both mutants were deficient in ATP hydrolysis (Beckouet et al., 2016; Elbatsh et al., 2016). These findings demonstrated an asymmetric requirement for the hydrolysis of two ATP molecules in Wapl-Pds5-mediated opening of the DNA exit gate. Therefore, DNA-dependent ATP hydrolysis at the apical site will disengage the ATPase domains and allow DNA to escape from the closure of Smc1 and Smc3. The mechanism by which Wapl-Pds5 opens the DNA exit gate of cohesin still remains elusive. Intriguingly, Wapl-Pds5 triggers the dissociation of N-terminal of Scc1 from Smc3 in the presence of ATP, but ATP hydrolysis is not required for this process (Murayama and Uhlmann, 2015). Therefore, Wapl-Pds5 most likely promotes cohesin release when the Smc1-Smc3 interface is closed again. In this scenario, the Smc3-Scc1 interaction might be unfavorable when the ATPase domains of Smc1 and Smc3 are engaged for steric reasons. The HEAT repeat-containing proteins Pds5, Wapl together with SA1/2 might act as the scaffold to rigidify Scc1, and therefore prevent Scc1 from moving with Smc3 when the Smc1 and Smc3 ATPase domains are held by ATP binding (Ouyang and Yu, 2017). In addition, Pds5 directly binds to the N-terminal region of Scc1 in competition with the Smc3 ATPase head, thus promoting ring opening or stabilizing the open form of the cohesin ring (Ouyang et al., 2016).

Cohesin released in the prophase pathway can be deacetylated by HDAC8 in mammalian cells, and deposited onto DNA in the next cell cycle (Deardorff et al., 2012). Recent structural and biochemical analyses have shown that Scc2 competes with Pds5 for the same binding site on

Scc1 (Kikuchi et al., 2016). This raises the possibility that Scc2-Scc4 displaces Wapl-Pds5 from cohesin and promotes cohesin loading onto chromosomes, while Wapl-Pds5 frees Scc2-Scc4 from loaded cohesin and contributes to cohesin release from chromosomes. The switching of binding partners of Scc1 between Scc2-Scc4 and Wapl-Pds5 promotes the dynamics of cohesin on chromosomes and allows for the temporal and spatial regulation of sister-chromatid cohesion.

By metaphase, only cohesin at centromeres is preserved by the Sgo1–PP2A complex (Kitajima et al., 2006; Tang et al., 2006). Sgo1 is initially recruited to kinetochores through directly binding to the H2A-pT120 histone mark added by the mitotic kinase Bub1 (Kawashima et al., 2010; Liu et al., 2013a; Liu et al., 2015). RNA Polymerase II-dependent transcription then drives Sgo1 from kinetochores to centromeres, where it directly binds to cohesin (Liu et al., 2015). The Sgo1–cohesin interaction also requires Cdk1-dependent phosphorylation of Sgo1 and specifically occurs during mitosis (Liu et al., 2013b). Sgo1 competes with Wapl for binding to a conserved site on SA2–Scc1 and directly shields cohesin from Wapl (Hara et al., 2014). In addition, Sgo1 also bridges an interaction between cohesin and PP2A and protects Sororin from hyperphosphorylation by mitotic kinases (Liu et al., 2013b). This preserves the binding of Sororin to cohesin and Pds5, which also antagonizes Wapl-dependent cohesin release (Ouyang et al., 2016). Moreover, the mitotic histone kinase Haspin at centromeres has recently been shown to bind to Pds5 through a conserved YSR motif in its N-terminal non-kinase domain (Goto et al., 2017; Zhou et al., 2017), in a way analogous to the YSR motif-dependent binding of Sororin or Wapl to Pds5. This Haspin-Pds5 interaction prevents Wapl-mediated cohesin removal and ensures proper sister-chromatid cohesion at centromeres. These mechanisms collaborate to

protect centromeric cohesion to the fullest extent to resist the spindle pulling force at sister kinetochores.

After all sister kinetochores are properly attached to microtubules emanating from the opposite spindle poles and are under tension, the spindle checkpoint is silenced, and the checkpoint target, APC/C bound to its mitotic activator Cdc20 (APC/C^{Cdc20}), becomes active (Jia et al., 2013; London and Biggins, 2014). APC/C^{Cdc20} mediates the ubiquitination of two key separase inhibitors, securin and cyclin B1, resulting in their degradation by the proteasome and leading to separase activation (Stemmann et al., 2001; Zou et al., 1999). Recently, the structures of active separase and the separase-securin complex explained how separase is inhibited by the pseudo-substrate securin and how its catalytic domain specifically recognizes and cleaves its substrate under the regulation of phosphorylation (Boland et al., 2017; Lin et al., 2016; Luo and Tong, 2017). Concurrent with separase activation, Pol II localization at metaphase kinetochores is also diminished (Liu et al., 2015). As a result, Sgo1 redistributes from centromeres to kinetochores, leaving cohesin at centromeres unprotected. Active separase then cleaves Scc1 at two different sites and releases centromeric cohesin from chromatin, triggering anaphase onset (Hauf et al., 2001). In yeast, the prophase pathway is not prominent, and most cohesin is cleaved by separase at the metaphase–anaphase transition to enable chromosome segregation (Uhlmann et al., 1999).

How does separase specifically recognize and cleave chromatin-bound centromeric cohesin while sparing soluble cohesin released in the prophase pathway? Biochemical analysis *in vitro* showed that separase binds to DNA directly, and cohesin cleavage by separase is stimulated by DNA (Sun et al., 2009). This finding provides a possible explanation for why only chromatin-

bound cohesin is cleaved by separase, allowing the bulk of cohesin released by Wapl in prophase to remain intact and to be recycled in the next cell cycle. Moreover, a recent study showed that the phosphorylation-dependent peptidyl-prolyl cis/trans isomerase Pin1 catalyzes a conformational change of separase, presumably involving a proline cis/trans isomerization event (Hellmuth et al., 2015). In early mitosis, Pin1 is required for cyclin B1–Cdk1-dependent inhibition of separase. Pin1-mediated isomerization also limits the half-life of active separase following chromosome segregation in late mitosis. Finally, separase is excluded from the nucleus by nuclear export (Sun et al., 2006). In conjunction with securin-dependent inhibition, these regulatory mechanisms fine-tune the proteolytic activity of separase and ensure that active separase cleaves and only cleaves cohesin at centromeres during the metaphase–anaphase transition, but not at other stages of the cell cycle.

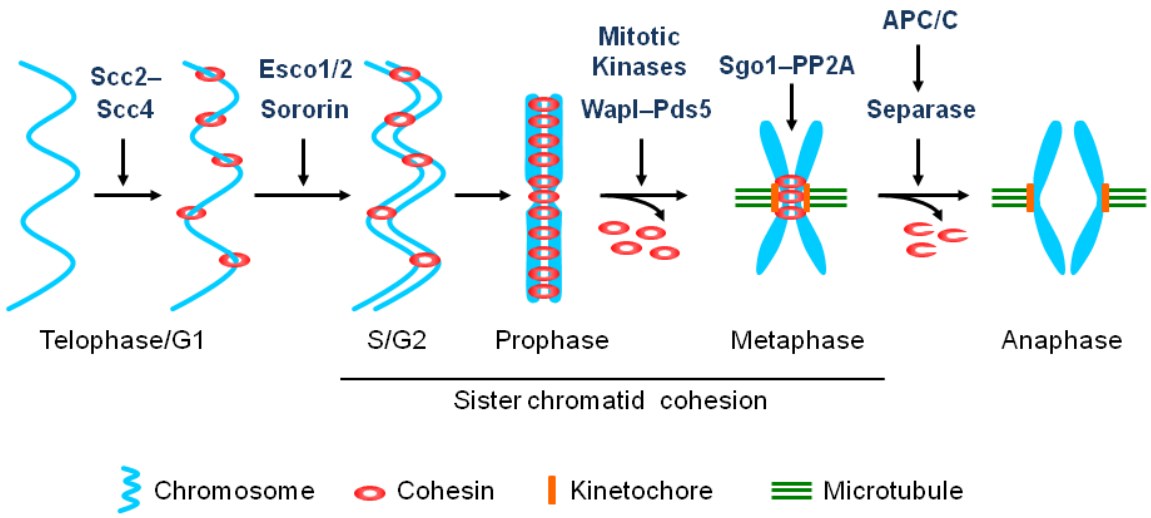

Figure 1-1. The cohesin cycle in human cells. The Scc2–Scc4 complex promotes cohesin loading onto chromosomes in telophase and early G1. During DNA replication in S phase, Esco1/2 and Sororin are required to stabilize cohesin on chromosomes and help to establish sister-chromatid cohesion. In prophase, cohesin on chromosome arms are released by mitotic kinases and the Wapl–Pds5 complex, whereas cohesin at centromeres is protected by Sgo1–PP2A until the metaphase–anaphase transition. After kinetochores attach to microtubules from opposite spindle poles and the spindle checkpoint is silenced, active separase cleaves centromeric cohesin and enables sister chromatid separation in anaphase.

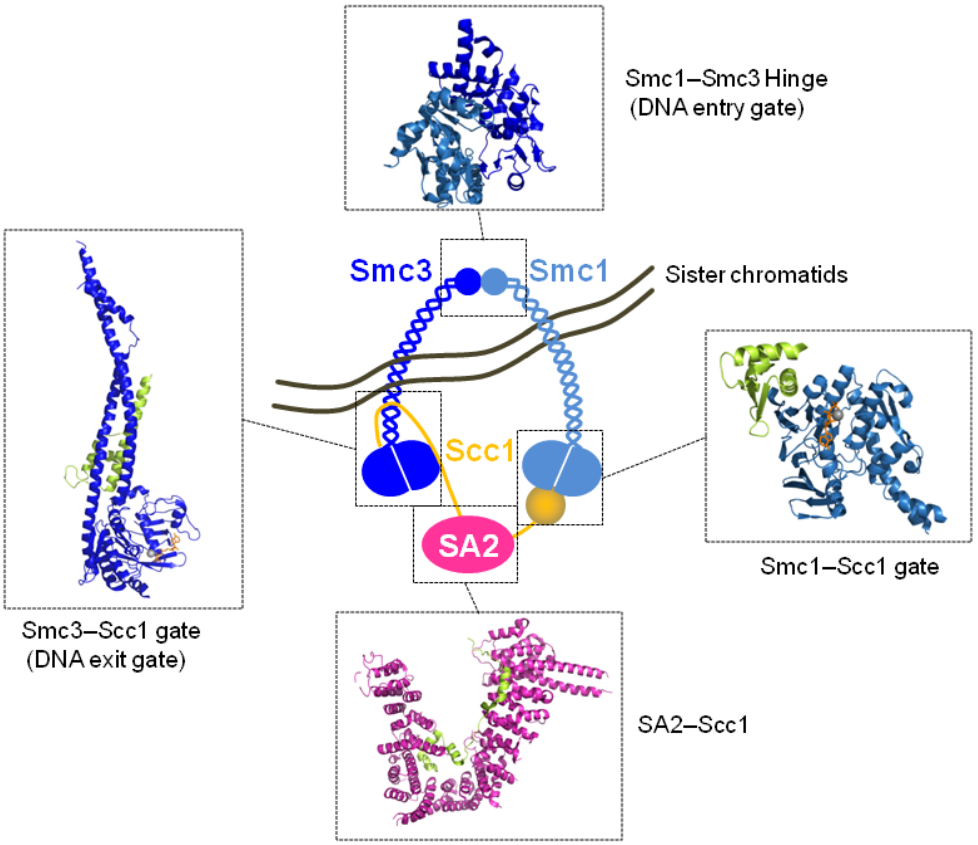

Figure 1-2. The architecture of the cohesin complex. Smc1, Smc3, Scc1, and SA1 or SA2 are core subunits of cohesin in human cells. They form a ring-shaped structure to topologically entrap sister chromatids. Crystal structures of all three potential gates of the cohesin ring (from different species) and the structure of SA2 bound to the central region of Scc1 have been determined, and are shown in ribbon diagrams.

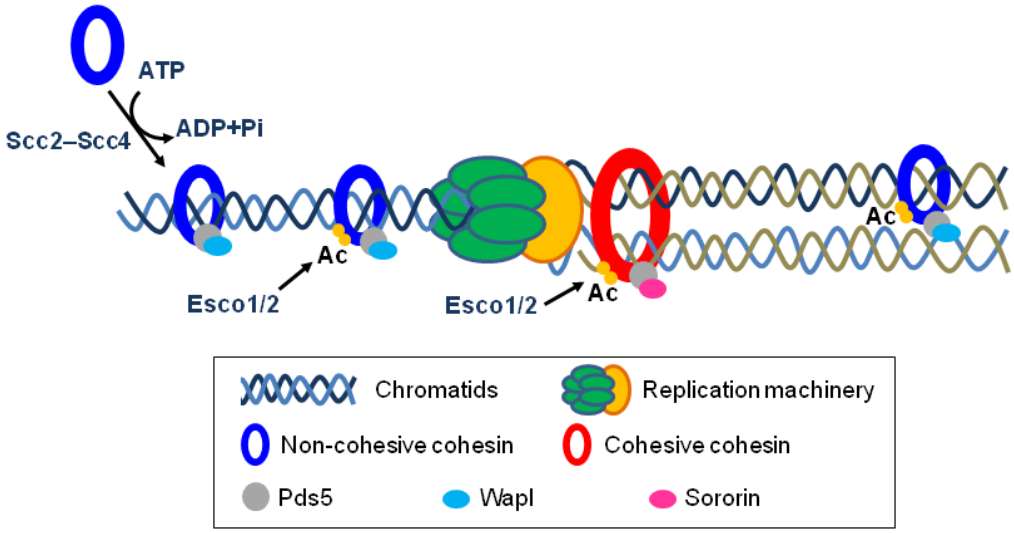

Figure 1-3. Critical steps involved in cohesion establishment. Cohesin is deposited onto DNA by the Scc2-Scc4 complex and acetylated by Eco1 in yeast and Esco1/2 in human cells. The ATPase activity of cohesin is required in both steps. Cohesin acetylation can occur independently of DNA replication, but only acetylation in association with the replication machinery enables the establishment of sister-chromatid cohesion. In metazoans, cohesion establishment also requires the binding of Sororin to acetylated cohesin.

CHAPTER II: STRUCTURE OF THE HUMAN COHESIN INHIBITOR WAPL

INTRODUCTION

Proper chromosome segregation during mitosis maintains genomic stability. Errors in this process cause aneuploidy, which contributes to tumorigenesis under certain contexts (Schvartzman et al., 2010). Timely establishment and dissolution of sister-chromatid cohesion are critical for accurate chromosome segregation and require the cell-cycle–regulated interactions between cohesin and its regulators (Nasmyth, 2011; Onn et al., 2008; Peters et al., 2008).

In human cells, cohesin consists of four core subunits: Structural maintenance of chromosomes 1 (Smc1), Smc3, sister chromatid cohesion protein 1 (Scc1), and stromal antigen 1 or 2 (SA1/2). Smc1 and Smc3 are related ATPases, and each contains an ATPase head domain, a long coiled-coil domain, and a hinge domain that mediates Smc1-Smc3 heterodimerization. The Smc1-Smc3 heterodimer associates with the Scc1-SA1/2 heterodimer to produce the intact cohesin. Specifically, the N- and C-terminal winged helix domains (WHDs) of Scc1 connect the ATPase domains of Smc3 and Smc1, respectively, forming a ring (Nasmyth, 2011).

Cohesin is loaded onto chromatin in telophase/G1, but the chromatin-bound cohesin at this stage is highly dynamic and is actively removed from chromatin by the cohesin inhibitor Wings apart-like protein (Wapl) (Gandhi et al., 2006; Kueng et al., 2006; Verni et al., 2000). During DNA replication in S phase, the ATPase head domain of Smc3 is acetylated by the acetyltransferase establishment of cohesion protein 1 (Eco1) (Hou and Zou, 2005; Ivanov et al.,

2002; Rolef Ben-Shahar et al., 2008; Rowland et al., 2009; Unal et al., 2008; Zhang et al., 2008a). In vertebrates, replication-coupled Smc3 acetylation enables the binding of precocious dissociation of sisters protein 5 (Pds5) and Sororin to cohesin (Lafont et al., 2010; Nishiyama et al., 2010; Rankin et al., 2005; Schmitz et al., 2007). Sororin counteracts Wapl to stabilize cohesin on replicated chromatin and establishes sister-chromatid cohesion (Nishiyama et al., 2010). In prophase, polo-like kinase 1 (Plk1) and cyclin-dependent kinase 1 (Cdk1) phosphorylate cohesin and Sororin and trigger cohesin release from chromosome arms (Dreier et al., 2011; Hauf et al., 2005; Nishiyama et al., 2010; Waizenegger et al., 2000; Zhang et al., 2011). A pool of cohesin at centromeres is protected by the shugoshin (Sgo1)-protein phosphatase 2A (PP2A) complex (Kitajima et al., 2006; Tang et al., 2006), which binds to cohesin, dephosphorylates Sororin, and protects cohesin from Wapl at centromeres (Liu et al., 2013b). After all sister kinetochores attach properly to the mitotic spindle and are under tension, separase cleaves centromeric cohesin to initiate sister-chromatid separation. The separated chromatids are evenly partitioned into the two daughter cells through their attachment to microtubules originating from the opposite spindle poles. Wapl inactivation alleviates both the requirement for Sororin in cohesion establishment in S phase and the need for Sgo1-PP2A in centromeric cohesion protection in mitosis (Gandhi et al., 2006; Kueng et al., 2006; Liu et al., 2013b; Nishiyama et al., 2010). Thus, Wapl is a critical negative regulator of cohesin.

Wapl-triggered cohesin release from chromatin requires the opening of the cohesin ring at the junction between the Smc3 ATPase domain and the N-terminal WHD of Scc1 in budding yeast, fly, and humans (Buheitel and Stemmann, 2013; Chan et al., 2012; Eichinger et al., 2013). Furthermore, the structure of the C-terminal domain of Wapl from the filamentous fungus

Ashbya gossypii has recently been determined (Chatterjee et al., 2013). The fungal Wapl proteins bind to the isolated Smc3 ATPase domain. It has been suggested that Wapl might trigger cohesin release from chromatin through stimulating the ATPase activity of cohesin, although this hypothesis remains to be biochemically tested.

In this study, we have determined the crystal structure of human Wapl (HsWapl). We have also systematically mapped the functional surface of Wapl using structure-based mutagenesis and performed in-depth functional and biochemical analyses of key Wapl mutants. Our results indicate that Wapl-mediated cohesin release from chromatin requires extensive physical contacts among Wapl, multiple cohesin subunits, and possibly an unknown effector. Our study reveals both similarities and important differences between the mechanisms of human and fungal Wapl proteins.

MATERIALS AND METHODS

Protein Expression, Purification, Characterization, and Crystallization

The C-terminal domain of human wings apart-like protein (Wapl-C; residues 631–1190) was expressed as an N-terminal His_6-tag fusion protein in *Escherichia coli* and purified with the Ni^{2+} – nitrilotriacetic acid resin (Qiagen). After treatment with the PreScission protease to remove the His_6 tag, the protein was further purified by anion exchange and size exclusion chromatography (SEC). Purified Wapl-C was concentrated to 11.8 mg/mL and stored at −80 °C. The selenomethionine (SeMet)-labeled Wapl-C was prepared by growing bacteria in M9 minimal medium containing L-selenomethionine and purified as described above for the native protein. The SeMet-labeled protein was concentrated to 7.5 mg/mL.

For protein binding assays and *Xenopus* egg extracts experiments, the full-length human Wapl (HsWapl), its N-terminal truncation mutants, and Wapl-C point mutants were expressed as GST fusion proteins in bacteria and purified by using glutathione–agarose beads. After cleavage of the GST moiety, the N-terminal truncation Wapl mutants were further purified with SEC. The Wapl point mutations were constructed with the QuikChange kit (Qiagen) following manufacturer's protocol.

For SEC coupled with multiangle light scattering (SEC-MALS), a Shimadzu Prominence HPLC system equipped with a Zenix SEC-300 column was connected in line with a miniDAWN-TREOS light scattering instrument (Wyatt Technologies) and an Optilab rEX refractometer (Wyatt Technologies). The light-scattering and refractive index instruments were calibrated by following the manufacturer's guidelines. After equilibrating the column with the

running buffer (pH 8.5) and establishing stable baselines for both the light-scattering and refractive index instruments, 60–75 μg of purified Wapl proteins in 30 μL of running buffer was applied to the column for each SEC-MALS experiment. Data were collected by using the ASTRA V software (Wyatt Technologies) and processed by following the manufacturer's manual.

Human Wapl-C was crystallized at 20 °C by using the sitting-drop vapor-diffusion method. Initial hits were obtained in two conditions: (i) 0.1 M Hepes (pH 7.5) and 1.5 M ammonium sulfate; and (ii) 0.1 M Hepes (pH 7.5) and 1.5 M lithium sulfate. Crystals were optimized by varying the pH and salt concentrations. The optimal crystallization condition was 0.1 M Hepes (pH 7.1), 1.4 M ammonium sulfate, and 10% (vol/vol) glycerol. The crystals were cryoprotected with reservoir solution supplemented with 10–20% (vol/vol) glycerol and then flash-cooled in liquid nitrogen.

Structure Determination

We processed diffraction datasets for both SeMet and native crystals using HKL3000 (Minor et al., 2006). During data processing, we applied computational corrections for absorption in a crystal and imprecise calculations of the Lorentz factor resulting from a minor misalignment of the goniostat (Borek et al., 2003; Otwinowski et al., 2003). We also applied the procedure to correct for the anisotropic diffraction, to adjust the error model, and to compensate the phasing signal for a radiation-induced increase of nonisomorphism within the crystal (Borek et al., 2010; Borek et al., 2013; Borek et al., 2007). These corrections were crucial for successful phasing.

The diffraction data of SeMet Wapl-C crystals were processed to 3.42 Å. The estimated level of anomalous signal was 7.4% of the native intensity to a resolution of 3.5 Å. We performed the search for heavy atom positions to a resolution of 4.8 Å with SHELXD (Schneider and Sheldrick, 2002; Sheldrick, 2008), run within HKL3000. Initially, 42 heavy atom positions were detected, with correlation coefficients CC_{All} = 44.56% and CC_{Weak} = 18.13%. The handedness of the solution was determined with SHELXE by analyzing the connectedness and contrast of the electron density maps. This analysis indicated that crystals exhibited the symmetry of space group $P4_12_12$, with cell dimensions of a = b = 107.540 Å and c = 300.608 Å, and contained two molecules in the asymmetric unit with a solvent content of 65%. Then, 32 positions of heavy atoms were refined to a resolution of 4.1 Å with MLPHARE, with occupancies and temperature factors refined together. We analyzed the heavy atom positions with high temperature factors and decided to refine a subset of them anisotropically, using the initial phases from MLPHARE, and extending them to a resolution of 3.87 Å. This operation allowed us to identify which heavy atom positions should be split into two atoms. After the procedure, the phasing power described by the figure of merit was 0.19.

The phases obtained after the initial refinement of the heavy atom positions with MLPHARE were improved with SOLVE/RESOLVE (Terwilliger, 2004; Terwilliger, 2003), DM (Cowtan and Main, 1998), and PARROT (Cowtan, 2010), each run within HKL3000 using diffraction data to a resolution 3.42 Å. RESOLVE was used to find the operator for the twofold noncrystallographic symmetry axis, which was then introduced to DM to perform density modification with NCS averaging. Then, the Hendrickson Lattman coefficients for the phases obtained by density modification with DM were combined with those for the phases obtained by

initial phasing with MLPHARE. This combination was done in a ratio of 9:1 for the final MLPHARE:DM phases. At this point, we applied the density modification PARROT from the CCP4 suite (Collaborative Computational Project, 1994). The PARROT density modification was followed by iterative model building with BUCCANEER (Cowtan, 2006), also from the CCP4 suite , which built into the electron density two polypeptide chains with 1,020 amino acids (91% of the model) and docking side chains for 928 of them (83% of the model). R_{work} and R_{free} were 32.6% and 39.2%, respectively, at this point.

Protein Binding Assays

For *in vitro* protein binding assays, the ^{35}S-labeled human Smc1, Smc3, the engineered Smc1 ATPase domain, SA2, and Scc1 and its fragments were obtained with *in vitro* translation in rabbit reticulocyte lysates (Promega). Human SA2 (residues 80–1,060) and Sororin (residues 91–252) were expressed in *E. coli* and purified. Pds5B (residues 1–1,120) was expressed in Sf9 insect cells and purified. GST–Wapl proteins were bound to glutathione–agarose beads and incubated with the indicated ^{35}S-labeled or unlabeled proteins. For the binding between Myc–Scc1$^{317–631}$ and HA–Smc1 ATPase domain, Affi-Prep Protein A beads (Bio-Rad) coupled to the anti-HA antibody (Roche) at a concentration of 1 mg/mL were incubated with ^{35}S-labeled Scc1 and Smc1 that had been co-translated *in vitro*. After washing, proteins bound to GST or antibody beads were resolved on SDS/PAGE and analyzed with a phosphorimager (Fuji).

Cell Culture, Transfection, and Synchronization

HeLa Tet-On cells were grown in DMEM (Invitrogen) supplemented with 10% FBS and 2 mM L-glutamine. Plasmid and siRNA transfections were performed with the Effectene reagent (Qiagen) and Lipofectamine RNAiMAX (Invitrogen), respectively, according to the manufacturers' protocols. The siRNA oligonucleotides targeting HsWapl (siWapl; 5'-CGGACTACCCTTAGCACAA-3') and Sgo1 (siSgo1; 5'-GAGGGGACCCUUUUACAGATT-3') were synthesized by Thermo Scientific. The siRNAs were transfected at a final concentration of 5 nM. The Scc1–Myc-expressing stable HeLa Tet-On cell line was described (Wu et al., 2012). Scc1–Myc expression was induced with 1 μg/mL doxycycline (Invitrogen). For mitotic synchronization, cells were treated with 2 mM thymidine for 17 h, released into fresh medium for 9 h, and blocked at mitosis with the addition of 5 μM nocodazole (Sigma) for 2 h.

Immunoblotting, Immunoprecipitation, and Immunofluorescence

For immunoblotting, cells were lysed in SDS sample buffer (pH 6.8), sonicated, and boiled. The lysates were separated by SDS/PAGE and blotted with the indicated antibodies. Horseradish peroxidase-linked donkey anti-rabbit or sheep anti-mouse IgGs (GE Healthcare) were used as the secondary antibodies. Immunoblots were developed by using the SuperSignal West Pico Chemiluminescent Substrate (Thermo Scientific) according to the manufacturer's protocol.

For immunoprecipitation, anti-Myc or anti-GFP were coupled to Affi-Prep Protein A beads (Bio-Rad) at a concentration of 1 mg/mL. Cells were lysed with the lysis buffer containing 25 mM Tris·HCl (pH 7.7), 100 mM NaCl, 0.1% (vol/vol) Nonidet P-40, 2 mM $MgCl_2$, 10% (vol/vol) glycerol, 5 mM NaF, 0.3 mM Na_3VO_4, 10 mM β-glycerophosphate, 1 mM DTT, protease inhibitor mixture (Roche), and 50 units/mL Turbo Nuclease (Accelagen). After 1-h

incubation on ice and 10-min incubation at 37 °C, all samples were centrifuged at 4 °C at 20,817 × g for 20 min. The supernatant was incubated with the antibody beads for 3 h at 4 °C. The beads were then washed three times with the lysis buffer containing 200 mM NaCl. Proteins bound to the beads were dissolved in SDS sample buffer, separated by SDS/PAGE, and blotted with the appropriate antibodies.

For immunofluorescence, cells were plated in four-well chamber slides (LabTek) and transfected with GFP–Wapl plasmids for 24 h, followed by siWapl transfection for another 48 h. Cells were first extracted with PBS containing 0.1% Triton X-100 for 1 min and then fixed in 4% paraformaldehyde for 30 min. After washing twice with PBS, cells were permeabilized with PBS containing 0.2% Triton X-100 and 3% BSA for 20 min, and incubated with appropriate primary antibodies in PBS containing 0.2% Triton X-100 and 3% BSA overnight at 4 °C. After being washed three times with PBS containing 0.2% Triton X-100, cells were incubated with fluorescent secondary antibodies in PBS containing 0.2% Triton X-100 and 3% BSA for 30 min at room temperature. The cells were again washed three times with PBS containing 0.2% Triton X-100 and stained with 1 μg/mL DAPI in PBS for 2 min. After the final washes, slides were mounted and viewed with a 100× objective on a DeltaVision deconvolution fluorescence microscope. A series of z-stack images were captured at 0.5-μm intervals, deconvolved, and projected. Image processing and quantification were performed with ImageJ.

Flow Cytometry

Cells were harvested with trypsinization and fixed in 70% ice-cold ethanol overnight. After being washed with PBS, cells were permeabilized with 0.25% Triton X-100/PBS on ice for 5

min. Then, cells were incubated with anti-MPM2 in PBS containing 1% BSA for 3 h at room temperature, followed by an incubation with Alexa Fluor 488 donkey anti-mouse secondary antibody (Invitrogen) for 30 min. After being washed with PBS, cells were resuspended in PBS containing 0.1% Triton X-100, RNase A, and propidium iodide and analyzed with a flow cytometer. Data were processed with the program FlowJo.

Metaphase Spreads

Synchronized HeLa Tet-On cells were collected by trypsinization, treated with the hypotonic solution (75 mM KCl), and fixed in the fixation solution (methanol/acetic acid, vol/vol: 3:1). After centrifugation, cells were resuspended in the fixation solution, incubated at 4 °C for 20 min, and washed twice with the fixation solution. Cells were then resuspended in the fixation solution and stored at −20 °C. Fixed cells were dropped onto microscope slides, dried at room temperature, and stained with 5% Giemsa staining buffer (pH 6.8). The slides were washed twice with running water, dried for 15–20 min at room temperature, mounted in Entellan mounting solution (Merck), and analyzed.

Chromosome Assembly Reactions in *Xenopus* Egg Extracts

Cytostatic factor (CSF)-arrested egg extracts were depleted with affinity-purified anti-*Xenopus* Wapl (anti-xWapl) antibody or mock depleted with normal rabbit IgG and supplemented as indicated with recombinant wild-type (WT) or mutant GST–HsWapl. Sperm nuclei were added to a concentration of 3,400 nuclei per μL, and the extracts were released into interphase by the addition of $CaCl_2$ to a final concentration of 0.6 mM. After 120 min, the

extracts were driven into mitosis by the addition of 1 vol of freshly prepared Wapl-depleted CSF extract. After an additional 120 min, the chromosomes were isolated as described (Song et al., 2012) and processed for anti-Smc3 immunofluorescence. Images were collected by using a Zeiss AxioImager microscope with band-pass emission filters, a Roper HQ2 CCD, and Axiovision software. Total fluorescence intensity per chromosome was measured by using the Axiovision software, normalized to the DAPI intensity, and plotted by using Prism graphing and analysis software. Distances of $\leqslant$0.2 μm could not be assessed and were scored as 0.2 μm.

Analytical Ultracentrifugation (AUC)

AUC sedimentation velocity experiments were carried out using standard protocols (http://www.analyticalultracentrifugation.com/SVprotocols.htm) and were analyzed using the c(s) distribution (Schuck, 2000).

RESULTS AND DISCUSSION

Crystal Structure of HsWapl

Wapl proteins from different species each have a divergent N-terminal domain with variable lengths and a conserved C-terminal domain (Wapl-C) (Figure 2-1A). To gain insight into the mechanism of Wapl-dependent cohesin release from chromatin, we sought to analyze HsWapl biochemically and structurally. The recombinant, purified full-length (FL) Wapl and several N-terminal truncation mutants, including ΔN100–, ΔN200–, and ΔN300–Wapl, eluted from size-exclusion columns (SECs) with apparent molecular masses much larger than the expected molecular masses for their respective monomers. By contrast, Wapl-C behaved as a monomer on SEC with the expected molar mass. We then determined the native molecular masses of these proteins with SEC coupled with multiangle light scattering (SEC-MALS). The FL Wapl had high polydispersity, indicating a tendency to aggregate. Both ΔN200–Wapl and Wapl-C (residues 631–1190) were monodispersed and had native molar masses of 118 and 58 kg/mol, similar to the molar masses of 111 and 63 kg/mol that were expected of their monomeric species (Figure 2-1B). Analytical ultracentrifugation also confirmed that Wapl-C was a monomer with a native molar mass of 61 kg/mol. These results indicate that HsWapl is largely monomeric and has a globular C-terminal domain. Its N-terminal region is unfolded and flexible, explaining why the FL and larger N-terminal truncation Wapl proteins have larger than expected hydrodynamic radii and apparent molecular masses, based on SEC.

We next determined the structure of Wapl-C using X-ray crystallography (Figure 2-1C and Table 2-1). Wapl-C has an elongated shape with two lobes and contains eight HEAT

(Huntingtin, Elongation factor 3, A subunit, and target of rapamycin) repeats with variable lengths and a short N-terminal extension. HEAT2 and HEAT8 each have two helixes (αA and αB) (Figure 2-1C and Figure 2-2). All other HEAT repeats each have two long helixes (αA and αB) and a third short helix (αC). HEAT3 contains a helical insert between αA and αB. The αA and αB helices in HEAT1–3 are shorter than those in HEAT4–8. HEAT1–3 repeats and the HEAT3 insert form the N lobe of Wapl-C. The longer HEAT4–8 repeats form the C lobe. The N-terminal extension (residues 631–640) is likely unfolded in solution, but folds into a helix in our structure due to crystal packing interactions (see Figure 2-8D below).

During the course of our work, the structure of the C-terminal domain of Wapl from the filamentous fungus A. gossypii was reported (Chatterjee et al., 2013). As expected, the structures of A. gossypii Wapl (AgWapl) and HsWapl had similar folds (Figure 2-3). Like HsWapl, AgWapl contains eight HEAT repeats, which form two lobes. AgWapl also contains a helical insert between helices αA and αB of HEAT3. A major difference between AgWapl and HsWapl is the relative orientation between their N and C lobes, suggesting the intriguing possibility that the connection between HEAT3 and HEAT4 is flexible, and these two repeats can rotate relative to each other.

Mapping the Functional Surface of Wapl-C

We failed to detect binding of human Wapl-C to known cohesin subunits and regulators *in vitro*, which prohibited us from determining the structure of Wapl-C bound to cohesin or its regulators. We thus systematically mutated Wapl-C surface residues that were conserved among metazoan Wapl proteins (Figure 2-4A and Figure 2-2) and examined the functions of these

mutants in human cells (Figure 2-4B). To test the Wapl mutants in a relatively high-throughput manner, we developed a flow cytometry assay for Wapl function. HeLa cells were first transfected with plasmids encoding GFP–Wapl WT or mutants and then transfected with siRNA oligonucleotides targeting Sgo1 (siSgo1), siRNA oligonucleotides targeting Wapl (siWapl), or both. Cells were stained with the DNA dye propidium iodide (PI) and the MPM2 antibody (which detected mitotic phosphoproteins) and subjected to flow cytometry (Figure 2-5).

Depletion of Sgo1 expectedly caused premature sister-chromatid separation and increased mitotic index (Figure 2-4B), as defined by the percentage of cells with 4N DNA contents and positive MPM2 staining. Because the loss of centromeric cohesion in Sgo1-depleted cells was Wapl-dependent (Gandhi et al., 2006; Kueng et al., 2006), co-depletion of Wapl rescued the mitotic arrest phenotype of Sgo1 RNAi cells. Transfection of GFP–Wapl WT or functionally intact Wapl mutants in cells depleted of both Sgo1 and Wapl restored Wapl function and again elevated the mitotic index. In contrast, transfection of functionally defective Wapl mutants did not restore the mitotic arrest in cells depleted of both Sgo1 and Wapl.

The functionally defective Wapl mutants affected residues in three surface patches on Wapl: patches I and II on the N lobe and patch III on the C lobe (Figure 2-4A and 4C). Patch II is not contiguous with patch I and is partially shielded by the two extra helices in HEAT3 (H3 insert). Intriguingly, mutations of the surface-conserved residues in the H3 insert, including E770K, E777K, E787K, and T790A, did not affect Wapl function in human cells (Figure 2-4B). This observation raised the intriguing possibility that the H3 insert might have an auto-inhibitory role. This hypothesis could not be rigorously tested, however, because a simple deletion of the entire

H3 insert seriously destabilized the Wapl protein in human cells. Future structural studies on the Wapl–Pds5 or Wapl–cohesin complexes are needed to resolve this issue.

Wapl Patch I and III Mutations Diminish Cohesin Release and Sister-Chromatid Resolution during Mitosis

The flow cytometry assay described in Figure 2-4B tested the functions of Wapl mutants indirectly. We next examined the functions of a selective subset of Wapl mutants using more direct, well-established cell biological assays, including metaphase chromosome spreads and immunofluorescence (Kueng et al., 2006). Because our preliminary results indicated that certain single mutants had partial function in these assays, we constructed three double mutants: V639A/K640E, D656K/D657K, and M1116A/I1120A. The first two mutants affected residues in patch I, whereas the third targeted patch III.

As expected, all three double mutants were functionally defective in the flow cytometry-based assay and failed to restore the mitotic arrest in siSgo1/siWapl cells (Figure 2-6A). These mutants were also defective in promoting sister-chromatid resolution during mitosis (Figure 2-6B and 6C). Most metaphase spreads of mock-transfected HeLa cells that had been arrested with nocodazole for a short duration had X-shaped chromosomes with their arms resolved (category I). Wapl depletion greatly increased the percentage of cells with partially resolved (category III) and unresolved (category IV) sister chromatids whose arms remained connected. Expression of wild-type (WT) GFP–Wapl, but not the three double mutants, rescued the defect in sister-chromatid resolution in mitotic siWapl cells, despite being expressed at similar levels (see Figure 2-8B below). Consistently, all three mutants were also defective in removing Scc1–Myc-

containing cohesin from mitotic chromosomes, based on immunofluorescence (Figure 2-6D and 6E). These results confirm the functional importance of patches I and III of Wapl-C.

To further ascertain the functional importance of these Wapl residues, we performed depletion-rescue experiments in mitotic *Xenopus* egg extracts. The endogenous *Xenopus* Wapl (xWapl) was efficiently depleted from this cell-free system by using anti-xWapl antibody beads (Figure 2-7A). Recombinant human GST–Wapl WT or D656K/D657K was added back to levels comparable to that of the endogenous xWapl. Immunodepletion of Wapl diminished sister-chromatid resolution, as evidenced by smaller inter-sister distances in the Wapl-depleted extract (Figure 2-7B and 7C). Consistent with this observation, more cohesin remained bound to chromosomes in this extract (Figure 2-7B and 7D). Addition of GST–HsWapl WT, but not D656K/D657K, back to the Wapl-depleted extract rescued the defects in sister-chromatid resolution and cohesin removal (Figure 2-7B, 7C and 7D). This result corroborates the functional importance of Wapl-C patch I residues.

N Lobe, but Not C Lobe, of Wapl-C Is Involved in Cohesin Binding

We next studied why the Wapl mutants were functionally defective. We first examined its binding to cohesin in human cells (Figure 2-8A). Myc–Wapl-C itself did not bind cohesin. FL Myc–Wapl bound to cohesin much more efficiently than did Myc–Wapl-N. Thus, although Wapl-C is insufficient for cohesin binding, it contributes to the Wapl–cohesin interaction in the context of the FL protein.

We next tested which patches of Wapl-C were involved in cohesin binding (Figure 2-8B). The GFP–Wapl V639A/K640E and D656K/D657K mutants bound cohesin less efficiently than

GFP–Wapl WT did. They also bound to Sororin more weakly (Figure 2-9A), presumably because the Wapl–Sororin interaction was bridged by cohesin and Pds5. Conversely, these two mutants bound to Pds5A as well as Wapl WT did (Figure 2-8B). V639 and K640 are located in the N-terminal extension (Figure 2-8C). D656 and D657 reside in the αA helix of HEAT1. All four residues are part of the conserved patch I. Therefore, the N lobe of Wapl-C contributes to cohesin binding.

In contrast, GFP–Wapl M1116A/I1120A bound to cohesin, Pds5A, and Sororin as efficiently as did GFP–Wapl WT (Figure 2-8B and Figure 2-9A). M1116 and I1120 are located in the αB helix of HEAT7 and lie at the center of the conserved patch III. We next mutated two additional residues in this patch, D979 and E1117, which were conserved in yeast Wpl1. The D979K and E1117K mutants also retained normal binding to cohesin and Sororin (Figure 2-9B). Therefore, despite being critical for the function of Wapl, patch III is not required for binding to cohesin and its known regulators, such as Pds5 and Sororin. Interestingly, a crystal-packing interaction involves the binding of the N-terminal extension helix of another Wapl molecule to patch III (Figure 2-8D). Specifically, V639 and K640 of the N-terminal extension make energetically favorable hydrophobic and electrostatic interactions with F978, D979, M1116, E1117, I1120, and F1165.

At first glance, this binding interface appears to be functionally relevant, because mutations of residues at both sides of the interface—the N-extension helix and patch III—disrupt Wapl function. Three lines of evidence, however, argue against the functional relevance of this crystal-packing interaction. First, if the N-extension–patch III interaction were relevant, it would indicate that Wapl-C forms a symmetric dimer. Wapl-C is predominantly a monomer in solution

(Figure 2-1B). Second, differently tagged Wapl proteins do not appreciably interact in human cells (Figure 2-10). Third, and perhaps most convincingly, although mutations of residues in both the N-extension helix and patch III disrupt Wapl function, they do so through different mechanisms. Whereas the patch III mutants are fully functional in cohesin binding, mutations of the N-extension helix weaken cohesin binding, suggesting that this helix might contact cohesin, as opposed to patch III of another Wapl molecule. Together, our results as a whole are more consistent with patch III interacting with an unknown Wapl effector. This functional surface of Wapl has contributed to artificial crystal-packing interactions. Identification of the putative Wapl effector is critical for understanding the mechanism and regulation of Wapl.

Wapl-N–Pds5 Binds to Scc1–SA2

Although Wapl-C is required for optimal binding to intact cohesin, it is insufficient to bind cohesin on its own. We next set out to map additional molecular interactions between FL Wapl and cohesin subunits *in vitro*. Consistent with a previous report (Shintomi and Hirano, 2009), we found that GST–Wapl bound efficiently to the Scc1–SA2 heterodimer, but not to the Smc1–Smc3 heterodimer or to either Scc1 or SA2 alone (Figure 2-11A). We also found that the GST–Wapl–Pds5B complex exhibited similar binding profiles. Unlike yeast Wpl1, which bound to an engineered Smc3 ATPase head domain, HsWapl or Wapl–Pds5B had no detectable binding to the isolated human Smc3 ATPase head domain.

We mapped a Wapl–Pds5-binding element within Scc1–SA2 to the complex between SA2 and the C-terminal half of Scc1 (residues 317–631) (Figure 2-12A). This binding required SA2, but not Pds5B (Figure 2-12B). Moreover, none of the functionally defective Wapl-C double

mutants exhibited deficient binding to Scc1–SA2 or SA2 bound to various Scc1 fragments in the presence or absence of Pds5B (Figure 2-12A, 12C, and Figure 2-11B). Instead, a region between residues 500–580 in Wapl-N was required for Wapl binding to $Scc1^{317–631}$–SA2 (Figure 2-12D and Figure 2-13A). Consistent with Pds5 playing a role in Wapl binding to SA2–Scc1 (Shintomi and Hirano, 2009), we detected a second interface between Pds5–Wapl and Scc1–SA2, involving Wapl-N, Pds5, and the N-terminal region of Scc1, $Scc1^{1–316}$ (Figure 2-13B). This interaction required Pds5B, but not SA2.

Three FGF motifs in Wapl-N have been implicated in binding to Scc1–SA2 (Shintomi and Hirano, 2009). Mutating the FGF motifs to EGE greatly reduced Wapl binding to Scc1–SA2. Conversely, our results showed that Wapl ΔN500, which lacked the FGF motifs, retained Scc1–SA2 binding. Furthermore, mutations of the FGF motifs to AGA only slightly diminished Wapl binding to $Scc1^{317–631}$–SA2 (Figure 2-12D) and did not affect the binding of Wapl–Pds5 to $Scc1^{1–316}$ (Figure 2-13C), indicating that these motifs contribute to, but are not strictly required for, the Wapl–cohesin interaction. The EGE mutations might have introduced destabilizing interactions at the Wapl–cohesin interface, in addition to disrupting favorable interactions.

Because mutations of the N lobe of Wapl-C weakened Wapl binding to intact cohesin, but not to Scc1–SA2, the N lobe of Wapl-C likely contacts cohesin subunits or associated factors other than Scc1–SA2. Thus, Wapl has an extensive surface for binding to cohesin. Two regions of Wapl-N bind to Scc1–SA2, whereas the N lobe of Wapl-C likely contacts other cohesin subunits or cofactors. Binding of Wapl-N to the N-terminal region of Scc1 requires Pds5B, but not SA2. In contrast, binding of Wapl-N to the C-terminal region of Scc1 requires SA2, but not Pds5B.

We next tested whether Wapl directly disrupted the Smc1– or Smc3–Scc1 interfaces. The ^{35}S-labeled, HA-tagged, engineered Smc1 ATPase head domain bound efficiently to Myc–Scc1$^{317–631}$ (Figure 2-12E). Addition of GST–Wapl or its mutants in the presence of SA2 did not diminish this interaction. Likewise, GST–Wapl or its mutants efficiently pulled down the complex between ^{35}S-labeled Smc3 head domain and Scc1 N-WHD, only when Pds5B was present (Figure 2-12F). This interaction was diminished by Sororin, which disrupted the Wapl–Pds5B interaction. Therefore, Wapl–Pds5 does not directly compete with the ATPase head domains of Smc1 and Smc3 for their respective binding to C- and N-WHD of Scc1. The mechanism by which Wapl–Pds5 releases cohesin from chromatin remains to be established, but may involve the ATPase activity of Smc1–Smc3.

Mechanistic Differences between Human and Yeast Wapl Proteins

A recent study showed that budding yeast Wpl1 bound to the isolated Smc3 ATPase head domain and reported a structure of AgWapl bound to a short peptide derived from the AgSmc3 ATPase domain (Figure 2-3) (Chatterjee et al., 2013). The Smc3 peptide bound to a site on AgWapl that roughly corresponded to patch III on HsWapl. Surprisingly, mutations of the corresponding patch III residues in yeast Wpl1 disrupted Wpl1 function, but only moderately reduced the binding affinity between Wpl1 and Smc3 (Chatterjee et al., 2013). Mutations of residues in the Wpl-binding motif of Smc3 had similarly moderate effects on the Wpl1–Smc3 affinity, but did not disrupt Wpl function. Considering our results that patch III of HsWapl does not contribute to cohesin binding and that functionally irrelevant crystal contacts tend to form at this site, the observed interactions between AgWapl and the AgSmc3 peptide need to be

interpreted with caution. Alternatively, HsWapl may interact with cohesin in a mode that is different from that of the fungal Wapl proteins, because several patch III residues are not conserved between yeast and humans (Figure 2-2).

Conversely, the patch I residues critical for HsWapl binding to cohesin are conserved in Wpl1 (Figure 2-2). Mutations of residues equivalent to HsWapl D656 and D657 in yeast Wpl1 diminished Wpl1 binding to the Smc3 ATPase domain. Therefore, the cohesin-binding activity of the Wapl N lobe is conserved from yeast to man. Future structural studies on the complexes between Wapl and larger cohesin subcomplexes are needed to fully elucidate the mechanisms by which Wapl promotes cohesin release from chromatin and to resolve the apparent differences between human and fungal Wapl proteins.

CONCLUSION

Our results show that HsWapl interacts with cohesin extensively with at least three functional regions (Figure 2-12G). Wapl-N–Pds5 binds to the Scc1–SA2 heterodimer, whereas the N lobe of Wapl-C likely contacts the Smc1–Smc3 heterodimer or other cohesin-associated factors. The interaction between Wapl-C N lobe and cohesin is functionally important. The Wapl-C C lobe does not contribute to the physical interaction between Wapl and cohesin and may instead interact with an unknown effector to promote cohesin release from chromatin.

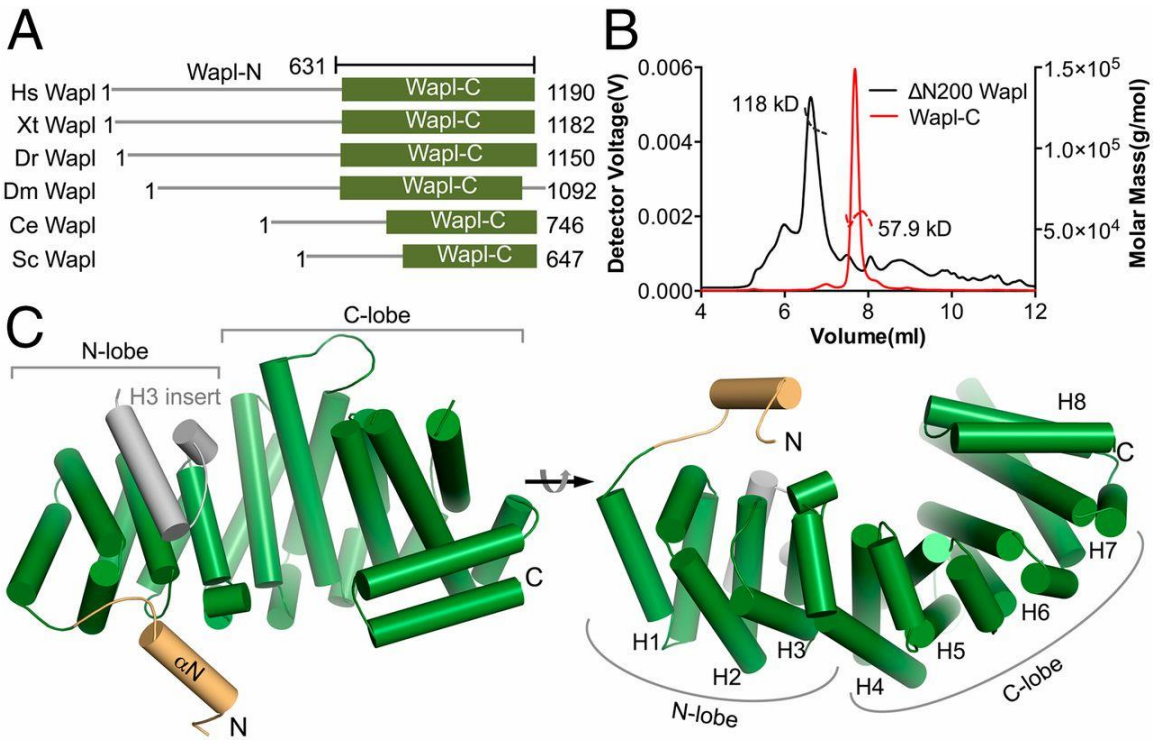

Figure 2-1. Structure of HsWapl. (**A**) Schematic drawing of the Wapl proteins from different species (Xt, *Xenopus tropicalis*; Dr, *Danio rerio*; Dm, *Drosophila melanogaster*; Ce, *Caenorhabditis elegans*; Sc, *Saccharomyces cerevisiae*). Wapl-C, the C-terminal domain of Wapl. The boundaries of human Wapl-C are indicated. (**B**) SEC-MALS profiles of human Wapl-C and ΔN200–Wapl. (**C**) Cartoon drawing of the crystal structure of human Wapl-C in two different orientations. The H3 insert and the N-terminal extension helix are colored gray and orange, respectively. The rest of the protein is colored green. The N and C lobes are labeled. The positions of the HEAT repeats 1–8 are indicated in *Right*. All structure figures were made with PyMOL (www.pymol.org).

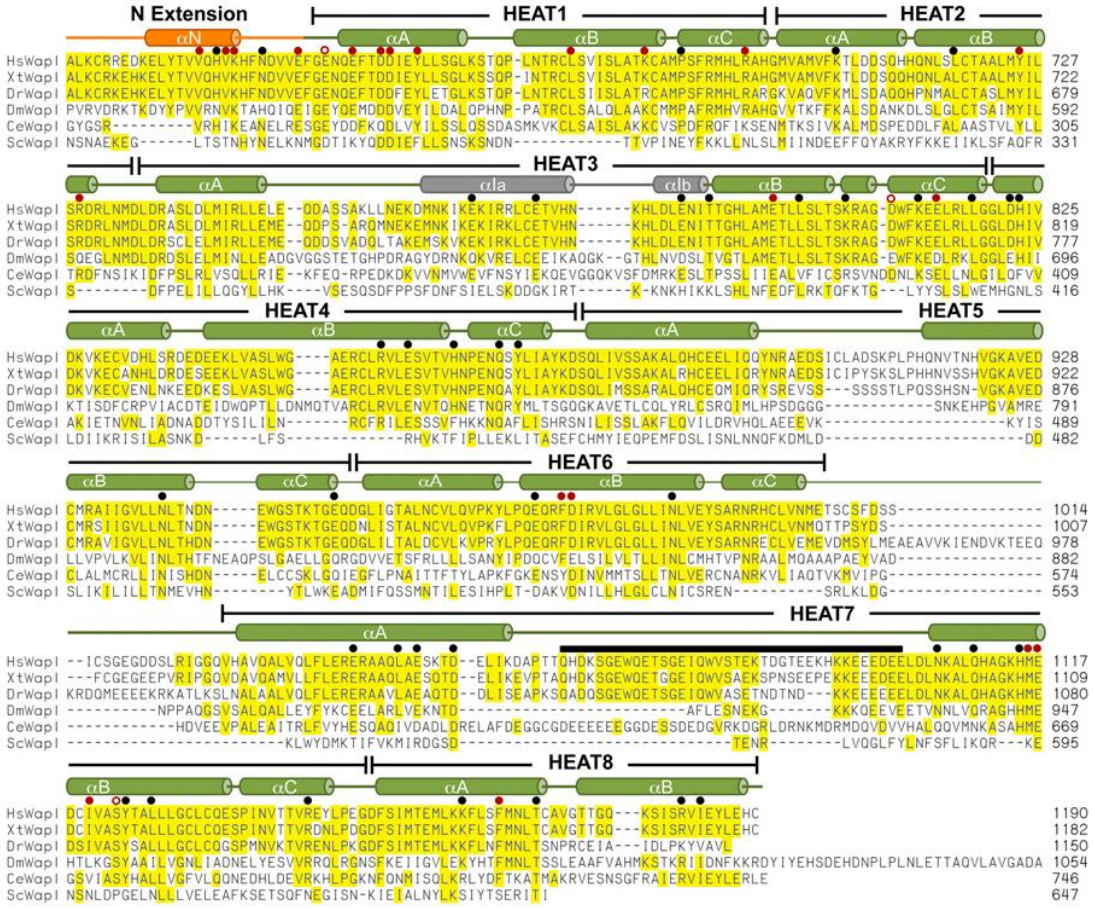

Figure 2-2. Sequence alignment of the C-terminal domain of Wapl proteins from various species (Hs, *Homo sapiens*; Xt, *Xenopus tropicalis*; Dr, *Danio rerio*; Dm, *Drosophila melanogaster*; Ce, *Caenorhabditis elegans*; Sc, *Saccharomyces cerevisiae*). The conserved residues are shaded yellow. The secondary structure elements of HsWapl are shown on top. Mutations of residues indicated by red or black dots in HsWapl do or do not disrupt Wapl function in human cells. Mutations of residues indicated by open circles destabilized the Wapl protein. A loop missing in the structure is indicated by a thick black line.

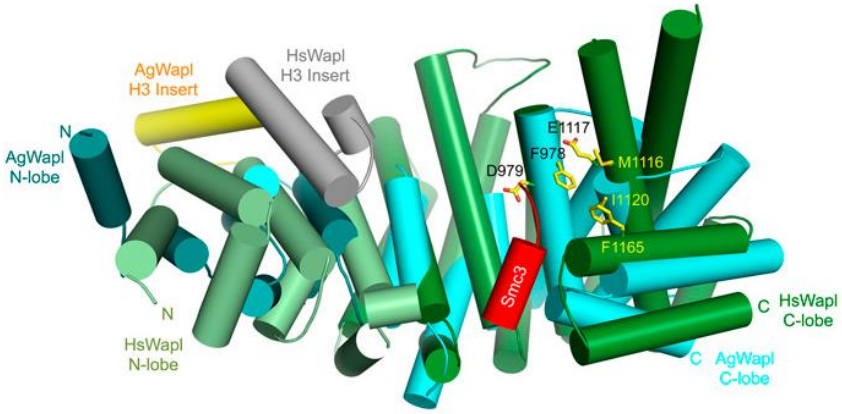

Figure 2-3. Cartoon drawing of the structures of human (Hs) and *A. gossypii* Wapl-C with their C lobes superimposed. The N and C lobes of HsWapl are colored light and dark green, respectively. Its H3 insert is colored gray. The patch III residues in HsWapl are shown in yellow sticks and labeled. The N and C lobes of AgWapl are colored dark and light cyan, respectively. Its H3 insert is colored yellow. The Smc3 peptide bound to AgWapl is colored red.

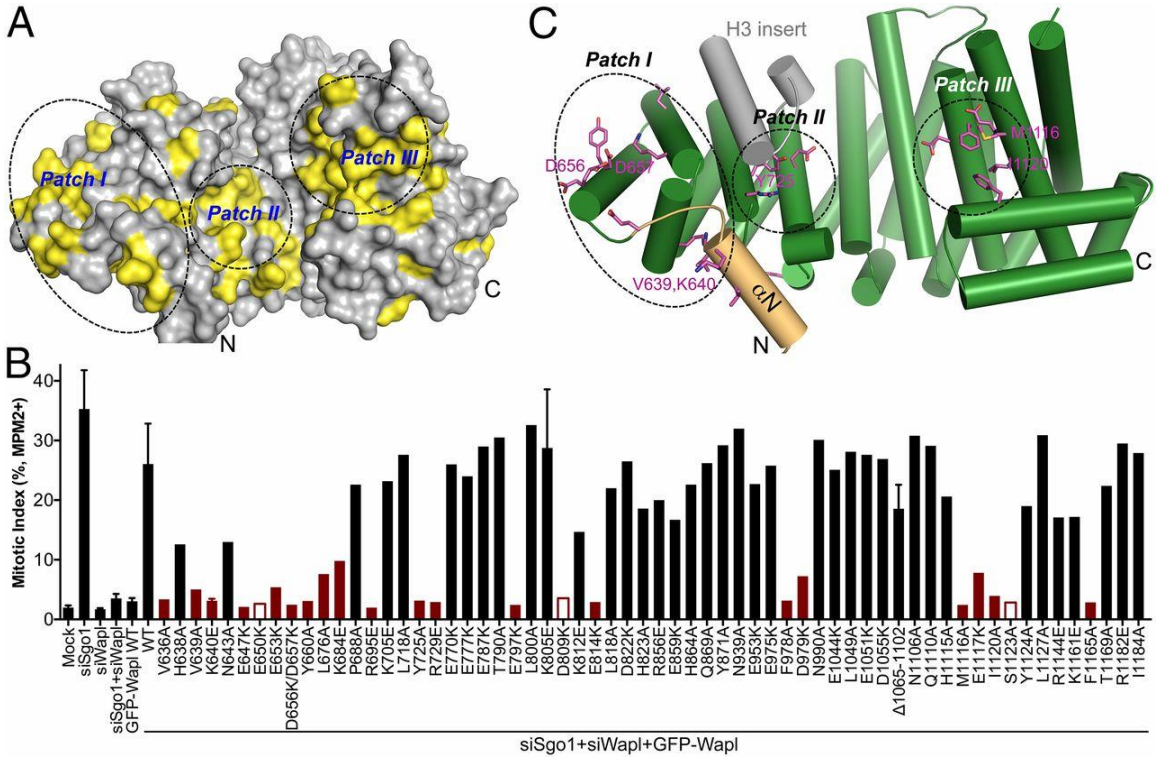

Figure 2-4. Mapping the functional surface of HsWapl. (**A**) Surface drawing of human Wapl-C with the conserved residues colored yellow. The N and C termini are labeled. Three conserved surface patches are circled. (**B**) HeLa Tet-On cells were transfected with plasmids encoding GFP–Wapl WT or mutants for 24 h and then transfected with siSgo1, siWapl, or both for another 24 h. Cells were harvested and analyzed by flow cytometry. The mitotic index (as defined by the percentage of cells with 4N DNA contents and positive MPM2 staining) is plotted. The functionally defective mutants are shown in red. The mutants that did not express are indicated by open red bars. For samples that have been repeated multiple times, the mean and SD are shown. (**C**) Cartoon drawing of human Wapl-C with the functionally defective mutants shown as purple sticks. The N and C termini and key residues are labeled. The color scheme is the same as in **Figure 2-1C**. The three conserved patches are circled.

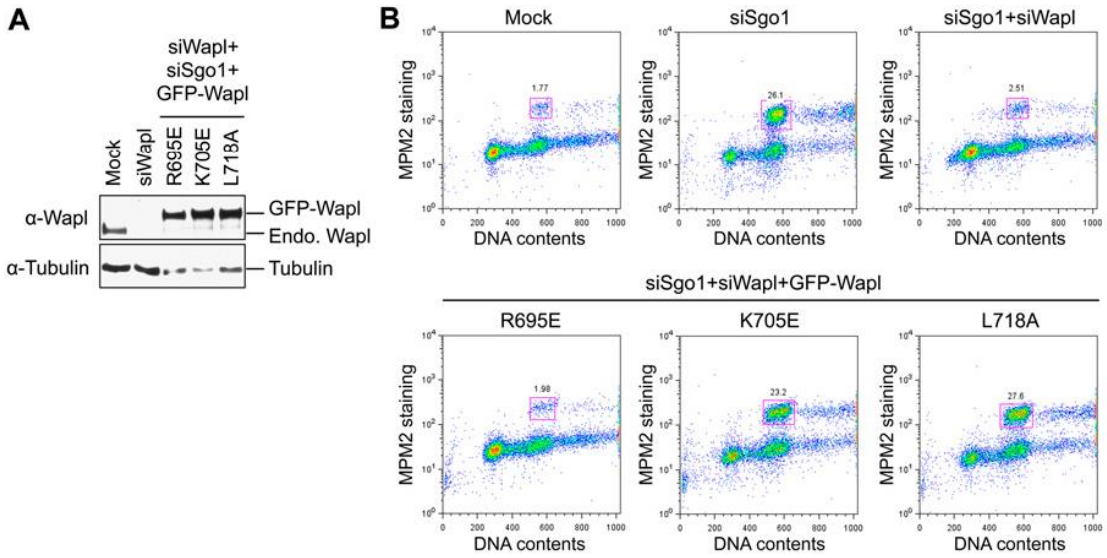

Figure 2-5. Mapping the functional surface of Wapl. (**A**) HeLa Tet-On cells were transfected with plasmids encoding representative GFP–Wapl mutants for 24 h and then transfected with siSgo1 and siWapl for another 24 h. The total lysates of these cells and cells that were mock or siWapl-transfected were blotted with anti-Wapl and anti-tubulin. More lysates of the mock or siWapl-transfected cells were loaded to better visualize the knockdown efficiency of endogenous Wapl. (**B**) HeLa Tet-On cells were transfected with plasmids encoding GFP–Wapl WT or mutants for 24 h and then transfected with siSgo1, siWapl, or both for another 24 h. Cells were harvested and analyzed by flow cytometry. Flow cytometry graphs of representative mutants are shown, with the populations of mitotic cells (defined as cells with 4N DNA contents and positive MPM2 staining) boxed and their percentages indicated.

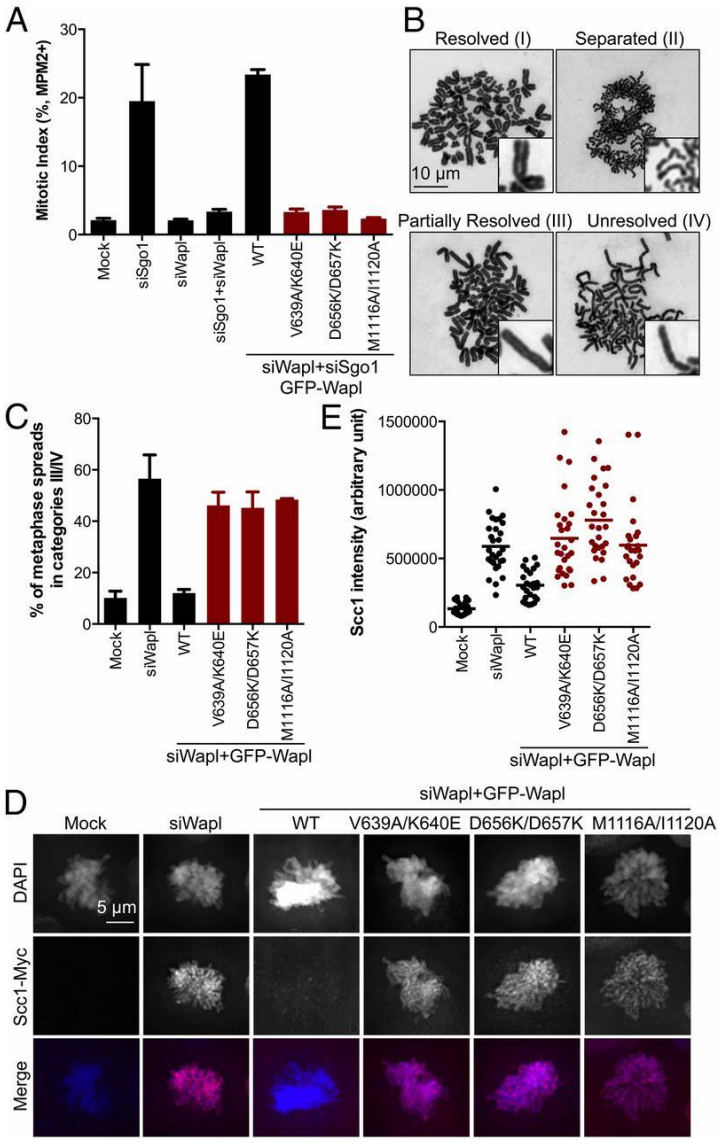

Figure 2-6. Identification of functionally defective HsWapl mutants. (**A**) Quantification of the mitotic index of HeLa Tet-On cells transfected with the indicated siRNAs and plasmids. The functionally defective Wapl mutants are shown in red bars. The mean and SD of two independent experiments are shown. (**B**) HeLa Tet-On cells transfected with RNAi-resistant GFP–Wapl WT or mutants were depleted of endogenous Wapl by RNAi. Cells were synchronized with thymidine, released into fresh medium for 9 h, treated with nocodazole for 2 h, and analyzed by metaphase spreads. Sample images in four major categories of chromosome morphology are shown. In category I, most sister chromatids are X-shaped. They maintain cohesion at centromeres, but lose cohesion at arms. In category II, sister chromatids are separated and scattered. In category III, the arm regions of sister chromatids are partially resolved. In category IV, sister chromatids are not fully condensed, and their arms are not

resolved. Representative sister chromatids are magnified and shown in Insets. (**C**) Quantification of the percentage of mitotic cells in **B** with categories III and IV chromosome morphology. The mean and SD of two independent experiments are shown. (**D**) Prometaphase HeLa Tet-On cells stably expressing Scc1–Myc that had been transfected with indicated plasmids and siRNAs were stained with DAPI (blue in merge) and anti-Myc (red in merge). (**E**) Quantification of the anti-Myc staining intensities of cells in **D**. Each dot in the graph represents a single cell (mock, n = 24; siWapl, n = 29; WT, n = 25; V639A/K640E, n = 28; D656K/D657K, n = 27; M1116A/I1120A, n = 25). The horizontal bars indicate the means.

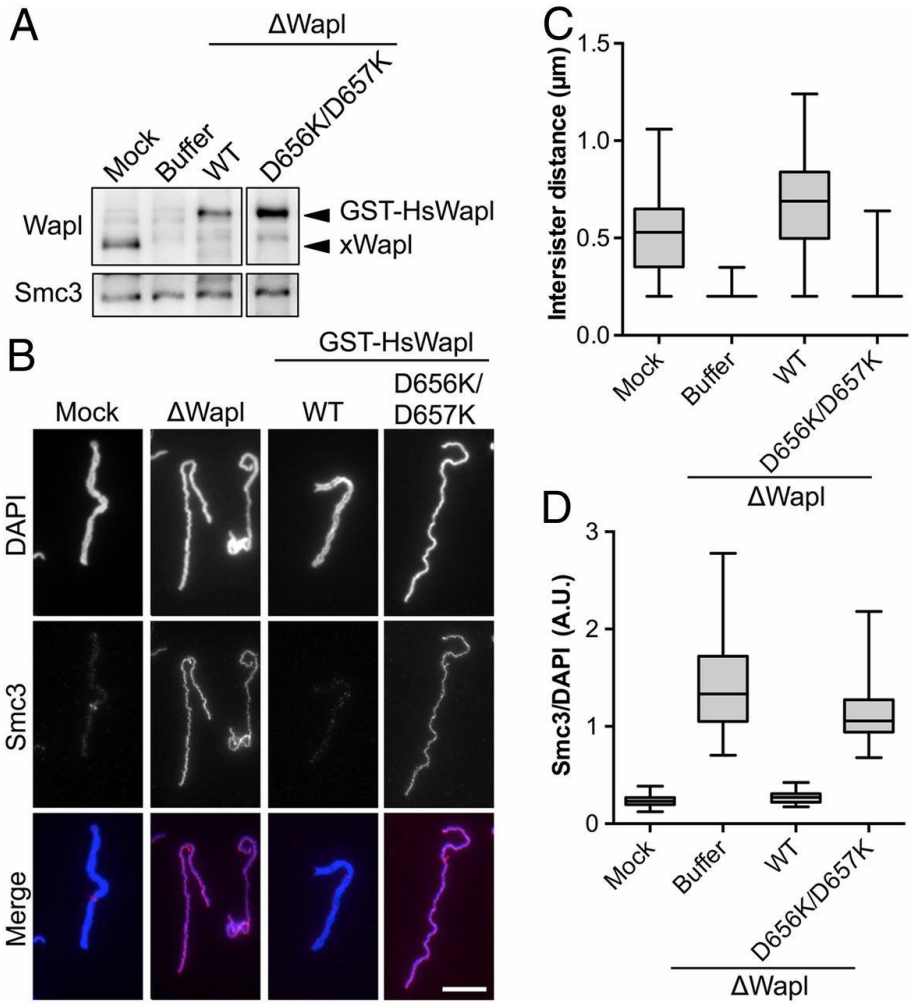

Figure 2-7. Wapl D656K/D657K is defective in *Xenopus* egg extracts. Mitotic chromosomes were assembled in *Xenopus* egg extract that was either mock depleted (mock) or depleted of Wapl (ΔWapl) and supplemented with recombinant human GST–Wapl WT or the D656K/D657K mutant. (**A**) Immunoblot showing the relative levels of Wapl and Smc3 in each reaction. (**B**) Chromosomes were immunostained for Smc3 and counterstained with DAPI. Representative images are shown. Scale bar, 10 μm. (**C**) Quantification of the inter-sister distance in each sample. (**D**) The amount of Smc3 on individual chromosomes was measured and is presented as Smc3 staining intensity normalized to DAPI staining intensity for the indicated samples ($n \geq 36$ per sample). A.U., arbitrary units.

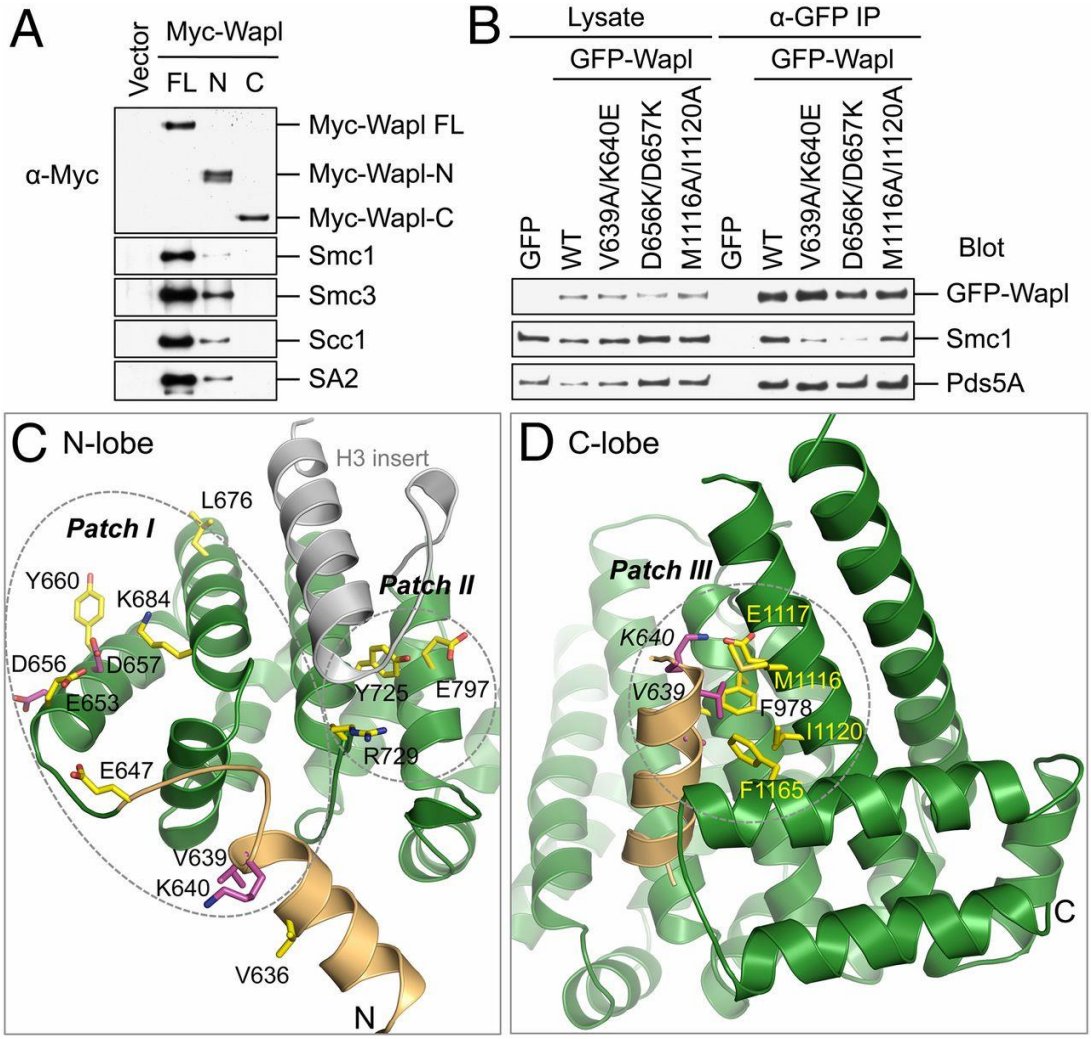

Figure 2-8. The N lobe, but not the C lobe, of Wapl-C is involved in binding to intact cohesin in human cells. (**A**) HeLa Tet-On cells were transfected with plasmids encoding Myc–Wapl FL, Wapl-N containing residues 1–600 (N), or Wapl-C containing residues 601–1190 (C) and then transfected with siWapl. Lysates were immunoprecipitated (IP) with anti-Myc beads. The IP was blotted with the indicated antibodies. (**B**) HeLa Tet-On cells were transfected with the indicated GFP–Wapl plasmids for 24 h and then transfected with siWapl for 48 h. The total cell lysate and anti-GFP IP were blotted with the indicated antibodies. (**C** and **D**) Cartoon drawing of the N and C lobe of Wapl-C with the functionally important residues shown in sticks and labeled. The residues mutated in the double mutants are colored purple and others are colored yellow. The three conserved patches are circled. In crystal, the N-terminal extension helix from one Wapl molecule contacts patch III of another.

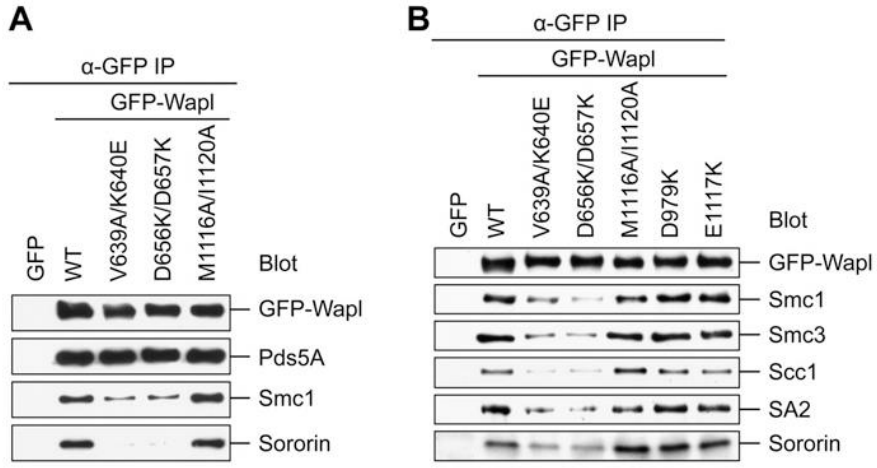

Figure 2-9. Patch I, but not patch III, of Wapl-C contributes to cohesin binding. (**A**) HeLa Tet-On cells were transfected with the indicated GFP–Wapl plasmids for 24 h and then transfected with siWapl for 48 h. The anti-GFP IP was blotted with the indicated antibodies. (**B**) HeLa Tet-On cells were transfected with the indicated GFP–Wapl plasmids for 24 h and then transfected with siWapl for 48 h. The anti-GFP IP was blotted with the indicated antibodies.

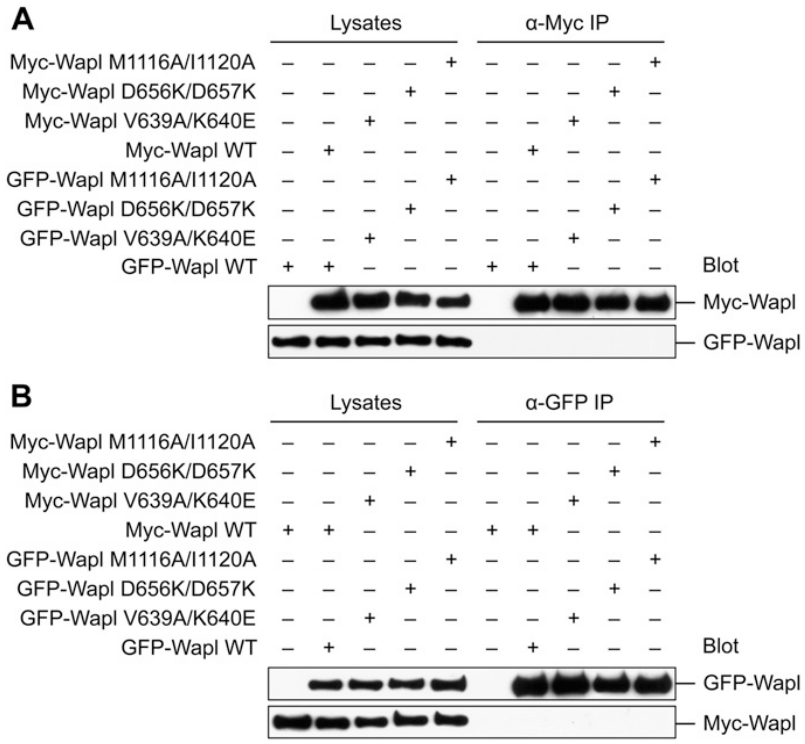

Figure 2-10. Wapl does not oligomerize in human cells. (**A**) Lysates and anti-Myc IP of HeLa Tet-On cells transfected with the indicated plasmids were blotted with anti-GFP and anti-Myc. (**B**) Lysates and anti-GFP IP of HeLa Tet-On cells transfected with the indicated plasmids were blotted with anti-GFP and anti-Myc.

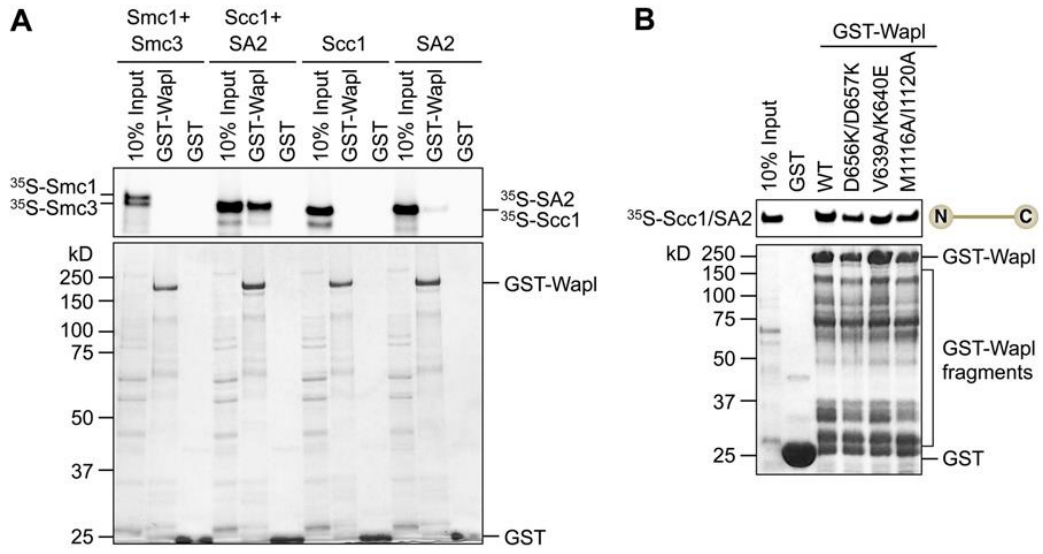

Figure 2-11. Wapl-C does not contribute to binding to Scc1–SA2. (**A**) GST or the GST–Wapl was immobilized on glutathione–agarose beads. Beads were incubated with ^{35}S-labeled human Smc1, Smc3, Scc1, and SA2. The bound proteins were separated by SDS-PAGE and analyzed with a phosphorimager (Upper) and Coomassie blue staining (Lower). (**B**) Beads containing GST or the indicated GST–Wapl proteins were incubated with ^{35}S-Scc1 and unlabeled SA2. The bound proteins were analyzed with a phosphorimager (Upper) and Coomassie blue staining (Lower).

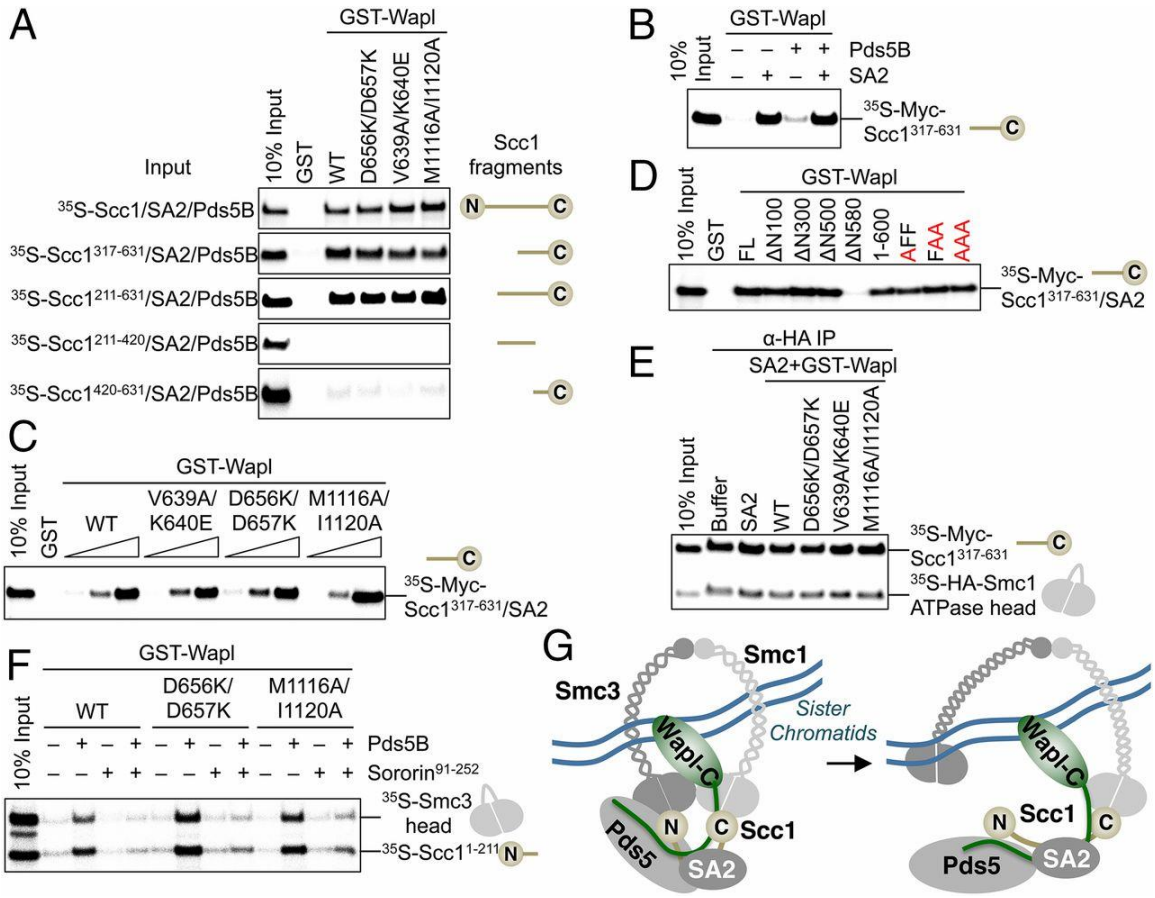

Figure 2-12. HsWapl binds to cohesin through multiple interfaces. (**A**) GST or the indicated GST–Wapl proteins were immobilized on glutathione–agarose beads. Beads were incubated with ^{35}S-labeled Scc1 or the indicated fragments in the presence of unlabeled, purified SA2 and Pds5B. The bound proteins were separated by SDS-PAGE and analyzed with a phosphorimager. (**B**) Beads containing GST–Wapl were incubated with ^{35}S-Scc1$^{317–631}$ in the presence (+) or absence (−) of Pds5B or SA2. The bound proteins were analyzed with a phosphorimager. (**C**) Beads containing GST or increasing amounts of the indicated GST–Wapl proteins were incubated with ^{35}S-Scc1$^{317–631}$ and unlabeled SA2. The bound proteins were analyzed with a phosphorimager. (**D**) Beads containing GST and indicated GST–Wapl proteins were incubated with ^{35}S-Scc1$^{317–631}$ and unlabeled SA2. The bound proteins were analyzed with a phosphorimager. (**E**) The anti-HA beads containing ^{35}S-Myc–Scc1$^{317–631}$ and HA–Smc1 ATPase domain were incubated with unlabeled SA2 and the indicated GST–Wapl proteins. The bound proteins were analyzed with a phosphorimager. (**F**) Beads containing the indicated GST–Wapl proteins were incubated with ^{35}S-Scc1$^{1–211}$ and ^{35}S-Smc3 ATPase head in the presence or absence of unlabeled Pds5B or Sororin. The bound proteins were analyzed with a phosphorimager. (**G**) Model for Wapl binding to cohesin and Wapl-dependent cohesin release from chromatin. Wapl-N binds to both Pds5 and Scc1–SA2 through two interfaces. The N lobe

of Wapl-C likely contacts Smc1–Smc3 or other associated proteins. The extensive interaction between Wapl–Pds5 and cohesin does not directly disrupt the Smc3–Scc1 or Smc1–Scc1 interfaces. Wapl might open the Smc3–Scc1 gate of the cohesin ring indirectly through stimulating the ATPase activity of chromatin-bound cohesin.

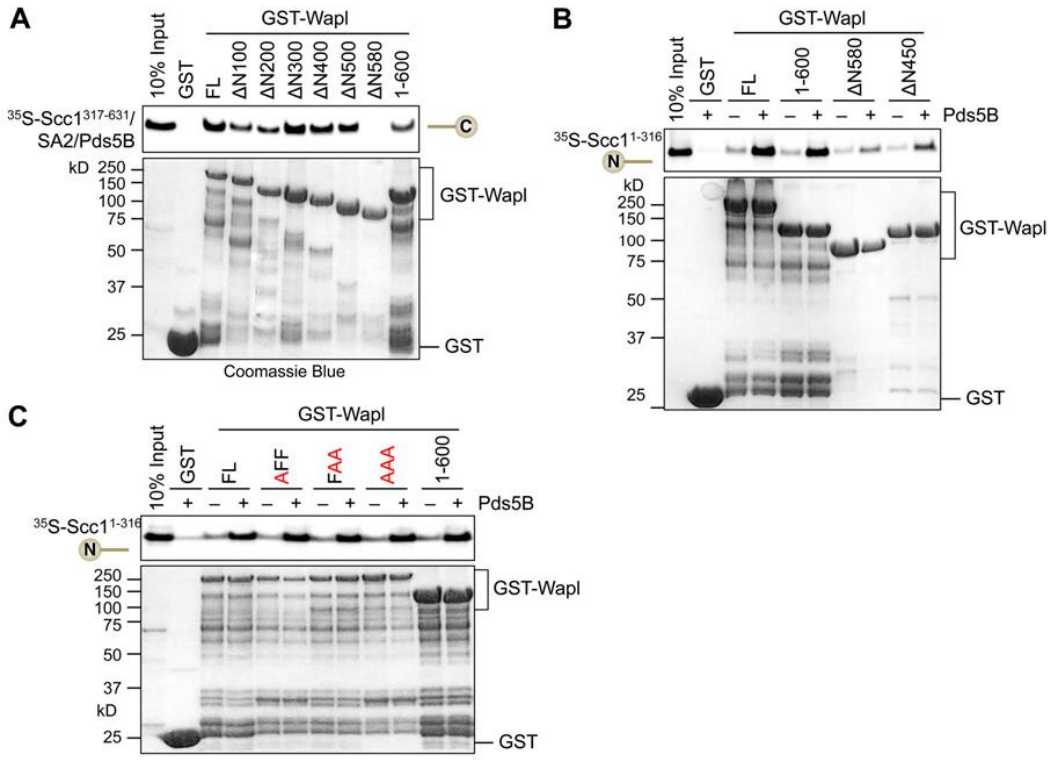

Figure 2-13. Wapl-N interacts with Scc1–SA2 through two interfaces. (**A**) GST or the indicated GST–Wapl proteins were immobilized on glutathione–agarose beads. Beads were incubated with ^{35}S-labeled Scc1$^{317–631}$ in the presence of unlabeled, purified SA2 and Pds5B. The bound proteins were separated by SDS-PAGE and analyzed with a phosphorimager (Upper) and Coomassie blue staining (Lower). (**B** and **C**) Beads containing GST or the indicated Wapl proteins were incubated with ^{35}S-Scc1$^{1–316}$ in the presence or absence of unlabeled Pds5B. The bound proteins were analyzed with a phosphorimager (Upper) and Coomassie blue staining (Lower).

Table 2-1. Data collection, phasing, and refinement statistics for Wapl structure

Data Collection		
Crystal	Native	SeMet
Energy, eV	12,684.1	12,683.7
Resolution range, Å	41.84-2.62 (2.67-2.62)[a]	37.56-3.42 (3.48-3.42)
Unique reflections	53,851 (2,608)	24,849 (1,196)
Multiplicity	4.8 (4.8)	7.2 (5.6)
Data completeness, %	99.6 (99.8)	98.2 (97.4)
R_{merge},[b] %	5.6 (55.8)	14.6 (100.0)
$I/\sigma(I)$	19.0 (3.6)	15.1 (1.5)
Wilson B value, Å^2	34.8	66.1
Refinement Statistics		
Crystal	Native	
Resolution range, Å	29.7-2.62 (2.71-2.62)	
No. of reflections R_{work} / R_{free}	51,154/2,584 (1,590/87)	
Data completeness, %	94.85 (64.35)	
Atoms (non-H protein/ligands/waters)	7,648/74/106	
R_{work}, %	18.4 (21.9)	
R_{free}, %	23.7 (31.2)	
Rmsd bond length, Å	0.002	
Rmsd bond angle, °	0.64	
Mean B value, Å^2 (protein/ligands/waters)	48.2/55.1/34.8	
Ramachandran plot,[c] % (favored/additional/disallowed)	96.8/3.0/0.2	
Maximum likelihood coordinate error	0.27	
Missing residues	A: 753-759, 1010-1028, 1061-1105. B: 753-761, 903-919, 1012-1030, 1055-1106.	

[a] Data for the outermost shell are given in parentheses.
[b] $R_{merge} = 100\ \Sigma_h\Sigma_i|I_{h,\ I} - \langle I_h\rangle|/\Sigma_h\Sigma_i\langle I_{h,\ I}\rangle$; where the outer sum ($h$) is over the unique reflections and the inner sum (i) is over the set of independent observations of each unique reflection.
[c] As defined by the validation suite MolProbity.

CHAPTER III: STRUCTURE OF COHESIN SUBCOMPLEX PINPOINTS DIRECT SHUGOSHIN-WAPL ANTAGONISM IN CENTROMERIC COHESION

INTRODUCTION

The ring-shaped cohesin complex maintains genome integrity through regulating sister-chromatid cohesion, DNA repair and transcription in eukaryotes (Merkenschlager and Odom, 2013; Nasmyth and Haering, 2009; Onn et al., 2008; Peters et al., 2008; Wu et al., 2012; Wu and Yu, 2012). Dysregulation of cohesin and its regulators has been implicated in human cancers and developmental diseases (Remeseiro et al., 2013; Solomon et al., 2011). Cohesin consists of an Smc1-Smc3 heterodimer and a non-Smc heterodimer (Nasmyth, 2011; Nasmyth and Haering, 2009). The Smc1 and Smc3 ATPases heterodimerize through their hinge domains (Figure 3-1a). Scc1 binds to the ATPase domains of Smc1 and Smc3 through its C- and N-terminal winged-helix domains, respectively, forming a ring. In human somatic cells, Scc1 binds through its central region to either SA1 or SA2, two homologous huntingtin, elongation factor 3, A subunit and TOR (HEAT) repeat-containing proteins.

The dynamics and mode of cohesin association with chromatin are tightly regulated by a set of cohesin regulators (Onn et al., 2008; Peters et al., 2008; Sherwood et al., 2010; Shintomi and Hirano, 2010). In telophase, cohesin is loaded onto chromatin by the cohesin loader Scc2-Scc4 (Ciosk et al., 2000; Gillespie and Hirano, 2004; Tonkin et al., 2004; Watrin et al., 2006). In G1, cohesin association with chromatin remains dynamic, and the chromatin-bound cohesin can be released by the cooperative actions of the adaptor protein Pds5 and the cohesin inhibitor Wapl

(Gandhi et al., 2006; Kueng et al., 2006; Losada et al., 2005). During S phase, the cohesin protector Sororin binds cohesin in part through Pds5 and antagonizes Wapl to establish cohesion (Lafont et al., 2010; Nishiyama et al., 2010; Rankin et al., 2005). During prophase in human somatic cells, the mitotic kinases Cdk1, Plk1 and Aurora B collaborate to phosphorylate cohesin and Sororin, triggering Wapl-dependent cohesin release from chromosome arms (Dreier et al., 2011; Hauf et al., 2005; Nishiyama et al., 2013). A pool of cohesin at centromeres is protected by the Sgo1-PP2A complex (Kitajima et al., 2006; Riedel et al., 2006; Tang et al., 2006), which keeps cohesin and Sororin in a hypophosphorylated state and maintains centromeric cohesion (Liu et al., 2013b). At the metaphase-anaphase transition, the proper kinetochore-microtubule attachment creates tension across sister kinetochores and silences the spindle checkpoint (Foley and Kapoor, 2013; Jia et al., 2013), thus leading to Separase activation. Kinetochore tension also triggers a redistribution of Sgo1 from centromeres to kinetochores (Lee et al., 2008; Liu et al., 2013a) that is thought to inactivate Sgo1 and allow cohesin cleavage by active Separase. Inactivation of Sgo1-mediated protection of centromeric cohesion leads to premature sister-chromatid separation and spindle checkpoint–dependent mitotic arrest (McGuinness et al., 2005; Tang et al., 2004a).

The SA2-Scc1 heterodimer mediates the binding between cohesin and its regulators, includingScc2-Scc4, Pds5, Wapl and Sgo1 (Liu et al., 2013b; Murayama and Uhlmann, 2014; Shintomi and Hirano, 2009). The mechanisms by which this non-Smc cohesin subcomplex coordinates these crucial molecular interactions are poorly understood. To gain structural insights into these interactions, we have determined the crystal structure of human SA2 bound to the SA2-binding region of Scc1 and have mapped the binding sites of Sgo1 and Wapl. Our

results establish a competition between Sgo1 and Wapl in cohesin binding and implicate a role for this direct antagonism in centromeric cohesion protection.

MATERIALS AND METHODS

Protein Expression and Purification

The cDNAs of human SA2 (residues 80-1060) and Scc1 (residues 281-420) were separately cloned into the FseI and AscI sites of a modified pFastBac HT vector (Invitrogen). The final constructs encoded an N-terminal His_6-Flag-tagged SA2 and an N-terminal His_6-strep-tagged Scc1, with a tobacco etch virus (TEV) protease cleavage site between the Flag tag and SA2, and a PreScission protease cleavage site between the strep tag and Scc1. Recombinant SA2 and Scc1 baculoviruses were constructed with the Bac-to-Bac system (Invitrogen) according to the manufacturer's protocols. For large-scale production of recombinant proteins, Hi5 insect cells (Sigma-Aldrich) were infected with both the SA2 and Scc1 baculoviruses and harvested at about 50 h after infection. Cells were resuspended in lysis buffer (50 mM Tris-HCl, pH 7.7, 150 mM KCl, 0.1% (v/v) Triton X-100 and a protease-inhibitor cocktail). After sonication and centrifugation, the supernatant was applied onto Ni^{2+}-NTA resin (Qiagen) equilibrated with lysis buffer, and incubated at 4 °C overnight. The resin was washed with wash buffer I (50 mM Tris-HCl, pH 7.7, 1.2 M KCl and 10 mM imidazole) and then washed with wash buffer II (20 mM HEPES, pH 7.4, 100 mM NaCl and 20 mM imidazole). The SA2-Scc1 complex was eluted with the elution buffer (20 mM HEPES, pH 7.4, 100 mM NaCl and 50-200 mM imidazole), and incubated with the TEV and PreScission proteases at 4 °C overnight. The complex with the tags removed was applied onto a HiTrap Q HP column (GE Healthcare) equilibrated with the QA buffer (50 mM Tris-HCl, pH 8.5) with an AKTA chromatography system (GE Healthcare). SA2-Scc1 was eluted with a linear salt gradient from 0 to 600 mM NaCl. SA2-Scc1 was further applied onto a HiLoad 16/60 Superdex 200 prep-grade column (GE Healthcare) equilibrated with

the purification buffer (20 mM Tris-HCl, pH 7.7, 300 mM NaCl and 5 mM TCEP). Purified SA2-Scc1 was concentrated to 7 mg/ml, flash frozen in liquid nitrogen and stored at -80 °C for crystallization or binding assays.

The SeMet-labeled SA2–Scc1 complex was expressed in Hi5 cells according to the manufacturer's protocols. Briefly, Hi5 cells cultured in the ESF921 medium (Expression Systems) were infected with both SA2 and Scc1 baculoviruses. The cells were incubated for 16 h and then supplied with 100 mg/l L-selenomethionine. After an additional 48 h, the cells were harvested, and the SeMet SA2-Scc1 complex was purified as described above.

Crystallization and Data Collection

All crystallization experiments were performed at 20 °C. Initial screening for the SA2-Scc1-MES complex was carried out by sitting-drop vapor diffusion with a Phoenix crystallization robot (Art Robbins Instruments), with commercially available screening kits from Hampton Research, Qiagen and Molecular Dimensions. Conditions were further optimized with the hanging-drop vapor-diffusion method. SA2-Scc1-MES crystals suitable for X-ray-diffraction experiments appeared within 1 week with a reservoir solution consisting of 0.12 M Morpheus Divalents Mix, 0.1 M Morpheus Buffer System 1 and 27-30% (v/v) Morpheus EOD_P8K (Molecular Dimensions). Similarly, the SA2-Scc1 crystals were grown in 1 week with a reservoir solution consisting of 0.12 M Morpheus Divalents Mix, 0.1 M imidazole-HCl, pH 6.5, and 27-30% (v/v) Morpheus EOD_P8K. All crystals were cryoprotected with a reservoir solution including 30% (v/v) Morpheus EOD_P8K before being flash frozen.

All X-ray diffraction data were collected at 100 K at the Structural Biology Center (Beamline 19ID) at Argonne National Laboratory. SA2-Scc1-MES (Native-MES), SeMet-labeled SA2-Scc1-MES (SeMet-MES), and SeMet-labeled SA2-Scc1 without MES (SeMet) crystals diffracted to 2.95 Å, 2.85 Å and 3.05 Å, respectively (Table 3-1). Diffraction data were processed with the HKL package (Otwinowski and Minor, 1997).

Structure Determination and Model Refinement

Initial phases for the SeMet-labeled SA2-Scc1 were obtained by single-wavelength anomalous dispersion (SAD) with AutoSol in the PHENIX package (Adams et al., 2010). Model building of the SA2 N-terminal HEAT repeats and Scc1 was done with AutoBuild in PHENIX. Subsequent model building was carried out with COOT (Emsley and Cowtan, 2004), and the structure was refined with PHENIX. Structures of the Native-MES and SeMet-MES complexes were solved by molecular replacement with PHENIX, with the SeMet structure (without MES) as the search model. Statistics for refinement are summarized in Table 3-1. The final model of the native SA2-Scc1-MES complex (Native-MES) contains residues 83-254, 261-438, 455-505, 512-543, 547-748, 752-805, 807-836, 853-933, 936-959, 965-986, 988-990, 993-1035 and 1037-1047 from SA2, residues 321-396 from Scc1 and one MES molecule. The final model of the SeMet SA2-Scc1-MES complex (SeMet-MES) contains residues 83-91, 93-255, 260-438, 455-505, 513-543, 548-748, 753-836, 853-959, 965-991, 994-1035 and 1037-1048 from SA2, residues 321-395 from Scc1 and one MES molecule. The final model of the SeMet SA2-Scc1 complex (SeMet) contains residues 83-253, 261-438, 456-505, 513-543, 546-674, 677-748, 753-804, 808-836, 852-932, 938-959, 966-986, 988-990 and 993-1049 from SA2, and residues 321-

394 from Scc1. Remaining residues of SA2 and Scc1 are disordered. All structure drawings in this study were created with PyMOL (http://www.pymol.org/) and depicted the SeMet-MES complex.

In Vitro Binding Assays

The cDNAs encoding full-length human SA2, full-length human Scc1, and the Scc1 fragment (residues 211-420) were cloned into the FseI and AscI sites of a modified pCS2-Myc vector. The SA2 and Scc1 mutants were constructed with the QuikChange Site-directed Mutagenesis Kit (Stratagene). The pCS2-Myc-SA2 (wild type and mutants) or pCS2-Myc-Scc1 (wild type and mutants) vectors were added either alone or as a mixture of 3:1 ratio to the TNT Quick Coupled Transcription Translation System (Promega) and incubated in the presence of [^{35}S] methionine at 30 °C for 90 min to produce ^{35}S-labeled Myc-SA2, Myc-Scc1 or the Myc-SA2-Scc1 complex.

To assay the binding between SA2 and Scc1, GST-SA2 (residues 80-1060) and GST-Scc1 (residues 211-420) were expressed in bacteria and purified with the glutathione-Sepharose 4B resin (GE Healthcare). The glutathione-Sepharose beads bound to GST-SA2 or GST-Scc1 were incubated with ^{35}S-labeled Myc-Scc1 (wild type and mutants) or Myc-SA2 (wild type and mutants), respectively, at 4 °C overnight, and washed four times with TBS containing 0.05% Tween 20. Beads bound to GST were used as negative controls in both cases. The bound proteins were separated by SDS-PAGE. The gels were stained with Coomassie blue, dried and analyzed with a phosphorimager (Fujifilm). Intensities of bound proteins were quantified with ImageJ.

To assay the interaction between Sgo1 and SA2-Scc1, synthetic Sgo1 (residues 313-353) and phospho-T346 Sgo1 (pSgo1) peptides (each with an extra C-terminal cysteine) were coupled to beads with the SulfoLink Immobilization Kit and Coupling Resin (Thermo Scientific) according to the manufacturer's instructions. Recombinant purified $SA2_{80-1060}$-$Scc1_{281-420}$ or the ^{35}S-labeled (wild-type and mutant) Myc-SA2-$Scc1_{211-420}$ complexes were incubated with Sgo1- or pSgo1-coupled beads at 4 °C overnight, and washed four times with TBS containing 0.05% Tween 20. The bound proteins were separated by SDS-PAGE and stained with Coomassie blue. For the assays with radioactive proteins, the gels were dried and analyzed with a phosphorimager (Fujifilm). Intensities of bound proteins were quantified with ImageJ.

To assay the binding between Wapl and SA2-Scc1, GST-$Wapl_{401-600}$ and GST-$Wapl_{410-590}$ (wild-type and mutants) were expressed in bacteria and purified with glutathione-Sepharose 4B beads. Beads bound to GST or GST-Wapl proteins were incubated with recombinant purified $SA2_{80-1060}$-$Scc1_{281-420}$ or the ^{35}S-labeled wild-type and mutant Myc-SA2-$Scc1_{211-420}$ complexes, in the presence of increasing concentrations of Sgo1 or pSgo1 peptides. The beads were washed with TBS containing 0.05% Tween 20. The bound proteins were analyzed and quantified as described above.

Isothermal Titration Calorimetry (ITC)

ITC was performed with a MicroCal iTC200 (GE Healthcare) at 20 °C. Calorimetric measurements were performed with purified SA2-Scc1 and synthetic unphosphorylated or phospho-T346 Sgo1 peptides containing residues 313-353. For each titration, 300 μl of 23 μM SA2-Scc1 in a buffer containing 20 mM Tris-HCl, pH 7.7, 100 mM NaCl and 5 mM TCEP was

added to the calorimeter cell. The Sgo1 or pSgo1 peptide (350 μM) in the same buffer was injected with 18 portions of 2 μl with an injection syringe. Binding parameters were evaluated with the Origin package provided with the instrument.

Cell Culture, Transfection and Synchronization

HeLa Tet-On cells were grown in DMEM (Invitrogen) supplemented with 10% FBS and 2 mM L-glutamine. Plasmid transfection was performed when cells reached a confluency of 50% with the Effectene reagent (Qiagen) according to the manufacturer's protocols. For siRNA transfection, cells were transfected with Lipofectamine RNAiMAX (Invitrogen) at 20-40% confluency according to the manufacturer's protocols, and analyzed at 24-48 h after transfection. The siRNA oligonucleotides targeting human Wapl (siWapl; 5′-CGGACTACCCTTAGCACAA-3′), Sgo1 (siSgo1; 5′-GAGGGGACCCUUUUACAGATT-3′), SA1 (siSA1; 5′-GAAUAGAGAUGUUUCGAAA-3′) and SA2 (siSA2; 5′-CCACUGAUGUCUUACCGAA-3′) were synthesized by Thermo Scientific. The siRNAs were transfected at a final concentration of 5 nM.

For mitotic synchronization, cells were treated with 2 mM thymidine for 16-18 h, released into fresh medium for 9 h and blocked at mitosis with the addition of 5 μM nocodazole (Sigma) for 2 h. For the cohesin-loading assay, cells were treated with 2 mM thymidine for 16-18 h and released into fresh medium for 11 h before fixation. For the cohesion fatigue assay, cells were released into medium containing 10 μM MG132 for an additional 2 h after nocodazole (300 nM) treatment.

For stable cell lines, HeLa Tet-On cells were transfected with pTRE2-GFP vector encoding wild-type human Sgo1. Clones were selected with 200 μg/ml hygromycin B. Inducible expression of GFP-Sgo1 was screened in the absence or presence of 1 μg/ml doxycycline (Invitrogen).

Antibodies, Immunoblotting and Immunoprecipitation

The anti-Wapl antibody was generated against a C-terminal fragment of human Wapl (residues 601-1190) as described (Wu et al., 2012). Rabbit polyclonal anti-GFP antibodies were raised against purified recombinant eGFP at Yenzym Antibodies. The following antibodies were purchased from the indicated commercial sources: anti-Myc (Roche, 11667203001), anti-SA2 (Santa Cruz, Biotechnology, sc-81852), anti-Scc1 (Bethyl Laboratories, A300-080A), anti-β-tubulin (Sigma, T4026) and MPM2 (Millipore, 05-368). The antibodies to Myc and Scc1 have been validated for immunoblotting and immunoprecipitation applications. The antibody to MPM2 has been validated for flow cytometry. The relevant validation information and references can be found at the manufacturers' websites. The antibody to SA2 is validated for immunoblotting in this study (Figure 3-2d), and the anti-GFP antibody is validated for both immunoblotting and immunoprecipitation (Figure 3-5c).

For immunoblotting, cells were lysed in the SDS sample buffer (pH 6.8), sonicated and boiled. The lysates were separated by SDS-PAGE and blotted with the desired primary antibodies. The primary antibodies in the form of crude sera were used at 1:1,000 dilutions, whereas purified antibodies were used at a final concentration of 1 μg/ml. Horseradish peroxidase-linked donkey anti-rabbit or sheep anti-mouse IgGs (GE Healthcare) were used as

secondary antibodies. Immunoblots were developed with the SuperSignal West Pico Chemiluminescent Substrate (Thermo Scientific) according to the manufacturer's protocols.

For immunoprecipitation, the anti-Myc or anti-GFP antibodies were coupled to Affi-Prep Protein A beads (Bio-Rad) at a concentration of 1 mg/ml. Cells were lysed with the lysis buffer containing 25 mM Tris-HCl, pH 7.7, 75 mM NaCl, 0.1% (v/v) Nonidet P-40, 2 mM $MgCl_2$, 10% (v/v) glycerol, 5 mM NaF, 0.3 mM Na_3VO_4, 10 mM β-glycerophosphate, 1 mM DTT, protease inhibitor mixture (Roche) and 50 units/ml Turbo Nuclease (Accelagen). After a 1-h incubation on ice and a 10-min incubation at 37 °C, all lysates were centrifuged at 4 °C at 20,817g for 20 min. The supernatants were incubated with the desired antibody beads for 3 h at 4 °C. The beads were then washed three times with the lysis buffer containing 200 mM NaCl. Proteins bound to beads were dissolved in SDS sample buffer, separated by SDS-PAGE and blotted with the appropriate antibodies.

Flow Cytometry

Cells were harvested with trypsinization and fixed in 70% ice-cold ethanol overnight. After being washed with PBS, cells were permeabilized with PBS containing 0.25% Triton X-100 on ice for 5 min. Then cells were incubated with the antibody to MPM2 in PBS containing 1% BSA for 3 h at room temperature, and this was followed by an incubation with a fluorescent secondary antibody (Invitrogen) for 30 min. After being washed with PBS, cells were resuspended in PBS containing 0.1% Triton X-100, RNase A and propidium iodide, and then analyzed with a flow cytometer. Data were processed with FlowJo.

Immunofluorescence and Metaphase Spreads

After synchronization, mitotic HeLa Tet-On cells were collected by shake-off. Cells were washed once with PBS, treated with 55 mM KCl hypotonic solution at 37 °C for 15 min and spun onto microscope slides with a Shandon Cytospin centrifuge. Cells on the slides were first permeabilized with the PHEM buffer (25 mM HEPES, pH 7.5, 10 mM EGTA, pH 8.0, 60 mM PIPES, pH 7.0, and 2 mM $MgCl_2$) containing 0.3% Triton X-100 for 5 min and then fixed in 4% paraformaldehyde for 10 min. Fixed cells were washed three times with PBS containing 0.1% Triton X-100 for 2 min each time, and were incubated with CREST in PBS containing 3% BSA and 0.1% Triton X-100 at 4 °C overnight. Cells were then washed three times with PBS containing 0.1% Triton X-100 for 2 min each time, and were incubated with fluorescent secondary antibodies (Molecular Probes) in PBS containing 3% BSA and 0.1% Triton X-100 for 1 h at room temperature. Cells were again washed three times with PBS containing 0.1% Triton X-100 and then stained with 1 μg/ml DAPI for 2 min. After the final washes, the slides were sealed with nail polish and viewed with a 100× objective on a DeltaVision fluorescence microscope (GE Healthcare). Image processing and quantification were performed with ImageJ.

For the cohesin-loading assay, cells were plated in four-well chamber slides (LabTeck). Cells were transfected with GFP-SA2 plasmids for 8 h, and this was followed by siSA1 and siSA2 transfection for another 36 h. Cells were first extracted with PHEM buffer containing 0.5% Triton X-100 for 5 min and then were fixed in 2% paraformaldehyde for 15 min. After being washed with PBS, cells were blocked in PBS containing 2% BSA for 1 h, and were incubated with the anti-GFP and anti-tubulin antibodies in PBS containing 0.2% Triton X-100 and 3% BSA overnight at 4 °C. After being washed three times with PBS containing 0.05%

Tween 20, cells were incubated with fluorescent secondary antibodies in PBS containing 0.2% Triton X-100 and 3% BSA for 1 h at room temperature. The cells were again washed three times with PBS containing 0.05% Tween 20 and stained with 1 μg/ml DAPI in PBS for 2 min. After final washes, slides were mounted and viewed with a 100× objective on a DeltaVision deconvolution fluorescence microscope. A series of z-stack images were captured at 0.2 μm intervals, deconvolved and projected. Image processing and quantification were performed with ImageJ.

RESULTS

Structure of Human SA2 Bound to Scc1

We coexpressed human SA2 and the SA2-binding region of Scc1 in insect cells, purified the resulting cohesin subcomplex and determined its crystal structure (Figure 3-1 and Table 3-1). SA2 and Scc1 form a simple 1:1 heterodimer. SA2 contains a helical N-terminal domain (N domain) followed by 17 HEAT repeats (termed R1-R17). The SA2 structure is shaped like a dragon. Two long helices of R1 and R2 resemble the snout of the dragon. The N domain, comprising seven helices, packs against R1 and resembles the head of the dragon. The body of the dragon bends sharply at R9 and R10. This bend divides SA2 into N and C halves. Scc1 consists of four short helices (termed αA-αD) and two long extended segments. These elements interact extensively with SA2 at four major sites as Scc1 sits astride the dragon (Figure 3-1 and Figure 3-2a). As expected, many residues at the SA2-Scc1 interface are highly conserved in metazoans.

At site I, the N-terminal loop of Scc1 makes mainly electrostatic interactions with SA2 residues in the N domain and at the ridge of R1 and R2 (Figure 3-1b). There are four salt bridges formed between R322, D327, K330 and E331 of Scc1 and E154, R213, D209 and R298 of SA2, respectively. In addition, Scc1 L324 packs against T149, F152 and V212, forming hydrophobic interactions. At site II, the αA helix of Scc1 packs against R2-R4 of SA2 (Figure 3-1c). The side chain packing between Scc1 and SA2 at this site appears to be suboptimal. For example, even though I337 and L341 of Scc1 are located in the vicinity of Y297 and W334 of SA2, there is minimal contact between their van der Waals surfaces. At site III, the loop connecting αA and αB of Scc1 interacts with the edge of R5 and R6 of SA2 (Figure 3-1d). Scc1 αB contacts R7, R9

and the R7-R8 loop in SA2. Specifically, L351, L353, A354, P355 and P356 of Scc1 develop hydrophobic interactions with L416, L473, H474, H476 and Y479 of SA2. Site IV is close to the bend, with αB, αC and αD of Scc1 interacting extensively with R11-R13 of the C half of SA2 (Figure 3-1e). In particular, L385, L388 and F389 located in αD of Scc1 make hydrophobic contacts with L742, W743, L745, M796 and I797 of SA2. Thus, Scc1 interacts with SA2 through an extensive interface that spans nearly the entire length of SA2.

Identification of a Binding Hotspot between SA2 and Scc1

To ascertain the functional importance of the observed SA2-Scc1 interface, we created about 50 SA2 and Scc1 mutants targeting conserved, surface-exposed residues at or near the SA2-Scc1 interface. Strikingly, among these mutants, only one, SA2 D793K, abolished the binding between SA2 and Scc1 (Figure 3-2b and Figure 3-3a, 3b, 3c, 3d). SA2 D793 is located at site IV. Its side chain forms hydrogen bonds with the backbone amides of A377 and Q378 of Scc1, which reside in the loop connecting αC and αD (Figure 3-2c). In agreement with this result, deletion of P376 and A377 in this loop, deletion of αD or mutation of the three hydrophobic residues in αD abolished Scc1 binding to SA2 (Figure 3-3e). Moreover, ectopic expression of Myc-SA2 wild type (WT), but not D793K, in HeLa cells rescued the premature sister-chromatid separation and mitotic arrest caused by co-depletion of SA1 and SA2 (Figure 3-2d, 2e, 2f and 2g). Therefore, SA2 and Scc1 interact through an extensive interface, with site IV being a binding hotspot. Interestingly, in the prefusion state of hemagglutinin (HA) of the influenza virus, an aspartate side chain of the fusion peptide forms similar hydrogen bonds to the

backbone amides of residues in a pocket on HA (Ivanovic et al., 2013). Disruption of this interaction is a rate-limiting step in viral-membrane fusion.

Identification of a Functional Sgo1-Binding Site on Cohesin

Human Sgo1 associates with cohesin during mitosis, and phosphorylation of Sgo1 at T346 enhances this association (Liu et al., 2013b). It is unclear, however, whether the cohesin-Sgo1 interaction is direct. Through systematic deletion mutagenesis (data not shown), we mapped the cohesin-binding region of Sgo1 to a 41-residue conserved motif containing T346. Both the unphosphorylated Sgo1 and phospho-T346 Sgo1 (pSgo1) peptides bound purified recombinant SA2-Scc1 (Figure 3-4a). pSgo1 bound more tightly than unphosphorylated Sgo1 did. As determined by isothermal titration calorimetry (ITC), unphosphorylated Sgo1 bound SA2-Scc1 with a Kd of 618 ± 80 nM (mean ± s.d. of three independent measurements), whereas pSgo1 had a Kd of 109 ± 35 nM (Figure 3-4b). Both peptides bound SA2-Scc1 with a stoichiometry of 1:1, results indicating that SA2-Scc1 has a single Sgo1-binding site. Thus, Sgo1 binds directly to the SA2-Scc1 cohesin subcomplex, and Sgo1 phosphorylation enhances, but is not required for, this binding.

Despite numerous attempts, we failed to obtain diffracting crystals of the SA2-Scc1-pSgo1 complex. The structural basis of phosphorylation-enhanced Sgo1 binding to cohesin remains to be established. We thus sought to define the Sgo1-binding site on SA2-Scc1 through mutagenesis. Among the SA2 and Scc1 mutations, SA2 Y297A, R298E, D326K, K330E, Y331A, W334A, D793K and K870E greatly diminished Sgo1 or pSgo1 binding *in vitro* (Figure 3-4c and Figure 3-5a, 5b). The SA2 D793K mutant lost binding to Sgo1 because it could not

bind Scc1. Another mutant, K870E, also had weakened Sgo1 binding. K870 is located at site IV, in proximity to D793. Mutation of this residue probably affects Sgo1 binding indirectly through affecting Scc1 binding. Aside from D793 and K870, all other residues critical for Sgo1 binding, including Y297, R298, D326, K330, Y331 and W334, are clustered near site II of the SA2-Scc1 interface (Figure 3-4d). When coexpressed with GFP-Sgo1 in HeLa cells, mutants targeting these residues also exhibited weaker binding to GFP-Sgo1 (Figure 3-5c). Moreover, the Sgo1 binding-deficient SA2 mutants, Y297A, R298E, Y331A and W334A, failed to rescue the mitotic-arrest phenotypes of HeLa cells depleted of SA1 and SA2 (Figure 3-4e, 4f and Figure 3-5d, 5e). Consistently with this, Y331A and W334A also failed to prevent premature sister-chromatid separation in these cells (Figure 3-4g). Collectively, these results establish site II of SA2-Scc1 as a functional Sgo1-binding site. The notion that Sgo1 binds near the SA2-Scc1 interface is also consistent with the fact that Sgo1 binds to only the SA2-Scc1 complex and does not associate with either SA2 or Scc1 alone (data not shown).

We noticed that a 2- (N-morpholino) ethanesulfonic acid (MES) molecule from the crystallization solution bound at the Sgo1-binding site (Figure 3-4d and Figure 3-6a, 6b). In particular, the sulfate group of MES makes hydrogen bonds and favorable electrostatic interactions with Y297 and R298 and is in the vicinity of Y331. Y297 and R298 belong to a signature FVHRYRD motif conserved in SA proteins in eukaryotes from yeast to humans. SA2 Y297F and Y331F were defective in Sgo1 binding (Figure 3-5c), thus implicating their hydroxyl groups in engaging in nonhydrophobic interactions with Sgo1. Thus, one intriguing possibility is that MES might mimic phospho-T346 of Sgo1. Future structural studies are needed to rigorously test this possibility.

The conserved FVHRYRD motif is involved in Scc2-Scc4 binding in fission yeast (Murayama and Uhlmann, 2014). Mutations of this motif cause a partial defect in topological cohesin loading to circular DNA *in vitro* and a cohesion defect in yeast cells (Murayama and Uhlmann, 2014). We tested whether this motif in human SA2 was also required for cohesin loading in human cells. GFP-SA2 Y297A and R298E localized to chromatin in telophase HeLa cells as efficiently as GFP-SA2 WT (Figure 3-6c, 6d). As a negative control, the Scc1 binding-deficient D793K mutant did not associate with chromatin. Therefore, we do not have evidence to indicate a role for the FVHRYRD motif of human SA2 in cohesin loading. Because Scc2-Scc4 interacts with multiple cohesin subunits (Murayama and Uhlmann, 2014), disruption of a single interaction surface might not block cohesin association with chromatin. Our results thus do not rule out a role of this motif in cohesin loading. Nevertheless, because SA2 Y297A and R298E do not show gross chromosome loading defects, their functional defects in human cells are probably due to their inability to bind Sgo1.

Sgo1 Competes with Wapl for Cohesin Binding

SA2-Scc1 also interacts with Wapl. In particular, several FGF motifs in the N-terminal region of Wapl have been implicated in SA2-Scc1 binding (Shintomi and Hirano, 2009). In addition, we have previously shown that a middle region of human Wapl (Wapl-M, residues 510-570) is critical for SA2-Scc1 binding *in vitro* (Ouyang et al., 2013) (Figure 3-7a). We further tested whether Wapl-M was required for Wapl function in human cells. As expected, depletion of Wapl greatly increased the percentage of mitotic cells with arm-closed sister chromatids (Figure 3-7b, 7c) because cohesin was not effectively removed from chromosome arms, and

sister chromosomes were not completely decatenated in Wapl-depleted cells (Haarhuis et al., 2013; Tedeschi et al., 2013; Yu, 2013). Expression of wild-type Wapl, but not the mutant with Wapl-M deleted (Δ510-570), rescued this arm-resolution deficiency. As expected from the well-established genetic antagonism between Sgo1 and Wapl in centromeric cohesion protection (Gandhi et al., 2006; Kueng et al., 2006), depletion of Wapl from HeLa cells rescued the premature sister-chromatid separation and the resulting mitotic arrest caused by Sgo1 depletion (Figure 3-8a, 8b). Restoring functional Wapl through increasing expression of Wapl wild type restored mitotic arrest in cells depleted of both Sgo1 and Wapl. When expressed at levels similar to those of wild type, Wapl Δ510-570 was less effective in restoring Wapl function and mitotic arrest in these cells. Collectively, our results suggest that the middle region of Wapl is critical for its function in human cells.

Because both Sgo1 and Wapl interact with SA2-Scc1, we tested whether Sgo1 and Wapl-M competed for binding to SA2-Scc1. A GST-Wapl fragment containing Wapl-M pulled down recombinant SA2-Scc1 purified from insect cells (Figure 3-7d). Addition of the pSgo1 peptide reduced SA2-Scc1 binding to GST-Wapl-M in a dose-dependent manner (Figure 3-7d, 7e). As expected, the unphosphorylated Sgo1 peptide was less effective in the competition. As a control, a shorter pSgo1 peptide (with five residues flanking pT346 on either side) showed no competition.

We then mapped the Wapl-binding site on SA2-Scc1. We focused our analysis on the conserved patch of residues at the Sgo1-binding site (Figure 3-7f, 7g). Indeed, mutations of K290, D326 and K330 abolished Myc-SA2 binding to endogenous Wapl in human cells (Figure 3-7h). Mutations of Y331 and W334 in SA2 diminished (but did not abolish) Wapl binding in

human cells. Four of the five Wapl binding-deficient SA2 mutants, including D326K, K330E, Y331A and W334A were also defective in Sgo1 binding. Mutation of SA2 Y328 had no effect on Wapl or Sgo1 binding. We further confirmed that the K290E, D326K and K330E mutations greatly reduced the binding of SA2-Scc1 to GST-Wapl-M *in vitro* (Figure 3-8c, 8d). Therefore, Sgo1 and Wapl compete with each other for cohesin binding, and they bind to overlapping sites on SA2-Scc1.

SA2 mutations or high concentrations of pSgo1 do not completely block Wapl binding to SA2-Scc1, thus suggesting that Wapl might bind SA2-Scc1 through multiple interfaces. In addition, the Wapl- and Sgo1-binding residues on SA2 are highly conserved in all metazoans, whereas the cohesin-binding motifs of Sgo1 and Wapl are conserved in only vertebrates and not in Drosophila or Caenorhabditis elegans. It is possible that certain conserved structural features of Sgo1 and Wapl cannot be easily gleaned from amino acid sequences alone. Alternatively, these SA2 residues are conserved for other purposes, such as binding Scc2-Scc4.

Direct Sgo1-Wapl Antagonism Strengthens Cohesion Protection

An established function of cohesin-bound Sgo1 is to recruit PP2A to cohesin and enable PP2A to protect Sororin from phosphorylation by Cdk1 (Liu et al., 2013b). Hypophosphorylated Sororin remains bound to Pds5 to counteract Wapl, thereby maintaining centromeric cohesion. Expression of the nonphosphorylatable Sororin 9A mutant with all Cdk1 sites mutated has been shown to bypass the requirement for Sgo1 in cohesion protection during normal mitotic progression (Liu et al., 2013b; Nishiyama et al., 2013). As shown above, pSgo1 binds to SA2-Scc1 with high affinity (around 100 nM) and directly competes with Wapl for cohesin binding.

We thus examined whether the strong Sgo1 binding to SA2-Scc1 had additional roles aside from enabling Sororin dephosphorylation by PP2A.

We first revisited the phenotypes of Sororin 9A-expressing cells depleted of Sgo1. As shown previously (Liu et al., 2013b), in the presence of nocodazole (which arrested cells in prometaphase, with all kinetochores not experiencing spindle-pulling force or tension), expression of Sororin 9A in HeLa cells prevented premature sister-chromatid separation caused by Sgo1 depletion (Figure 3-9a). In stark contrast, in cells treated with the proteasome inhibitor MG132 (which arrested cells at metaphase, with persistent spindle-pulling force and kinetochore tension), Sgo1 depletion caused massive premature sister-chromatid separation even in cells expressing Sororin 9A (Figure 3-9a). Thus, in the absence of the spindle-pulling force at kinetochores, hypophosphorylated Sororin alone presumably suffices to protect centromeric cohesion. When kinetochores are under persistent tension, both Sgo1 and hypophosphorylated Sororin are required to maintain sister-chromatid cohesion. This result suggests that, in addition to promoting Sororin dephosphorylation, Sgo1 has other roles in cohesion protection.

We hypothesized that the direct competition between Sgo1 and Wapl for cohesin binding might allow Sgo1 to shield cohesin from Wapl and account for the Sororin-independent function of Sgo1 in cohesion protection. A strong prediction of this hypothesis was that cohesin containing Wapl binding-deficient SA2 mutants should alleviate the need for Sgo1 protection. Indeed, overexpression of SA2 K290E, D326K or K330E mutants that lost Wapl binding in HeLa cells partially rescued the premature sister-chromatid separation (Figure 3-10a, 10b, and 10c) and mitotic arrest (Figure 3-9b) caused by Sgo1 depletion. As controls, expression of SA2 mutants that retained partial or full Wapl binding, including Y328A, Y331A and W334A, failed

to bypass Sgo1 requirement in cohesion protection. Expression of other SA2 mutants targeting a conserved patch of residues in the C half or the Scc1 binding-deficient D793K mutant also had no effect. Finally, overexpression of SA2 D326K or K330E even rescued the gradual loss of cohesion in the presence of prolonged MG132-induced metaphase arrest, a phenotype termed cohesion fatigue (Daum et al., 2011) (Figure 3-10d). These results suggest that a critical function of Sgo1 in cohesion protection is to directly shield cohesin from Wapl through binding to SA2-Scc1.

DISCUSSION

In this study, we have determined the crystal structure of the SA2-Scc1 cohesin subcomplex, which is the interaction hub for cohesin regulators. Further biochemical and functional analyses have uncovered direct competition between the cohesion protector Sgo1 and the cohesion inhibitor Wapl for cohesin binding and have demonstrated the relevance of this competition in cohesion protection.

Sgo1 forms a homodimer through its N-terminal coiled-coil domain that binds PP2A (Tang et al., 2006). One Sgo1 dimer binds to one PP2A complex (Xu et al., 2009). We have shown that the pSgo1 peptide binds with 1:1 stoichiometry to SA2-Scc1. In principle, the two monomers of the Sgo1 dimer could each bind one cohesin complex, thus bridging two cohesin rings. We do not have evidence that this type of Sgo1-dependent cohesin cross-linking occurs in human cells. More importantly, the SA2 D326K and K330E mutants, which are defective in Sgo1 binding, can bypass the requirement for Sgo1 in cohesion, by virtue of their inability to interact with Wapl. Because these mutants cannot physically link cohesin rings, the putative Sgo1-mediated cohesin cross-linking (even if it does occur) is unlikely to directly contribute to sister-chromatid cohesion.

The results presented herein, along with previously published results, suggest the following model for cohesion establishment and maintenance in human cells (Figure 3-9c). During telophase and G1, cohesin is loaded on chromosomes but undergoes Wapl-dependent dynamic release from chromosomes. This release involves an opening of the cohesin ring at the Smc3-Scc1 juncture (Buheitel and Stemmann, 2013; Eichinger et al., 2013) and requires an interaction

between Pds5 and the N-terminal region of Wapl (Wapl-N) and interactions between cohesin and the middle region and C-terminal domain of Wapl. The mechanism by which Wapl-Pds5 disrupts the Smc3-Scc1 interface is unknown but is unlikely to be due to direct competition for binding (Chatterjee et al., 2013; Ouyang et al., 2013). One possibility is that Wapl-Pds5 allosterically stimulates the intrinsic ATPase activity of cohesin, possibly by stabilizing the transition state. ATP hydrolysis transiently disrupts the Smc3-Scc1 interface and triggers the opening of the cohesin ring and its release from chromatin.

During S phase, Smc3 acetylation enables the binding of Sororin to Pds5. Sororin blocks the Pds5-Wapl-N interaction but does not completely displace Wapl from cohesin (Liu et al., 2013b; Nishiyama et al., 2010) because Wapl-M and Wapl-C can still associate with cohesin. This form of cohesin stably associates with sister chromatids and establishes cohesion. During mitosis, phosphorylation of Sororin by mitotic kinases disrupts the Sororin-Pds5 interaction (Nishiyama et al., 2010), and Wapl-N reengages Pds5 to trigger cohesin release from chromosome arms.

At centromeres, however, phosphorylated Sgo1 binds SA2-Scc1 to protect cohesin from Wapl in two ways. First, Sgo1 recruits PP2A to cohesin (Liu et al., 2013b), and this keeps Sororin hypophosphorylated and bound to Pds5. Pds5-bound Sororin antagonizes Wapl-N. Second, Sgo1 directly competes with Wapl-M for binding to SA2-Scc1. As a result, cohesin bound to both Sgo1 and Sororin (indirectly through Pds5) is completely shielded from Wapl (Liu et al., 2013b). These two mechanisms collaborate to protect centromeric cohesion to the fullest extent. Strong centromeric cohesion is required to resist the spindle pulling force at sister kinetochores, and it enables the generation of kinetochore tension necessary for spindle-checkpoint inactivation and accurate chromosome segregation.

Another major function of shugoshin proteins is to protect meiotic cohesin at centromeres from separase-mediated cleavage during meiosis I (Katis et al., 2004; Kitajima et al., 2004). One mechanism by which shugoshin protects meiotic cohesin from separase is probably through PP2A-dependent dephosphorylation of Rec8 (the meiotic counterpart of Scc1) (Xu et al., 2009). Human Sgo1 appears to be capable of inhibiting separase-dependent removal of mitotic cohesin from centromeres, when the Sgo1-cohesin interaction is not disrupted properly (Lee et al., 2008; Liu et al., 2013a). Interestingly, the two separase-cleavage sites in human Scc1 flank the central SA2-binding region of Scc1 delineated in our structure (Hauf et al., 2001). In the future, it will be interesting to test whether SA2 contributes to Scc1 cleavage by providing a docking site for separase, and if it does so, to test whether Sgo1 binding to SA2-Scc1 also shields cohesin from separase.

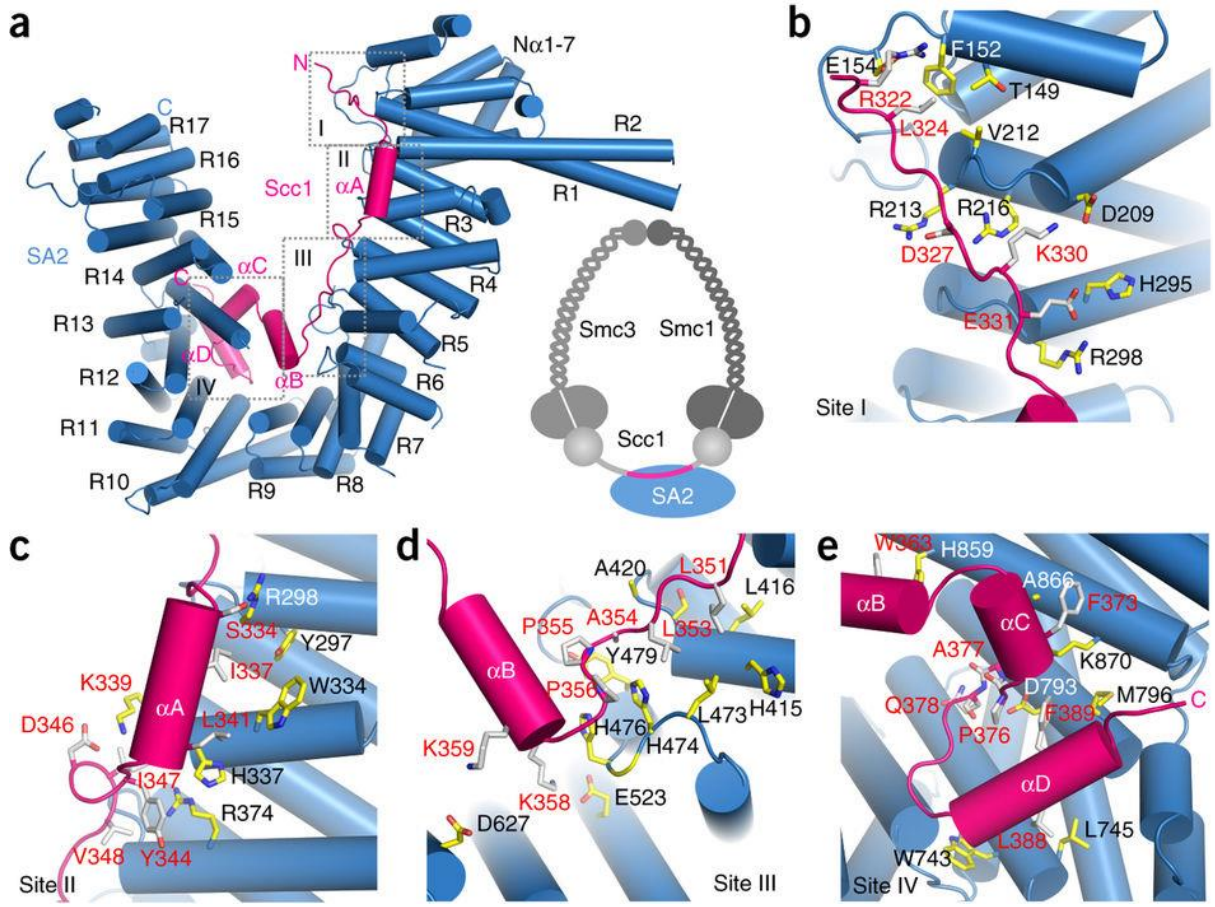

Figure 3-1. Structure and binding interface of human SA2–Scc1. (**a**) Cartoon diagram of the crystal structure of human SA2 in complex with the SA2-binding region of Scc1, with SA2 colored blue and Scc1 colored pink. The N-terminal helical domain and the 17 HEAT repeats (R1–R17) of SA2 are labeled. The N- and C termini of SA2 and Scc1 are indicated. The four major contact sites (I–IV) between SA2 and Scc1 are boxed in dashed lines. A schematic drawing of the cohesin architecture is shown at bottom right. (**b**–**e**) Zoomed-in views of sites I–IV, respectively. SA2 and Scc1 residues are in yellow and gray sticks, respectively, and Scc1 residues are labeled in red.

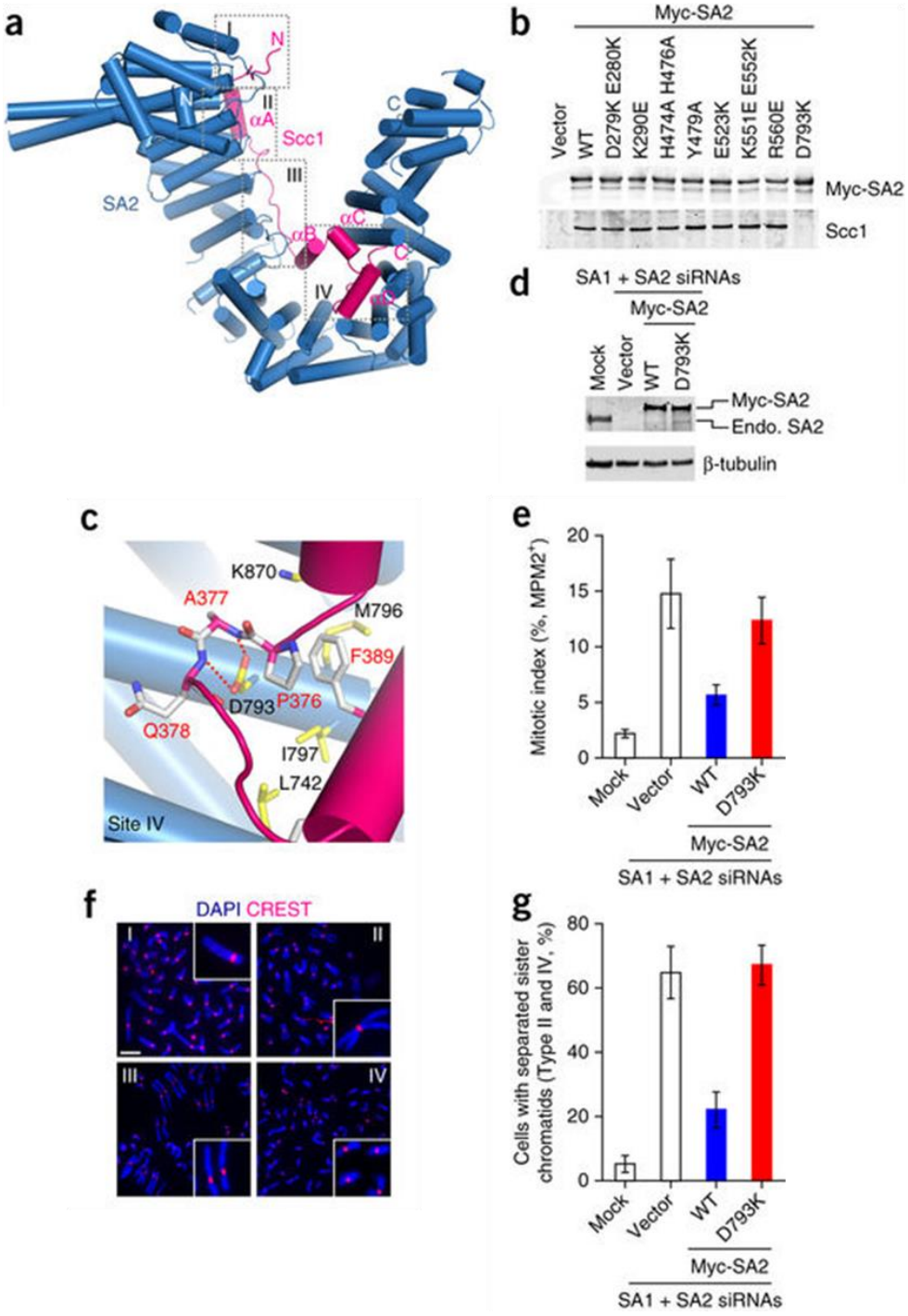

Figure 3-2. Identification of a binding hotspot between SA2 and Scc1. (**a**) Cartoon diagram of the structure of human SA2-Scc1, with SA2 and Scc1 colored blue and pink, respectively, in an orientation rotated 180° relative to that in **Figure 3-1a**. The N and C termini of both proteins and the four helices of Scc1 are labeled. The four SA2-Scc1 contact sites are boxed. (**b**) Anti-Myc and anti-Scc1 immunoblots of anti-Myc immunoprecipitates of HeLa cells transfected with

the indicated Myc-SA2 plasmids. WT, wild type. (**c**) Zoomed-in view of contact site IV, with SA2 and Scc1 residues in yellow and gray sticks, respectively. Scc1 residues are labeled in red. The dashed red lines indicate hydrogen bonds. (**d**) Anti-SA2 and anti–β-tubulin immunoblots of lysates of HeLa cells transfected with the indicated short interfering RNAs (siRNAs) and plasmids. WT, wild type; endo, endogenous. (**e**) Quantification of the mitotic indices (defined as the percentage of MPM2-positive cells with 4n DNA content) of cells in **d**. Error bars, s.d. (n = 4 independent experiments). (**f**) Four major types of metaphase spreads of cells in **d**. Spreads were stained with DAPI (blue) and the kinetochore marker CREST (red). Selected sister chromatids are magnified and shown in insets. Scale bar, 5 μm. (**g**) Quantification of the percentage of cells in **d** with type III and IV chromosome morphologies as in **f**. Error bars, s.d. (n = 4 independent experiments).

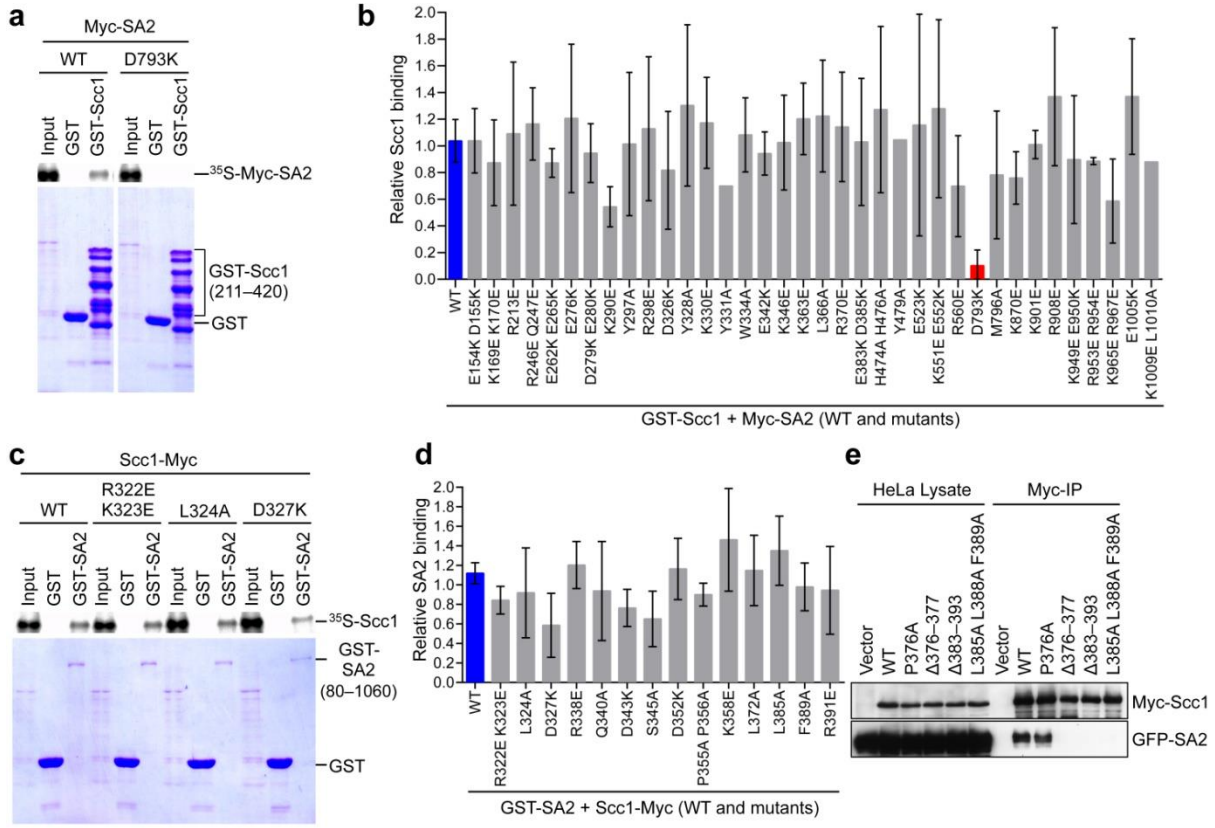

Figure 3-3. Mutational analysis of the SA2-Scc1 interaction *in vitro* and in human cells. (**a**) Autoradiograph (top) and Coomassie stained gel (bottom) of ^{35}S-labeled Myc-SA2 proteins (input) and the same proteins bound to GST or GST-Scc1 beads. WT, wild type. (**b**) Quantification of the *in vitro* binding assays in **a**. The binding intensities were normalized to the amount of input for each SA2 protein. Error bars, s.d. (n = 3, independent experiments). The Y331A, Y479A, K1009E L1010A mutants were tested twice. Only the means were shown for these samples. (**c**) Autoradiograph (top) and Coomassie stained gel (bottom) of ^{35}S-labeled Scc1-Myc proteins (input) and the same proteins bound to GST or GST-SA2 beads. WT, wild type. (**d**) Quantification of the *in vitro* binding assays in **c**. The binding intensities were normalized to the amount of input for each Scc1 protein. Error bars, s.d. (n = 3, independent experiments). (**e**) Anti-Myc or anti-GFP immunoblots of lysates and anti-Myc IP of HeLa cells co-transfected with plasmids encoding GFP-SA2 and the indicated Myc-Scc1 proteins. WT, wild type.

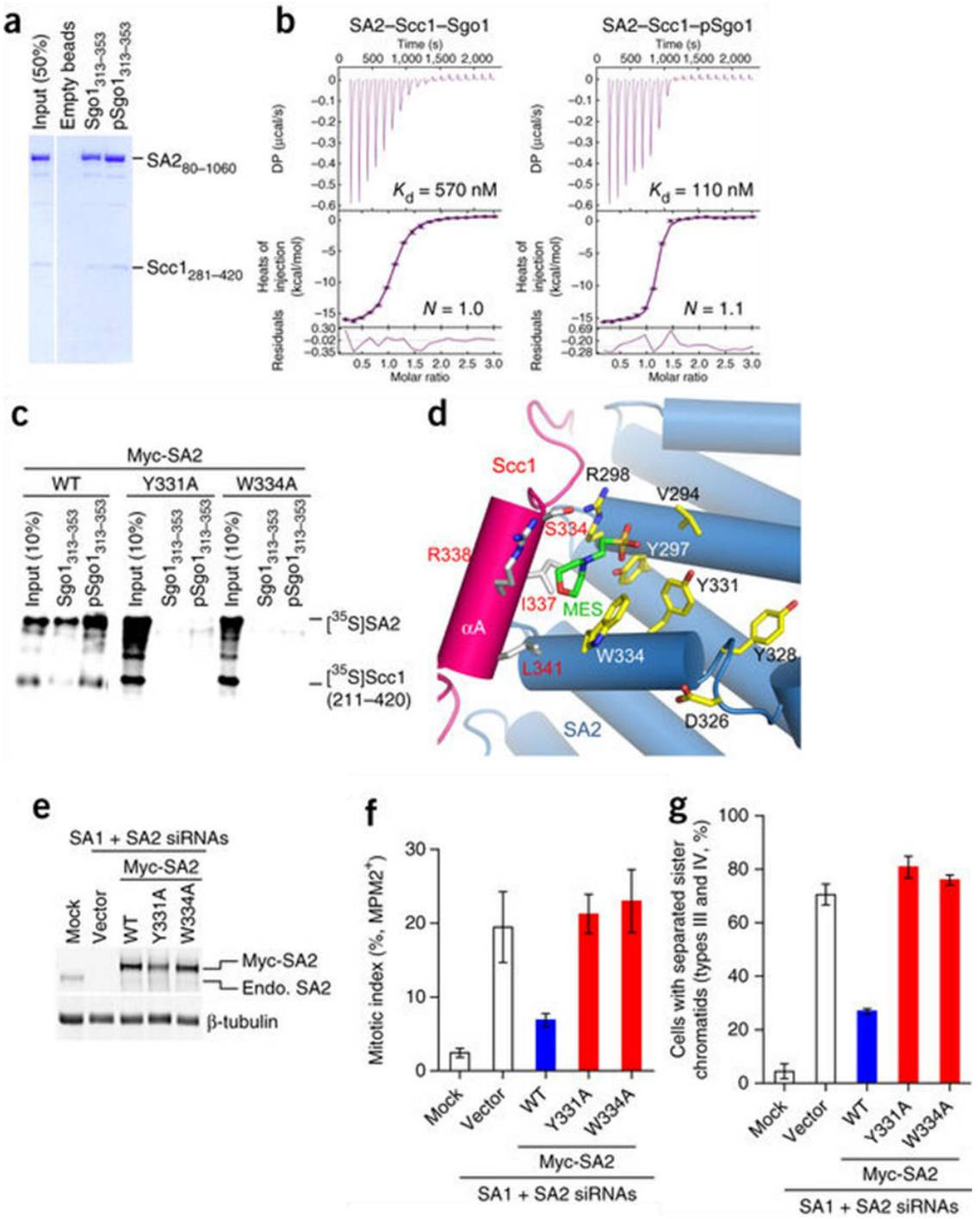

Figure 3-4. A conserved, functional Sgo1-binding site of SA2–Scc1. (**a**) Coomassie-stained SDS-PAGE gel of recombinant SA2–Scc1 (input) and the same complex bound to the indicated beads. (**b**) ITC curves of the binding between SA2–Scc1 and unphosphorylated or phospho-T346 Sgo1 peptides, with K_d and binding stoichiometry (N) indicated. DP, differential power. (**c**) Autoradiograph of ^{35}S-labeled SA2–Scc1 proteins (input) and the same proteins bound to beads

coupled to unphosphorylated or phospho-T346 Sgo1 peptides. WT, wild type. (**d**) The Sgo1-binding site of SA2–Scc1. Color and labeling schemes are as in **Figure 3-1c**. A MES molecule bound at this site is shown in sticks. (**e**) Anti-SA2 and anti–β-tubulin immunoblots of lysates of HeLa cells transfected with the indicated siRNAs and Myc-SA2 plasmids. The positions of the endogenous and Myc-SA2 are indicated. WT, wild type. (**f**) Quantification of the mitotic indices (defined as the percentage of MPM2-positive, 4n cells) of cells in **e**. Error bars, s.d. (n = 4 independent experiments). (**g**) Quantification of the percentages of mitotic cells in **e** with separated sister chromatids (type III and IV metaphase spreads). Error bars, range (n = 2 independent experiments).

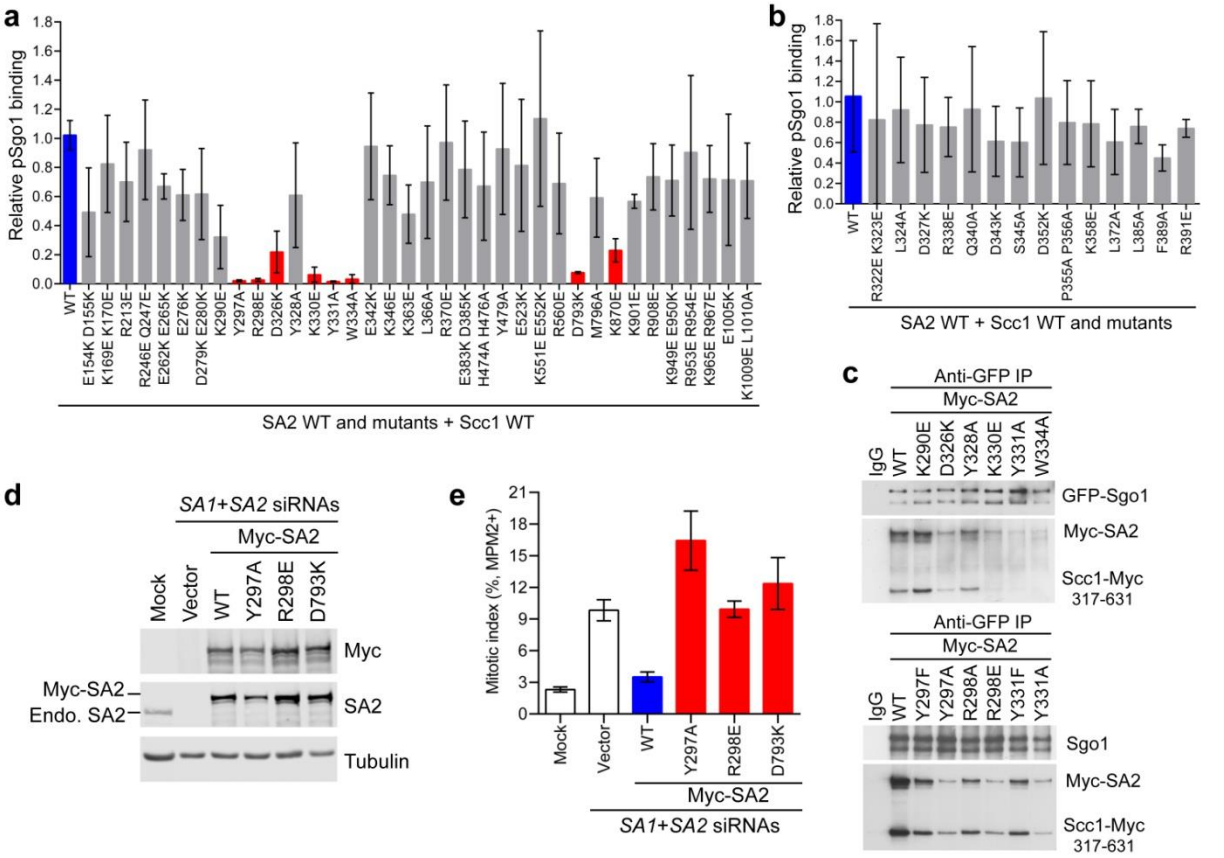

Figure 3-5. Identification of a Sgo1-binding site on SA2–Scc1. (**a**,**b**) Quantification of normalized intensities of the indicated ^{35}S-labeled SA2–Scc1 proteins bound to beads coupled to phospho-T346 Sgo1 peptides. WT, wild type. Error bars, s.d. (n = 3, independent experiments). (**c**) Anti-Myc, anti-GFP, and anti-Sgo1 blots of lgG and anti-GFP IP from GFP-Sgo1-expressing HeLa cells co-transfected with Scc1-Myc and the indicated Myc-SA2 plasmids. WT, wild type. (**d**) Anti-Myc, anti-SA2, and anti-tubulin blots of lysates of HeLa cells transfected with the indicated siRNAs and plasmids. WT, wild type. (**e**) Quantification of mitotic indices (defined as MPM2-positive, 4N cells) of cells in **d**. Error bars, s.d. (n = 7, independent experiments).

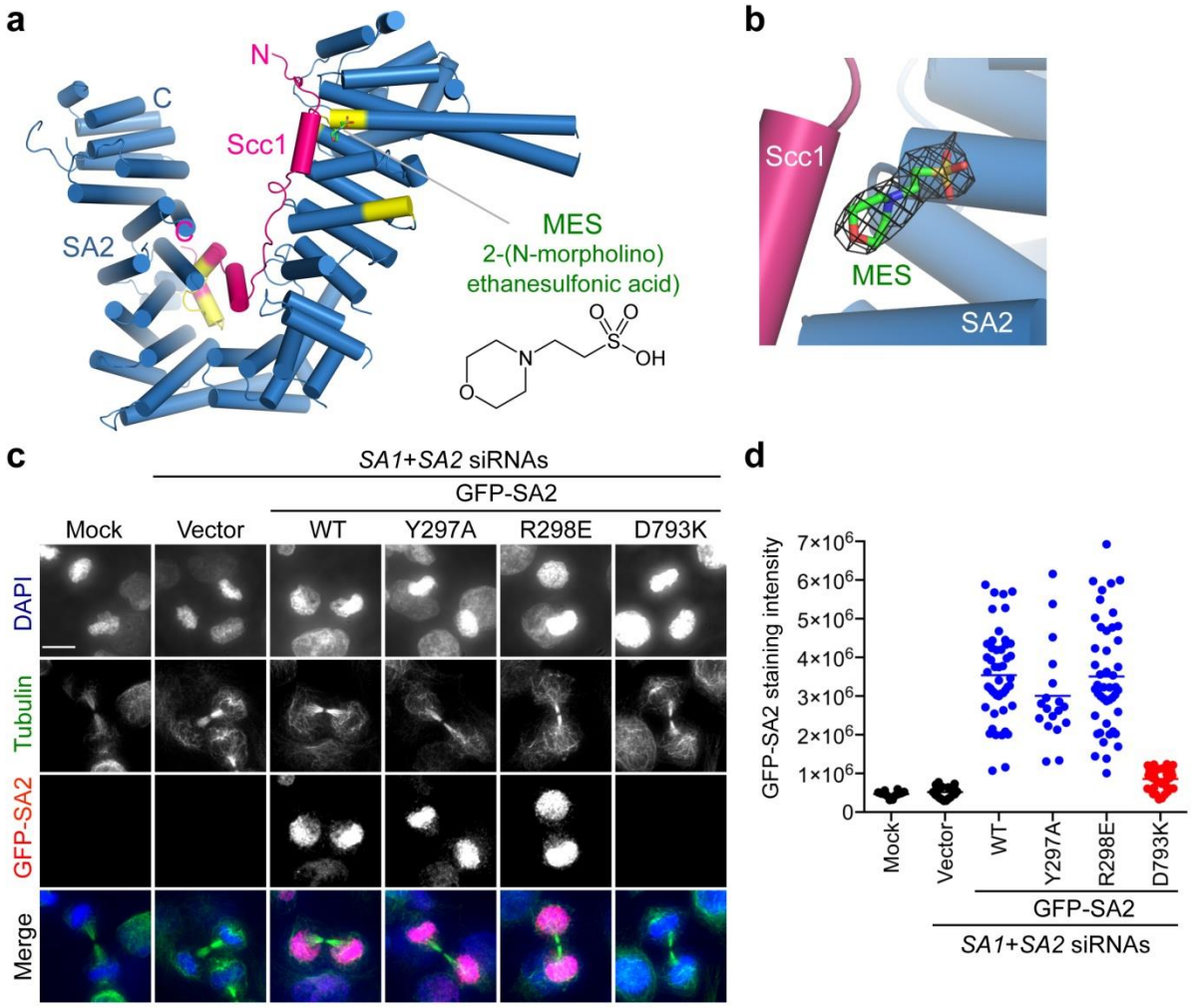

Figure 3-6. The conserved FVHRYRD motif of SA2 is not required for cohesin loading in human cells. (**a**) Cartoon diagram of the structure of human SA2–Scc1, with SA2 colored blue and Scc1 colored pink. The conserved SA2–Scc1 regions implicated in binding the cohesin loader Scc2–Scc4 are colored yellow. The MES molecule bound near the SA2–Scc1 interface is shown in sticks. The chemical structure of MES is shown in the lower right corner. (**b**) A zoomed-in view of the MES-binding site, with the kicked OMIT map of electron density around MES shown at a contour level of 3σ. (**c**) DAPI (blue in merge), anti-GFP (red in merge), and anti-tubulin (green in merge) staining of telophase HeLa cells transfected with the indicated GFP-SA2 plasmids and siRNAs. WT, wild type. Scale bar, 10 μm. (**d**) Quantification of the anti-GFP staining intensities of cells in **c**. Each dot in the graph represents a single cell (Mock, n = 12; Vector, n = 22; WT, n = 48; Y297A, n = 18; R298E, n = 46; D793K, n = 40). The horizontal bars indicate the means.

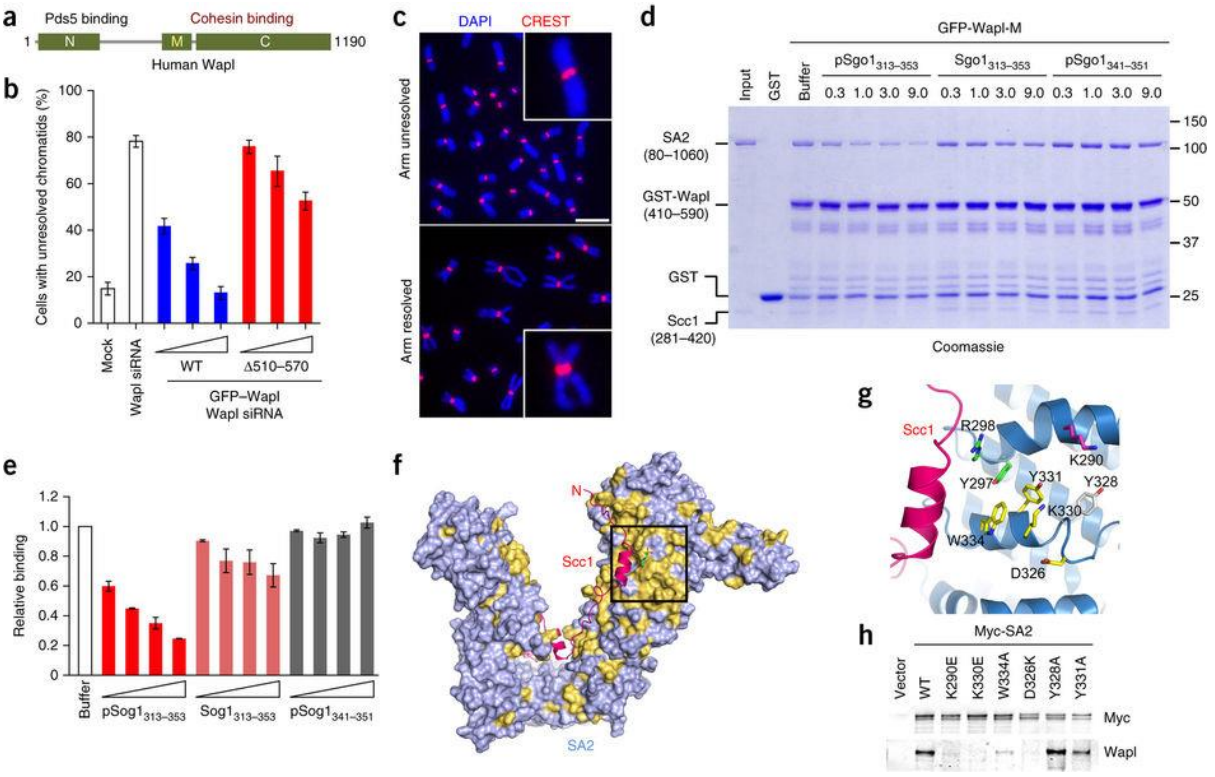

Figure 3-7. Competition between Wapl and Sgo1 for cohesin binding. (**a**) Schematic drawing of domains and motifs of human Wapl. (**b**) Quantification of the percentages of mitotic HeLa cells (transfected with the Wapl siRNA and increasing concentrations of the indicated plasmids) that had arm-closed chromosomes. WT, wild type. Error bars, range (n = 2 independent experiments). (**c**) Representative metaphase spreads of cells in **b** with arm-closed (n = 487) or arm-separated (n = 540) chromosomes. Selected sister chromatids are magnified in inset. Scale bar, 5 μm. (**d**) Coomassie-stained SDS-PAGE gel of recombinant SA2–Scc1 (input) and the same complex bound to GST or GST-Wapl, in the presence of increasing concentrations (shown above gel, in μM) of the indicated Sgo1 peptides. Molecular weights (kDa) are indicated at right. (**e**) Quantification of the relative SA2 band intensities of the binding reaction shown in **d**. Error bars, range (n = 2 independent experiments). (**f**) Surface diagram of SA2, with Scc1 shown in ribbons and MES shown in sticks. The SA2 residues conserved in metazoans are colored yellow. The conserved patch at or near the Sgo1-binding site is boxed. (**g**) Ribbon drawing of the boxed region in **f**, with conserved, surface-exposed SA2 residues shown in sticks. Residues critical for binding to Wapl, Sgo1 or both are colored magenta, green and yellow, respectively. (**h**) Anti-Myc and anti-Wapl immunoblots of anti-Myc immunoprecipitates of HeLa cells transfected with the indicated plasmids. WT, wild type.

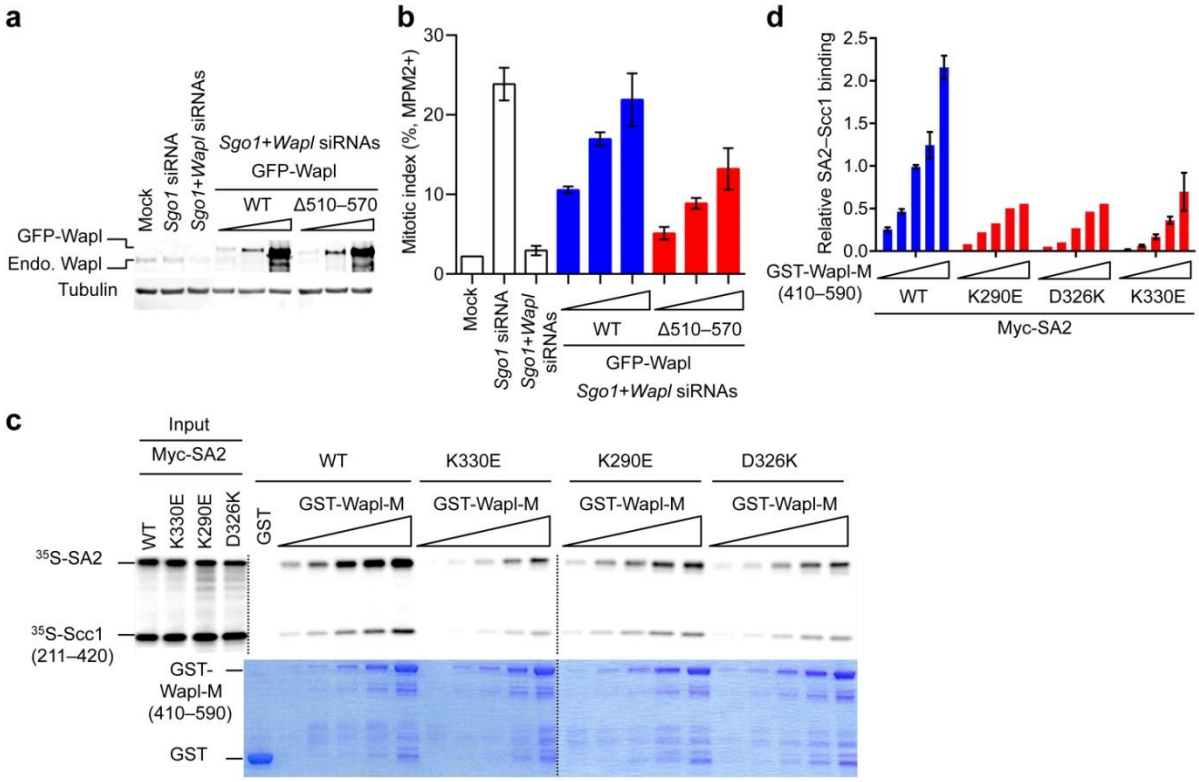

Figure 3-8. Identification of a Wapl-binding site on SA2–Scc1. (**a**) Anti-Wapl and anti-tubulin blots of lysates of HeLa cells transfected with the indicated siRNAs with or without increasing amounts of the indicated GFP-Wapl plasmids. WT, wild type. The positions of the endogenous and GFP-Wapl are labeled. (**b**) Quantification of mitotic indices (defined as MPM2-positive, 4N cells) of cells in **a**. Error bars, range (n = 2, independent experiments). (**c**) Autoradiograph (top) and Coomassie stained gel (bottom) of ^{35}S-labeled Myc-SA2–Scc1 proteins (input) and the same proteins bound to beads containing GST or increasing amounts of GST-Wapl-M. WT, wild type. (**d**) Quantification of the *in vitro* binding assays in **c**. The binding intensities were normalized to the amount of each input. Error bars, range (n = 2, independent experiments). The K290E and D326K mutants were only tested once.

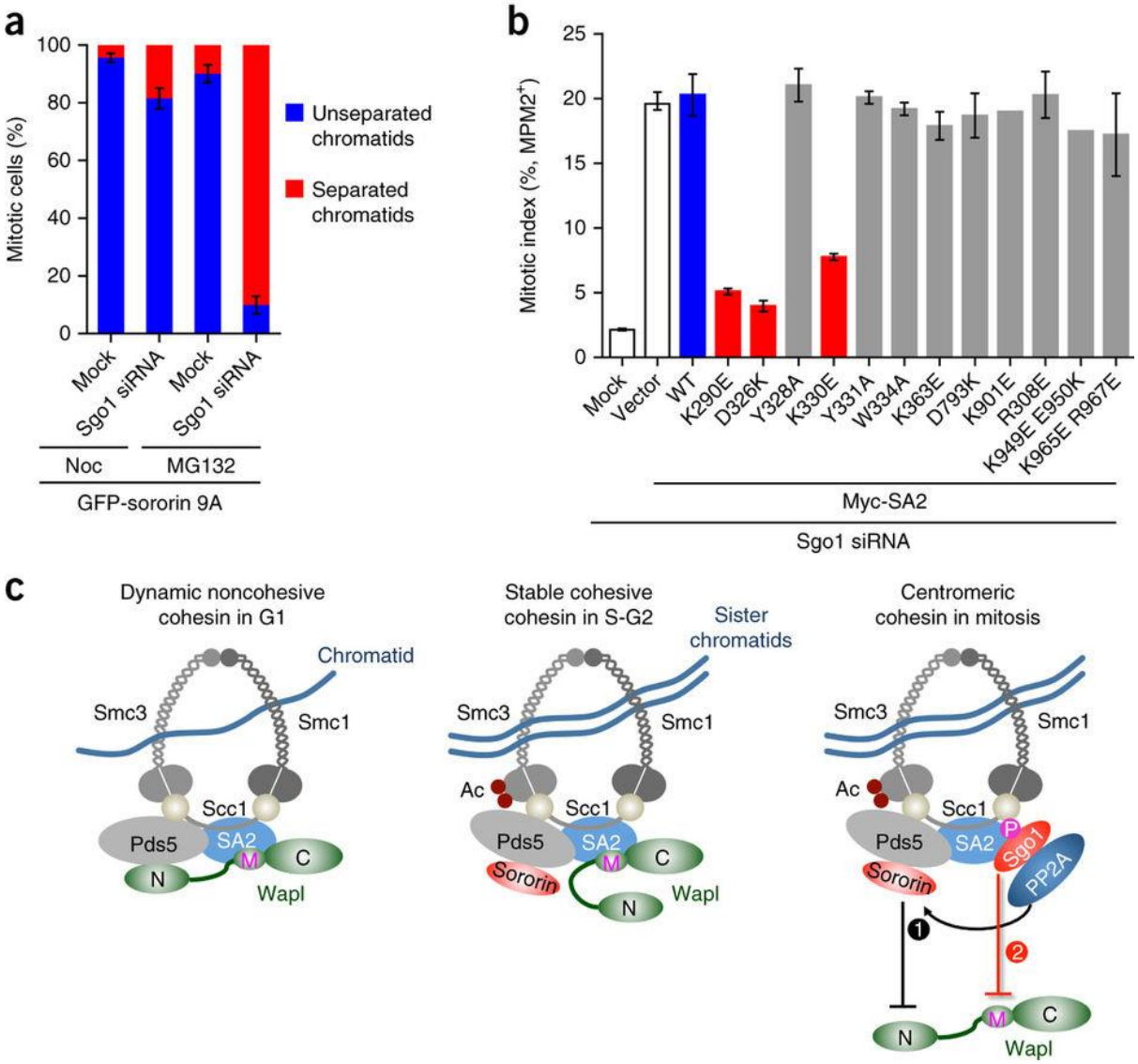

Figure 3-9. Sgo1 prevents Wapl from accessing a functional site on cohesin. (**a**) Quantification of the percentages of mitotic GFP–Sororin 9A–expressing HeLa cells (transfected with the indicated siRNAs and arrested in prometaphase with nocodazole or at metaphase with MG132) that had unseparated chromatids (types I and II) and separated chromatids (types III and IV). Error bars, range (n = 2 independent experiments). (**b**) Quantification of the mitotic indices (defined as the percentage of cells with 4n DNA content and positive MPM2 staining) of HeLa cells transfected with Sgo1 siRNA and the indicated Myc-SA2 plasmids. WT, wild type. Error bars, range (n = 2 independent experiments). The K901E and K949E E950K mutants were tested only once. (**c**) Model for Sororin- and Sgo1-dependent cohesion protection during the cell cycle. Sgo1 protects centromeric cohesion in two ways: enabling Sororin dephosphorylation by PP2A (1) and directly shielding SA2–Scc1 from Wapl (2). Ac, acetyl group.

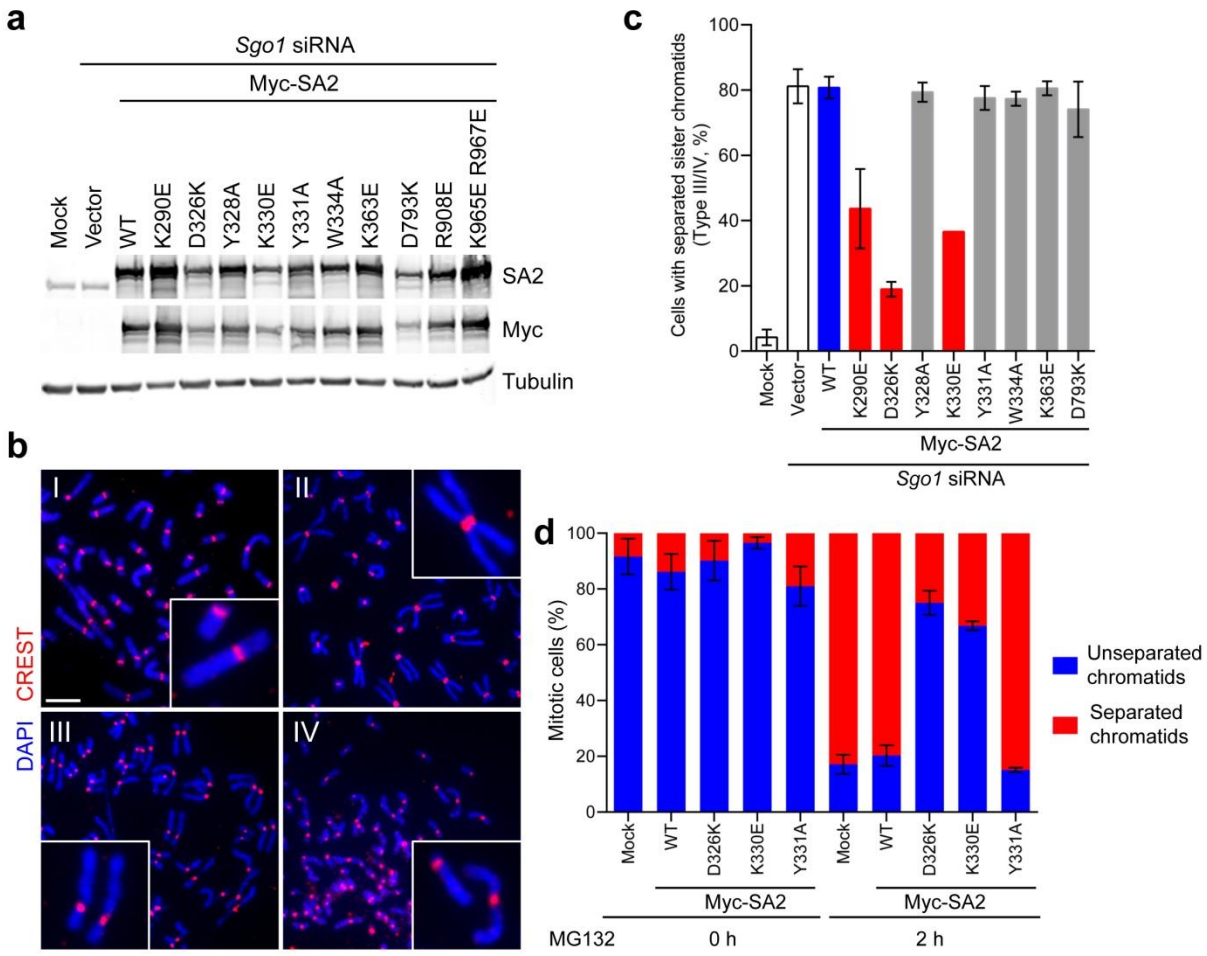

Figure 3-10. Expression of Wapl binding–deficient SA2 mutants bypasses Sgo1 requirement in cohesion protection and rescues cohesion fatigue. (**a**) Anti-SA2, anti-Myc, and anti-tubulin blots of lysates of HeLa cells transfected with the indicated siRNA and plasmids. WT, wild type. (**b**) Four major types (I-IV) of metaphase spreads of cells in **a**, stained with DAPI (blue) and the kinetochore marker CREST (red). Selected sister chromatids were magnified and shown in insets. Scale bar, 5 μm. (**c**) Quantification of the percentage of cells in **a** with type III and IV chromosome morphologies as in **b**. Error bars, range (n = 2, independent experiments). The K330E mutant was tested only once. (**d**) Quantification of the percentages of mitotic HeLa cells (transfected with the indicated Myc-SA2 plasmids, arrested in nocodazole, and released into medium containing MG132 for 2 hrs) that had types III/IV chromosome morphology. WT, wild type. Error bars, s.d. for mock, WT, D326K (n = 3, independent experiments); range for K330E and Y331A (n = 2, independent experiments).

Table 3-1. Data collection and refinement statistics

	Native SA2-Scc1-MES	SeMet SA2-Scc1	SeMet SA2-Scc1-MES
Data Collection			
Space group	$P2_12_12_1$	$P2_12_12_1$	$P2_12_12_1$
Cell dimensions			
a, *b*, *c* (Å)	78.455, 107.275 180.103	78.606, 108.752 181.791	78.733, 108.045 180.835
Wavelength (Å)	0.97918	0.97918	0.97924
Resolution (Å)	2.95	3.05	2.85
R_{sym}	0.111 (0.959)	0.102 (1.00)	0.098 (1.00)
$I/\sigma I$	19.0 (1.8)	19.9 (1.5)	20.1 (1.5)
Completeness (%)	100.0 (99.8)	100.0 (99.9)	99.9 (99.9)
Redundancy	6.2 (6.2)	10.0 (8.9)	8.8 (8.2)
Refinement			
Resolution (Å)	47.68 - 2.95	45.45 - 3.05	41.71 - 2.85
No. reflections	32,803	30,393	36,729
R_{work} / R_{free} (%)	18.8 / 25.1	19.5 / 23.8	20.9 / 22.5
No. atoms			
Protein	7,974	7,909	7,982
Ligand/ion	12	0	12
Water	0	22	14
B factor (Å^2)			
Protein	88.1	80.6	59.5
Ligand/ion	82.9	-	60.3
Water	-	50.3	29.8
r.m.s. deviations			
Bond lengths(Å)	0.009	0.007	0.005
Bond angles (°)	1.21	1.03	0.87

Data sets were collected with one native crystal with MES in the crystallization buffer, one selenomethionine (SeMet) crystal without MES and one SeMet crystal with MES. Values in parentheses are for highest-resolution shell.

CHAPTER IV: STRUCTURE BASIS AND IP_6 REQUIREMENT FOR PDS5-DEPENDENT COHESIN DYNAMICS

INTRODUCTION

Cohesin regulates diverse cellular processes, including chromosome segregation and compaction, DNA repair, and transcription (Haarhuis et al., 2014; Nasmyth and Haering, 2009; Onn et al., 2008; Peters et al., 2008). All functions of cohesin likely involve its unique ability to topologically entrap chromosomes within its ring (Haering et al., 2008). Dynamic entrapment of distal elements in the same chromosome by cohesin in G1 produces chromosome loops and impacts transcription (Merkenschlager and Odom, 2013). Stable cohesin entrapment of sister chromatids coupled to DNA replication or induced by DNA damage establishes sister-chromatid cohesion, which is critical for accurate chromosome segregation and homology-directed DNA repair (Rolef Ben-Shahar et al., 2008; Strom et al., 2007; Unal et al., 2008; Wu et al., 2012). Mutations of cohesin and its regulators perturb many facets of chromosome biology and are linked to human cancers and developmental diseases (Bose and Gerton, 2010; Solomon et al., 2011).

Chromosome entrapment by cohesin is regulated during the cell cycle. Chromosome-bound cohesin is highly dynamic in G1. The Huntingtin-elongation factor 3-A subunit-TOR (HEAT) repeat proteins, Pds5 and Wapl, release cohesin from chromosomes in a reaction that requires the opening of the cohesin ring at the Smc3-Scc1 interface (termed the DNA exit gate) (Beckouet et al., 2016; Buheitel and Stemmann, 2013; Chan et al., 2012; Gandhi et al., 2006; Gligoris et al., 2014; Huis in 't Veld et al., 2014; Kueng et al., 2006; Murayama and Uhlmann, 2015; Rowland

et al., 2009). During S phase, DNA replication-coupled Smc3 acetylation by Esco1/2 inhibits Pds5-Wapl-dependent cohesin-releasing activity and establishes sister-chromatid cohesion (Chan et al., 2012; Rolef Ben-Shahar et al., 2008; Rowland et al., 2009; Sherwood et al., 2010; Unal et al., 2008). In metazoans, cohesion establishment also requires Sororin, which competes with Wapl for binding to Pds5 (Nishiyama et al., 2010; Rankin, 2005). In mitosis, cohesin is removed from chromosomes by Pds5-Wapl-dependent release and separase-dependent cleavage (Gandhi et al., 2006; Kueng et al., 2006; Shintomi and Hirano, 2009; Uhlmann et al., 2000), leading to chromosome segregation.

Paradoxically, Pds5 has both positive and negative functions in cohesion regulation (Chan et al., 2012; Losada et al., 2005; Rowland et al., 2009; Shintomi and Hirano, 2009; Sutani et al., 2009). Pds5 promotes Smc3 acetylation through recruiting Esco1 to cohesin (Minamino et al., 2015; Vaur et al., 2012). In vertebrates, Pds5 interacts with Sororin (Nishiyama et al., 2010). These Pds5-dependent events are expected to stabilize cohesin on chromosomes and strengthen sister-chromatid cohesion. On the other hand, Pds5 engages and collaborates with Wapl to promote the release of cohesin from chromosomes (Murayama and Uhlmann, 2015; Nishiyama et al., 2010; Shintomi and Hirano, 2009).

To better define the dual functions of Pds5, we determined the crystal structure of human Pds5B bound to a conserved tyrosine-serine-arginine (YSR) motif found in both Wapl and Sororin. The YSR motifs of Wapl and Sororin bind to the same conserved site on Pds5B and compete for Pds5B binding, helping to explain the well-established Wapl-Sororin antagonism in cohesin regulation. Our structure unexpectedly reveals inositol hexakisphosphate (IP_6) as a tightly bound cofactor of Pds5. The IP_6-binding segment of Pds5 and its flanking region form a

jaw-like structure to engage the N-terminal region of Scc1 and inhibit its binding to Smc3. These findings suggest a rather direct role of Pds5 in cohesin release from chromosomes, possibly through stabilizing a fleeting, open state of cohesin during its ATPase cycle.

MATERIALS AND METHODS

Protein Expression and Purification

Recombinant human Pds5B proteins were expressed in insect cells using the Bac-to-Bac system (Invitrogen) and purified with a combination of affinity and conventional chromatography. Briefly, baculoviruses encoding $Pds5B_{1–1120}$ and $Pds5B_{21–1120}$ proteins with an N-terminal His_6 tag were prepared with standard protocols. Hi5 cells were harvested after being infected with the Pds5B baculovirus for 56 h. Cell pellet was resuspended with the lysis buffer (50 mM Tris-HCl pH 7.7, 150 mM KCl, 0.1% Triton X-100, 20 mM imidazole, 1X protease inhibitor cocktail, 10 mM β-mercaptoethanol) and sonicated. After centrifugation, the supernatant was applied to Ni^{2+}-NTA beads equilibrated with the lysis buffer. After successive washes with the wash buffer I (50 mM Tris-HCl pH 7.7, 1.2 M KCl, 20 mM imidazole) and wash buffer II (50 mM Tris-HCl pH 7.7, 300 mM KCl, 20 mM imidazole), the bound Pds5B protein was eluted with the elution buffer (50 mM Tris-HCl pH 7.7, 300 mM KCl, 500 mM imidazole). The fractions containing Pds5B were pooled, supplemented with 1 mM EDTA, and digested with the tobacco etch virus (TEV) protease at 4˚C overnight to remove the His_6 tag. The cleaved Pds5B protein was further purified with Resource Q and Superdex 200 columns (GE Healthcare). The protein was stored in the storage buffer (20 mM Tris-HCl, pH 8.5, 200 mM NaCl, 5 mM TCEP).

For preparation of the selenomethionine-containing $Pds5B_{21–1120}$ protein, Hi5 cells grown in the ESF921 medium (Expression Systems) were infected with the Pds5B baculovirus, and pelleted at 20 h post-infection. The cell pellet was washed and resuspended with the ESF921 medium without methionine. The cells were incubated with shaking for 6 h to deplete the

remaining L-methionine, and then pelleted again and resuspended into the ESF921 medium without methionine that had been supplemented with 100 mg/ml L-selenomethionine. After 30 h incubation, the cells were harvested. Selenomethionine-containing $Pds5B_{21–1120}$ was purified following the same procedure described for the native protein.

Crystallization, Data Collection, and Structure Determination

The $Pds5B_{21–1120}$ protein was concentrated to 11.2 mg/ml, and a synthetic $Wapl_{1–33}$ peptide was added to a 1:5 molar ratio. Crystal screening trays were set up with the sitting drop vapor diffusion method at 20˚C. Initially crystals were observed in 4 similar conditions: 0.2 M sodium citrate and 20% PEG3350 (v/v) without buffer or with 0.1 M Bis-Tris propane buffers at pH 6.5, pH 7.5, or pH 8.5. Single crystals were obtained by the seeding method. Crystals of selenomethionine-containing Pds5B were obtained by seeding using the native protein crystals as seeds. The crystals were cryoprotected with the reservoir solution supplemented with 18% (v/v) glycerol and then flash-cooled in liquid nitrogen. The space group of the crystal is $P2_12_12_1$, with cell dimensions of a = 121 Å, b = 162 Å, and c = 173 Å. There are two molecules in the asymmetric unit with a 63% solvent content.

Diffraction data on a selenomethionine-derivatized crystal of Pds5B–Wapl to a d_{min} of 2.7 Å were collected at beamline 19-ID (Structural Biology Center Collaborative Access Team) at the Advanced Photon Source (Argonne National Laboratory, Argonne, IL) and processed with HKL3000 (Minor et al., 2006), with applied corrections for effects resulting from absorption in a crystal and for radiation damage (Borek et al., 2003; Otwinowski et al., 2003), the calculation of an optimal error model, and corrections to compensate the phasing signal for a radiation-induced

increase of non-isomorphism within the crystal (Borek et al., 2010; Borek et al., 2013). These corrections were crucial for successful phasing. Selenium heavy atom positions were located within the program SHELXD (Schneider and Sheldrick, 2002); 73 of 66 possible Se positions were located due to statistical disorder of some SeMet residues. Phases obtained from a single-wavelength selenium anomalous dispersion experiment were refined, and the phases improved via density modification and 2-fold noncrystallographic symmetry averaging within the program PHENIX (Adams et al., 2010).

A partial model built with phases obtained from this dataset was refined against the SeMet diffraction data, with I+ and I– intensities merged in the Reflection File Editor tool of PHENIX. After the initial round of refinement, chain A of Pds5B was overlapped on chain B and vice versa to add parts of the model that had been automatically built in one chain but not the other. Alternate rounds of refinement in PHENIX with rebuilding guided by electron density map inspection in COOT (Emsley et al., 2010) led to the interpretation of ordered densities for the Pds5B polypeptide chain and bound inositol hexakisphosphate (IP_6). Electron density for chain A of Pds5B was stronger and more complete than density for chain B, and chain A coordinates exhibited lower refined atomic displacement parameters. Towards the final rounds of refinement, density for a 5-residue peptide bound near residue D189 in chain A of Pds5B became better defined, and was modeled as residues KTYSR of the Wapl peptide. The parameters of data collection, phasing, and refinement statistics of the final model are shown in Table 4-1.

Protein Binding Assays

For assaying the binding of Pds5 to Wapl, Sororin, and Scc1 *in vitro*, various truncation or point mutants of human Wapl, Sororin, and Scc1 were constructed with the pGEX6p1 vector to produce GST fusions of these proteins. These GST-Wapl, GST-Sororin, and GST-Scc1 proteins were expressed in *E. coli* and purified with the glutathione-Sepharose 4B resin (GE Healthcare). Beads bound to GST-Wapl, GST-Sororin, or GST-Scc1 proteins were incubated with purified recombinant $Pds5B_{1–1120}$/$Pds5B_{21–1120}$ wild type and mutant proteins or ^{35}S-labeled full-length Pds5B wild type and mutant proteins obtained through the TNT Quick Coupled Transcription/Translation System (Promega). (In the competition assay, beads bound to GST-Wapl were incubated with purified Pds5B, in the absence or presence of increasing amount of a synthetic $Sororin_{132–171}$ peptide.) The beads were washed four times with TBS supplemented with 0.1% Tween 20 (TBST) for binding assays with GST-Wapl and GST-Sororin, and with the wash buffer (50 mM Tris-HCl, pH 8.0, 150 mM NaCl, 2 mM TCEP) for the GST-Scc1 assays. The bound proteins were separated on SDS-PAGE gels, which were stained with Coomassie or analyzed with a phosphorimager (Fujifilm) or both. The intensities of bound ^{35}S-Pds5B were quantified with Image J.

Human Smc3 head domain (HD) (residues 1–251 connected to residues 956–1217 of human Smc3 with a five-glycine linker) was expressed as a GST fusion protein in *E. coli* and purified with Glutathione-Sepharose resin. The ^{35}S-labeled $Scc1_{1–210}$ and $Scc1_{21–210}$ (wild type and 4E) proteins were obtained through *in vitro* translation. For assaying the effects of Pds5B on the preformed DNA exit gate of cohesin, beads bound to GST or GST-Smc3 HD were incubated with ^{35}S-labeled $Scc1_{1–210}$ wild type or 4E for 1h at 4˚C, and washed with TBST. Purified recombinant Pds5B, Wapl, SA2, or their combinations were then added to the beads. After

another 1 h incubation at 4˚C, the beads were washed with TBST, and the bound proteins were separated with SDS-PAGE and analyzed with a phosphoimager.

For assaying the effects of Pds5B on the formation of the DNA exit gate, ^{35}S-labeled Scc1$_{1–210}$ or Scc1$_{21–210}$ (wild type or 4E) were first incubated with Pds5B, Wapl, SA2 or combinations of these proteins at room temperature for 30 min. The protein mixture was then added to beads bound to GST or GST-Smc3 HD. After another 1 h incubation at 4˚C, the beads were washed four times with TBST, and the bound proteins were analyzed with a phosphorimager.

Isothermal Titration Calorimetry (ITC)

The affinity between purified recombinant Pds5B$_{1–1120}$ and Sororin$_{91–252}$ proteins was measured with a MicroCal iTC200 instrument (GE Healthcare) at 20˚C. A 23 μM of Pds5B sample in the ITC buffer (20 mM Tris-HCl, pH 8.5, 200 mM NaCl) was titrated with 298 μM of Sororin in the same buffer. For measuring the affinity between Pds5B$_{1–1120}$ and Scc1$_{76–150}$, ITC was performed using a MicroCal VP-ITC instrument (GE Healthcare) at 20˚C. A 4.25 μM of Pds5B sample in the buffer containing 20 mM Tris-HCl, pH 8.5, 150 mM NaCl, 2 mM TCEP was titrated with 53.7 μM of Scc1 in the same buffer. In both cases, binding parameters were calculated with the NITPIC software.

Isolation and NMR Analysis of IP$_6$ from Recombinant Pds5B

The isolation of IP$_6$ from human Pds5B expressed and purified from insect cells was performed essentially as described (Sheard et al., 2010). Briefly, 13 mg of purified Pds5B$_{21–1120}$ at 1 mg/ml concentration in the storage buffer was mixed with equal volume of Tris-saturated

phenol (Acros Organics). The mixture was inverted and incubated at room temperature for 30 min until phase separation. After centrifugation at 20,800 g for 5 min, the upper aqueous phase was collected and diluted with the Tris buffer (25 mM Tris-HCl, pH 8.0). The phenol phase was extracted again with the Tris buffer, and the aqueous phase was collected. The two extractions were then combined and further purified by gravity flow on Q sepharose anionexchange resin (GE Healthecare). After the beads were washed with 10 column volume of 0.1 N formic acid, the bound ligand was eluted with 0–2 M step gradients of ammonium formate. The phosphate content of each fraction was analyzed by mixing with perchloric acid in Pyrex culture tubes. The inorganic phosphate was released by heating with continuous shaking to dryness, and dissolved in distilled water after the tubes cooled down to room temperature. Phosphate content was measured with the ATPase assay kit (Innova Biosciences). Peak fractions containing phosphate were collected and lyophilized. Typically, about 19 μg of IP_6 can be extracted from 13 mg of Pds5B.

IP_6 purchased from Sigma was dissolved into a buffer containing 20 mM sodium phosphate (pH 6.8), 89 mM KCl, and 1.8 mM deuterated EDTA (D16, 98%; Cambridge Isotope). The sample was lyophilized overnight and dissolved in fresh D_2O (D, 99.96%; Cambridge Isotope). The final sample concentration of this IP_6 standard was 10 mM. About 9 μg of IP_6 purified from Pds5B was dissolved into a buffer containing 20 mM sodium phosphate (pH 6.8), 50 mM KCl, and 1 mM deuterated EDTA. The sample was then lyophilized overnight and dissolved in fresh D_2O. The final sample concentration of IP_6 extracted from Pds5 was about 10 μM. The 1D ^1H NMR spectra were acquired on both samples at 30˚C using an Agilent DD2 600 MHz spectrometer equipped with four channels and pulsed-field gradients. The ^2H signal of D_2O was

used as a field frequency lock. The spectra were obtained with a 2000 Hz spectral window, a 4.0 s acquisition time, and a 1.5 s relaxation delay. Data were processed and analyzed with the Agilent VnmrJ 4.2 software.

The spectra of the IP_6 standard and IP_6 isolated from Pds5B are highly similar, and contain a distinct double-triplet near 4.90 ppm, a two-proton quartet near 4.43 ppm, and overlapping three-proton resonances near 4.17 ppm. The 4.90 ppm double-triplet is from H-2, as this is the sole equatorial proton on the inositol ring, and is shifted downfield relative to the five other protons that are in axial positions. Two of the three resonances at 4.17 ppm show triple-triplet line shape, indicating that these arise from H-1 and H-3. These resonances are chemically equivalent due to the axis of symmetry through positions 2 and 5. The two-proton quartet at 4.43 ppm arises from chemically equivalent H-4 and H-6 resonances due to the symmetry axis. The remaining one-proton quartet at 4.17 ppm is from H-5.

Mammalian Cell Culture, Transfection, and Synchronization

HeLa Tet-On cells were grown in DMEM (Invitrogen) supplemented with 10% fetal bovine serum (FBS) and 2 mM Lglutamine. When cells reached a confluency of 50%, plasmid transfection was performed using the Effectene reagent (Qiagen) according to the manufacturer's protocols. All mammalian expression plasmids used in this study were derived from modified pCS2 vectors. The human Wapl and Pds5B cDNAs (which contained silent mutations in the siRNA-targeted region) were inserted into these vectors. The final vectors encoded RNAi-resistant Wapl and Pds5B proteins fused to GFP or Myc at their N-termini. Wapl and Pds5B mutants were constructed with site-directed mutagenesis. All constructs were verified by DNA

sequencing. For making stable cell lines, HeLa Tet-On cells were transfected with a pTRE2 plasmid encoding human Smc1 with its C-terminus fused to GFP. Clones were selected with 200 μg/ml hygromycin B. Inducible expression of Smc1-GFP was screened in the absence or presence of 1 μg/ml doxycycline (Invitrogen). For siRNA transfection, cells were transfected with Lipofectamine RNAiMAX (Invitrogen) at 20%-40% confluency according to the manufacturer's protocols, and analyzed at 24-48 h after transfection. The siRNA oligonucleotides targeting human Pds5A (siPds5A; 5'-UGUAAAAGCUCUCAACGAA-3'), Pds5B (siPds5B; 5'-GAACUUCUACCUUAAGAUU-3'), Wapl (siWapl; 5'-CGGACTACCCTTAGCACAA-3'), Sgo1 (siSgo1; 5'-GAGGGGACCCUUUUACAGATT-3'), Sororin (siSororin; 5'-CAGAAAGCCCAUCGUCUUA-3'), Esco1 and Esco2 (ON-TARGETplus Set of 4) were synthesized by GE Healthcare. The siRNAs were transfected at a final concentration of 5 nM. For experiments in Figure 4-2F and Figure 4-6C, HeLa Tet-On cells were transfected first siWapl or siPds5A/B for 24 h and then with GFP-Wapl or Myc-Pds5B WT or mutant plasmids for another 24 h. The expression levels of GFP-Wapl proteins were controlled by using different doses of GFP-Wapl plasmids. For mitotic synchronization, cells were treated with 2 mM thymidine for 16–18 h, released into fresh medium for 9 h, and blocked at mitosis with the addition of 5 μM nocodazole (Sigma) for 2 h.

Antibodies, Immunoblotting, and Immunoprecipitation

The anti-Wapl antibody was generated against a C-terminal fragment of human Wapl (residues 601–1190) as described previously (Wu et al., 2012). Rabbit polyclonal antibodies against eGFP, human Sororin$_{91–252}$, and human Pds5B$_{1140–1310}$ were raised at Yenzym Antibodies

with purified recombinant proteins as antigens. The following antibodies were purchased from the indicated commercial sources: anti-Myc (Roche, 11667203001), anti-HA (Roche, 11583816001), anti-mCherry (BioVision Inc, 5993-100), anti-Smc1 (Bethyl Laboratories, A300-055A), anti-Smc3 (Bethyl Laboratories, A300-060A), anti-SA2 (Santa Cruz, Biotechnology, sc-81852), anti-Pds5A (Bethyl Laboratories, A300-089A), anti-β-tubulin (Sigma, T4026), anti-Esco2 (Bethyl Laboratories, A301-689A), MPM2 (Millipore, 05-368), and CREST serum (ImmunoVision). Anti-Esco1 and anti-Smc3 K105Ac antibodies were gifts from Susannah Rankin (Oklahoma Medical Research Foundation) and Prasad Jallepalli (Memorial Sloan Kettering Cancer Center), respectively. The antibodies to Myc and GFP have been validated for immunoblotting and immunoprecipitation applications. The antibodies to HA, mCherry, Smc1, Smc3, SA2, Pds5A and Tubulin have been validated for immunoblotting. The antibody to MPM2 has been validated for flow cytometry. The relevant validation information and references can be found at the manufacturers' websites. The antibody to Sororin is validated for immunoblotting, and the anti-Pds5B antibody is validated for both immunoblotting and immunoprecipitation in this study.

For immunoblotting, cells were lysed in the SDS sample buffer (pH 6.8), sonicated, and boiled. The lysates were separated by SDS-PAGE and blotted with the desired primary antibodies. The primary antibodies were used at a final concentration of 1 μg/ml. Anti-mouse IgG (H+L) (Dylight 680 conjugates), anti-rabbit IgG (H+L) (Dylight 800 conjugates) (Cell Signaling), or horseradish peroxidase-linked donkey anti-rabbit or sheep anti-mouse IgGs (GE healthcare) were used as secondary antibodies. The blots were either scanned with an Odyssey

Infrared Imaging System (LI-COR) or developed with the SuperSignal West Pico Chemiluminescent Substrate (Thermo Scientific) according to the manufacturer's protocols.

For immunoprecipitation, the anti-Myc, anti-GFP, anti-Pds5B, anti-Sororin, or anti-Wapl antibodies were coupled to Affi-Prep Protein A beads (Bio-Rad) at a concentration of 1 mg/ml. Cells were lysed with the lysis buffer containing 25 mM Tris-HCl (pH 7.7), 50 mM NaCl, 0.1% (v/v) Nonidet P-40, 2 mM $MgCl_2$, 10% (v/v) glycerol, 5 mM NaF, 0.3 mM Na_3VO_4, 10 mM β-glycerophosphate, 1 mM DTT, protease inhibitor mixture (Roche), and 50 units/ml Turbo Nuclease (Accelagen). After a 1-h incubation on ice and a 10-min incubation at 37˚C, all lysates were centrifuged at 4˚C at 20,817 g for 20 min. The supernatants were incubated with the desired antibody beads for 3 h at 4˚C. The beads were then washed three times with the lysis buffer containing 200 mM NaCl. Proteins bound to beads were dissolved in SDS sample buffer, separated by SDS-PAGE, and blotted with the appropriate antibodies.

Flow Cytometry

Cells were harvested with trypsinization and fixed in 70% ice-cold ethanol overnight. After being washed with PBS, cells were permeabilized with PBS containing 0.25% Triton X-100 on ice for 5 min. Then, cells were incubated with the antibody to MPM2 in PBS containing 1% BSA for 3 h at room temperature, followed by an incubation with a fluorescent secondary antibody (Invitrogen) for 30 min. After being washed with PBS, cells were resuspended in PBS containing 0.1% Triton X-100, RNase A, and propidium iodide, and analyzed with a flow cytometer. Data were processed with FlowJo.

Metaphase Spreads and Immunofluorescence

After synchronization, mitotic HeLa Tet-On cells were collected by shake-off. Cells were washed once with PBS, treated with 55 mM KCl hypotonic solution at 37˚C for 15 min, and spun onto microscope slides with a Shandon Cytospin centrifuge. Cells on the slides were first permeabilized with the PHEM buffer (25 mM HEPES pH 7.5, 10 mM EGTA pH 8.0, 60 mM PIPES pH 7.0, 2 mM $MgCl_2$) containing 0.3% Triton X-100 for 5 min and then fixed in 4% paraformaldehyde for 10 min. Fixed cells were washed three times with PBS containing 0.1% Triton X-100 for 2 min each time, and incubated with CREST in PBS containing 3% BSA and 0.1% Triton X-100 at 4˚C overnight. Cells were then washed three times with PBS containing 0.1% Triton X-100 for 2 min each time, and incubated with fluorescent secondary antibodies (Molecular Probes) in PBS containing 3% BSA and 0.1% Triton X-100 for 1 h at room temperature. Cells were again washed three times with PBS containing 0.1% Triton X-100 and stained with 1 μg/ml DAPI for 2 min. After the final washes, the slides were sealed with nail polish and viewed with a 100X objective on a DeltaVision fluorescence microscope (GE Healthcare). Image processing and quantification were performed with Image J.

Fluorescence In Situ Hybridization (FISH)

The BAC clone RP11-466L19 was purchased from Empire Genomics. FISH probes were labeled with 5-Fluorescein dUTP (Enzo Life Sciences) using the Nick Translation Kit (Abbott Molecular). Human cot-1 DNA (Invitrogen) and salmon sperm DNA (Invitrogen) were added, and probes were precipitated and resuspended in the hybridization buffer (Cytocell). HeLa Tet-on cells were transfected with Pds5A/B or Sororin siRNAs before synchronization with 2 mM

thymidine for 16-18 h. Cells were then released intro fresh medium for 4 h and fixed with methanol and acetic acid (ratio 3:1). Fixed cells were dropped onto slides and in situ hybridized at 80˚C with DNA probes. Slides were sequentially washed with 0.1% SDS in 0.5 X SSC at 70 ˚C for 5 min, 1 X PBS at room temperature for 10 min and 0.1% Tween 20 in 1 X PBS at room temperature for 10 min. Slides were then mounted with ProLong Gold (Life Technologies) and viewed with a 100X objective on a DeltaVision fluorescence microscope (GE Healthcare). Image processing and quantification were performed with ImageJ.

Fluorescence Recovery after Photobleaching (FRAP)

HeLa cells stably expressing Smc1-GFP were plated into chambered coverglass, transfected with empty vector or RNAi-resistant mCherry-Pds5B WT or mutant plasmids, and then transfected with siPds5A and siPds5B. A final concentration of 1 μg/ml doxycycline was always maintained in the culture medium. FRAP was performed using a custom built spinning disk confocal microscope (BioVision) equipped for live-cell imaging and operated with the MetaMorph and iLas2 software. Single stack images were captured with a 100X objective. A small circular region in each cell was bleached with a 405 nm laser at 100% intensity. Images were acquired with both 488-nm and 561-nm lasers before bleaching, and with a 488-nm laser at 30 sec intervals for 60 min after bleaching. For data analysis, a region of interest (ROI) that equals to the bleached area was defined in ImageJ. The integrated density of GFP in this region was measured before bleaching as I_{pre}, immediately after bleaching as I_0, and at each time point after bleaching as I_t. $(I_t-I_0)/I_{pre}$ was plotted against time. Individual data sets were fitted to a

single exponential function using the GraphPad Prism software to determine the half-life and plateau of recovery.

RESULTS

Identification of a Conserved Pds5-Binding Motif in Human Wapl and Sororin

We characterized the binding of bacterially expressed human Wapl and Sororin to human Pds5B expressed and purified from insect cells. Through systematic deletion mutagenesis, we mapped the Pds5B-binding region of Wapl to residues 1–33 (Figure 4-1A and 1B). Similarly, we mapped the Pds5B-binding region of Sororin to residues 131–171 (Figure 4-1C). A synthetic Sororin peptide (residues 132–171) competed effectively with GST-Wapl$_{1–33}$ for binding to Pds5B (Figure 4-2A). As measured by isothermal titration calorimetry (ITC), a C-terminal fragment of Sororin containing this region bound to Pds5B with a dissociation constant (KD) of 3.0 μM (Figure 4-2B). We could not detect the binding of Wapl$_{1–33}$ to Pds5B using ITC, suggesting that Wapl$_{1–33}$ bound more weakly to Pds5B. The Pds5B-binding sequences of both Wapl and Sororin contained a previously unknown YSR motif (with the consensus of [K/R][S/T]YSR) conserved in vertebrates (Figure 4-2C). Mutation of the YSR motif to ASE (YSR > ASE) in Wapl or Sororin reduced their binding to Pds5 *in vitro* (Figure 4-1D and 1E) and in human cells (Figure 4-2D and 2E). Thus, Wapl and Sororin compete for Pds5 binding through a similar conserved motif.

Both Wapl and Sororin also contain phenylalanine-glycine-phenylalanine (FGF) motifs, which have been implicated in their antagonism (Nishiyama et al., 2010; Shintomi and Hirano, 2009). The first FGF motif of Wapl and the only FGF motif in Sororin are located in close proximity to their YSR motif (Figure 4-2C). We tested the contributions of FGF motifs of Wapl and Sororin to Pds5 binding. Mutation of FGF to AGA (FGF > AGA) in Wapl slightly weakens the binding of Wapl$_{1–100}$ to Pds5 *in vitro*, whereas mutation of FGF in Sororin had no effect on

Pds5 binding (Figure 4-1D and 1E). In contrast, these FGF mutations substantially reduced the binding of Wapl or Sororin to Pds5B or cohesin in human cells (Figure 4-2D and 2E). Thus, the FGF motif of Wapl and Sororin might primarily compete for binding to cohesin, and cohesin might strengthen Pds5-Wapl and Pds5-Sororin interactions in vivo.

To verify the functional importance of the YSR and FGF motifs, we depleted endogenous Wapl from human cells with RNA interference (RNAi), complemented them with RNAi-resistant Wapl wild-type (WT), the YSR > ASE mutant, or the FGF > AGA mutant, and performed chromosome spreads of these cells enriched in mitosis (Figure 4-2F and 2G). Depletion of Wapl hindered the resolution of chromosome arms in early mitosis, presumably due to defective cohesin removal through the prophase pathway. Expression of GFP-Wapl WT restored arm resolution in Wapl RNAi cells in a dose-dependent manner. Wapl YSR > ASE or FGF > AGA was less efficient in rescuing the arm-resolution defect caused by Wapl depletion. Thus, both the YSR and FGF motifs of Wapl are functionally important.

Structure of Human Pds5B Bound to the Wapl YSR Motif

We next crystallized human Pds5B (residues 21–1120) bound to $Wapl_{1–33}$ and determined the structure using X-ray crystallography to 2.7 Å resolution (Table 4-1). Pds5B consists of 20 HEAT repeats and a helical insert domain (HID) and folds into a structure shaped like a big dipper or a plier lever (Figure 4-3A and Figure 4-4). Although the boundaries of some HEAT repeats were correctly predicted in previous studies (Huis in 't Veld et al., 2014; Panizza et al., 2000), the curvature of these repeats was not correctly modeled. The N-terminal eight HEAT repeats form the handle of the lever. The HID resembles the pivot, where the two levers of a plier

connect. The HEAT repeats H9–H20 and the HID form the jaw. An extra N-terminal helix and a C-terminal extension pack against the first and last HEAT repeat, respectively. There is a sharp bend at HEAT repeats 15 and 16. At this bend lies an unanticipated cofactor of Pds5, inositol hexakisphosphate (IP_6). The curved structure of Pds5B is reminiscent of that of SA2 or its yeast ortholog Scc3 (Hara et al., 2014; Roig et al., 2014). Interestingly, the sharp bend in SA2 forms a critical Scc1-binding site (Hara et al., 2014).

Only one of two Pds5B molecules in one asymmetric unit bound to Wapl. The electron density corresponding to Wapl was weak, with only that belonging to residues 7–11 (KTYSR) being visible (Figure 4-5A). Wapl binds along the ridge of HEAT repeats 1–3 at the tip of the handle (Figure 4-3A). K7, Y9, S10, and R11 of Wapl form polar, electrostatic, and hydrophobic interactions with Q47, A92, F88, I143, E146, E187, and D189 of Pds5B (Figure 4-3B), consistent with the importance of the YSR motif in Pds5 binding. Most of the Wapl-binding residues of Pds5 are conserved among various organisms (Figure 4-4). Importantly, single point mutations of several corresponding Wapl-binding residues in the budding yeast Pds5 suppress the cohesion defects of *eco1-1* mutant (Rowland et al., 2009).

To validate this Wapl-binding surface of Pds5, we mutated the hydrophobic or polar residues to alanine and introduced charge-reversal mutations to charged residues. We also created the A92P mutant, based on a yeast Pds5 mutation that suppressed *eco1-1* phenotypes (Heidinger-Pauli et al., 2010). All mutations, except I143A, greatly reduced the binding of $Wapl_{1–100}$ to Pds5B *in vitro* (Figure 4-3C and Figure 4-5B). These mutations also reduced the binding of Sororin to Pds5B (Figure 4-5B and 5C), suggesting that Sororin and Wapl bound to a

similar site on Pds5B. As a negative control, the E94K mutation targeting an adjacent residue that did not contact Wapl had no effect on Wapl or Sororin binding to Pds5B.

The YSR motifs of vertebrate Wapl and Sororin thus compete for binding to a similar site on Pds5 that is conserved from yeast to man. Furthermore, residues 2–8 (RAYGKRG) of the budding yeast Wapl (Wpl) partially conform to the consensus of the YSR motif and may bind to the same site on yeast Pds5. It is possible that an unidentified YSR-containing factor in yeast may counteract the binding of Wapl to Pds5 in that organism.

Mutual Wapl-Sororin Antagonism at the YSR-Binding Site of Pds5

We expressed a subset of Wapl-binding-deficient Pds5B mutants in human cells and tested their binding to endogenous Wapl, Sororin, and cohesin. The D86K, A92P, and E187K mutations weakened or abolished binding of Pds5B to Wapl or Sororin, but had no effect on its binding to Smc1, a core subunit of cohesin (Figure 4-6A and 6B). Thus, the cohesin-binding surface of Pds5B is distinct from its Wapl- and Sororin-binding site.

To identify Pds5 residues required for cohesin binding, we systematically mutated conserved surface-exposed residues and tested the binding of these mutants to cohesin, Wapl, and Sororin in human cells (Figure 4-6A and 6B). Among them, the K400E/R401E and Y445A/N447A mutants exhibited reduced binding to Smc1, with Y445A/N447A being more deficient. Both mutants were also deficient in binding to Wapl or Sororin, suggesting that cohesin was required for the association of Wapl and Sororin with Pds5 in vivo. This finding is consistent with the fact that other regions of Wapl and Sororin have been implicated in cohesin binding (Hara et al., 2014; Ouyang et al., 2013; Wu et al., 2011). Thus, the YSR motif is

required, but not sufficient, to mediate the binding of Wapl or Sororin to Pds5 in human cells. Additional interfaces between Wapl/Sororin and cohesin are needed to form detectable cohesin-Pds5-Wapl or cohesin-Pds5-Sororin ternary interactions. We note, however that the Y445A/N447A mutant retains cohesin-independent binding to GST-Wapl or GST-Sororin *in vitro* (see Figure 4-11 below), indicating that this mutant is not globally unfolded.

Consistent with a previous report (Shintomi and Hirano, 2009), depletion of both Pds5A and Pds5B in HeLa cells caused arm-resolution defects in mitotic chromosome spreads (Figure 4-6C and Figure 4-7A), a phenotype similar to that seen with Wapl depletion (Gandhi et al., 2006; Kueng et al., 2006). Like Wapl inactivation (Kueng et al., 2006; Tedeschi et al., 2013), depletion of Pds5A/B caused worm-like cohesin assembly on interphase chromatin (Figure 4-7B) and, as revealed by fluorescence recovery after photobleaching (FRAP), reduced the kinetics and extent of cohesin turnover on chromatin (Figure 4-7C and 7D). For unknown reasons, the kinetics of cohesin turnover in control and Wapl RNAi cells in this study was faster than that reported previously (Kueng et al., 2006). Co-depletion of Pds5A/B and Wapl did not further impede the kinetics of cohesin exchange, but slightly decreased the pool of dynamic cohesin (Figure 4-7C). Collectively, these results confirm that Pds5 collaborates with Wapl to promote cohesin release from chromosomes in both mitosis and interphase.

Expression of Pds5B WT restored arm resolution in Pds5A/B-depleted cells (Figure 4-6C). In contrast, expression of Wapl-binding-deficient Pds5B mutants, including D86K, E146K, E187K, and D189K, failed to rescue the arm-resolution defects. Likewise, the cohesin-binding-deficient Pds5B Y445A/N447A mutant also failed to complement. In addition, as revealed by FRAP, expression of Pds5B WT, but not the Wapl-binding-deficient D86K mutant, restored the

kinetics of cohesin turnover on interphase chromatin (Figure 4-6D and Figure 4-7E). In fact, Pds5B D86K appeared to further slow down cohesin dynamics, suggesting that it might dominant-negatively inhibit the residual, endogenous Pds5B. Taken together, these results establish the functional importance of the Wapl-binding site in Pds5 in cohesin release.

Pds5 plays both negative and positive roles in sister-chromatid cohesion in diverse organisms (Chan et al., 2012; Losada et al., 2005; Rowland et al., 2009; Shintomi and Hirano, 2009; Sutani et al., 2009). Unlike Wapl depletion (Ouyang et al., 2013), depletion of Pds5A/B in human cells did not rescue the cohesion defects and the resulting spindle checkpoint-dependent mitotic arrest caused by Sgo1 or Sororin depletion (Figure 4-8A and 8B). Furthermore, depletion of Pds5A/B inhibited two well-established cohesin stabilization mechanisms: Smc3 acetylation and subsequent Sororin association with cohesin (Figure 4-8C and 8D). Although depletion of Pds5A or Pds5B or both did not produce cohesion defects in metaphase spreads (Figure 4-8E), depletion of either protein weakened sister-chromatid cohesion in interphase cells, consistent with the molecular defects (Figure 4-8F and 8G). Therefore, even though depletion of Pds5A/B ostensibly produces phenotypes similar to depletion of Wapl, Pds5 actually plays dual roles in cohesin dynamics.

IP_6 as a Structural Cofactor of Pds5

IP_6 is an abundant lipid-derived metabolite in eukaryotic cells (Monserrate and York, 2010). As opposed to lower inositol polyphosphates with signaling functions (e.g., IP3), IP_6 and other higher inositol polyphosphates (e.g., IP5 and IP4) have been shown to be structural cofactors for the human RNA-editing enzyme ADAR2 (Macbeth et al., 2005), the plant hormone receptors

(Sheard et al., 2010; Tan et al., 2007), and the yeast mRNA export helicase Dbp5 complex (Montpetit et al., 2011), among other proteins. In many cases, these inositol polyphosphates directly participate in protein-protein or protein-ligand interactions.

During the refinement of the Pds5B structure, we noticed an electron density located near the sharp bend of Pds5B at HEAT repeats 13–17. Both Pds5B molecules in the asymmetric unit contained this density, which fitted well with IP_6 (Figure 4-9A). The 1D ^1H nuclear magnetic resonance (NMR) spectrum of the cofactor isolated from purified Pds5B from insect cells matched perfectly with that of authentic IP_6 (Figure 4-9B), confirming its identity. IP_6 binds at a positively charged surface at the bottom of the jaw of Pds5B (Figure 4-9C). Several basic IP_6-binding residues, including K727, K830, K888, and K925, are conserved from yeast to man (Figure 4-9A and Figure 4-4), suggesting that IP_6 binding is a conserved feature of Pds5.

We then mutated the IP_6-binding residues in Pds5B. When the same amounts of plasmids were used in transient transfection of HeLa cells, the protein levels of Pds5B K727E/Y728A, K830E/R834E, and K925E/K928E mutants were much lower than that of the WT, whereas the levels of K888E and R932E were similar to WT levels (Figure 4-9D). Similar patterns were observed with the expression of these Pds5B mutants in insect cells. These findings suggest that IP_6 binding is required for the structural integrity of Pds5B. The single mutants presumably retain IP_6 binding and are thus stable. Unfortunately, our NMR-based assay required milligram amounts of Pds5 protein, and we lacked a sensitive IP_6 detection assay that could directly verify IP_6 binding by human Pds5B WT (or the lack of IP_6 binding by Pds5B mutants) in human cells.

Contributions of the IP_6-Binding Segment of Pds5B to Cohesin Binding

We have identified four conserved residues in Pds5B that are required for cohesin binding (Figure 4-6B). K400 and R401 are located in the loop connecting the two helices in HEAT repeat H9, whereas Y445 and N447 reside in the loop of H10 (Figure 4-4). They define a critical cohesin-binding site of Pds5B on one side of the jaw, which is near the pivot of the lever and connects to the handle (Figure 4-10A). This pivot site, however, was not sufficient to mediate Pds5B binding to cohesin, as a Pds5B mutant with the C-terminal eight HEAT repeats (H13–H20) deleted (Δ722–1116) was deficient in binding to cohesin, Wapl, or Sororin in human cells (Figure 4-10B). Consequently, Pds5B Δ722–1116 failed to support the arm resolution of sister chromatids during early mitosis of Pds5A/B-depleted HeLa cells (Figure 4-10C). Therefore, the C-terminal region, including the IP_6-binding segment, contributes to cohesin binding.

To test whether IP_6 was required for the Pds5B-cohesin interaction in human cells, we normalized the expression of Pds5B mutants deficient for IP_6 binding to that of WT by using more mutant plasmids in transfections. Even when expressed at similar levels, the IP6-binding-deficient Pds5B mutants, including K727E/Y728A, K830E/R834E, and K925E/K928E, were deficient in binding to cohesin, Wapl, or Sororin (Figure 4-10D). Because cohesin was required for the binding of Pds5B to Wapl or Sororin in human cells, the defects of these Pds5B mutants in Wapl or Sororin binding could be an indirect consequence of their inability to bind cohesin. Consistent with this notion, the same Pds5B mutants retained binding to recombinant $Wapl_{1–100}$ and $Sororin_{131–252}$ *in vitro* (Figure 4-11). This finding also indicated that the IP_6-binding-deficient Pds5B mutants were still folded in the N-terminal region. These results suggest that IP_6 is required for cohesin binding by Pds5B.

Both the N-terminal side of the jaw and IP_6 at the bottom of jaw are required for Pds5B to bind cohesin. The C-terminal side of the jaw, especially the αB helix of HEAT repeat H18, is in spatial proximity to the cohesin-binding site near the pivot (Figure 4-10E). We tested whether this helix was involved in cohesin binding. Indeed, mutation of two surface-exposed residues on this helix, V963 and K964, reduced Pds5B binding to cohesin, albeit to a lesser degree than the K400E/R401E and Y445A/N447A mutations did (Figure 4-10E and 10F). Thus, the HEAT repeats C-terminal to the IP_6-binding segment contribute an auxiliary cohesin-contacting site. We propose that one mechanism by which IP_6 contributes to cohesin binding is to sharply bend Pds5B at repeat H15, juxtaposing two cohesin-contacting sites that are otherwise spatially separated (Figure 4-10G).

Inhibition of the Binding of Scc1 to Smc3 by Pds5B

Several recent studies have implicated the Smc3-Scc1 interface as an evolutionarily conserved DNA exit gate of the cohesin ring (Buheitel and Stemmann, 2013; Chan et al., 2012; Gligoris et al., 2014; Huis in 't Veld et al., 2014). At this interface, the N-terminal helical domain (NHD) of Scc1 binds to the coiled-coil region of Smc3 that is adjacent to its ATPase domain, forming a four-helix bundle (Gligoris et al., 2014). Human cohesin with four conserved hydrophobic Scc1 residues at this interface mutated to glutamate (Scc1 4E) is loaded on chromatin, but dissociates from chromatin with abnormally fast kinetics in a Wapl-independent manner, suggesting that the cohesin-releasing activity might act through disrupting the Smc3-Scc1 interface (Huis in 't Veld et al., 2014).

We next defined the element within cohesin that interacted with the IP_6-dependent cohesin-binding surface of Pds5B. The $Scc1_{1–210}$-Myc fragment and its N-terminally truncated species bound efficiently to GFP-Pds5B in HeLa cells (Figure 4-12A). An $Scc1_{76–150}$ fragment immediately C-terminal to the Smc3-binding NHD retained partial binding to Pds5B. Mutations of cohesin-binding residues located at either side of the jaw in Pds5B weakened its binding to both Scc1 fragments. Recombinant purified $Scc1_{76–150}$ bound to Pds5B surprisingly tightly, with a KD of 4.3 nM, as measured by ITC (Figure 4-12B). Purified recombinant Pds5B V963/K964E and Y445A/N447A mutants also bound more weakly to $Scc1_{76–150}$ *in vitro* (Figure 4-12C). Because mutations of the corresponding region in yeast Scc1 are known to disrupt Pds5 binding, $Scc1_{76–150}$ contains a conserved Pds5-binding element that binds at the IP_6-dependent cohesin-binding site in Pds5. $Scc1_{76–150}$ bound to Pds5B less tightly than $Scc1_{1–210}$ in human cells, indicating that other Scc1 elements, possibly the NHD, contribute to Pds5 binding. Full-length Scc1 or any fragments containing the NHD were, however, either not expressed or insoluble in bacteria or insect cells, preventing us from measuring the affinity between Pds5B and larger Scc1 fragments.

The fact that Pds5B bound with high affinity to an Scc1 region bordering the Smc3-binding NHD promoted us to test whether Pds5B could disrupt the Smc3-Scc1 interface. An Smc3 head domain (HD) containing the ATPase domain and an adjacent coiled-coil segment bound strongly to $Scc1_{1–210}$, but only weakly to $Scc1_{1–210}$ 4E, in human cells (Figure 4-12D). Likewise, GST-Smc3 HD bound efficiently to *in vitro* translated $Scc1_{1–210}$ and weakly to Scc1 4E (Figure 4-13A). These results indicate that we can construct an isolated DNA exit gate of cohesin with a functional Smc3-Scc1 interface. Unlike the uncleaved $Scc1_{1–210}$, the N-terminally truncated

species of $Scc1_{1–210}$ 4E completely lost binding to Smc3 HD (Figure 4-13A). Furthermore, deletion of the N-terminal 20 residues of Scc1 on its own did not reduce binding to Smc3 HD, but, when combined with the 4E mutation, completely abolished Smc3 binding (Figure 4-14). Thus, the N-terminal tail of Scc1 can mediate weak binding to Smc3 HD when the Scc1 NHD-Smc3 helical interactions are disrupted. The weak binding of Scc1 4E to Smc3 might help to explain the apparently normal loading of Scc1 4E-containing cohesin onto chromatin (Huis in 't Veld et al., 2014).

Consistent with our previous study (Ouyang et al., 2013), addition of Pds5B either alone or together with SA2 or Wapl did not reduce the amount of Scc1 already bound to Smc3 HD (Figure 4-13A), indicating that these releasing factors cannot disrupt the preformed DNA exit gate *in vitro*. This finding is rather expected, as the release of cohesin from chromatin likely requires its ATPase activity, and the isolated Smc3 HD is not a functional ATPase in the absence of Smc1. Indeed, when Scc1 in the context of intact cohesin is cleaved, Wapl-Pds5 can release the N-terminal fragment Scc1 from Smc3 (Beckouet et al., 2016; Murayama and Uhlmann, 2015).

Interestingly, a pre-incubation of Pds5B with $Scc1_{1–210}$ or $Scc1_{21–210}$ (prior to the addition of Smc3 HD) greatly reduced the Smc3-Scc1 interaction (Figure 4-13B, 13C, and Figure 4-14). As an important control, pre-incubating Scc1 with Pds5B Y445A/N447A deficient in Scc1 binding did not have any effect. SA2 and the C-terminal fragment of Wapl ($Wapl_{501–1190}$) did not prevent Scc1 binding to Smc3, although addition of both appeared to slightly enhance the effects of Pds5B. Pds5B also reduced the residual binding of Scc1 4E to Smc3 mediated by the N-tail of Scc1. This result suggests that Pds5B might hinder the closure of the DNA exit gate of cohesin,

but cannot disrupt the already closed one. We infer from this finding that the half-life of the isolated Smc3-Scc1 complex must be exceedingly long *in vitro*. There is little exchange between free and Smc3-bound states of Scc1 during the time course of our experiments.

DISCUSSION

Our results presented herein confirm and extend the current paradigm that Pds5 has both positive and negative roles in cohesin regulation. Although we could not observe cohesion defects in Pds5A/B-depleted cells using metaphase spreads, we have provided evidence to suggest that Pds5A/B depletion caused phenotypes congruent with cohesion establishment defects. Conversely, we have clearly established a requirement for Pds5 in cohesin release in human cells. One mechanism by which Pds5 promotes cohesin release is to promote the productive association of Wapl with cohesin, through engaging the YSR motif of Wapl with the N-terminal handle and binding to Scc1 through the C-terminal IP_6-bound jaw (Figure 4-13D). This mechanism is antagonized by the YSR motif of Sororin and possibly other unidentified factors in yeast and human.

One possible explanation for why we could not observe cohesion defects in metaphase spreads of Pds5 RNAi cells is that a small amount of Pds5 suffices to perform the positive functions in cohesion establishment, whereas a larger amount of Pds5 is needed to perform its Wapl-dependent cohesin release functions. A partial depletion of Pds5 is expected to more severely cripple the cohesin-release function of Pds5. This notion is consistent with the role of Pds5 in promoting Smc3 acetylation by Esco1, which is a catalytic process. In contrast, the cohesin-release function of Pds5 involves its stoichiometric binding to Wapl and cohesin.

The dual roles of Pds5 in cohesin dynamics may underlie the peculiar behavior of the Pds5B A92P mutant. Unlike other Wapl-binding-deficient mutants, Pds5B A92P supported chromosome-arm resolution (Figure 4-6C). We propose that Wapl and Sororin are mutually antagonistic in sister-chromatid cohesion. The net balance of their activities determines cohesion status. Pds5 recruits both Wapl and Sororin to cohesin. Most Pds5B mutations destabilize Wapl binding more severely than Sororin binding, thus displaying cohesin-release defects. Pds5B A92P disrupts Sororin binding more thoroughly than Wapl binding (Figure 4-6A and 6B) and is thus still functional in supporting cohesin release from chromatin.

Mutation of FGF motif in Sororin weakens sister-chromatid cohesion in *Xenopus* egg extracts (Nishiyama et al., 2010). In contrast, a previous study has shown that deletion of a region encompassing both YSR and FGF motifs of Sororin did not cause overt cohesion defects in human cells (Wu et al., 2011), a finding we could reproduce. Because both motifs of Wapl are important for cohesin release in human cells, we suspect that another protein might act redundantly with the YSR and FGF motifs of Sororin to antagonize these motifs of Wapl in human cells.

Unexpectedly, we have identified IP_6 as a structural cofactor of Pds5. Because IP_6 and other inositol polyphosphates often reside at functional interfaces and directly contribute to protein-protein interactions, we suspect that IP_6 in Pds5 might also form direct contact with cohesin. Because IP_6 is an abundant metabolite and is required for the structural integrity of Pds5, IP_6 is likely a constitutive structural cofactor of Pds5. On the other hand, we cannot exclude possible

regulatory roles of IP_6. In the future, it will be interesting to test whether the levels of IP_6 fluctuate during the cell cycle.

In addition to the scaffolding role of Pds5, Scc1 binding by the Pds5 jaw appears to directly counteract the formation of the Smc3-Scc1 interface, which is a DNA exit gate of cohesin. The mechanism by which Pds5 inhibits the binding of Scc1 to Smc3 remains to be established. Because Scc1 4E deficient in Smc3 binding can still interact with Pds5 (Figure 4-12D), Pds5 is unlikely to compete with Smc3 for the same binding interface on Scc1. It is possible that Pds5 molds the N-terminal region of free Scc1 into an alternative conformation, which is not compatible for Smc3 binding.

A recent study by Uhlmann and coworkers has provided key insight into Wapl-Pds5-mediated cohesin release (Murayama and Uhlmann, 2015). Wapl-Pds5 does not stimulate the ATPase activity of cohesin, but requires the re-binding of ATP to nucleotide-free cohesin to open the cohesin ring. Based on this important insight and our results presented here, we propose the following speculative mechanism to explain the opening of cohesin ring by Wapl-Pds5 (Figure 4-13D). Cohesin contains two interlocked gates: an inner gate formed by the ATPase heads of Smc1 and Smc3 and stabilized by ATP, and an outer gate formed by the Scc1-Smc3 interface. ATP hydrolysis opens the inner gate, allowing the entrapped DNA to move freely in the large ring whose outer gate is closed. We speculate that Wapl-Pds5 might preferably recognize the inner-gate-open conformation of cohesin. Binding of ATP to the nucleotide-free cohesin-Wapl-Pds5 complex closes the inner gate, but produces a fleeting outer-gate-open state

of cohesin, in which the N-tail and NHD of Scc1 are detached from Smc3 HD. This open state during the ATPase cycle might be too transient to allow cohesin release from chromatin. The IP_6-bound jaw of Pds5 binds to the N-terminal region of Scc1 and inhibits its re-association with Smc3. In effect, Pds5 stabilizes a transient, open state of cohesin and prolongs its lifetime, thereby promoting cohesin release from chromosomes. Even though Pds5 is likely the primary regulator of the latter step, Wapl might also be a facilitator, as previously proposed (Gandhi et al., 2006).

By virtue of its ability to topologically embrace chromosomes, the ring-shaped cohesin complex mediates diverse, fundamental cellular processes, including transcription, DNA repair, and chromosome segregation. Our findings reveal the structural basis of the Wapl-Sororin antagonism in cohesin regulation, provide rationales for the dual functions of Pds5 in cohesin dynamics, and suggest a testable model for Pds5-dependent cohesin release from chromosomes.

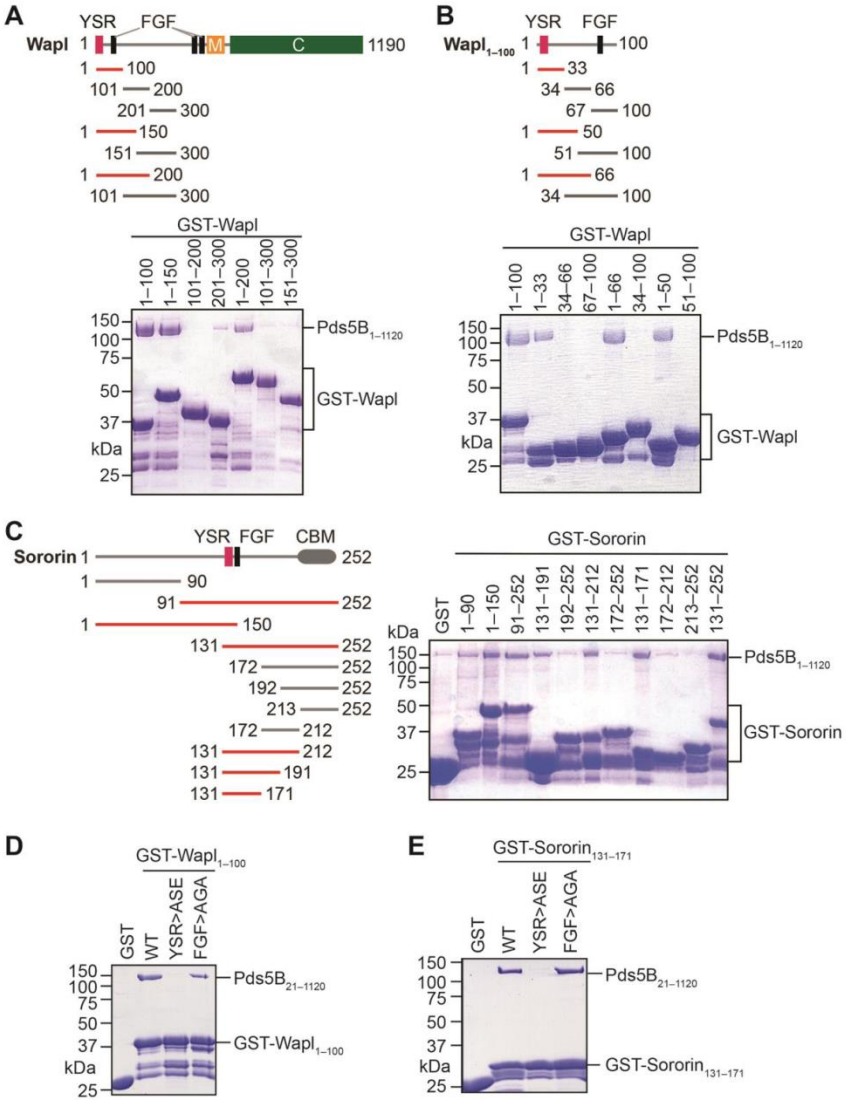

Figure 4-1. Mapping Pds5-binding motifs of human Wapl and Sororin. (**A** and **B**) Schematic drawings of domains and motifs of human Wapl, with the boundaries of the Wapl fragments tested in the experiment shown below. The Wapl fragments that can bind to Pds5B are colored red. The bottom panel shows a Coomassie-stained SDS-PAGE gel of recombinant Pds5B$_{1–1120}$ bound to beads containing different GST-Wapl fragments. (**C**) Schematic drawings of domains and motifs of human Sororin are shown on the left, with the boundaries of the Sororin fragments tested in the experiment shown below. The Sororin fragments that can bind to Pds5B are colored red. The right panel shows a Coomassie-stained SDS-PAGE gel of recombinant Pds5B$_{1–1120}$ bound to beads containing different GST-Sororin fragments. (**D** and **E**) Coomassie-stained gel of Pds5B bound to glutathione-agarose beads containing GST or the indicated GST-Wapl or GST-Sororin proteins. WT, wild type.

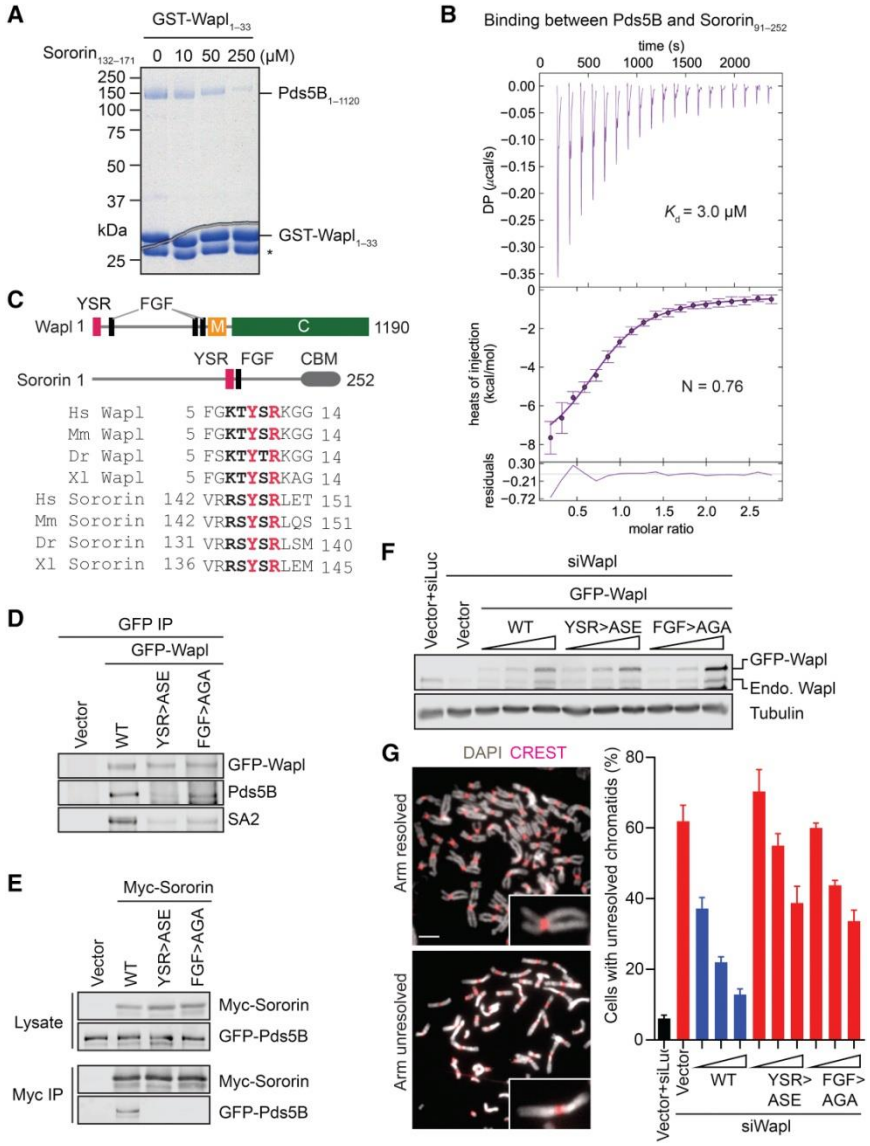

Figure 4-2. Identification of a functional Pds5-binding motif in human Wapl and Sororin. (**A**) Coomassie-stained SDS-PAGE gel of recombinant human Pds5B$_{1–1120}$ bound to GST-Wapl$_{1–33}$, in the absence or presence of increasing concentrations of a Sororin peptide. Asterisk indicates a proteolytic fragment of GST-Wapl$_{1–33}$. (**B**) Isothermal titration calorimetry (ITC) curves of the binding between purified recombinant human Pds5B$_{1–1120}$ and Sororin$_{91–252}$, with KD and binding stoichiometry (N) indicated. DP, differential power. (**C**) Schematic drawing of domains and motifs of human Wapl and Sororin, and sequence alignment of the YSR motifs of Wapl and Sororin from human (Hs), mouse (Mm), zebrafish (Dr), and *Xenopus* (Xl). CBM, cohesin-binding motif. (**D**) Anti-GFP, anti-Pds5B, and anti-SA2 blots of anti-GFP immunoprecipitates (IP) of HeLa cells transfected with the indicated GFP-Wapl plasmids. WT, wild-type; ASE, Y9A/R11E; AGA, F73A/F75A. (**E**) Anti-Myc and anti-GFP blots of lysates and

anti-Myc IP of HeLa cells transfected with plasmids encoding GFP-Pds5B and the indicated Myc-Sororin proteins. WT, wild-type; ASE, Y146A/R148E; AGA, F166A/F168A. (**F**) Anti-Wapl and anti-β-tubulin immunoblots of lysates of HeLa cells that were transfected with Wapl siRNA and increasing amounts of the indicated GFP-Wapl plasmids. Endo, endogenous. The increase of the untagged Wapl band intensity in GFP-Wapl samples was due to proteolysis of GFP-Wapl proteins or internal translation start of the transgene. (**G**) Representative metaphase spreads of cells in **F** with arm-resolved or arm-unresolved chromosomes. Spreads were stained with DAPI (gray) and the kinetochore marker CREST (red). Selected sister chromatids are magnified in inset. Scale bar, 5 μm. Quantification of the percentages of mitotic cells in **F** that had arm-unresolved chromosomes. Error bars, SD (n = 3 independent experiments).

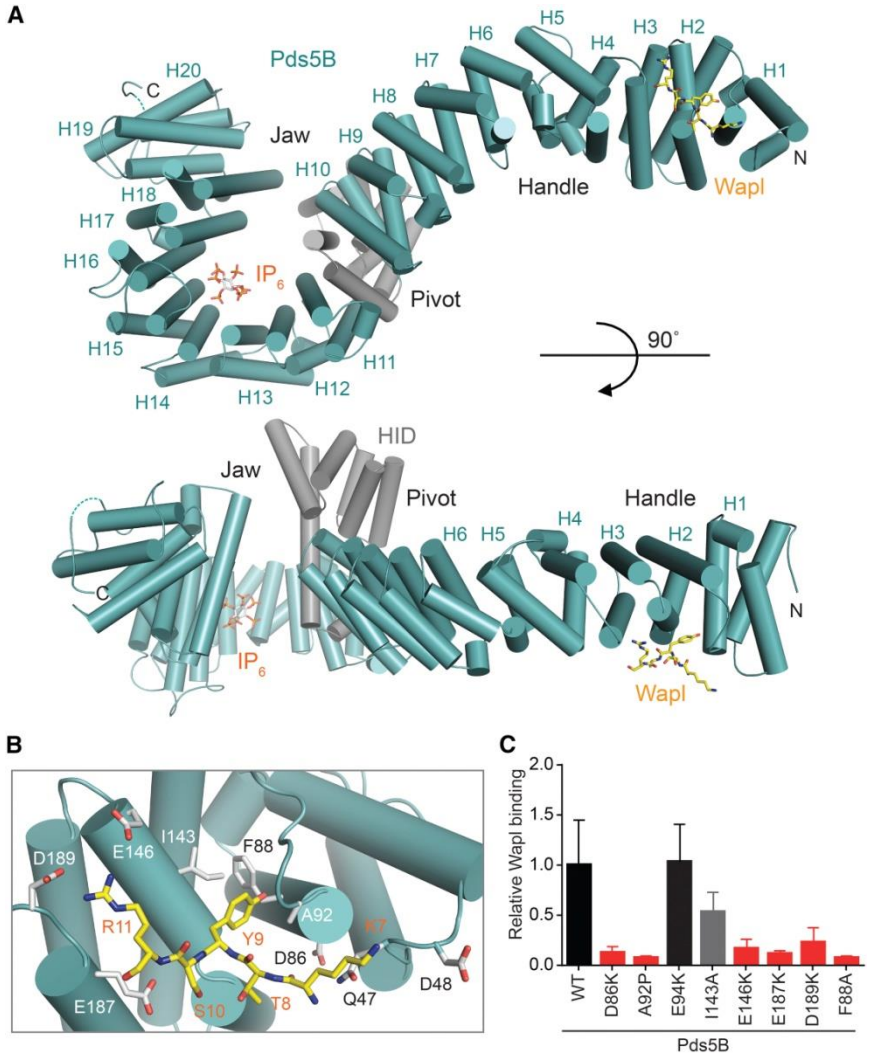

Figure 4-3. Crystal structure of human Pds5B bound to YSR motif of Wapl. (**A**) Cartoon drawing of the crystal structure of human Pds5B in complex with the YSR motif of Wapl in two different orientations. The HEAT repeats and the helical insert domain (HID) are colored teal and gray, respectively. The Wapl peptide and IP_6 are shown as sticks. The N and C termini and the 20 HEAT repeats (H1–H20) are labeled. Pds5B is shaped like a plier lever, with H1–H8 resembling the handle, the HID resembling the pivot, and H9–H20 forming the jaw. All structure figures are made with PyMOL. (**B**) Zoomed-in view of the Pds5B-Wapl interface. Pds5B and Wapl residues are shown as gray and yellow sticks, respectively. (**C**) Quantification of the relative ^{35}S-Pds5B intensities bound to GST-Wapl$_{1–150}$. Error bars, SD (n = 3 independent experiments).

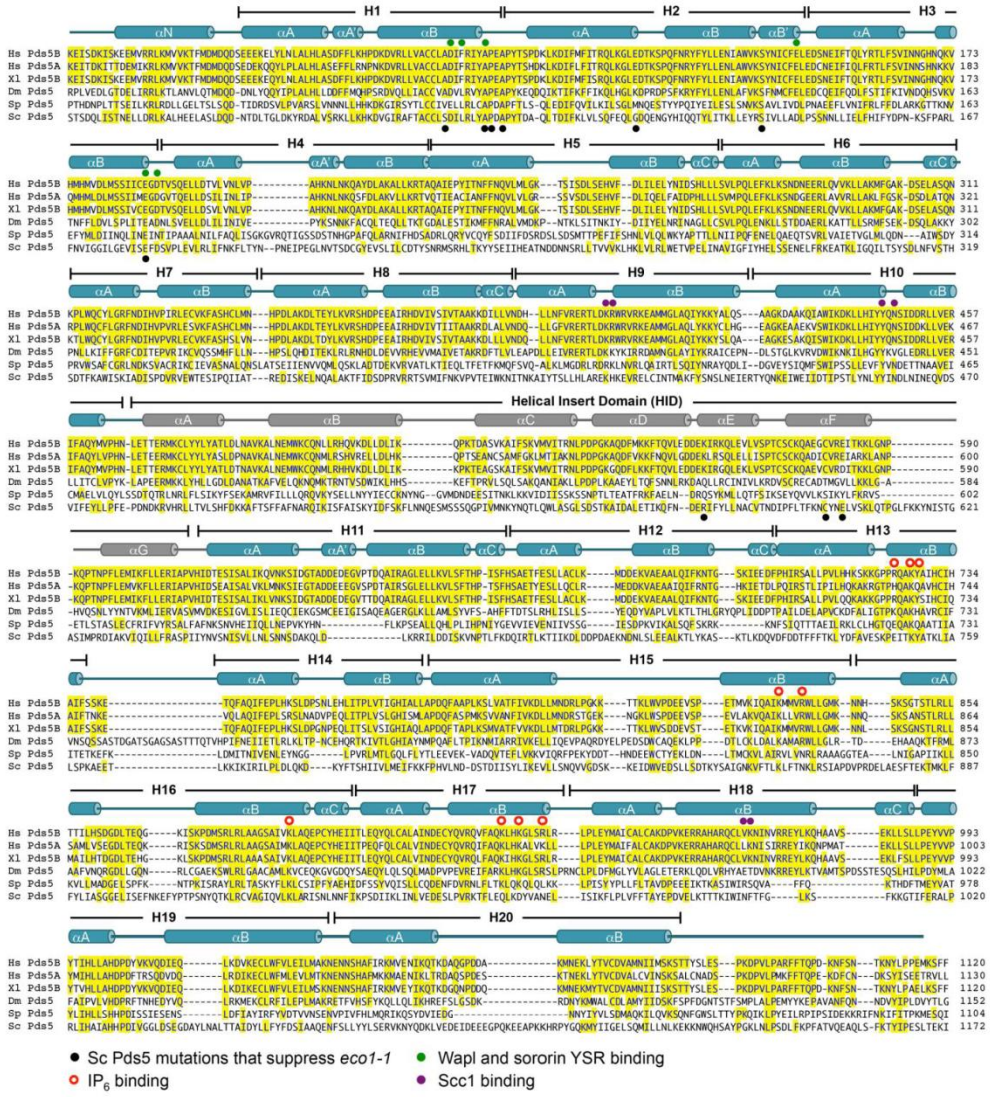

Figure 4-4. Sequence alignment of Pds5 proteins from various species. The abbreviations are: Hs, *Homo sapiens*; Xl, *Xenopus laevis*, Dm, *Drosophila melanogaster*; Sp, *Schizosaccharomyces pombe*; Sc, *Saccharomyces cerevisiae*. The conserved residues are shaded yellow. The secondary structure elements of Hs Pds5B are shown on top. The positions of Sc Pds5 mutants that suppress *eco1-1* are indicated by black dots. Hs Pds5B residues that bind Wapl YSR, Scc1, or IP_6 are also indicated.

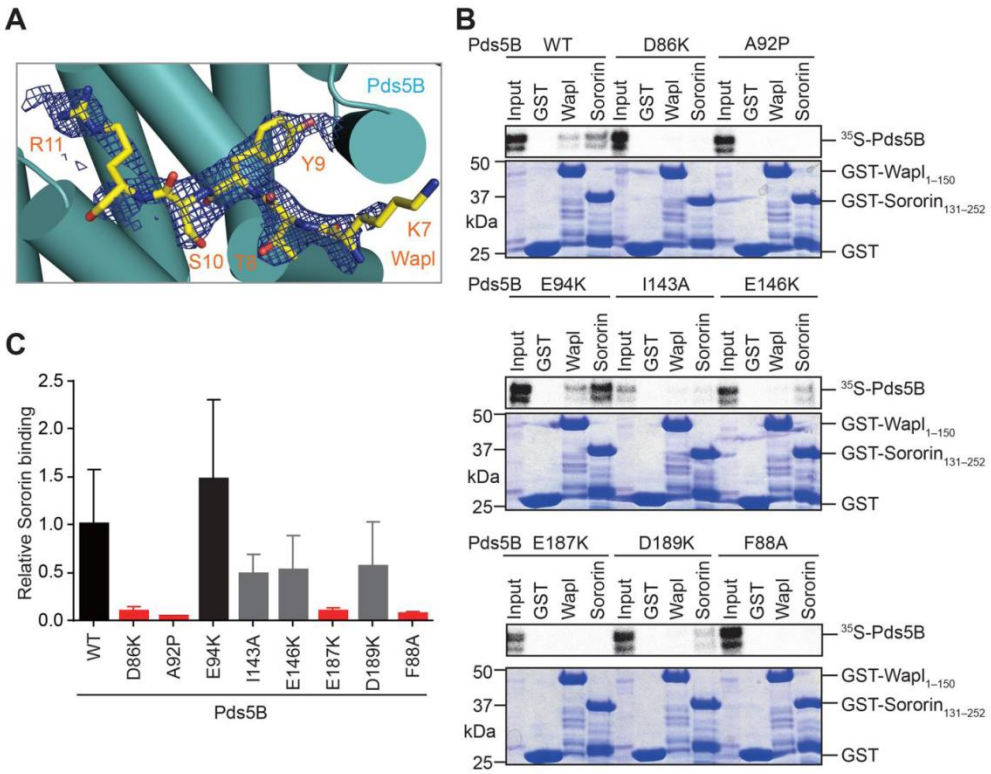

Figure 4-5. Biochemical analysis of the YSR-binding site of Pds5B. (**A**) The *2Fo-Fc* electron density map (blue mesh) of the Wapl peptide (sticks) contoured at 1.0 σ. (**B**) Autoradiograph (top) and Coomassie stained gel (bottom) of input ^{35}S-Pds5B proteins (WT, wild type; or mutants) and the same proteins bound to beads containing GST, GST-Wapl$_{1–150}$, or GST-Sororin$_{131–252}$. (**C**) Quantification of the relative ^{35}S-Pds5B intensities bound to GST-Sororin$_{131–252}$. Error bars, SD (n = 3 independent experiments).

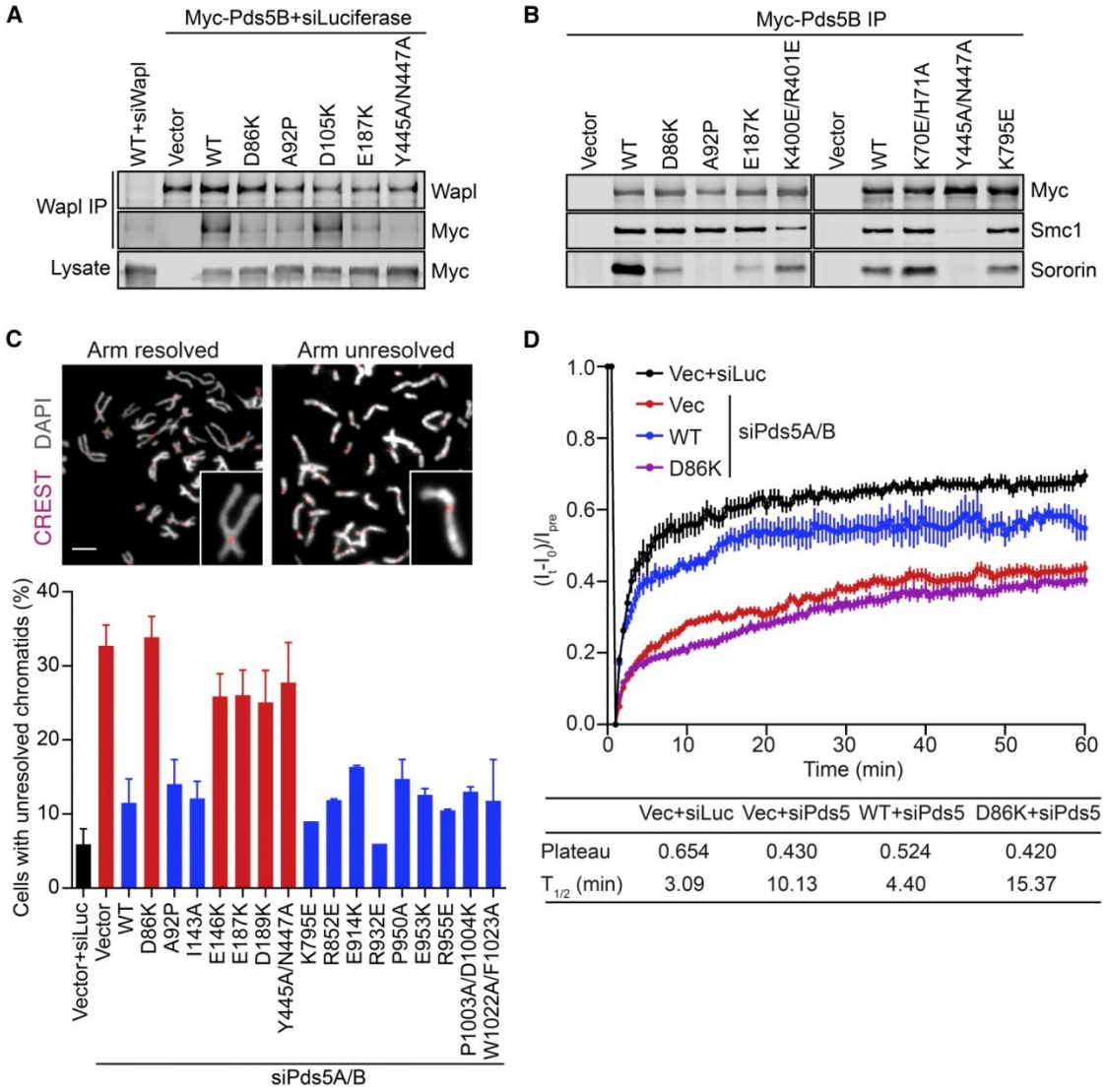

	Vec+siLuc	Vec+siPds5	WT+siPds5	D86K+siPds5
Plateau	0.654	0.430	0.524	0.420
$T_{1/2}$ (min)	3.09	10.13	4.40	15.37

Figure 4-6. Biochemical and functional analyses of the YSR-binding site of Pds5B. (**A**) Immunoblots of the lysates and anti-Wapl immunoprecipitates (IP) of HeLa cells transfected with the indicated plasmids and siRNAs. WT, wild-type. (**B**) Anti-Myc, anti-Smc1, and anti-Sororin blots of anti-Myc IP of HeLa cells transfected with the indicated Myc-Pds5B plasmids. The two gel panels were from two different experiments. The mutants can only be compared to the WT control in the same experiment. (**C**) Representative metaphase spreads of cells with arm-resolved or arm-unresolved chromosomes (upper panels). Spreads were stained with DAPI (gray) and the kinetochore marker CREST (red). Selected sister chromatids are magnified in inset. Scale bar, 5 μm. Quantification of the percentages of mitotic HeLa cells (transfected with the indicated Myc-Pds5B plasmids and Pds5A/B siRNAs) that had arm-unresolved chromosomes (lower panel). WT, wild-type. Error bars, SD ($n \geq 3$ independent experiments for all samples except those of K795E and R932E, which were performed only once; > 100 cells

were counted for each sample in each experiment). (**D**) Recovery curves of normalized Smc1-GFP intensity of cells transfected with the indicated mCherry-Pds5B plasmids followed by Luciferase (Luc) or Pds5A/B siRNAs. Vec, vector; WT, wild-type; I_{pre}, intensity before bleaching; I_0, intensity immediately after bleaching; I_t, intensity at each time point after bleaching. Error bars, SEM (Vec + siLuc, n = 15 cells; Vec + siPds5A/B, n = 18; WT + siPds5A/B, n = 12; D86K + siPds5A/B, n = 15). The plateau and half-life of recovery for each sample are tabulated below.

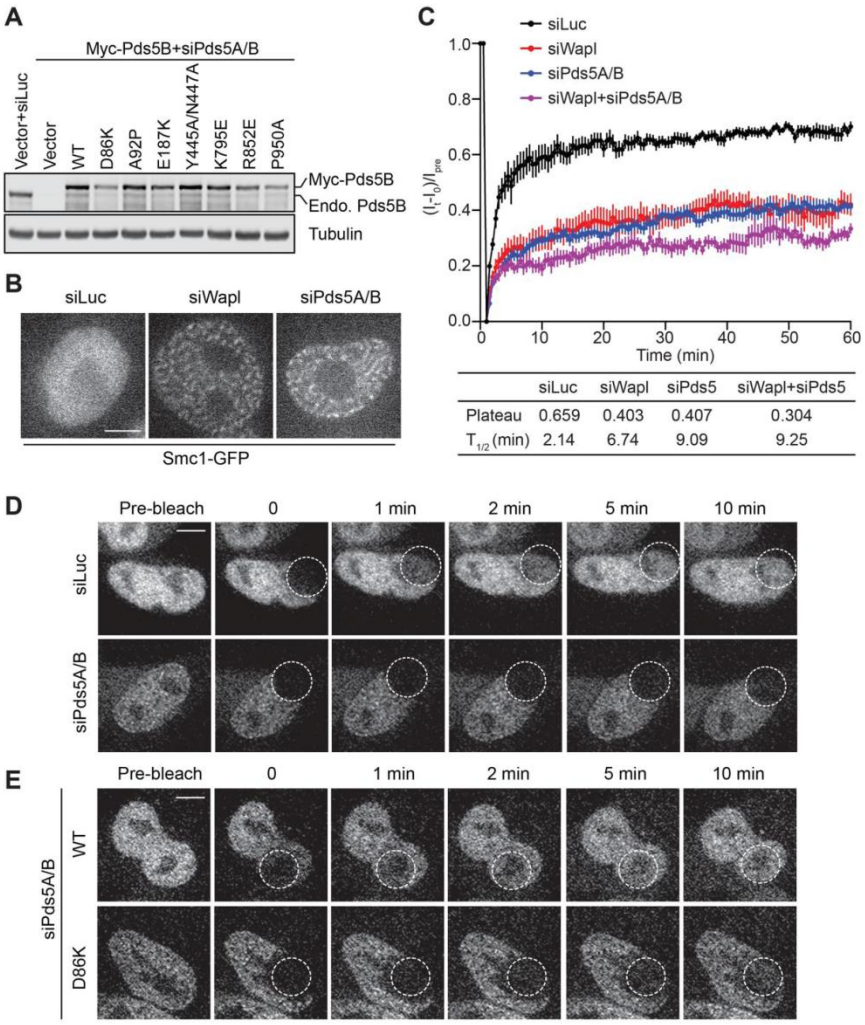

Figure 4-7. Functional analysis of the YSR-binding site of Pds5B. (**A**) Anti-Pds5B and anti-β-tubulin immunoblots of lysates of HeLa cells in **Figure 4-6C** that were transfected with the indicated Myc-Pds5B plasmids and Pds5A/B siRNAs. WT, wild type. Endo, endogenous. (**B**) Representative fluorescence microscopy images of Smc1-GFP-expressing HeLa cells that were transfected with the indicated siRNAs. Scale bar, 5 μm. (**C**) Recovery curves of normalized Smc1-GFP intensity of HeLa cells transfected with the indicated siRNAs. I_{pre}, intensity before bleaching; I_0, intensity immediately after bleaching; I_t, intensity at each time point after bleaching. Error bars, SEM (n = 3 independent experiments, with a total of 10 cells per sample analyzed). The plateau and half-life of recovery for each sample are tabulated below. (**D**) Representative fluorescence microscopy images of cells in **C** that were transfected with the indicated siRNAs and analyzed at the indicated timepoints after photobleaching. Bleached regions are outlined. Scale bar, 5 μm. (**E**) Representative fluorescence microscopy images of cells expressing Smc1-GFP in **Figure 4-6D** that were transfected with the indicated Myc-Pds5B

plasmids and Pds5A/B siRNAs and analyzed at the indicated timepoints after photobleaching. Bleached regions are outlined. Scale bar, 5 μm.

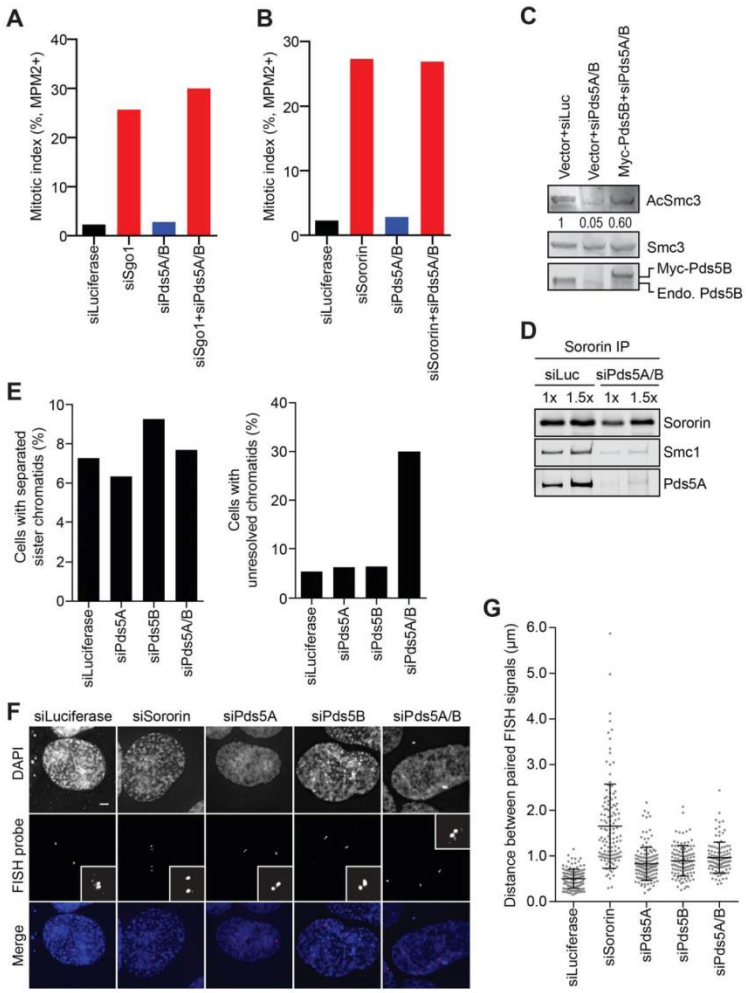

Figure 4-8. Positive roles of Pds5B in sister-chromatid cohesion. (**A** and **B**) Quantification of the mitotic indices (defined as the percentage of MPM2-positive cells with 4N DNA content) of cells transfected with the indicated siRNAs. (**C**) Immunoblots of chromatin extracts of HeLa cells that were transfected with the indicated plasmids and siRNAs and synchronized in S phase (released for 4 h after thymidine treatment). AcSmc3, acetylated Smc3. Endo, endogenous. The relative AcSmc3 signal intensities are shown below the anti-AcSmc3 blot. (**D**) Anti-Sororin, anti-Smc1, and anti-Pds5A blots of varying amounts of anti-Sororin immunoprecipitates (IP) of HeLa cells that were transfected with the indicated siRNAs and synchronized in S phase (released for 4 h after thymidine treatment). (**E**) Quantification of the percentages of mitotic HeLa cells that were transfected with the indicated siRNAs and had separated sister chromosomes (left panel) or arm-unresolved chromosomes (right panel) in metaphase spreads. Experiments were performed once. More than 100 cells were counted for each sample. (**F**) Images of G2-enriched HeLa Tet-On cells transfected with the indicated siRNAs and stained

with DAPI (blue) and the FISH probe (red) which detected a chromosome 3 locus. Selected paired FISH signals are magnified in inset. Scale bar, 5μm. (**G**) Quantification of the distances between paired FISH signals. Error bars, SD (experiments were performed twice. More than 20 cells were analyzed for each sample in each independent experiment).

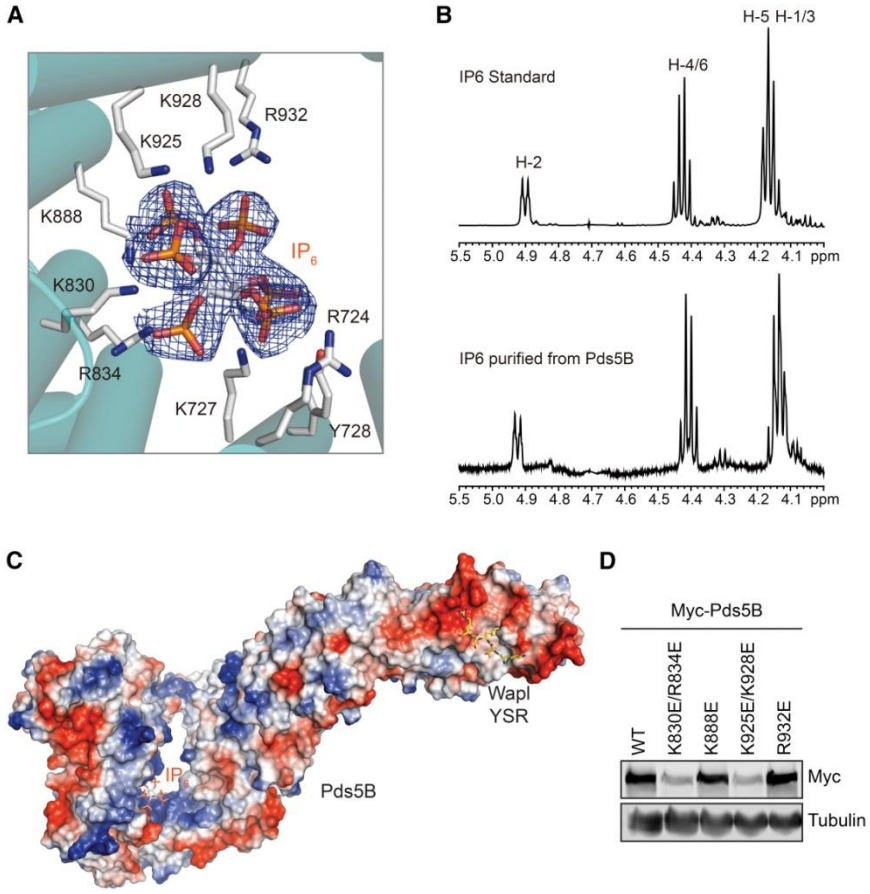

Figure 4-9. IP_6 as a structural cofactor of Pds5B. (**A**) Zoomed-in view of the IP_6-binding site of Pds5B. IP_6 is shown as stick, along with its *2Fo-Fc* electron density map (blue mesh) contoured at 1.0 σ. IP_6-binding residues are shown as sticks and labeled. (**B**) 1D ^1H NMR spectra of authentic IP_6 standard (top) and IP_6 isolated from recombinant human Pds5B, with the ^1H assignment indicated. (**C**) Surface drawing of human Pds5B colored with its electrostatic potential (blue, positive; red, negative). IP_6 and the Wapl peptide are shown in sticks. (**D**) Anti-Myc and anti-β-tubulin immunoblots of lysates of HeLa cells transfected with the same amount of the indicated Myc-Pds5B plasmids. WT, wild-type.

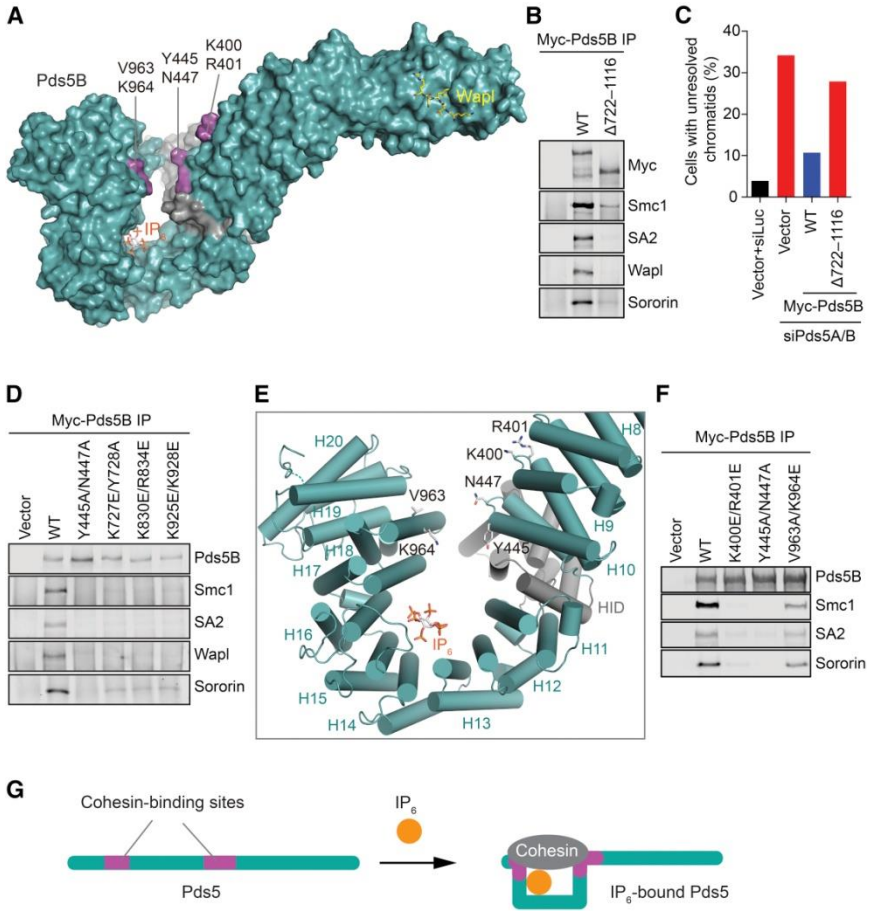

Figure 4-10. Requirement for IP_6 in cohesin binding by Pds5B. (**A**) Surface drawing of Pds5B, with the cohesin-binding residues colored purple and labeled. IP_6 and the Wapl peptide are shown in sticks. (**B**) Immunoblots of anti-Myc immunoprecipitates (IP) of HeLa cells that were transfected with the indicated Myc-Pds5B plasmids. (**C**) Quantification of the percentages of mitotic HeLa cells (transfected with the indicated plasmids and siRNAs) that had arm-unresolved chromosomes. (**D**) Immunoblots of anti-Myc immunoprecipitates (IP) of HeLa cells transfected with the indicated Myc-Pds5B plasmids. WT, wild-type. (**E**) Cartoon diagram of the jaw of Pds5B, with IP_6 and cohesin-binding residues shown in sticks. HID, helical insert domain. (**F**) Immunoblots of anti-Myc immunoprecipitates (IP) of HeLa cells transfected with the indicated Myc-Pds5B plasmids. WT, wild-type. (**G**) Model for IP_6-dependent cohesin binding by Pds5.

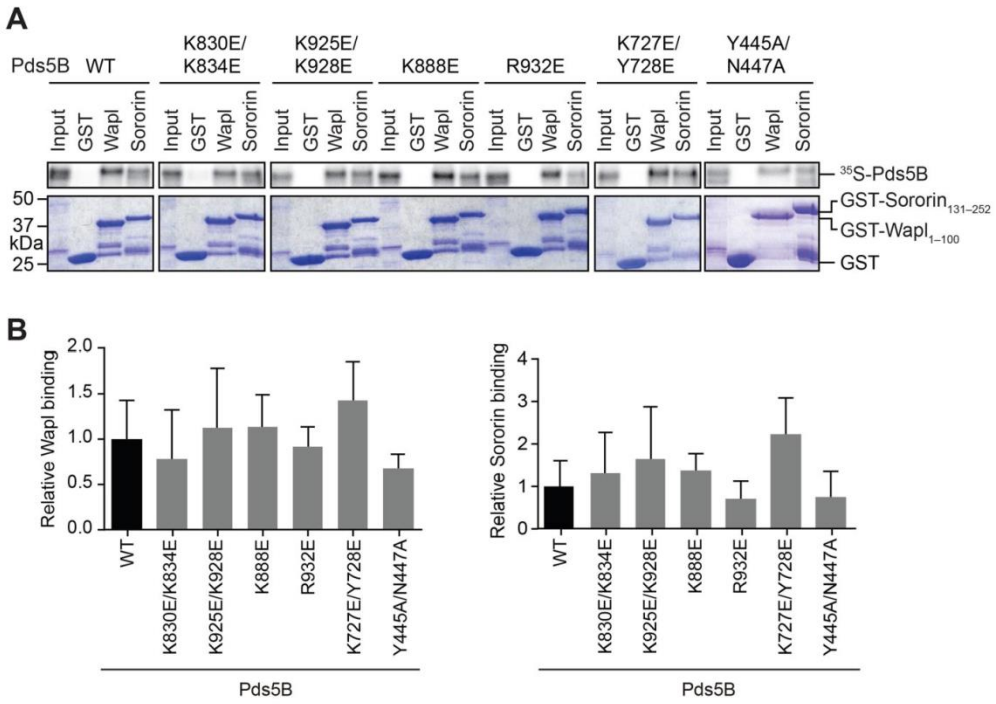

Figure 4-11. Binding of IP_6-binding-deficient Pds5B mutants to Wapl and Sororin. (**A**) Autoradiograph (top) and Coomassie stained gel (bottom) of input ^{35}S-Pds5B proteins (WT or mutants) and the same proteins bound to beads containing GST, GST-Wapl$_{1–100}$, or GST-Sororin$_{131–252}$. (**B**) Quantification of the relative ^{35}S-Pds5B intensities bound to GST-Wapl beads (left) or GST-Sororin beads (right) in binding reactions in **A**. Error bars, SD (n = 3 independent experiments).

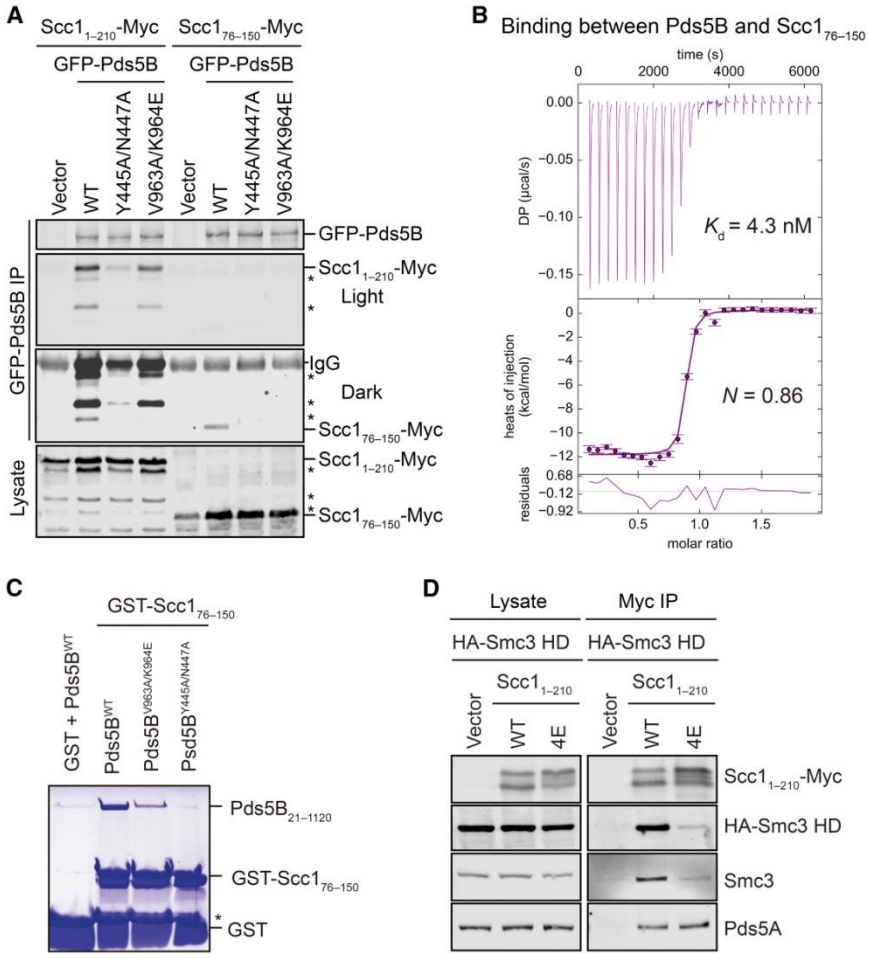

Figure 4-12. Identification of the Pds5B-binding region in Scc1. (**A**) Immunoblots of lysate and anti-GFP immunoprecipitates (IP) of HeLa cells transfected with the indicated Scc1-Myc and GFP-Pds5B plasmids. Asterisks indicate N-terminally truncated forms of $Scc1_{1–210}$-Myc. WT, wild-type. (**B**) ITC curves of the binding between purified recombinant $Pds5B_{21–1120}$ and $Scc1_{76–150}$, with the dissociation constant (KD) and binding stoichiometry (N) indicated. DP, differential power. (**C**) Coomassie-stained SDS-PAGE gel of recombinant human $Pds5B_{21–1120}$ wild-type (WT) or mutant proteins bound to beads containing GST or GST-$Scc1_{76–150}$. Asterisk indicates a proteolytic fragment of GST-$Scc1_{76–150}$. (**D**) Anti-Myc, anti-HA, anti-Smc3, and anti-Pds5A blots of lysates and anti-Myc immunoprecipitates (IP) of HeLa cells that were transfected with plasmids encoding HA-Smc3 HD and the indicated $Scc1_{1–210}$-Myc plasmids. WT, wild-type; 4E, L53E/L59E/Y67E/L74E.

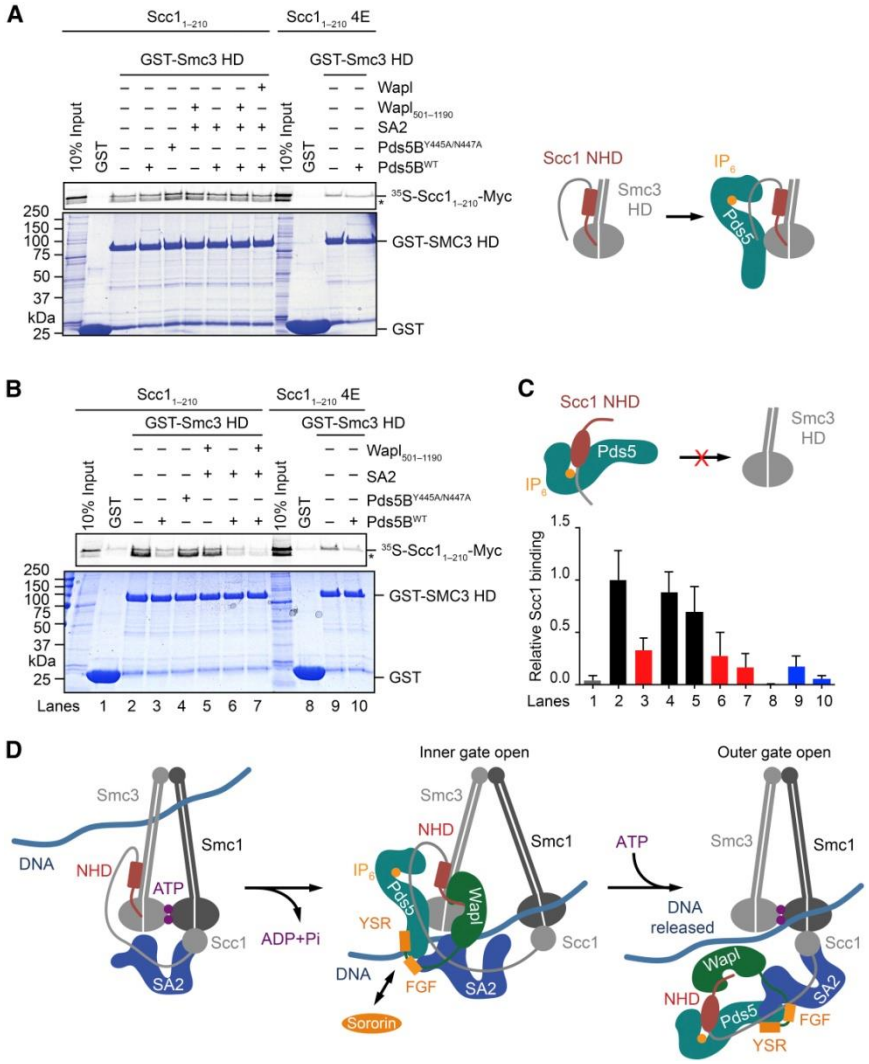

Figure 4-13. Inhibition of DNA exit gate closure by Pds5B. (**A**) Beads bound to GST or GST-Smc3 head domain (HD) were incubated with *in vitro* translated ^{35}S-labeled Scc1$_{1–210}$ or Scc1$_{1–210}$ 4E and washed. The beads were then incubated with the indicated combinations of Pds5B (WT or Y445A/N447A), full-length Wapl, Wapl$_{501–1190}$, and SA2. After washing, the bound proteins were separated on SDS-PAGE and analyzed with a phosphoimager (top panel) and Coomassie staining (bottom panel). Asterisk indicates N-terminally truncated forms of Scc1$_{1–210}$. The schematic drawing on the right shows that Pds5B does not disrupt the preformed Smc3-Scc1 complex. (**B**) Binding between GST-Smc3 head domain (HD) and *in vitro* translated ^{35}S-Scc1$_{1–210}$ (WT or 4E) that had been pre-incubated with the indicated combinations of Pds5B (WT or Y445A/N447A), Wapl$_{501–1190}$, and SA2. Autoradiograph (top) and Coomassie-stained gel (bottom) of 10% input proteins and proteins bound to GST or GST-Smc3 HD beads are shown. Asterisk indicates N-terminally truncated forms of Scc1$_{1–210}$. (**C**) Quantification of the relative Scc1 intensities of the indicated lanes in **B**. Error bars, SD (n = 3 independent experiments). The

schematic drawing on top shows that Pds5-bound Scc1 is deficient in Smc3 binding. (**D**) A speculative model for Pds5-dependent cohesin release from chromosomes. Pds5 bridges the interaction between cohesin and the YSR motif of Wapl to strengthen binding of Wapl-Pds5 to cohesin. This function of Pds5 is antagonized by the YSR motif of Sororin. Pds5 inhibits the formation of the Smc3-Scc1 interaction, suggesting that Pds5 might also promote cohesin release through stabilizing a transient open state of cohesin.

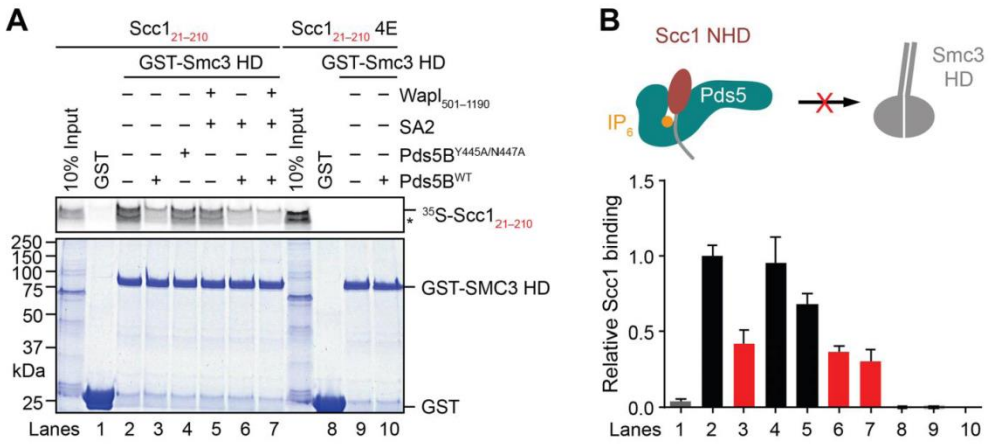

Figure 4-14. Inhibition of DNA exit gate closure by Pds5B. (**A**) Binding between GST-Smc3 head domain (HD) and *in vitro* translated ^{35}S-Scc1$_{21–210}$ (WT or 4E) that had been pre-incubated with the indicated combinations of Pds5B (WT or Y445A/N447A), Wapl$_{501–1190}$, and SA2. Autoradiograph (top) and Coomassie stained gel (bottom) of 10% input proteins and proteins bound to GST or GST-Smc3 HD beads are shown. Asterisk indicates N-terminally truncated forms of Scc1$_{21–210}$. (**B**) Quantification of the relative Scc1 intensities of the indicated lanes in **A**. Error bars, SD (n = 3 independent experiments). The schematic drawing on top shows that prior Pds5 binding to Scc1 inhibits the subsequent binding of Scc1 to Smc3.

Table 4-1. Data collection, structure determination, and refinement statistics of human Pds5B bound to Wapl$_{1-33}$

Data Collection	
Space group	$P2_12_12_1$
Cell constants a, b, c (Å)	120.76, 162.37, 173.06
Wavelength (Å)	0.97918
Resolution range (Å)	40.6-2.70 (2.75-2.70)[a]
Unique reflections	92,470 (4,540)
Multiplicity	8.1 (6.6)
Data completeness (%)	99.9 (99.4)
R_{merge} (%)[b,c]	9.5 (100)
R_{pim} (%)[c,d]	4.7 (76.5)
$I/\sigma(I)$	18.4 (1.2)
Wilson B value (Å^2)	38.1
Phase Determination	
Anomalous scatterers	Se, 73 out of 66 possible sites
Refinement Statistics	
Resolution range (Å)	40.6-2.71 (2.78-2.71)
No. of reflections R_{work} / R_{free}	81,101/1,991 (2,181/61)
Data completeness (%)	87.4 (34.0)
Atoms (non-H protein/peptide/IP_6)	17,387/45/72
R_{work} (%)	21.6 (32.9)
R_{free} (%)	25.3 (43.3)
Rmsd bond length (Å)	0.003
Rmsd bond angle (°)	0.62
Mean B value (Å^2) (protein, chain A/IP_6, chain A/protein, chain B/IP_6, chainB/peptide, chain C)	41.4/33.4/63.4/46.4/91.6
Ramachandran plot (%) (favored/additional/disallowed)[e]	97.2/2.6/0.2
Missing residues	A: 584-594, 1102-1107, 1117-1120. B: 46-48, 91-94, 539-543, 587-595, 1101-1107. C: 1-6, 12-33.

[a] Data for the outermost shell are given in parentheses.

[b] $R_{merge} = 100\ \Sigma_h\Sigma_i|I_{h,\,i} - \langle I_h\rangle|/\Sigma_h\Sigma_i\langle I_{h,\,I}\rangle$, where the outer sum ($h$) is over the unique reflections and the inner sum (i) is over the set of independent observations of each unique reflection.

[c] Bijvoet pairs were kept separate for data processing.

[d] $R_{pim} = 100\ \Sigma_h\Sigma_i[1/(n_h-1)]^{1/2}|I_{h,\,i} - \langle I_h\rangle|/\Sigma_h\Sigma_i\langle I_{h,\,I}\rangle$, where n_h is the number of observations of reflections h.

[e] As defined by the validation suite MolProbity.

CHAPTER V: MCM-DEPENDENT COHESIN LOADING PROMOTES SISTER-CHROMATID COHESION ESTABLISHMENT DURING DNA REPLICATION

INTRODUCTION

Cohesin is a ring-shaped ATPase with a central pore of 30-40 nm in diameter (Gruber et al., 2003; Huis in 't Veld et al., 2014). In human somatic cells, the cohesin complex consists of four subunits: Smc1, Smc3, Scc1 and either SA1 or SA2. Cohesin performs critical functions in many fundamental chromosome-based processes, including sister-chromatid cohesion, DNA damage repair, transcription, and chromatin compaction in eukaryotes (Bose and Gerton, 2010; Haarhuis et al., 2017; Nasmyth and Haering, 2009).

Cohesin medicated sister-chromatid cohesion is essential for proper chromosome segregation and faithful transmission of genetic information during the cell cycle (Peters and Nishiyama, 2012). Failure to establish or resolve cohesion in a timely manner leads to aneuploidy, which contributes to tumorigenesis (Losada, 2014; Remeseiro et al., 2013). Several lines of evidence suggest that cohesin embraces two replicated sister chromatids in its ring structure to generate cohesive linkages between them and enables sister-chromatid cohesion establishment (Gligoris et al., 2014; Gruber et al., 2003; Haering et al., 2008).

The association of cohesin with chromatin is regulated by a set of cohesin regulators in a cell-cycle-dependent manner. Cohesin is loaded onto chromatin in telophase and G1 by a mechanism that depends on the Scc2/4 complex (Ciosk et al., 2000; Watrin et al., 2006). The topological loading of cohesin onto DNA by the Scc2/4 loader complex has been reconstituted *in*

vitro using recombinant fission yeast proteins (Murayama and Uhlmann, 2014). It has been shown that the Scc2/4 complex promotes cohesin loading at specific chromosomal loci in budding yeast (Uhlmann, 2016). In *Xenopus* egg extracts, Scc2/4 is recruited to the pre-replication complex (pre-RC) in a process that also requires the Cdc7-DBF4 protein kinase (DDK) (Gillespie and Hirano, 2004; Takahashi et al., 2008; Takahashi et al., 2004). The Cdc7 kinase activity is essential for Scc2/4 and cohesin loading onto chromatin (Takahashi et al., 2008). Before DNA replication, the chromatin-bound cohesin is dynamic and actively removed from chromatin by the cohesin inhibitor Wapl with help of Pds5 (Gandhi et al., 2006; Kueng et al., 2006). Concomitantly with DNA replication in S phase, a pool of cohesin is converted to the cohesive form that is stably associated with chromatin and mediates sister-chromatid cohesion (Gerlich et al., 2006; Kueng et al., 2006). Cohesion establishment requires the acetylation of two conserved lysine residues on the Smc3 subunit by the acetyltransferase Eco1 (Esco1 and Esco2 in vertebrates) and subsequent recruitment of cohesin-stabilizing factor Sororin to the cohesin complex in metazoans (Chan et al., 2012; Hou and Zou, 2005; Ladurner et al., 2016; Lafont et al., 2010; Nishiyama et al., 2010; Rolef Ben-Shahar et al., 2008; Unal et al., 2008). Smc3 acetylation and Sororin antagonize the cohesin-releasing activity of Pds5-Wapl (Nishiyama et al., 2010). However, cohesin acetylation can occur efficiently before and after DNA replication. Esco1 in human cells has been shown to constitutively co-localize and mediate the acetylation of cohesin throughout the cell cycle (Minamino et al., 2015; Rahman et al., 2015). Thus, Smc3 acetylation is necessary but not sufficient for cohesion establishment.

Several publications have suggested that only cohesin acetylation in association with the DNA replication machinery promotes sister-chromatid cohesion (Song et al., 2012). Esco2 but

not Esco1 mediated Smc3 acetylation is regulated during the cell cycle, and the interaction between Esco2 and the replication machinery is essential for cohesion establishment (Alomer et al., 2017; Moldovan et al., 2006; Song et al., 2012), indicating that replication-dependent cohesin acetylation enables cohesion establishment. Furthermore, down-regulation of many DNA replication factors including Ctf4 (WDHD1 in vertebrates), Tof1 (Timeless in vertebrates), Csm3 (Tipin in vertebrates), Chl1 (DDX11 in vertebrates) leads to cohesion defects in yeast and human cells (Chan et al., 2003; Errico et al., 2009; Leman et al., 2010; Parish et al., 2006; Peters and Nishiyama, 2012; Rudra and Skibbens, 2013; Samora et al., 2016; Tanaka et al., 2009). These results imply that cohesion establishment is tightly coupled to DNA replication (Sherwood et al., 2010).

In eukaryotic cells, DNA replication is initiated via the ordered recruitment of numerous proteins onto replication origins. In G1, the mini-chromosome maintenance 2-7 (MCM2-7) helicase complex is loaded onto chromatin as a double hexamer by the origin recognition complex (ORC), Cdc6, and Cdt1, resulting in the formation of the pre-RC (Bell and Dutta, 2002; Fragkos et al., 2015; Masai et al., 2010). Activation of replication origins involves the dissociation of the MCM double hexamer into two active MCM helicase that form the two replisomes capable of unwinding DNA and initiating DNA replication. This step is induced by the phosphorylation of MCM by DDK at the G1/S boundary (Labib, 2010). This phosphorylation is essential for the subsequent recruitment of Cdc45 and GINS, and the formation of the active CMG helicase (Aparicio et al., 2009; Bruck and Kaplan, 2015; Heller et al., 2011; Sheu and Stillman, 2006).

During S phase, numerous replisome components are recruited to the active replication forks to promote efficient fork progression and to ensure fork stabilization, including Ctf4/WDHD1, Tof1/Timeless, Csm3/Tipin, Chl1/DDX11 and RPA. Ctf4/WDHD1 is known to form a homotrimer to link the CMG helicase to the DNA polymerase α-primase complex within the replisome (Kang et al., 2013; Simon et al., 2014; Villa et al., 2016). It has been shown to be important for sister-chromatid cohesion in yeast and *Xenopus* (Borges et al., 2013; Errico et al., 2009; Lengronne et al., 2006; Tanaka et al., 2009; Xu et al., 2007). Tof/Timeless and Csm3/Tipin form a complex and mutually stabilize each other. Depletion of Timeless or Tipin has been shown to impair sister-chromatid cohesion and mitotic progression in human cells (Errico et al., 2009; Leman et al., 2010). Chl1/DDX11 is a member of the XPD family of helicases with important functions in genome stability. DDX11-deficient mice are embryonic lethal, and aneuploidy is observed in DDX11-deficient cells (Inoue et al., 2007). Mutations in human DDX11 lead to the Warsaw breakage syndrome with chromosomal breakage and sister-chromatid cohesion defects (van der Lelij et al., 2010). Recently, it has been shown that Chl1 is recruited to the DNA replication fork through an interaction with Ctf4 in budding yeast. This interaction with Ctf4, but not its helicase activity, is required for the cohesion function of Chl1 (Samora et al., 2016). RPA is a heterotrimeric single-stranded DNA-binding protein that is highly conserved in eukaryotes. At DNA double-strand breaks (DSBs), the yeast Mre11-Rad50-Xrs2 (MRX) complex, which also has a ring structure resembling cohesin, has been shown to be directly recruited by RPA to hold sister chromatids together at breaks (Seeber et al., 2016). Additionally, a model has been proposed in which enzymes and proteins responsible for processing Okazaki fragments would act in concert at the lagging strand with the above

replisome components to facilitate cohesion in budding yeast (Farina et al., 2008; Moldovan et al., 2006; Rudra and Skibbens, 2012). However, how efficient lagging strand synthesis promotes sister-chromatid cohesion has not been elucidated (Leman and Noguchi, 2014; Skibbens, 2009).

To gain insights to cohesion establishment during DNA replication, we investigate the roles of replication factors in cohesin loading and interphase cohesion. Our results demonstrate a conserved mechanism of MCM-dependent cohesin loading onto chromosomes in metazoans. We provide evidence to suggest that the association of Scc2/4 and cohesin with the replication machinery is required for cohesion establishment. Our study provides insights into how cohesion establishment and DNA replication are coordinated.

MATERIALS AND METHODS

Mammalian Cell Culture, Cell Transfection, and Cell Synchronization

HeLa Tet-On cells were grown in DMEM (Invitrogen) supplemented with 10% fetal bovine serum (FBS) and 2 mM L-glutamine. When cells reached a confluency of 50%, plasmid transfection was performed using the Effectene reagent (Qiagen) according to the manufacturer's protocols. All mammalian expression plasmids used in this study were derived from modified pCS2 vectors. The human MCM2, WDHD1, Timeless and RPA2 cDNAs that contain silent mutations in the siRNA-targeted regions were inserted into these vectors with HA or Myc tag at their N-termini. All constructs were verified by DNA sequencing. The Scc1–Myc-expressing stable HeLa Tet-On cell line was made as described previously. Scc1–Myc expression was induced with 1 μg/ml doxycycline. For siRNA transfection, cells were transfected with Lipofectamine RNAiMAX (Invitrogen) at 20%-40% confluency according to the manufacturer's protocols, and analyzed at 24–48 h after transfection. The siRNAs were transfected at a final concentration of 5 nM.

To synchronize cells in G1/S, cells were treated with 2 mM thymidine for 16–18 hr. For immunofluorescence staining of cells in telophase, cells were treated with 2 mM thymidine for 16–18 hr and released into fresh medium containing 300 nM nocodazole (Sigma) for 12 hr to block cells at mitosis. Cells were then washed with PBS for three times and released to fresh medium for 4 hr. To inhibit the kinase activity of Cdc7, cells were treated with XL413 (Tocris Bioscience) at 5 μM for 6 hr.

Antibodies and Immunoblotting

The following antibodies were used for immunoblotting, immunofluorescence and immunoprecipitation: anti-Scc2 (Bethyl Laboratories, A301-779A), anti-Scc4 (Abcam, ab183033), anti-Smc1 (Bethyl Laboratories, A300-055A), anti-Smc3 (Bethyl Laboratories, A300-060A), anti-SA2 (Santa Cruz, Biotechnology, sc-81852), anti-Rad21 (Bethyl Laboratories, A300-080A), anti-Esco2 (Bethyl Laboratories, A301-689A), anti-MCM2 (Bethyl Laboratories, A300-191A), anti-MCM4 (Bethyl Laboratories, A300-193A), anti-MCM5 (Bethyl Laboratories, A300-195A), anti-MCM2 pSer40/41 (Bethyl Laboratories, A300-788A), anti-MCM2 pSer53 (Bethyl Laboratories, A300-756A), anti-Cdc7 (Bethyl Laboratories, A302-504A), anti-WDHD1 (Bethyl Laboratories, A301-141A), anti-Timeless (Bethyl Laboratories, A300-961A), anti-Tipin (Bethyl Laboratories, A301-474A), anti-DDX11 (Santa Cruz Biotechnology, sc-68855), anti-Cdc45 (Santa Cruz Biotechnology, sc-55569; Cell Signaling, D7G6), anti-GINS1 (Bethyl Laboratories, A304-170A), anti-RPA2 (Millipore, MABE285; Bethyl Laboratories, A300-244A), anti-Orc2 (Bethyl Laboratories, A302-734A), anti-CHAF1A (Bethyl Laboratories, A301-481A), anti-Ligase1 (Abcam, ab615), anti-Fen1 (Bethyl Laboratories, A300-255A), anti-Myc (Roche, 11667203001), anti-α-tubulin (Sigma, T9026; Bio-Rad, MCA77G), anti-Histone H3 (Abcam, ab1791). Anti-Smc3 K105Ac antibody was gift from Prasad Jallepalli (Memorial Sloan Kettering Cancer Center). The anti-Wapl and anti-Sororin antibody was generated against human $Wapl_{601–1190}$ and human $Sororin_{91–252}$ respectively, as previously described.

For immunoblotting, cells were lysed in the SDS sample buffer (pH 6.8), sonicated, and boiled. The lysates were separated by SDS-PAGE and blotted with the desired primary antibodies. The primary antibodies were used at a final concentration of 1 μg/ml. Anti-mouse

IgG (H+L) (Dylight 680 conjugates) and anti-rabbit IgG (H+L) (Dylight 800 conjugates) (Cell Signaling) were used as secondary antibodies. The blots were scanned with an Odyssey Infrared Imaging System (LI-COR) according to the manufacturer's protocols.

Immunoprecipitation

For immunoprecipitation, the anti-MCM2, anti-Scc2 or anti-Sororin antibodies were coupled to the Affi-Prep Protein A beads (Bio-Rad) at a concentration of 1 mg/ml. Cells were lysed with the lysis buffer containing 25 mM Tris-HCl (pH 7.7), 50 mM NaCl, 0.1% (v/v) Nonidet P-40, 2 mM $MgCl_2$, 10% (v/v) glycerol, 5 mM NaF, 0.3 mM Na_3VO_4, 10 mM β-glycerophosphate, 1 mM DTT, complete EDTA-free protease inhibitor cocktail (Roche) and 50 units/ml Turbo Nuclease (Accelagen). After a 1-h incubation on ice and a 10-min incubation at 37˚C, all lysates were centrifuged at 4˚C at 20,817 g for 20 min. The supernatants were incubated with the desired antibody beads for 3 hr at 4˚C. The beads were then washed three times with the lysis buffer. Proteins bound to beads were dissolved in SDS sample buffer, separated by SDS-PAGE, and blotted with the appropriate antibodies.

Immunofluorescence

HeLa Tet-On cells were cultured and treated in the Nunc™ Lab-Tek™ II CC2™ Chamber Slides. Cells on the slides were first permeabilized with the PHEM buffer (25 mM HEPES pH 7.5, 10 mM EGTA pH 8.0, 60 mM PIPES pH 7.0, 2 mM $MgCl_2$) containing 0.5% Triton X-100 for 5 min and then fixed in 2% paraformaldehyde for 15 min. Fixed cells were blocked in PBS containing 2% BSA for 30 min and then incubated with desired antibodies in PBS containing 3%

BSA and 0.1% Triton X-100 at 4˚C overnight. Cells were then washed three times with PBST for 5 min each time, and incubated with fluorescent secondary antibodies (Molecular Probes) in PBS containing 3% BSA and 0.1% Triton X-100 for 1 hr at room temperature. Cells were again washed three times with PBST and stained with 1 μg/ml DAPI in PBS for 5 min. After the final wash with PBS, the slides were mounted with VECTASHIELD antifade mounting medium (Vector Laboratories), sealed with nail polish, and viewed with a 100X objective on a DeltaVision fluorescence microscope (GE Healthcare). Image processing and quantification were performed with Image J.

Chromatin Fractionation

Cells were harvested by trypsinization and washed once with PBS. Cells were then resuspended with ice-cold fractionation buffer containing 25 mM Tris-HCl pH 7.7, 50 mM NaCl, 0.1% (v/v) Nonidet P-40, 2 mM $MgCl_2$, 10% (v/v) glycerol, 5 mM NaF, 0.3 mM Na_3VO_4, 10 mM β-glycerophosphate, 1 mM DTT, complete EDTA-free protease inhibitor cocktail (Roche) and 5 mM sodium butyrate. The cell suspension was passed through a 27G X 1/2 in (0.4 X 13 mm) needle 7-10 times, and incubated on ice for 10 min. Cell lysates were then centrifuged at 4˚C at 3,000 g for 5 min. The pellet was gently resuspended and washed with the fractionation buffer for three times. The chromatin fractions were then lysed in SDS sample buffer, sonicated, boiled, separated by SDS-PAGE, and blotted with the desired primary antibodies.

Fluorescence In Situ Hybridization (FISH)

The BAC clone RP11-466L19 was purchased from Empire Genomics. FISH probes were labeled with 5-Fluorescein dUTP (Enzo Life Sciences) using the Nick Translation Kit (Abbott Molecular). Probes were precipitated with human cot-1 DNA (Invitrogen) and salmon sperm DNA (Invitrogen), and then resuspended in the hybridization solution (Cytocell). HeLa Tet-on cells were transfected with siRNAs, synchronized with 2 mM thymidine for 16-18 hr and then released to fresh medium for 4 hr. Cells were harvested by trypsinization, treated with 75 mM KCl hypotonic solution for 25 min at 37 ˚C, and then fixed with ice-cold methanol and acetic acid (ratio 3:1). Fixed cells were dropped onto pre-warmed slides, in situ hybridized at 80˚C with DNA probes and incubated at 37 ˚C overnight. Slides were sequentially washed with 0.1% SDS in 0.5 X SSC at 70 ˚C for 5 min, 1 X PBS at room temperature for 10 min and 0.1% Tween 20 in 1 X PBS at room temperature for 10 min. Slides were then mounted with ProLong Gold (Life Technologies) and viewed with a 100X objective on a DeltaVision fluorescence microscope (GE Healthcare). Image processing and quantification were performed with ImageJ.

Chromatin Immunoprecipitation (ChIP) followed by Next-Generation Sequencing (NGS)

HeLa Tet-On cells were synchronized with 2 mM thymidine for 16–18 hr. Cells at full confluency from two 100 mm dishes were collected for each ChIP experiment. Cells in the plate were chemically cross-linked by the addition of 1% of formaldehyde for 10 min followed with 125 mM glycine for 5 min at room temperature with shaking. Cells were then rinsed twice with ice-cold PBS and scraped from plate into PBS containing 2 X protease inhibitor. Cells were centrifuged at 4˚C at 500 g for 5 min and washed one more time with PBS. Cells were lysed in sonication buffer containing 10 mM Tris-HCl pH 7.4, 1 mM EDTA pH 8.0, 0.1% SDS, 1%

Triton X-100, 0.1% Sodium deoxycholate, 0.25% Sarkosyl, 1 mM DTT, protease inhibitor cocktail (Roche) and sonicated on ice to solubilize and shear cross-linked DNA to 300-500 bp. The resulting whole cell extract was centrifuged at 4˚C at 13,000 rpm for 10 min and the supernatant was transfer to a new tube and incubated with the appropriate antibody at 4˚C overnight. Each sample was then incubated with pre-washed Dynabeads Protein A or G (Invitrogen) magnetic beads at 4˚C for 3 hr. Beads were washed twice with sonication buffer, twice with sonication buffer containing 0.3 M NaCl, twice with LiCl buffer (10 mM Tris-HCl pH 8.1, 1 mM EDTA pH 8.0, 250 mM LiCl, 0.5% (v/v) Nonidet P-40, 0.5% Sodium deoxycholate), and twice with TE buffer (10 mM Tris-HCl pH 7.5, 1 mM EDTA pH 8.0). Bound complexes were eluted from the beads and crosslinking was reversed by overnight incubation at 65˚C in SDS elution buffer (50 mM Tris-HCl pH 8.1, 1 mM EDTA pH 8.0, 1% SDS). Immunoprecipitated DNA was treated with RNase A (Qiagen) and Proteinase K (New England Biolabs), then purified using Qiagen PCR purification Kit according to the manufacturer's protocols.

For Rad21 and Scc2 occupied genomic regions, anti-Rad21-ChIP Grade (Abcam, ab992) and anti-Scc2 (Bethyl Laboratories, A301-779A) were used for ChIP-seq experiments, respectively.

For ChIP-seq analysis, single-end reads of 75 bp were generated. After mapping reads to human genome (hg19) by bowtie2 (v2.2.3) (Langmead and Salzberg, 2012) with parameter "--sensitive", we perform filtering by first removing alignments with mapping quality less than 10, and then removing duplicate reads identified by Picard MarkDuplicates (v1.127) (http://broadinstitute.github.io/picard). The enriched regions (peaks) were identified using

MACS2 (v2.0.10) (Zhang et al., 2008b), with a q-value cut-off of 0.05 for broad peaks. Peak regions were annotated by HOMER (Ross-Innes et al., 2012). Co-localization plots were made using deepTools (v1.6) (Ramirez et al., 2016).

Propidium Iodine Staining and Flow Cytometry

Cells were harvested with trypsinization and fixed in 70% ice-cold ethanol overnight. After being washed with PBS once, cells were resuspended in PBS containing 0.1% Triton X-100, 20 μg/ml propidium iodide (Sigma) and 200 μg/ml RNase A (Qiagen), and incubated at room temperature for 1 hr. The samples were analyzed on a FACSCalibur flow cytometer (BD Biosciences). Data were processed with the FlowJo software.

RESULTS

Cohesin Loading Is Dependent on MCM2-7 during Early S Phase

Previous studies have reported that recruitment of cohesin and the Scc2/4 cohesin loader complex requires the pre-replication complex containing the MCM2-7 proteins at origins of replication in *Xenopus* egg extracts (Gillespie and Hirano, 2004; Takahashi et al., 2008; Takahashi et al., 2004). Conflicting data suggest that MCM and cohesin are loaded independently on chromatin, although the MCM-cohesin interaction could be detected in mammalian cells (Guillou et al., 2010). To obtain insights into the role of MCM2-7 in cohesin loading during replication, we examined the chromatin-bound cohesin after RNAi-mediated silencing of MCM in human cells.

We used HeLa Tet-On cells stably expressing Scc1-Myc. Scc1-Myc is functional, as it could rescue cohesion defects caused by depletion of the endogenous Scc1. When cells were synchronized at G1/S, the intensity of Scc1-Myc on chromatin was greatly impaired when MCM2 or Scc2 was depleted (Figure 5-1A, 1B and 1C). The Scc1-Myc signal on chromatin could be restored when RNAi-resistant MCM2 was ectopically expressed (Figure 5-2A). Moreover, Scc1-Myc intensity in G1/S cells was reduced when other subunits of MCM2-7 were silenced (Figure 5-2B), suggesting that the entire MCM2-7 complex is required for cohesin loading during early S phase. However, MCM2-7 was not strictly required for cohesin loading in telophase cells (Figure 5-1D and 1E). Similarly, MCM depletion also reduces the association of endogenous SA2 with chromatin in thymidine-treated G1/S cells (Figure 5-2C), but only slightly reduced chromatin-bound SA2 in telophase cells (Figure 5-2D). MCM2 overexpression elevated

the Scc1-Myc intensity on chromatin to a level higher than that in control cells. To rule out the possibility that ectopic MCM2 alone promotes cohesin loading, we examined the level of MCM5 on chromatin when MCM2 was overexpressed. MCM2 overexpression also elevated MCM5 levels on chromatin (Figure 5-2E and 2F). Thus, MCM2 overexpression likely increases the amount of the MCM2-7 complex on chromatin, resulting in hyperactive cohesin loading.

Cohesin is reported to be loaded onto chromatin by a mechanism that depends on Scc2/4. To understand why MCM2-7 is required for cohesin loading during early S phase, we next checked the interactions among MCM2-7, cohesin and Scc2/4 at different phases during the cell cycle. MCM2 associated with Scc2/4 and cohesin in G1/S cells, and this interaction was not observed in G2 or mitotic cells (Figure 5-1F). To narrow down the time window of this MCM-Scc2/4-cohesin interaction, we collected cells that were released from thymidine at different time points and again performed MCM2 immunoprecipitation. The MCM-Scc2/4-cohesin interaction reached peak levels when cells were in early S phase (Figure 5-1G and 1H). Importantly, all the lysates for immunoprecipitation were treated with Turbo nuclease. Thus, the observed MCM-Scc2/4-cohesin interaction is unlikely to be bridged by chromatin. Therefore, our results showed that the MCM complex is required for cohesin loading during early S phase, and MCM2-7, Scc2/4 and cohesin form a DNA-independent mega-complex at this stage.

DDK Is Required for Cohesin Loading and MCM-Scc2/4-Cohesin Interaction

DDK has been shown to be essential for chromatin association of Scc2/4 in *Xenopus* egg extracts (Takahashi et al., 2008). We examined whether DDK is required for cohesin association with chromatin and MCM-Scc2/4-cohesin interaction in human cells during early S phase.

Consistent with the findings in *Xenopus*, cohesin loading onto chromosomes was greatly reduced when Cdc7, the kinase subunit of DDK was depleted in G1/S cells (Figure 5-3A, 3B and Figure 5-4B). However, chromatin-bound cohesin was only slightly affected by Cdc7 depletion in telophase cells (Figure 5-4C and 4D). Immunoprecipitation of MCM2 or Scc2 showed that inactivation of Cdc7 disrupted MCM binding to cohesin and Scc2/4 complex in G1/S cells (Figure 5-3C and Figure 5-4A).

Next, we tested whether MCM binding to Scc2/4 is independent of cohesin or vice versa. In MCM2 immunoprecipitates, depletion of Scc2/4 prevented the association of MCM to cohesin. When cohesin was depleted from cells, Scc2/4 was unstable and no longer bound to MCM (Figure 5-3D). To obtain insights into the genome-wide distribution of MCM, Scc2/4 and cohesin, we performed chromatin immunoprecipitation followed by next generation sequencing (ChIP-seq). Mcm2 ChIP-seq signals were broadly distributed throughout the genome as previously reported (data not shown). Interestingly, Scc1 peaks were found to overlap with the majority of the Scc2 peaks (Figure 5-3E and 3F). Overall, these results suggest that DDK is required for the MCM-Scc2/4-cohesin interaction during early S phase. In the MCM-Scc2/4-cohesin mega-complex, Scc2/4 binding and cohesin binding to MCM are mutually dependent.

Phosphorylation of MCM2-7 by DDK Is Critical for Cohesin Loading and the Integrity of the MCM-Scc2/4-Cohesin Complex

DDK is known to directly phosphorylate the MCM2-7 complex and promote the loading of replication initiation factors (Francis et al., 2009; Heller et al., 2011). The kinase subunit Cdc7 requires a regulatory subunit, either DBF4 or DRF1, to activate its kinase activity (Hughes et al.,

2012; Yoshizawa-Sugata et al., 2005). In the MCM2 immunoprecipitation experiment, the stability of Cdc7 is affected, and the phosphorylation of MCM2 is reduced when DBF4 or DRF1 is depleted in cells (Figure 5-5A). Notably, phosphorylated MCM2 migrates faster than the unphosphorylated form on the SDS-PAGE gel. Single depletion of DBF4 or DRF1 partially reduced the phosphorylation of MCM2 and the MCM-Scc2/4-cohesin interaction, while double depletion abolished the phosphorylation of MCM2 and MCM binding to Scc2/4 or cohesin (Figure 5-5A). Intriguingly, we also noticed that, in the previous Scc2 immunoprecipitation experiment, Scc2 only pulled down the phosphorylated MCM2, but not the unphosphorylated form (Figure 5-4A). Therefore, our results suggest that phosphorylation of MCM by DDK is required for cohesin loading and for the MCM-Scc2/4-cohesin interaction.

To further test this hypothesis, we checked cohesin loading in cells treated with the Cdc7 kinase inhibitor XL413 during early S phase. XL413 treatment effectively blocked the phosphorylation of MCM2 (Figure 5-6A), but did not affect the stability of Cdc7. Chromatin-bound cohesin was greatly reduced in XL413-treated G1/S cells (Figure 5-5B, 5C and Figure 5-6B, 6C, 6D). However, in telophase cells, cohesin loading was not significantly decreased by XL413 (Figure 5-5D and 5E). Next, we examined whether inactivation of the DDK kinase activity affected the MCM-Scc2/4-cohesin interaction. In the MCM2 immunoprecipitates, the interaction between MCM and Scc2/4 in cells treated with XL413 was reduced to an extent similar to that in cells depleted of Cdc7 (Figure 5-6E). The interaction between MCM and Cdc7 remained intact in XL413-treated cells. Additionally, the reduction of binding between MCM and cohesin in XL413-treated cells was not as dramatic as that in Cdc7-depleted cells, indicating that DDK might have a scaffolding role in promoting the MCM-cohesin interaction.

Altogether, our data strongly suggest that phosphorylation of MCM by DDK is required for cohesin loading and for stable MCM-Scc2/4-cohesin interaction during early S phase.

Cdc45 and GINS Are Not Required for MCM-Dependent Cohesin Loading

For replication initiation, the MCM2-7 double hexamer recruits Cdc45 and GINS to form the active CMG helicase complex. Cdc45 and GINS are required for the MCM helicase activity, the initiation of DNA replication, and the progression of the replication fork (Aparicio et al., 2009; Costa et al., 2011; Ilves et al., 2010). We tested whether helicase activation and replication initiation affected the integrity of the MCM-Scc2/4-cohesin complex and MCM-dependent cohesin loading. We examined the MCM-Scc2/4-cohesin interaction and chromatin-bound cohesin in cells depleted of Cdc45 or GINS during early S phase. In MCM2 immunoprecipitates, MCM binding to Scc2/4 or cohesin was not reduced in Cdc45- or GINS1-depleted cells (Figure 5-7A). Chromatin-bound cohesin was also not decreased in cells depleted of Cdc45 or GINS1 (Figure 5-7B and 7C). These data suggest that Cdc45 and GINS are not required for MCM-Scc2/4-cohesin interaction and cohesin loading. Because the MCM-Scc2/4-cohesin interaction peaks in S phase cells released from thymidine and initiated replication, helicase activation and replication initiation likely do not block this interaction. Thus, the formation of MCM-Scc2/4-cohesin complex is independent of helicase activation and replication initiation (Figure 5-7D).

Replisome Components Contribute to Sister-Chromatid Cohesion

Next, we tested whether this MCM-Scc2/4-cohesin interaction indeed persists at active replication forks and whether this MCM-mediated cohesin loading is required for cohesion

establishment during DNA replication. Once replication is initiated, a large number of replication proteins are recruited to the replication forks. Obviously, depletion of replication-related proteins causes replication defects, which leads to DNA damage and G2 arrest. Therefore, it is difficult to enrich cells in mitosis and examine sister-chromatid cohesion with metaphase spreads.

To examine cohesion in interphase, we developed a FISH probe that specifically recognizes a locus on chromosome 3. After depletion of individual replisome component, we collected cells that were release from thymidine for 4 hr and measured the distance between paired FISH dots in S phase cells. Sororin is known to stabilize sister-chromatid cohesion by antagonizing the cohesin inhibitor Wapl. Indeed, Sororin inactivation gave rise to strong cohesion defects, as evidenced by the greatly increased distances between the paired FISH signals in our FISH assay. Based on this FISH assay, several replisome components were also required for cohesion establishment (Figure 5-8A and 8B). Specifically, MCM2 depletion showed cohesion defect. Depletion of WDHD1, Timeless, Tipin or DDX11 at active replication forks produced mild cohesion defect. Strikingly, co-depletion of WDHD1 and Timeless produced strong cohesion defects. Consistently, the interaction between Sororin and cohesin was dramatically reduced in cells co-depleted of WDHD1 and Timeless, but was only modestly reduced with each single depletion (Figure 5-9A). To rule out siRNA off-target effects, we tried to rescue the cohesion defects by introducing RNAi-resistant WDHD1 or Timeless into cells with WDHD1 and Timeless co-depletion. Gratifyingly, expression of either WDHD1 or Timeless partially rescued the cohesion defect in cells co-depleted of WDHD1 and Timeless (Figure 5-8C and 8D). Unexpectedly, Wapl inactivation also rescued the cohesion defects caused by WDHD1 and

Timeless co-depletion (Figure 5-8D and 8E), which is different from the situation in yeast (Borges et al., 2013).

Ctf4 in yeast has been reported to form an interaction hub that links DNA replication with sister-chromatid cohesion establishment. The interaction between Ctf4 and cohesin is mediated by DDX11 during S phase in yeast (Samora et al., 2016). Our data showed that depletion of Timeless synergized with DDX11 depletion to produce cohesion defects. Interestingly, depletion of WDHD1 did not synergize with DDX11 depletion, suggesting that DDX11 might play a role downstream of WDHD1 in human cells to contribute to sister-chromatid cohesion establishment.

We did not observe strong cohesion defects with Scc2 depletion, even though chromatin-bound cohesin was greatly reduced when Scc2 was silenced during early S phase. Similarly, Cdc7, DBF4, DRF1, Cdc45 or GINS1 did not produce strong cohesion defects. In fact, we noticed that in our FISH assay, many cells only had two single FISH dots in cells depleted of Scc2, Cdc7, DBF4, DRF1, Cdc45 or GINS1, suggesting that this locus was not replicated properly (Figure 5-9B). Moreover, we discovered that cells can replicate their DNA and progress through S phase slowly during prolonged thymidine treatment. However, this slow DNA replication was blocked when Scc2, Cdc7, DBF4, DRF1, Cdc45 or GINS1 was depleted (Figure 5-9C). Thus, Scc2 is required for proper DNA replication, and this might explain why cohesion defect is not strong in Scc2-depleted cells.

Cohesion Establishment Occurs Before Lagging Strand Maturation and Histone Deposition

We next tested whether all replication factors are involved in cohesion establishment. During DNA replication, Fen1 removes 5' overhanging flaps and processes the 5' ends of Okazaki fragments in lagging strand DNA synthesis. DNA Ligase1 is responsible for joining Okazaki fragments formed during discontinuous DNA synthesis on the lagging strand. Chromatin is reassembled by recycling of modified parental histones and deposition of new ones onto daughter strands. CHAF1A is the core component of the CHAF1 complex that mediates chromatin assembly during DNA replication. We examined the cohesion status in S phase cells depleted of Fen1, Ligase1 or CHAF1A (Figure 5-9D, 9E and 9F). Interestingly, we did not observe cohesion defects when these factors that regulate the Okazaki fragment maturation or histone deposition were depleted (Figure 5-8F). Thus, not all replication factors are required for interphase cohesion in human cells. Our results further suggest that cohesion establishment occurs before the processing and ligation of Okazaki fragment and histone deposition (Figure 5-8G).

Replisome Components Are Required for Cohesin Loading and Stable MCM-Scc2/4-Cohesin Interaction

Because depletion of several replisome components resulted in cohesion defects, we next examined whether cohesin loading and the integrity of the MCM-Scc2/4-cohesin complex were impaired under these conditions. Indeed, MCM2 binding to Scc2/4 or cohesin was reduced when WDHD1 or Timeless was depleted in G1/S cells that were synchronized with thymidine (Figure 5-10A and Figure 5-11A). The binding was further reduced with double depletion (Figure 5-10A). Similarly, DDX11 depletion led to reduced binding of MCM to Scc2/4 and cohesin

(Figure 5-10B). Consistently, WDHD1 depletion or Timeless depletion also had an impact on cohesin loading (Figure 5-10C and 10D) in thymidine-synchronized cells.

Replisome components are sequentially recruited to the replication forks during DNA replication. We showed that some components are required for the proper MCM-Scc2/4-cohesin interaction, such as Cdc7, WDHD1 and Timeless. However, some are dispensable for the interaction, such as Cdc45 and GINS. To better understand the hierarchy of different replisome components in regulating the MCM-Scc2/4-cohesin interaction, we performed the MCM2 immunoprecipitation experiment after simultaneously depleting two different replisome components. Previous publications have shown that phosphorylation of MCM by Cdc7 is a prerequisite of replication initiation and Cdc45 recruitment during DNA replication. We found that co-depletion of Cdc7 and Cdc45 had similar effects as the Cdc7 single depletion did (Figure 5-11B). In addition, Cdc45 depletion reversed the binding defect caused by Timeless depletion. Thus, Cdc7 is required for the recruitment of cohesin and Scc2 to the pre-RC whereas Timeless is only required for cohesin and Scc2 recruitment at the active CMG helicase.

RPA at Active Replication Forks Is Essential for Cohesion Establishment

WDHD1 and Timeless are thought to be recruited to the active replication forks. We isolated the chromatin fraction from cells at different stages during the cell cycle. Our data showed that WDHD1 and Timeless were enriched on chromatin during S phase (Figure 5-11C, 11D and 11E). However, it has been shown that Timeless can interact with MCM2-7 prior to DNA replication to suppress chromatin accumulation of aberrant CMG complexes (Xu et al.,

2016). We tested the role of the RPA complex, which is only recruited to the active replication forks and stabilizes single-stranded DNA (ssDNA) during DNA replication.

Depletion of RPA2 abolished MCM2 binding to Scc2/4 and cohesin in thymidine-treated cells (Figure 5-12A). The MCM-Scc2/4-cohesin interaction was restored in cells co-depleted of Cdc45 and RPA2 (Figure 5-13A). Consistent with the immunoprecipitation result, cohesin level on chromatin was significantly reduced in RPA2-depleted cells (Figure 5-12B, 12C and Figure 5-13B). Next, we examined whether RPA plays a role in cohesion establishment by the FISH assay. Indeed, RPA2-depleted cells displayed strong cohesion defect (Figure 5-12D and 12E). We could partially rescue the cohesion defects in RPA2-depleted cells by overexpressing RNAi-resistant RPA2 (Figure 5-13C and 13D). Taken together, we conclude that RPA is required for cohesin loading, stable MCM-Scc2/4-cohesin interaction and cohesion establishment. This finding strongly suggests that the simultaneous recruitment of Scc2/4 and cohesin to the active replication forks is critical for sister-chromatid cohesion establishment during DNA replication.

Notably, RPA2 depletion weakened Cdc7 binding to MCM in the MCM2 immunoprecipitation experiment (Figure 5-12A). We suspect that RPA as well as other fork stabilizing factors might maintain the MCM-Scc2/4-cohesin interaction indirectly through affecting DDK function. We then examined the phosphorylation status of MCM2 in thymidine-treated cells. Our data showed that RPA2 depletion only slightly reduced the phosphorylation of MCM2 (Figure 5-13E). With these results, we propose that the initial recruitment of Scc2/4 and cohesin to the MCM complex requires DDK phosphorylation on MCM. The MCM-Scc2/4-cohesin interaction is further maintained at active replication forks, with the help of a group of replisome components including RPA. The additional requirement of these stabilizing factors at

active replication forks to maintain proper MCM-Scc2/4-cohesin interaction suggests that MCM might interact with Scc2/4 and cohesin in a different mode that potentially allows for the release of cohesin from the complex and the deposition of cohesin behind the replication forks.

DISCUSSION

MCM-Dependent Cohesin Loading

Taking advantage of the thymidine treatment, we were able to detect MCM-dependent cohesin loading onto chromatin during early S phase. The effect of MCM in cohesin loading is not that obvious in telophase cells. This might explain why chromatin-bound cohesin is not reduced after MCM silencing in asynchronous cells, as the majority of such cells are in G1 (Guillou et al., 2010).

To analyze the chromatin-bound cohesin, we performed both Scc1-Myc staining in the Scc1-Myc expressing cells and endogenous SA2 staining in HeLa cells. Our previous work has shown that this RNAi-resistant Scc1-Myc could rescue the cohesion defect caused by Scc1 depletion and the expression level of this Scc1-Myc is lower that of the endogenous Scc1 (Wu et al., 2012). In our experiments, the residual Scc1-Myc intensities are comparable when SA2, Scc2 or MCM2 is depleted in G1/S cells stably expressing Scc1-Myc. However, it is intriguing that the reduction of endogenous SA2 is less complete in Scc2- or Scc1-depleted cells. It is possible that SA2 is capable of binding to chromatin independent of the cohesin complex, which might be interesting to probe in the future.

A Conserved Cohesin Loading Mechanism in Metazoans

In *Drosophila,* genome-wide chromatin immunoprecipitation experiments have revealed a high concordance between sites of ORC and cohesin binding onto chromosomes, suggesting that ORC might be required for recruiting cohesin to DNA replication origins (MacAlpine et al.,

2010). In *Xenopus* egg extract, several studies have shown that recruitment of Scc2/4 and cohesin to chromatin depends on pre-RCs (Gillespie and Hirano, 2004; Takahashi et al., 2008; Takahashi et al., 2004). In addition, Scc2/4 has been reported to exist in a stable complex with DDK, and the kinase activity of DDK is required to tether Scc2/4 and cohesin to pre-RCs (Takahashi et al., 2008). Unlike in *Drosophila* and *Xenopus*, the association of cohesin with chromatin in yeast is not affected when pre-RC assembly is inhibited by Cdc6 depletion (Uhlmann and Nasmyth, 1998). DNA replication takes place normally in Scc2 and Scc4 mutants in yeast (Ciosk et al., 2000). Here, our studies demonstrate that cohesin association with chromatin in human cells requires the MCM complex, which is the core component in pre-RCs as well as in active replisomes. The MCM-Scc2/4-cohesin interaction is dependent on the kinase activity of DDK as has been reported in *Xenopus*. Thus, this replication-coupled cohesin loading is a conserved mechanism in metazoans.

A Second Wave of Cohesin Loading During DNA Replication

Although the diameter of the cohesin ring is 30-40 nm when fully open, a recent single-molecule study has reported that the functional pore of cohesin cannot be larger than about 19 nm when cohesin is bound to chromatin (Stigler et al., 2016). The DNA replication machinery is a macromolecular protein complex composed of numerous proteins. It is very unlikely that the replication fork can pass through the interior of the closed cohesin ring that already loaded on the un-replicated chromosomes. Therefore, we propose that cohesin is displaced when it encounters replication fork on chromosomes, and a second round of cohesin loading behind the replication fork enables the sister-chromatid cohesion establishment during DNA replication.

Biochemical studies have shown that the Scc2/4 complex and the Wapl/Pds5 complex can open the cohesin ring at the Smc3-Scc1 interface and promote the topological DNA loading/unloading of the cohesin complex (Murayama and Uhlmann, 2014, 2015). We failed to detect Wapl/Pds5 in the MCM2 immunoprecipitation experiments, but we could observe the MCM-Scc2/4-cohesin interaction in a cell-cycle-dependent manner. In fact, there is an increased association of Scc2/4 with chromatin together with the recruitment of replisome components during S phase (Figure 5-11C, 11D and 11E). Thus, we propose that the cohesin ring is transiently opened by the Scc2/4 loader complex at the replication fork and then loaded behind the replication fork. Depletion of Scc2/4 did not cause massive cohesion defects, which might be due to the fact that replication initiation and progression were impaired in Scc2/4-depleted cells, as we discussed previously. We have shown extensively that the integrity of the MCM-Scc2/4-cohesin complex is critical for cohesion establishment during DNA replication. Scc2/4 and cohesin are mutually dependent on each other in their association with the MCM complex. In yeast, it has been suggested that the Scc2/4 loader complex is dispensable for cohesion in S phase (Lengronne et al., 2006). Our results suggest that the Scc2/4 loader complex plays an important role in cohesion establishment during DNA replication in human cells.

RPA in Cohesion Establishment

RPA is known to stabilize single-stranded DNA (ssDNA) that exists either at replication forks or at DNA damage sites. Previous studies and our work demonstrate that cohesion establishment is coupled to DNA replication during S phase. After S phase, in the presence of DNA double strand breaks, cohesin can also establish cohesion through a DNA replication-

independent pathway and promote DSB repair through homologous recombination (HR). Under both circumstances, RPA is recruited due to the presence of ssDNA. Here, we report that RPA is required for the stable MCM2-7-Scc2/4-cohesin interaction at active replication forks and establishment of sister-chromatid cohesion. Instead of MCM2-7 in DNA replication, the MCM8-9 hetero-hexamer complex has been reported to play important roles in HR-mediated repair of DSBs. It has been shown recently that MCM8-9 is required for DNA resection by the MRN (MRE11-RAD50-NBS1) complex at DSBs to generate ssDNA and facilitate RPA binding (Lee et al., 2015). Therefore, a similar requirement of RPA for postreplicative cohesion establishment might also exist during DSB repair.

The Timing of Cohesion Establishment

Several replisome components, but not all of them, are required for cohesion establishment during DNA replication. Our data revealed that Okazaki fragment maturation and histone deposition occur after cohesion establishment, suggesting that cohesin is deposited behind the replication fork where there is completely replicated leading strand together with discontinuously replicated lagging strand. Because RPA is required for coating ssDNA as well as cohesion establishment during DNA replication, it makes sense that cohesion is established before ssDNA is fully converted to dsDNA during Okazaki fragment processing and ligation. Intuitively, it is easier to target the nucleosome-free regions of both sister chromatids and promote cohesin loading prior to histone deposition, because the effective pore size of the cohesin ring may not be able to accommodate two 10 nm chromatin fibers.

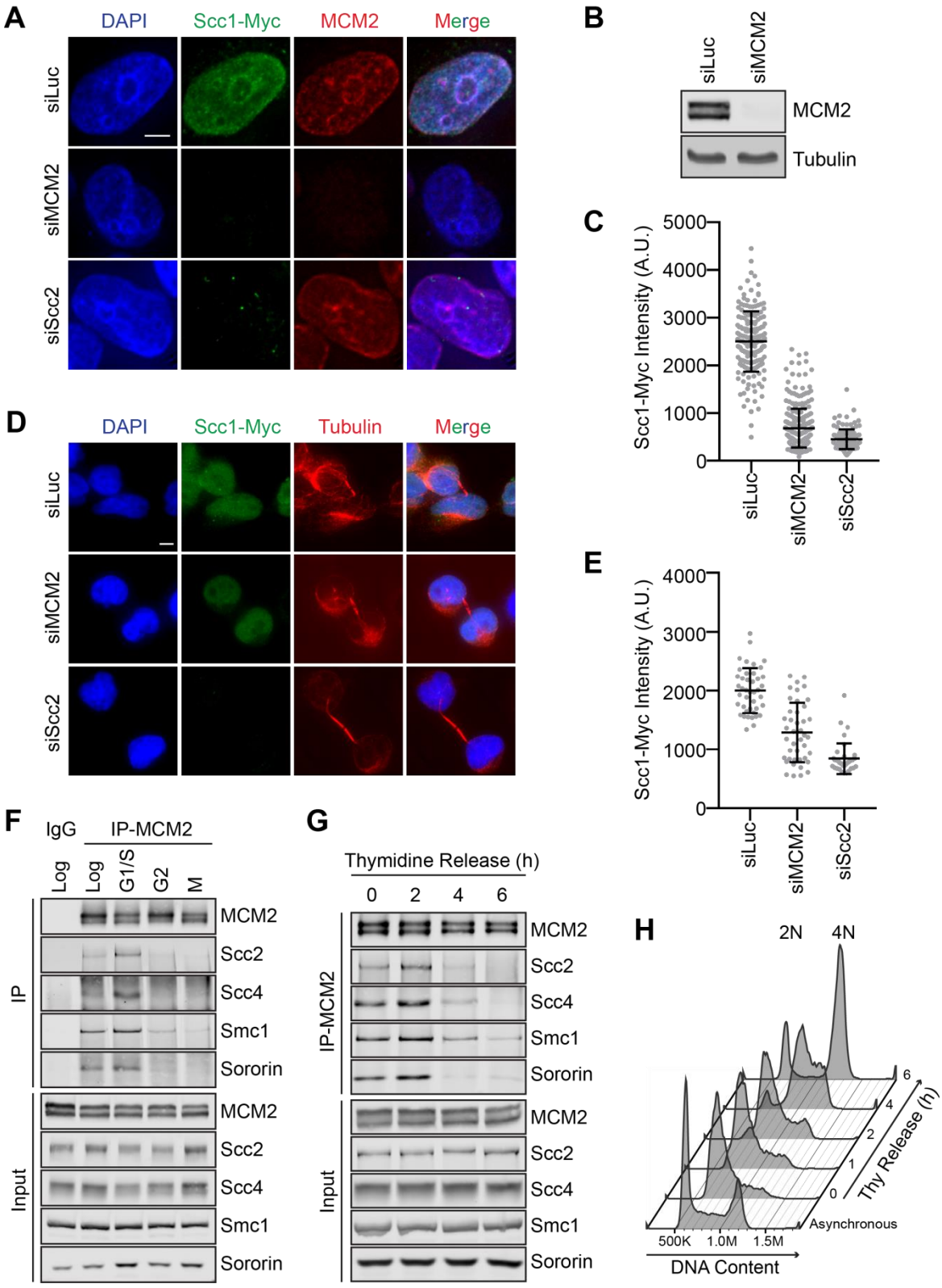
A
DAPI
Scc1-Myc
MCM2
Merge
siLuc
siMCM2
siScc2
B
siLuc
siMCM2
MCM2
Tubulin
C
Scc1-Myc Intensity (A.U.)
5000
4000
3000
2000
1000
0
siLuc
siMCM2
siScc2
D
DAPI
Scc1-Myc
Tubulin
Merge
siLuc
siMCM2
siScc2
E
Scc1-Myc Intensity (A.U.)
4000
3000
2000
1000
0
siLuc
siMCM2
siScc2
F
IgG
IP-MCM2
Log
Log
G1/S
G2
M
IP
Input
MCM2
Scc2
Scc4
Smc1
Sororin
G
Thymidine Release (h)
0
2
4
6
IP-MCM2
Input
MCM2
Scc2
Scc4
Smc1
Sororin
H
2N
4N
6
4
2
1
0
Thy Release (h)
Asynchronous
500K
1.0M
1.5M
DNA Content

Figure 5-1. MCM2-7 is required for cohesin loading during early DNA replication. (**A**) DAPI, anti-Myc, and anti-MCM2 staining of HeLa cells that stably expressing Scc1-Myc. Cells were transfected with the indicated siRNAs and arrested in G1/S with thymidine. Scale bar, 5 μm. (**B**) Lysates of HeLa cells either mock-transfected or transfected with siMCM2 were blotted with the indicated antibodies. (**C**) Quantification of the Scc1-Myc intensities of cells in **A**. Each dot in the graph represents a single cell (siLuc, n=184; siMCM2, n=295; siScc2, n=115). The horizontal bars and error bars indicate the means and standard errors, respectively. (**D**) DAPI, anti-Myc, and anti-tubulin staining of telophase HeLa cells that stably expressing Scc1-Myc. Cells were transfected with the indicated siRNAs and released from Nocodazole for 4 hr before fixation. Scale bar, 5 μm. (**E**) Quantification of the Scc1-Myc intensities of cells in **D**. Each dot in the graph represents a single cell (siLuc, n=42; siMCM2, n=42; siScc2, n=38). The horizontal bars and error bars indicate the means and standard errors, respectively. (**F**) Asynchronous HeLa cells and cells synchronized in G1/S by thymidine, in G2 by Cdk1 inhibitor or in mitosis by Nocodazole were collected and lysed in the presence of nuclease. The total cell lysates (Input) and anti-MCM2 immunoprecipitate were blotted with the indicated antibodies. IgG immunoprecipitate from asynchronous cells was used as a negative control. (**G**) HeLa cells were synchronized with thymidine for 16-18 hr, released from thymidine and harvested at different time points as indicated. Cells were lysed in the presence of nuclease. The total cell lysates (Input) and anti-MCM2 immunoprecipitate were blotted with the indicated antibodies. (**H**) Asynchronous HeLa cells and cells released from thymidine for the indicated time points were harvested and DNA content was analyzed by flow cytometry.

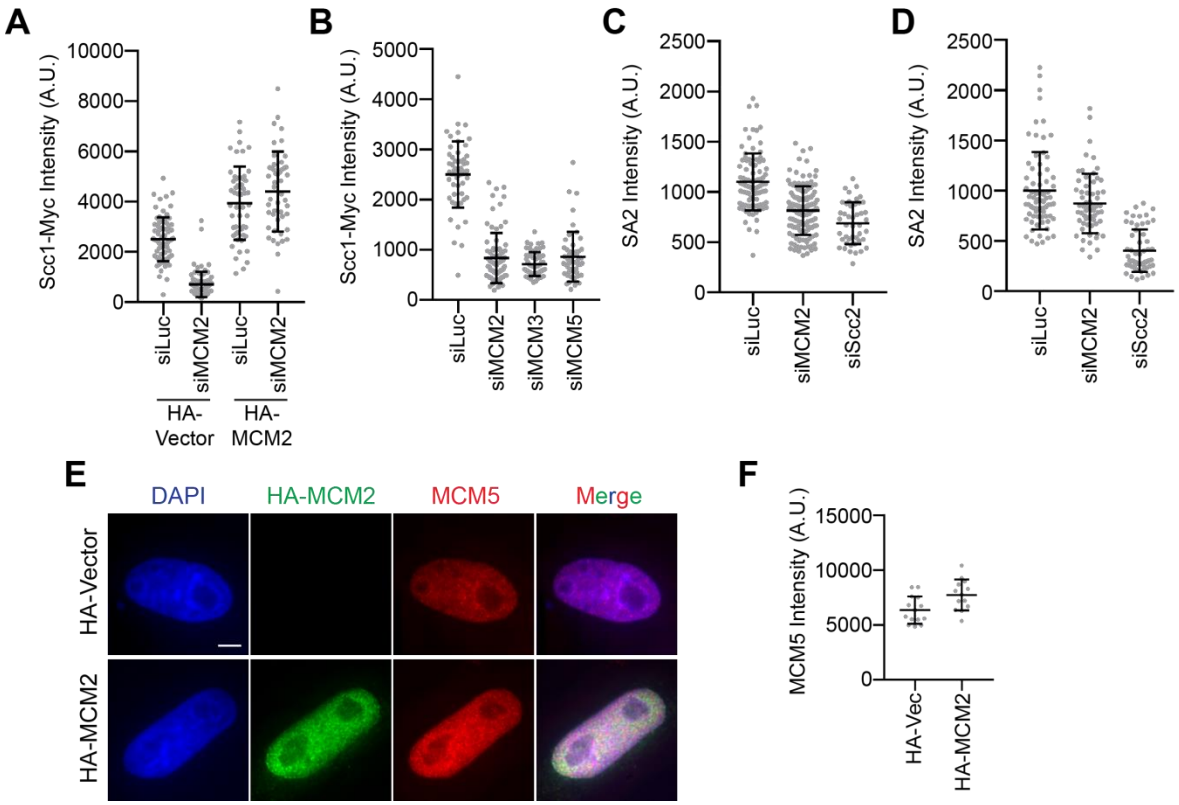

Figure 5-2. The requirement of MCM2-7 in cohesin loading in G1/S cells. (**A**) Quantification of the Scc1-Myc intensities in HeLa cells transfected with the indicated plasmids and siRNAs and synchronized in G1/S with thymidine. Each dot in the graph represents a single cell (HA-Vector+siLuc, n=73; HA-Vector+siMCM2, n=77; HA-MCM2+siLuc, n=52; HA-MCM2+siMCM2, n=48). The horizontal bars and error bars indicate the means and standard errors, respectively. (**B**) Quantification of the Scc1-Myc intensities in HeLa cells transfected with the indicated siRNAs and synchronized in G1/S with thymidine. Each dot in the graph represents a single cell (siLuc, n=55; siMCM2, n=78; siMCM3, n=57; siMCM5, n=51). The horizontal bars and error bars indicate the means and standard errors, respectively. (**C**) Quantification of the SA2 intensities in HeLa cells transfected with the indicated siRNAs and synchronized in G1/S with thymidine. Each dot in the graph represents a single cell (siLuc, n=89; siMCM2, n=130; siScc2, n=45). The horizontal bars and error bars indicate the means and standard errors, respectively. (**D**) Quantification of the SA2 intensities in telophase HeLa cells transfected with the indicated siRNAs. Each dot in the graph represents a single cell (siLuc, n=74; siMCM2, n=61; siScc2, n=58). The horizontal bars and error bars indicate the means and standard errors, respectively. (**E**) DAPI, anti-HA, and anti-MCM5 staining of HeLa cells transfected with the indicated plasmids. Scale bar, 5 μm. (**F**) Quantification of MCM5 intensities of cells in **E**. Each dot in the graph represents a single cell (HA-Vec, n=14; HA-MCM2, n=13). The horizontal bars and error bars indicate the means and standard errors, respectively.

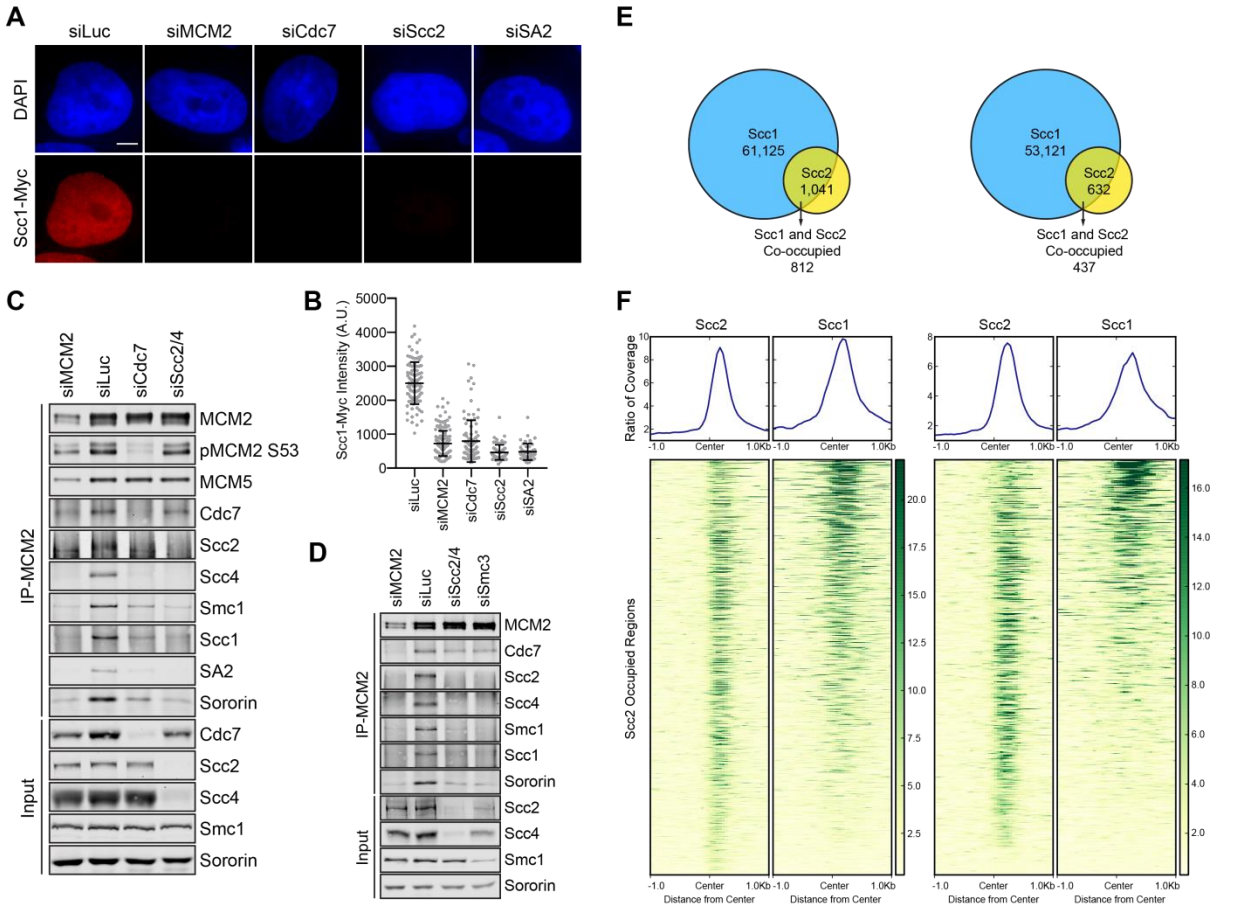

Figure 5-3. The MCM-Scc2/4-cohesin interaction is mediated by DDK. (**A**) DAPI and anti-Myc staining of HeLa cells that stably expressing Scc1-Myc. Cells were transfected with the indicated siRNAs and arrested in G1/S with thymidine. Scale bar, 5 μm. (**B**) Quantification of the Scc1-Myc intensities of cells in **A**. Each dot in the graph represents a single cell (siLuc, n=101; siMCM2, n=141; siCdc7, n=102; siScc2, n=69; siSA2, n=52). The horizontal bars and error bars indicate the means and standard errors, respectively. (**C**) Lysates of HeLa cells transfected with the indicated siRNAs and synchronized in G1/S were treated with nuclease and immunoprecipitated with anti-MCM2. The total lysates (Input) and anti-MCM2 immunoprecipitate were blotted with the indicated antibodies. (**D**) HeLa cells were transfected with the indicated siRNAs, arrested in G1/S with thymidine treatment, and lysed in the presence of nuclease. The total lysates (Input) and anti-MCM2 immunoprecipitate were blotted with the indicated antibodies. (**E**) Venn diagram showing the overlap of cohesin (Scc1) occupied sites with those bound by Scc2 in two experiments. (**F**) Region map showing that at majority of the Scc2 occupied regions, the occupancy of Scc1 is detected reproducibly in two experiment.

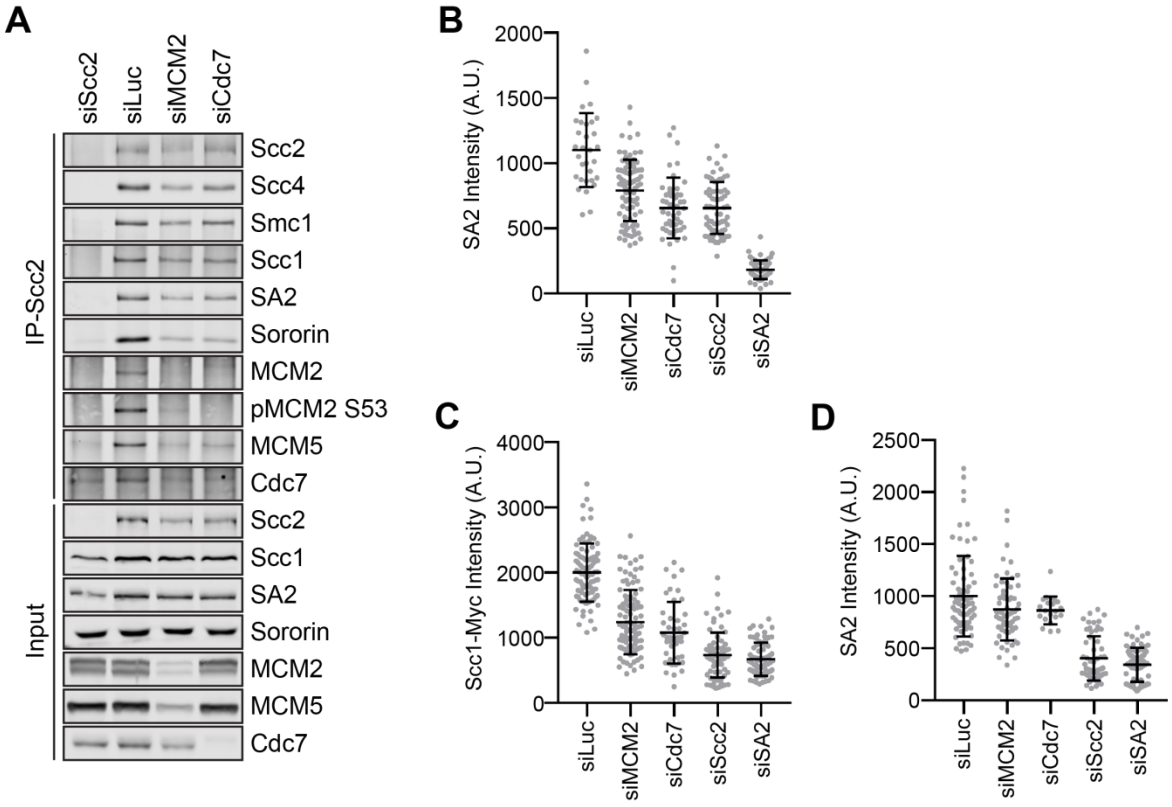

Figure 5-4. The regulation of chromatin-bound cohesin in G1/S and telophase cells. (**A**) Lysates of HeLa cells transfected with the indicated siRNAs and synchronized in G1/S were treated with nuclease and immunoprecipitated with anti-Scc2. The total lysates (Input) and anti-Scc2 immunoprecipitate were blotted with the indicated antibodies. (**B**) Quantification of the SA2 intensities in HeLa cells transfected with the indicated siRNAs and synchronized in G1/S with thymidine. Each dot in the graph represents a single cell (siLuc, n=31; siMCM2, n=84; siCdc7, n=47; siScc2, n=66; siSA2, n=62). The horizontal bars and error bars indicate the means and standard errors, respectively. (**C**) Quantification of the Scc1-Myc intensities in Scc1-Myc expressing telophase cells that transfected with the indicated siRNAs. Each dot in the graph represents a single cell (siLuc, n=90; siMCM2, n=96; siCdc7, n=45; siScc2, n=75; siSA2, n=76). The horizontal bars and error bars indicate the means and standard errors, respectively. (**D**) Quantification of the SA2 intensities in telophase HeLa cells transfected with the indicated siRNAs. Each dot in the graph represents a single cell (siLuc, n=74; siMCM2, n=61; siCdc7, n=20; siScc2, n=58; siSA2, n=69). The horizontal bars and error bars indicate the means and standard errors, respectively.

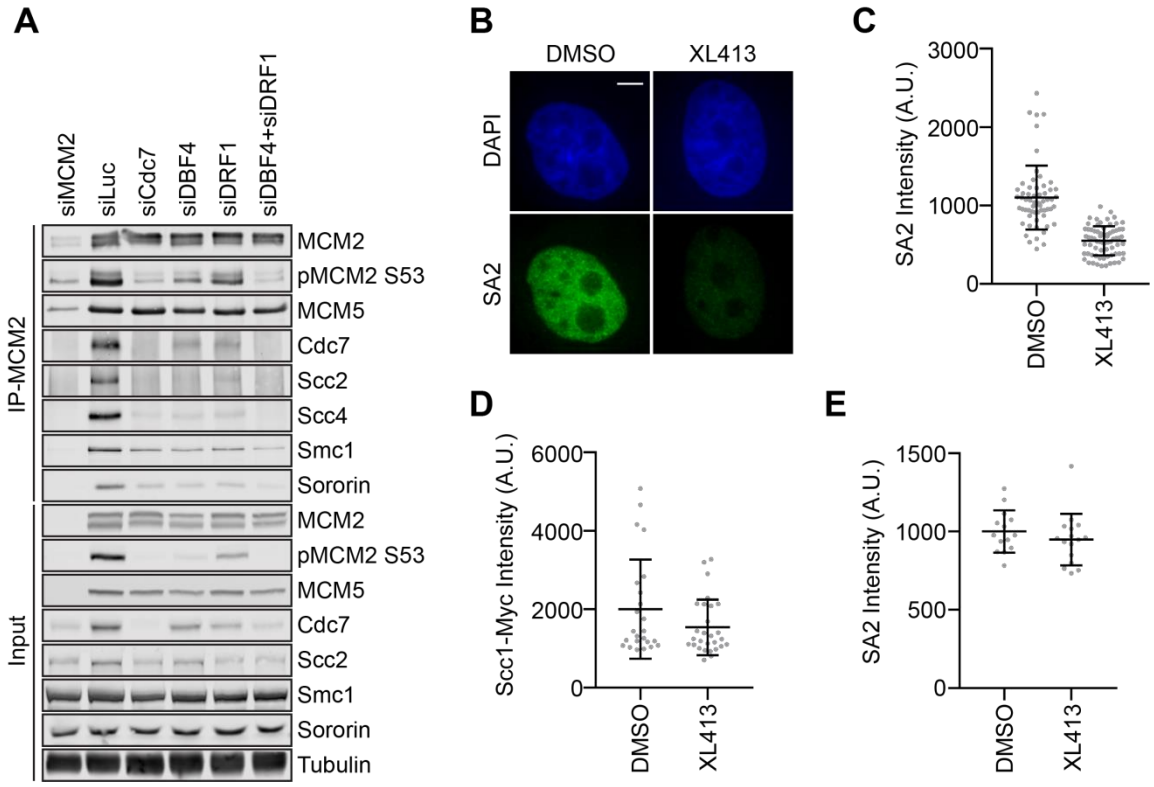

Figure 5-5. MCM phosphorylation by DDK is critical for cohesin loading. (**A**) HeLa cells were transfected with the indicated siRNAs, enriched in G1/S by thymidine, and lysed in the presence of nuclease. The total lysates (Input) and anti-MCM2 immunoprecipitate were blotted with the indicated antibodies. (**B**) DAPI and anti-SA2 staining of HeLa cells that were mock-treated or treated with the DDK kinase inhibitor XL413 in G1/S. Scale bar, 5 μm. (**C**) Quantification of the SA2 intensities of cells in **B**. Each dot in the graph represents a single cell (DMSO, n=60; XL413, n=71). The horizontal bars and error bars indicate the means and standard errors, respectively. (D) Quantification of the Scc1-Myc intensities in Scc1-Myc expressing telophase cells in the absence or presence of the DDK kinase inhibitor XL413. Each dot in the graph represents a single cell (DMSO, n=24; XL413, n=28). The horizontal bars and error bars indicate the means and standard errors, respectively. (**E**) Quantification of the SA2 intensities in telophase HeLa cells without or with the DDK kinase inhibitor XL413. Each dot in the graph represents a single cell (DMSO, n=14; XL413, n=16). The horizontal bars and error bars indicate the means and standard errors, respectively.

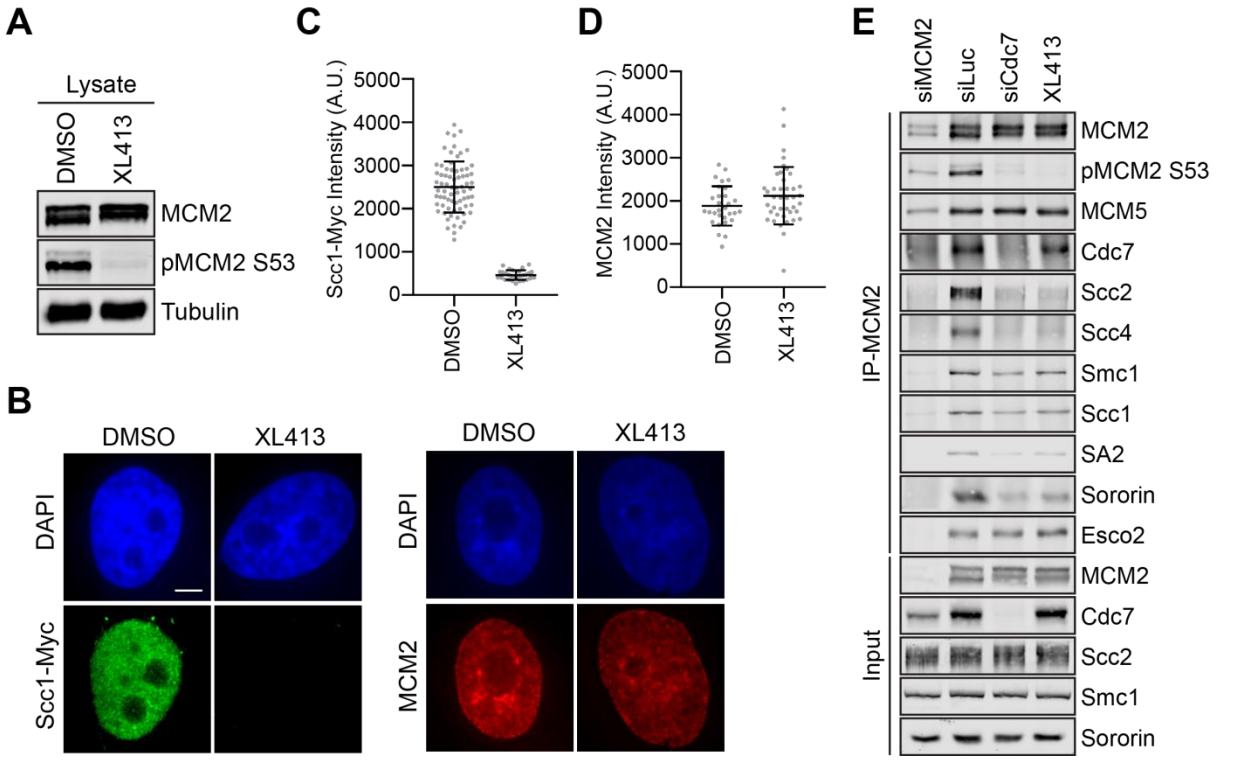

Figure 5-6. Phosphorylation of MCM2-7 by DDK is required for stable MCM-Scc2/4-cohesin interaction. (**A**) Lysates of HeLa cells either mock-treated or treated with the DDK kinase inhibitor XL413 were blotted with the indicated antibodies. (**B**) DAPI, anti-Myc, and anti-MCM2 staining of Scc1-Myc expressing HeLa cells that were mock-treated or treated with the DDK kinase inhibitor XL413 in G1/S. Scale bar, 5 μm. (**C**) Quantification of the Scc1-Myc intensities of cells in **B**. Each dot in the graph represents a single cell (DMSO, n=72; XL413, n=29). The horizontal bars and error bars indicate the means and standard errors, respectively. (**D**) Quantification of the MCM2 intensities of cells in **B**. Each dot in the graph represents a single cell (DMSO, n=30; XL413, n=41). The horizontal bars and error bars indicate the means and standard errors, respectively. (**E**) HeLa cells were either transfected with the indicated siRNAs or treated with the DDK kinase inhibitor XL413, accumulated in G1/S by thymidine, and lysed in the presence of nuclease. The total lysates (Input) and anti-MCM2 immunoprecipitate were blotted with the indicated antibodies.

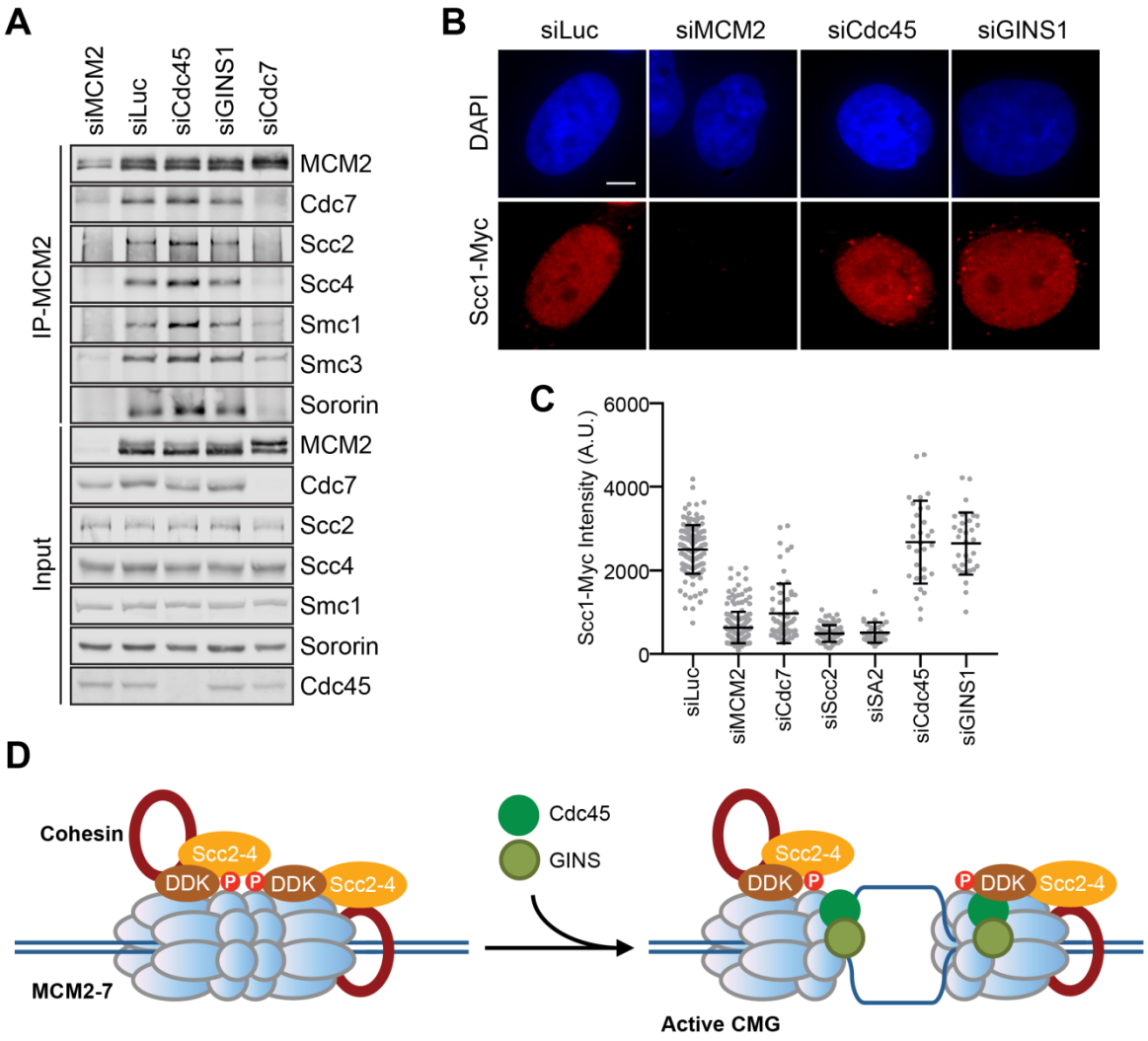

Figure 5-7. Cdc45 and GINS are dispensable for cohesin loading and MCM-Scc2/4-cohesin interaction. (**A**) HeLa cells were transfected with the indicated siRNAs, arrested in G1/S by thymidine, and lysed in the presence of nuclease. The total lysates (Input) and anti-MCM2 immunoprecipitate were blotted with the indicated antibodies. (**B**) DAPI and anti-Myc staining of HeLa cells that stably expressing Scc1-Myc. Cells were transfected with the indicated siRNAs and arrested in G1/S with thymidine. Scale bar, 5 μm. (**C**) Quantification of the Scc1-Myc intensities of cells in **B**. Each dot in the graph represents a single cell (siLuc, n=128; siMCM2, n=196; siCdc7, n=59; siScc2, n=70; siSA2, n=38; siCdc45, n=31; siGINS1, n=32). The horizontal bars and error bars indicate the means and standard errors, respectively. (**D**) A model for the Cdc45- and GINS-independent MCM-Scc2/4-cohesin interaction and cohesin loading.

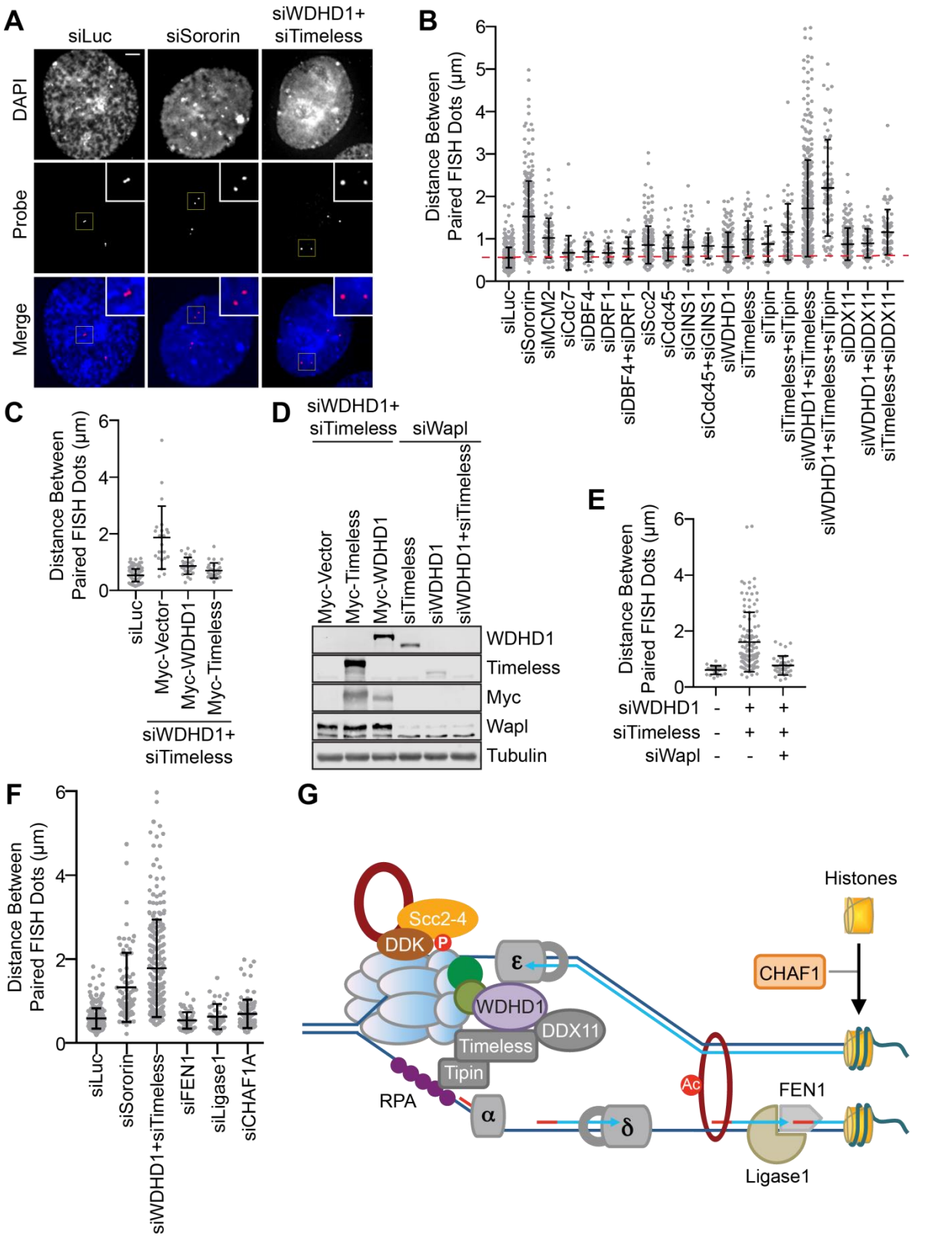
A
siLuc
siSororin
siWDHD1+
siTimeless
DAPI
Probe
Merge
B
Distance Between
Paired FISH Dots (μm)
siLuc
siSororin
siMCM2
siCdc7
siDBF4
siDRF1
siDBF4+siDRF1
siScc2
siCdc45
siGINS1
siCdc45+siGINS1
siWDHD1
siTimeless
siTipin
siTimeless+siTipin
siWDHD1+siTimeless
siWDHD1+siTimeless+siTipin
siDDX11
siWDHD1+siDDX11
siTimeless+siDDX11
C
Distance Between
Paired FISH Dots (μm)
siLuc
Myc-Vector
Myc-WDHD1
Myc-Timeless
siWDHD1+
siTimeless
D
siWDHD1+
siTimeless
siWapl
Myc-Vector
Myc-Timeless
Myc-WDHD1
siTimeless
siWDHD1
siWDHD1+siTimeless
WDHD1
Timeless
Myc
Wapl
Tubulin
E
Distance Between
Paired FISH Dots (μm)
siWDHD1
siTimeless
siWapl
F
Distance Between
Paired FISH Dots (μm)
siLuc
siSororin
siWDHD1+siTimeless
siFEN1
siLigase1
siCHAF1A
G
Histones
Scc2-4
DDK
P
ε
CHAF1
WDHD1
DDX11
Timeless
Tipin
RPA
α
δ
Ac
FEN1
Ligase1

Figure 5-8. Replisome components are required for cohesion establishment. (**A**) Representative images of G2-enriched HeLa cells transfected with the indicated siRNAs and stained with DAPI (blue in merge) and the FISH probe (red in merge). Selected paired FISH signals are magnified in inset. Scale bar, 5 μm. (**B**) Quantification of the distances between paired FISH signals in G2-enriched HeLa cells transfected with the indicated siRNAs. Each dot in the graph represents a single cell (siLuc, n=502; siSororin, n=243; siMCM2, n=70; siCdc7, n=44; siDBF4, n=30; siDRF1, n=30; siDBF4+siDRF1, n=32; siScc2, n=191; siCdc45, n=66; siGINS1, n=68; siCdc45+siGINS1, n=26; siWDHD1, n=198; siTimeless, n=58; siTipin, n=31; siTimeless+siTipin, n=51; siWDHD1+siTimeless, n=375; siWDHD1+siTimeless+siTipin, n=71; siDDX11, n=154; siWDHD1+siDDX11, n=52; siTimeless+siDDX11, n=65). The horizontal bars and error bars indicate the means and standard errors, respectively. (**C**) Quantification of the distances between paired FISH signals in G2-enriched HeLa cells transfected with the indicated plasmids and siRNAs. Each dot in the graph represents a single cell (siLuc, n=150; Myc-Vector, n=22; Myc-WDHD1, n=28; Myc-Timeless, n=30). The horizontal bars and error bars indicate the means and standard errors, respectively. (**D**) Lysates of HeLa cells transfected with the indicated plasmids and siRNAs were blotted with the indicated antibodies. (**E**) Quantification of the distances between paired FISH signals in G2-enriched HeLa cells transfected with the indicated siRNAs. Each dot in the graph represents a single cell (siLuc, n=22; siWDHD1+siTimeless, n=114; siWDHD1+siTimeless+siWapl, n=36). The horizontal bars and error bars indicate the means and standard errors, respectively. (**F**) Quantification of the distances between paired FISH signals in G2-enriched HeLa cells transfected with the indicated siRNAs. Each dot in the graph represents a single cell (siLuc, n=382; siSororin, n=82; siWDHD1+siTimeless, n=226; siFen1, n=60; siLigase1, n=44; siCHAF1A, n=110). The horizontal bars and error bars indicate the means and standard errors, respectively. (**G**) A model showing that several replisome components at active replication forks are required for cohesion establishment. Cohesion establishment occurs before the maturation of Okazaki fragments and the deposition of histones during DNA replication.

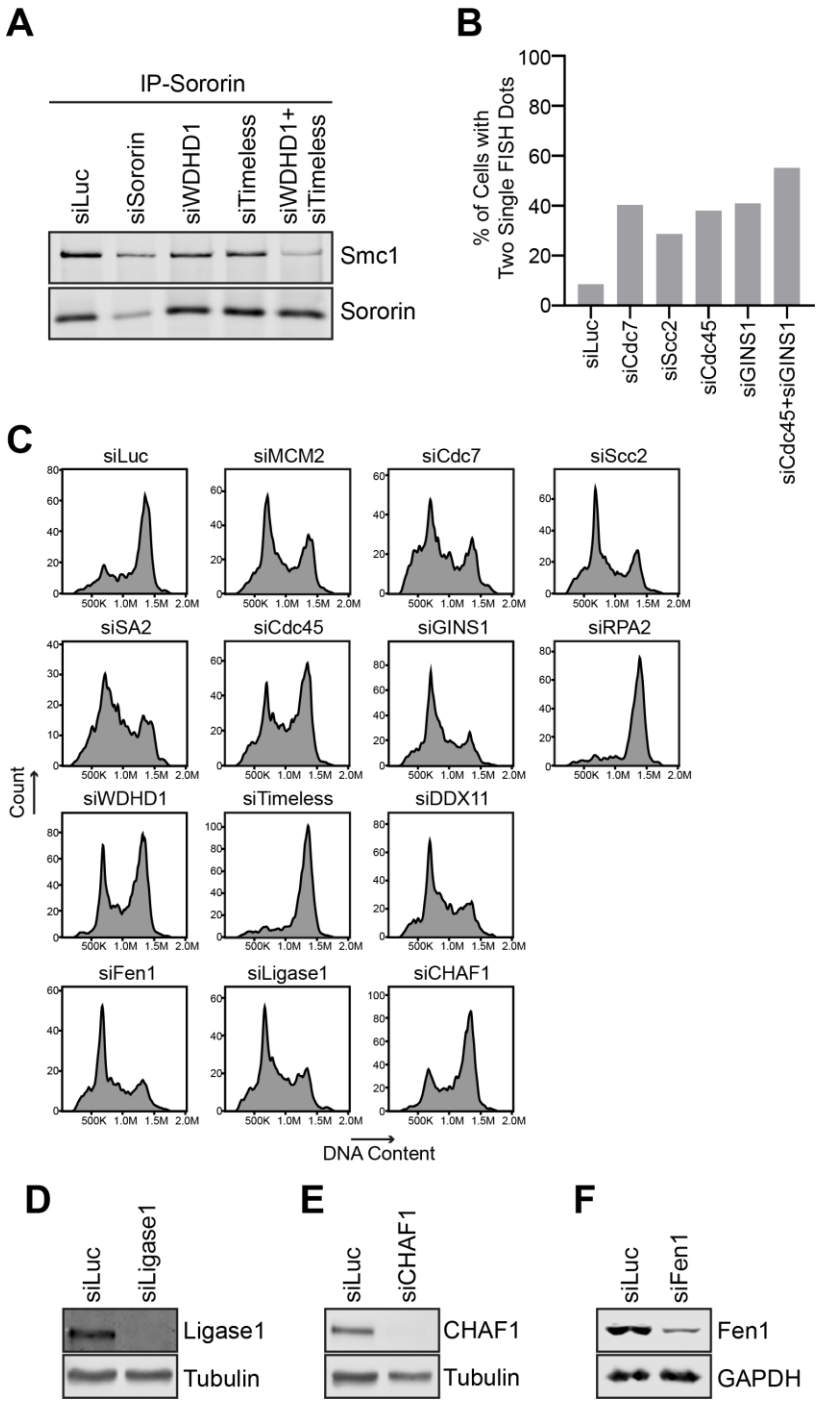

Figure 5-9. Replisome components are required for cohesion and replication initiation. (**A**) HeLa cells were transfected with the indicated siRNAs, arrested in G1/S by thymidine, and lysed in the presence of nuclease. Anti-Sororin immunoprecipitate were blotted with the indicated antibodies. (**B**) Quantification of the percentage of cells with two unreplicated single FISH dots after cells were transfected with the indicated siRNAs and released to G2 (siLuc, n=81; siCdc7, n=109; siScc2, n=66; siCdc45, n=71; siGINS1, n=139; siCdc45+siGINS1, n=116). (**C**) HeLa

cells were transfected with the indicated siRNAs, treated with thymidine for 2 days and harvested. DNA content analysis was performed by flow cytometry. (**D**, **E**, **F**) Lysates of HeLa transfected with the indicated siRNAs were blotted with the indicated antibodies.

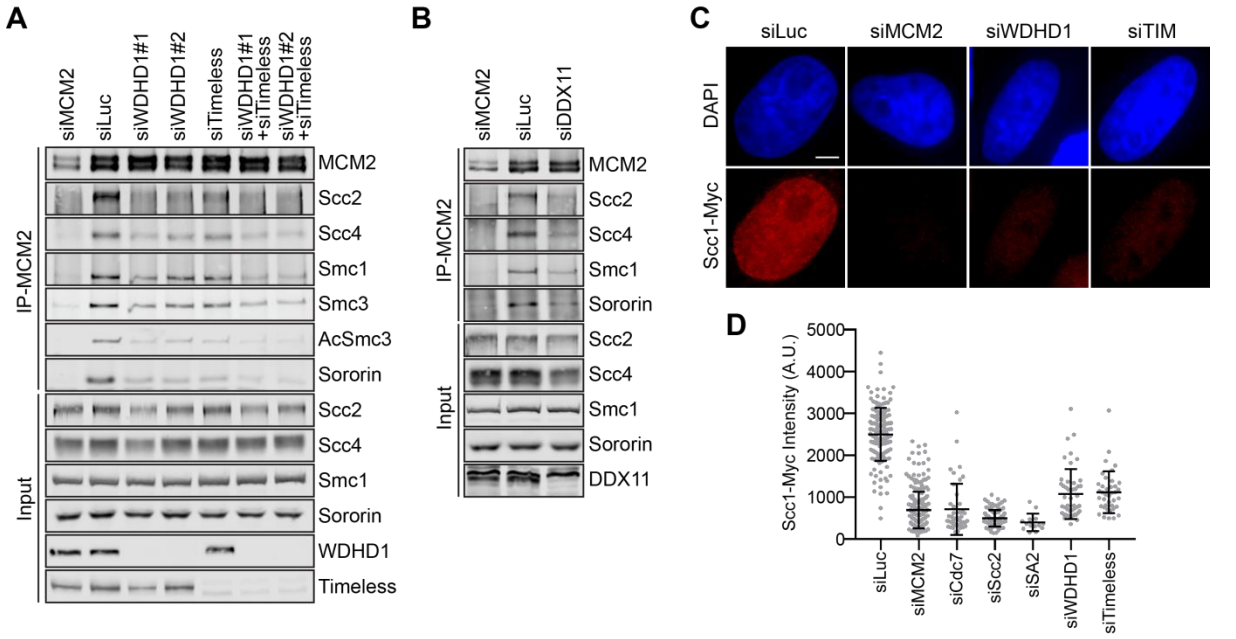

Figure 5-10. Replisome components are required for the integrity of the MCM-Scc2/4-cohesin complex. (**A**) HeLa cells were transfected with the indicated siRNAs, arrested in G1/S by thymidine, and lysed in the presence of nuclease. The total lysates (Input) and anti-MCM2 immunoprecipitate were blotted with the indicated antibodies. (**B**) Lysates of HeLa cells transfected with the indicated siRNAs and synchronized in G1/S with thymidine were immunoprecipitated with anti-MCM2. The total cell lysates (Input) and anti-MCM2 immunoprecipitate were blotted with the indicated antibodies. (**C**) DAPI and anti-Myc staining of HeLa cells that stably expressing Scc1-Myc. Cells were transfected with the indicated siRNAs and arrested in G1/S with thymidine. Scale bar, 5 μm. (**D**) Quantification of the Scc1-Myc intensities of cells in **C**. Each dot in the graph represents a single cell (siLuc, n=151; siMCM2, n=238; siCdc7, n=43; siScc2, n=97; siSA2, n=14; siWDHD1, n=47; siTimeless, n=39). The horizontal bars and error bars indicate the means and standard errors, respectively.

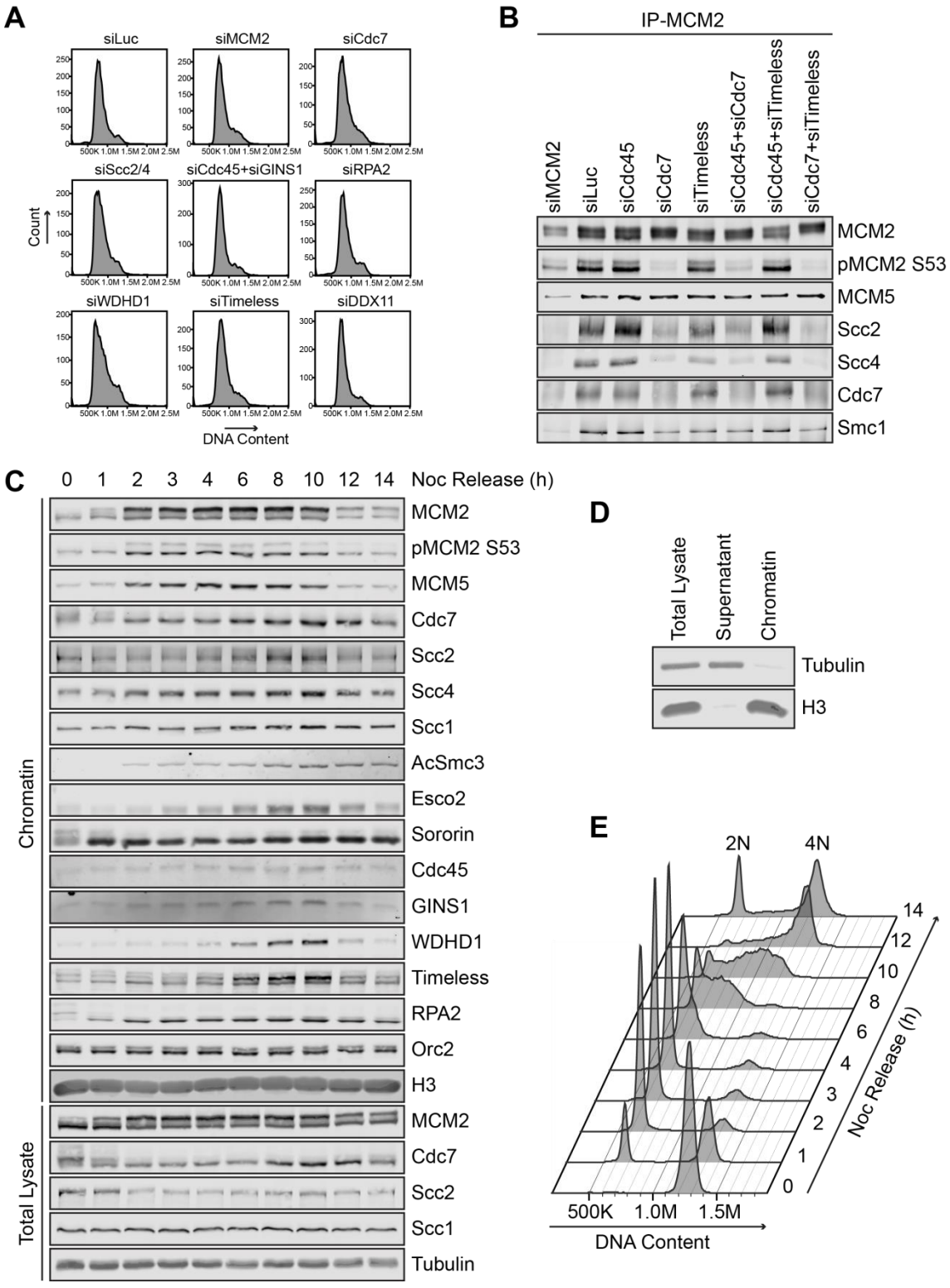

Figure 5-11. MCM-Scc2/4-cohesin interaction is regulated by replisome components at replication forks. (**A**) HeLa cells were transfected with the indicated siRNAs and treated with

thymidine for 16-18 hr. DNA content was analyzed by flow cytometry. (**B**) HeLa cells were transfected with the indicated siRNAs, arrested in G1/S by thymidine, and lysed in the presence of nuclease. Anti-MCM2 immunoprecipitate were blotted with the indicated antibodies. (**C**) HeLa cells were synchronized in mitosis by Nocodazole and released from Nocodazole for the indicated times. Cells were lysed and chromatin fraction was isolated. Total lysate and chromatin fraction were blotted with the indicated antibodies. (**D**) Total lysate, supernatant and chromatin fraction from **C** were blotted with anti-tubulin and anti-Histone H3. (**E**) DNA content analysis of cells in **C** was performed by flow cytometry.

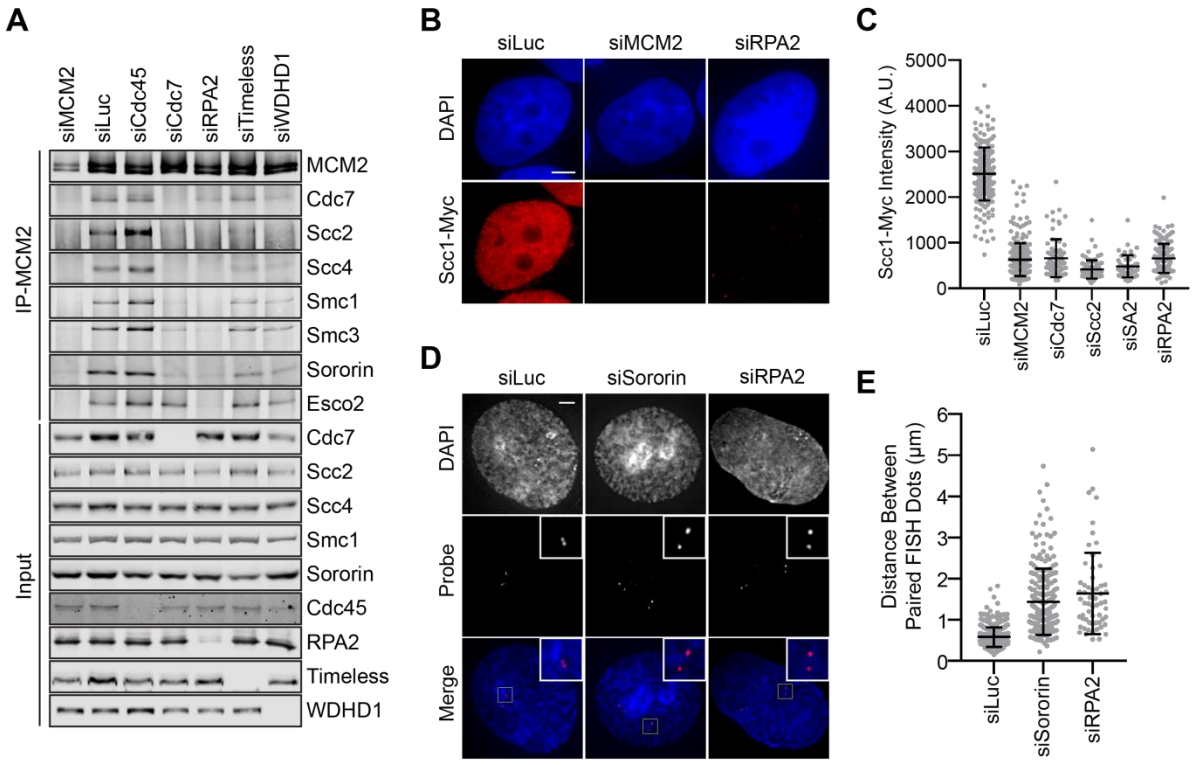

Figure 5-12. RPA at active replication forks is essential for sister-chromatid cohesion establishment. (**A**) HeLa cells were transfected with the indicated siRNAs, synchronized in G1/S by thymidine, and lysed in the presence of nuclease. The total lysates (Input) and anti-MCM2 immunoprecipitate were blotted with the indicated antibodies. (**B**) DAPI and anti-Myc staining of HeLa cells that stably expressing Scc1-Myc. Cells were transfected with the indicated siRNAs and arrested in G1/S with thymidine. Scale bar, 5 μm. (**C**) Quantification of the Scc1-Myc intensities of cells in **B**. Each dot in the graph represents a single cell (siLuc, n=215; siMCM2, n=298; siCdc7, n=75; siScc2, n=91; siSA2, n=52; siRPA2, n=131). The horizontal bars and error bars indicate the means and standard errors, respectively. (**D**) Representative images of G2-enriched HeLa cells transfected with the indicated siRNAs and stained with DAPI (blue in merge) and the FISH probe (red in merge). Selected paired FISH signals are magnified in inset. Scale bar, 5 μm. (**E**) Quantification of the distances between paired FISH signals of cells in **D**. Each dot in the graph represents a single cell (siLuc, n=439; siSororin, n=226; siRPA2, n=59). The horizontal bars and error bars indicate the means and standard errors, respectively.

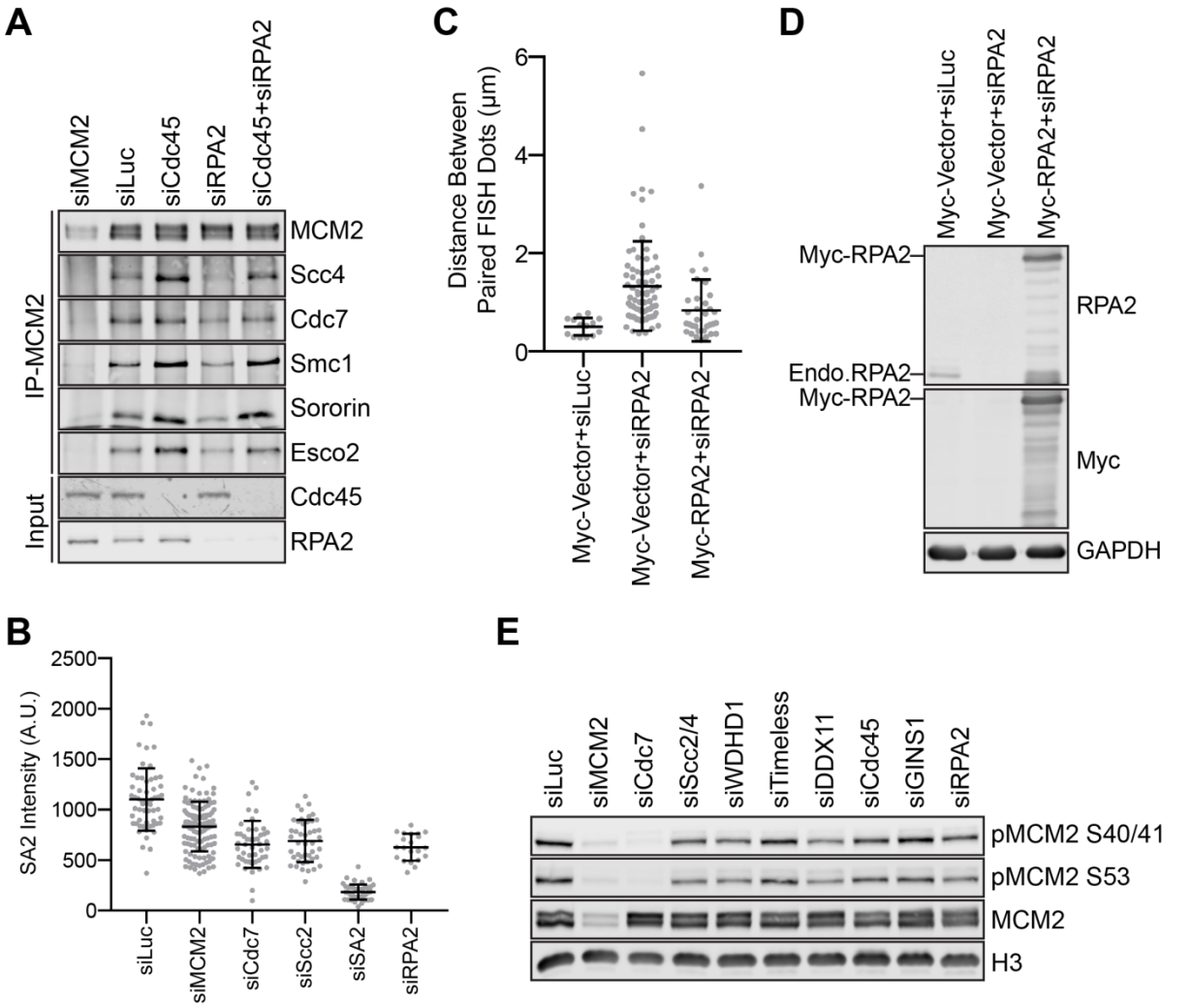

Figure 5-13. RPA2 depletion disrupts MCM-Scc2/4-cohesin interaction with only minor impact on MCM phosphorylation status. (**A**) HeLa cells were transfected with the indicated siRNAs, arrested in G1/S by thymidine, and lysed in the presence of nuclease. Anti-MCM2 immunoprecipitate were blotted with the indicated antibodies. (**B**) Quantification of the SA2 intensities in HeLa cells transfected with the indicated siRNAs and synchronized in G1/S. Each dot in the graph represents a single cell (siLuc, n=58; siMCM2, n=117; siCdc7, n=47; siScc2, n=45; siSA2, n=48; siRPA2, n=21). The horizontal bars and error bars indicate the means and standard errors, respectively. (**C**) Quantification of the distances between paired FISH signals in G2-enriched HeLa cells transfected with the indicated plasmids and siRNAs. Each dot in the graph represents a single cell (Myc-Vector+siLuc, n=14; Myc-Vector+siRPA2, n=78; Myc-RPA2+siRPA2, n=34). The horizontal bars and error bars indicate the means and standard errors, respectively. (**D**) Lysates of HeLa cells in **C** were blotted with the indicated antibodies. (**E**) Lysates of HeLa cells transfected with the indicated siRNAs were blotted with the indicated antibodies.

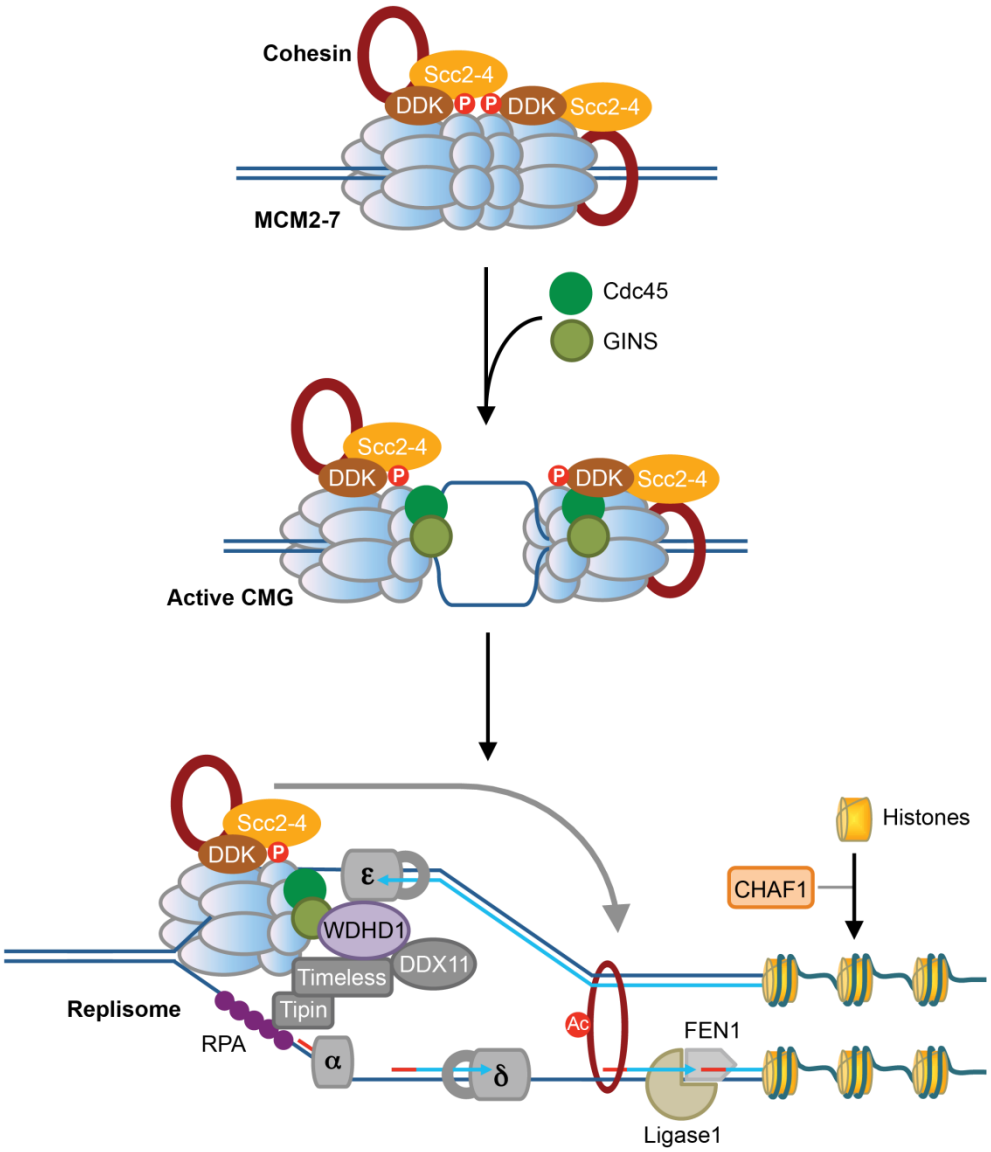

Figure 5-14. A model for how DNA replication-coupled cohesin loading promotes sister-chromatid cohesion establishment.

Table 5-1. siRNAs used in this study

siRNAs	Sequences
siLuciferase	5’-UCAUUCCGGAUACUGCGAU-3’
siMCM2	5’-GAAGAUCUUUGCCAGCAUU-3’ 5’-GGAUAAGGCUCGUCAGAUC-3’ 5’-GCCGUGGGCUCCUGUAUGA-3’ 5’-GGAUGUGAGUCAUGCGGAU-3’
siMCM3	5’-GGACAUCAAUAUUCUUCUA-3’ 5’-GCAGGUAUGACCAGUAUAA-3’ 5’-GGAAAUGCCUCAAGUACAC-3’ 5’-GACCAUAGAGCGACGUUAU-3’
siMCM5	5’-GAAGAUCCCUGGCAUCAUC-3’ 5’-GAACAGGGUUACCAUCAUG-3’ 5’-GGACAACAUUGACUUCAUG-3’ 5’-CCAAGGAGGUAGCUGAUGA-3’
siScc2	5’-CUGAUAAACUAGAACGAAA-3’
siScc4	5’-GAGAAGGCGUGGUUGAUAU-3’
siSA2	5’-CCACUGAUGUCUUACCGAA-3’
siScc1	5’-GGAAGAAGCAUUUGCAUUG-3’
siSororin	5’-CAGAAAGCCCAUCGUCUUA-3’
siWapl	5’-CGGACTACCCTTAGCACAA-3’
siCdc7	5’-CAGGAAAGGUGUUCACAAA-3’ 5’-CUACACAAAUGCACAAAUU-3’ 5’-GUACGGGAAUAUAUGCUUA-3’ 5’-GCAUUCAUCAGUUUGGUAU-3’
siDBF4	5’-GAACACACAUUAAGUGAAA-3’ 5’-GCACAAACCUUGGGUCGAA-3’ 5’-GAGCAGAAUUUCCUGUAUA-3’ 5’-CCAAACAGAUGGCGAUAAG-3’
siDRF1	5’-GGAAACAUCGGCCAUGGUU-3’ 5’-AAACAUCGGCCAUGGUUGA-3’ 5’-GGAAACCCGUUGACUCGGU-3’ 5’-GAGCGAACCGGGAAAGGGA-3’
siWDHD1	5’-GGUAAUACGUGGACUCCUA-3’ 5’-GCUGUGAAUUUAGCCAUUA-3’
siTimeless	5’-GGAAGACGCUGUUGGUAAA-3’
siTipin	5’-UGGAUUAAACGAAGACAUU-3’
siDDX11	5’-GCAGAGCUGUACCGGGUUU-3’ 5’-CGGCAGAACCUUUGUGUAA-3’ 5’-GAGGAAGAACACAUAACUA-3’ 5’-UGUUCAAGGUGCAGCGAUA-3’

siCdc45	5’-GCACACGGAUCUCCUUUGA-3’ 5’-GCAAACACCUGCUCAAGUC-3’ 5’-GGACGUGGAUGCUCUGUGU-3’ 5’-UCAAUGUCGUCAAUGUAUA-3’
siGINS1	5’-GAAAUGGAGUGGUUUAAUA-3’ 5’-GAUGAAAGCUUUGUAUGAA-3’ 5’-GCACUUCAGUCCUAUUAAA-3’ 5’-CAACGAGGAUGGACUCAGA-3’
siRPA2	5’-GAUCAAUGCACACAUGGUA-3’ 5’-CAAAAUAGAUGACAUGACA-3’ 5’-GAGUGAAGCAGGGAACUUU-3’ 5’-GUGGAACAGUGGAUUCGAA-3’
siCHAF1A	5’-GAAAGGAGCAGGACAGUUG-3’ 5’-ACACGAAGCUCCUGGACUA-3’ 5’-AAACAACUGUCAUGUGGGU-3’ 5’-GACAUAGACUUUAGACCGA-3’
siLigase1	5’-GGCAUGAUCCUGAAGCAGA-3’
siFen1	5’-UCACUAAGCAGCACAAUGA-3’ 5’-AGAAUGACAUCAAGAGCUA-3’ 5’-GGGCAUCCCUUAUCUUGAU-3’ 5’-CCCAAGGGAUCCACUAAGA-3’

CHAPTER VI: PERSPECTIVES

I have described four related projects in this dissertation. In each case, my research has addressed certain questions, but also raised new ones. In the first story, I systematically mapped the functional surface of Wapl-C with structure-based mutagenesis. Among all the mutants that are deficient in promoting cohesion resolution in mitosis, I showed that mutations at the N lobe of Wapl-C are involved in cohesin binding. However, I cannot explain why the mutations at C lobe of Wapl-C disrupt its function. One possibility is that residues at the C lobe directly bind to the ATPase domain of cohesin to promote cohesin release, as suggested by others (Chatterjee et al., 2013; Huis in 't Veld et al., 2014). High-resolution structures of cohesin in contact with Wapl-C will be invaluable to understand the molecular basis of Wapl-mediated cohesin removal from chromosomes during mitosis. It is also possible that these residues contact a yet identified effector to promote cohesin release. If so, we as a field need to search for such interactors. Finally, a loop missing in the Wapl-C structure has several putative Cdk1 and Plk1 sites. Loop deletion mutation of Wapl is partially functional. Whether the phosphorylation regulation of this loop is involved in Wapl-mediated cohesin release remains to be determined.

In the second project, with help of SA2-Scc1 structure, I showed that Scc1 makes extensive contacts with SA2, with one binding hot spot. I further investigated the interactions between SA2/Scc1 and cohesin regulators, and showed that mutations of SA2 residues that disrupt Wapl binding bypass the requirement of Sgo1 in centromeric cohesion protection, suggesting the direct competition between Sgo1 and Wapl. In addition, Sgo1 recruits PP2A to keep Sororin hypophosphorylated and associated with Pds5, thus antagonizing Wapl binding to cohesin

through Pds5 (Liu et al., 2013b). These two mechanisms collaborate to ensure centromeric cohesion. It has been known that SA2 and Scc1 are specifically phosphorylated in mitosis. Previous studies have shown that phosphorylation of SA2 at its C-terminal disordered region is essential for Wapl-mediated cohesin dissociation during prophase (Hauf et al., 2005). However, the C-terminal phosphorylation sites are not included in the SA2-Scc1 structure. Phosphorylation of Scc1 is required for efficient cleavage by separase during the metaphase-anaphase transition (Hauf et al., 2005). Shugoshin has been shown to protect meiotic cohesin from separase through PP2A-dependent dephosphorylation (Kitajima et al., 2006). To fully understand the role of Sgo1-PP2A in centromeric cohesion protection, we need to examine if Sgo1-PP2A inhibits these phosphorylation events of SA2 and Scc1 to prevent Wapl-dependent cohesin release and separase-dependent cohesin cleavage.

In the third project, I defined the dual functions of Pds5 in cohesion regulation by showing the direct competition between Sororin and Wapl in Pds5 binding. Interestingly, mutations of YSR motif in Sororin reduced its binding to Pds5 and cohesin, but did not cause overt cohesion defect in human cells. It is possible that another protein might act redundantly with the YSR motif of Sororin to antagonize the YSR motif in Wapl, a possibility worth testing in the future. In addition to providing a landing pad for Sororin or Wapl, Pds5 directly interacts with the N-terminal region of Scc1 close to its interface with Smc3, which is the DNA exit gate of cohesin. Pds5 cannot disrupt the Smc3-Scc1 interface, but Scc1 binding by Pds5 is incompatible with its interaction to Smc3 ATPase head. Wapl directly binds to Pds5 and possibly to the ATPase domain of cohesin (Chatterjee et al., 2013). *In vitro* reconstitution experiments suggest that Wapl-Pds5 cannot stimulate the ATPase activity of cohesin, but requires ATP rebinding to the

nucleotide-free cohesin to open the DNA exit gate (Murayama and Uhlmann, 2015). These results together suggest that Wapl-Pds5 might directly disengage the Smc3-Scc1 interface to promote cohesin release. However, the molecular mechanism has not been completely elucidated. Therefore, structures of intact cohesin bound to Wapl-Pds5 in different nucleotide states will be informative to advance our understanding of Wapl-Pds5-mediated cohesin release from chromosomes.

In the last project, my data revealed that DNA replication-coupled cohesin loading is required for the establishment of sister-chromatid cohesion. Because cohesion establishment and DNA replication are tightly coupled, I further explored the roles of several replication proteins in cohesion establishment and identified key molecules required for cohesin loading, cohesin binding to replication forks and cohesion establishment. However, it is always difficult to separate their functions in cohesion establishment from those in supporting replication fork progression. I was able to detect the cell-cycle dependent interactions among cohesin, the cohesin loader Scc2/4 complex and the replication machinery. In the near future, it is important to identify the receptors of cohesin and Scc2/4 in the replication machinery and to further examine the requirement of *de novo* cohesin loading in cohesion establishment during DNA replication. Surprisingly, in addition to MCM phosphorylation, the MCM-Scc2/4-cohesin interaction requires additional stabilization by replisome components at active replication forks, suggesting that the MCM-Scc2/4-cohesin mega-complex might have distinct conformations before and after replication initiation. High-resolution structures of cohesin, Scc2/4 in association with the replication machinery will be needed to fully understand how DNA replication and cohesion establishment are coordinated and how cohesin interplays with the

replication machinery during DNA replication. Moreover, reconstitution of these processes with purified proteins *in vitro* together with structural and biochemical approaches will be extremely valuable for future in-depth mechanistic studies of cohesin loading.

BIBLIOGRAPHY

Adams, P.D., Afonine, P.V., Bunkoczi, G., Chen, V.B., Davis, I.W., Echols, N., Headd, J.J., Hung, L.W., Kapral, G.J., Grosse-Kunstleve, R.W., *et al.* (2010). PHENIX: a comprehensive Python-based system for macromolecular structure solution. Acta Crystallogr D Biol Crystallogr *66*, 213-221.

Alomer, R.M., da Silva, E.M.L., Chen, J., Piekarz, K.M., McDonald, K., Sansam, C.G., Sansam, C.L., and Rankin, S. (2017). Esco1 and Esco2 regulate distinct cohesin functions during cell cycle progression. Proc Natl Acad Sci U S A.

Aparicio, T., Guillou, E., Coloma, J., Montoya, G., and Mendez, J. (2009). The human GINS complex associates with Cdc45 and MCM and is essential for DNA replication. Nucleic Acids Res *37*, 2087-2095.

Beckouet, F., Srinivasan, M., Roig, M.B., Chan, K.L., Scheinost, J.C., Batty, P., Hu, B., Petela, N., Gligoris, T., Smith, A.C., *et al.* (2016). Releasing Activity Disengages Cohesin's Smc3/Scc1 Interface in a Process Blocked by Acetylation. Mol Cell *61*, 563-574.

Bell, S.P., and Dutta, A. (2002). DNA replication in eukaryotic cells. Annu Rev Biochem *71*, 333-374.

Boland, A., Martin, T.G., Zhang, Z., Yang, J., Bai, X.C., Chang, L., Scheres, S.H., and Barford, D. (2017). Cryo-EM structure of a metazoan separase-securin complex at near-atomic resolution. Nat Struct Mol Biol *24*, 414-418.

Borek, D., Cymborowski, M., Machius, M., Minor, W., and Otwinowski, Z. (2010). Diffraction data analysis in the presence of radiation damage. Acta Crystallogr D Biol Crystallogr *66*, 426-436.

Borek, D., Dauter, Z., and Otwinowski, Z. (2013). Identification of patterns in diffraction intensities affected by radiation exposure. J Synchrotron Radiat *20*, 37-48.

Borek, D., Ginell, S.L., Cymborowski, M., Minor, W., and Otwinowski, Z. (2007). The many faces of radiation-induced changes. J Synchrotron Radiat *14*, 24-33.

Borek, D., Minor, W., and Otwinowski, Z. (2003). Measurement errors and their consequences in protein crystallography. Acta Crystallogr D Biol Crystallogr *59*, 2031-2038.

Borges, V., Smith, D.J., Whitehouse, I., and Uhlmann, F. (2013). An Eco1-independent sister chromatid cohesion establishment pathway in S. cerevisiae. Chromosoma *122*, 121-134.

Bose, T., and Gerton, J.L. (2010). Cohesinopathies, gene expression, and chromatin organization. J Cell Biol *189*, 201-210.

Bruck, I., and Kaplan, D.L. (2015). Conserved mechanism for coordinating replication fork helicase assembly with phosphorylation of the helicase. Proc Natl Acad Sci U S A *112*, 11223-11228.

Buheitel, J., and Stemmann, O. (2013). Prophase pathway-dependent removal of cohesin from human chromosomes requires opening of the Smc3-Scc1 gate. EMBO J *32*, 666-676.

Busslinger, G.A., Stocsits, R.R., van der Lelij, P., Axelsson, E., Tedeschi, A., Galjart, N., and Peters, J.M. (2017). Cohesin is positioned in mammalian genomes by transcription, CTCF and Wapl. Nature *544*, 503-507.

Camdere, G., Guacci, V., Stricklin, J., and Koshland, D. (2015). The ATPases of cohesin interface with regulators to modulate cohesin-mediated DNA tethering. Elife *4*.

Carretero, M., Ruiz-Torres, M., Rodriguez-Corsino, M., Barthelemy, I., and Losada, A. (2013). Pds5B is required for cohesion establishment and Aurora B accumulation at centromeres. EMBO J *32*, 2938-2949.

Chan, K.L., Gligoris, T., Upcher, W., Kato, Y., Shirahige, K., Nasmyth, K., and Beckouet, F. (2013). Pds5 promotes and protects cohesin acetylation. Proc Natl Acad Sci U S A *110*, 13020-13025.

Chan, K.L., Roig, M.B., Hu, B., Beckouet, F., Metson, J., and Nasmyth, K. (2012). Cohesin's DNA exit gate is distinct from its entrance gate and is regulated by acetylation. Cell *150*, 961-974.

Chan, R.C., Chan, A., Jeon, M., Wu, T.F., Pasqualone, D., Rougvie, A.E., and Meyer, B.J. (2003). Chromosome cohesion is regulated by a clock gene paralogue TIM-1. Nature *423*, 1002-1009.

Chao, W.C., Murayama, Y., Munoz, S., Costa, A., Uhlmann, F., and Singleton, M.R. (2015). Structural Studies Reveal the Functional Modularity of the Scc2-Scc4 Cohesin Loader. Cell Rep *12*, 719-725.

Chao, W.C., Murayama, Y., Munoz, S., Jones, A.W., Wade, B.O., Purkiss, A.G., Hu, X.W., Borg, A., Snijders, A.P., Uhlmann, F., *et al.* (2017). Structure of the cohesin loader Scc2. Nat Commun *8*, 13952.

Chatterjee, A., Zakian, S., Hu, X.W., and Singleton, M.R. (2013). Structural insights into the regulation of cohesion establishment by Wpl1. EMBO J *32*, 677-687.

Chen, J. (2013). Molecular mechanism of the Escherichia coli maltose transporter. Curr Opin Struct Biol *23*, 492-498.

Ciosk, R., Shirayama, M., Shevchenko, A., Tanaka, T., Toth, A., Shevchenko, A., and Nasmyth, K. (2000). Cohesin's binding to chromosomes depends on a separate complex consisting of Scc2 and Scc4 proteins. Mol Cell *5*, 243-254.

Collaborative Computational Project, N. (1994). The CCP4 suite: programs for protein crystallography. Acta Crystallogr D Biol Crystallogr *50*, 760-763.

Costa, A., Ilves, I., Tamberg, N., Petojevic, T., Nogales, E., Botchan, M.R., and Berger, J.M. (2011). The structural basis for MCM2-7 helicase activation by GINS and Cdc45. Nat Struct Mol Biol *18*, 471-477.

Cowtan, K. (2006). The Buccaneer software for automated model building. 1. Tracing protein chains. Acta Crystallogr D Biol Crystallogr *62*, 1002-1011.

Cowtan, K. (2010). Recent developments in classical density modification. Acta Crystallogr D Biol Crystallogr *66*, 470-478.

Cowtan, K., and Main, P. (1998). Miscellaneous algorithms for density modification. Acta Crystallogr D Biol Crystallogr *54*, 487-493.

Daum, J.R., Potapova, T.A., Sivakumar, S., Daniel, J.J., Flynn, J.N., Rankin, S., and Gorbsky, G.J. (2011). Cohesion fatigue induces chromatid separation in cells delayed at metaphase. Curr Biol *21*, 1018-1024.

Davidson, I.F., Goetz, D., Zaczek, M.P., Molodtsov, M.I., Huis In 't Veld, P.J., Weissmann, F., Litos, G., Cisneros, D.A., Ocampo-Hafalla, M., Ladurner, R., *et al.* (2016). Rapid movement and transcriptional re-localization of human cohesin on DNA. EMBO J *35*, 2671-2685.

de Wit, E., Vos, E.S., Holwerda, S.J., Valdes-Quezada, C., Verstegen, M.J., Teunissen, H., Splinter, E., Wijchers, P.J., Krijger, P.H., and de Laat, W. (2015). CTCF Binding Polarity Determines Chromatin Looping. Mol Cell *60*, 676-684.

Deardorff, M.A., Bando, M., Nakato, R., Watrin, E., Itoh, T., Minamino, M., Saitoh, K., Komata, M., Katou, Y., Clark, D., *et al.* (2012). HDAC8 mutations in Cornelia de Lange syndrome affect the cohesin acetylation cycle. Nature *489*, 313-317.

Deshpande, R.A., Williams, G.J., Limbo, O., Williams, R.S., Kuhnlein, J., Lee, J.H., Classen, S., Guenther, G., Russell, P., Tainer, J.A., *et al.* (2016). ATP-driven Rad50 conformations regulate DNA tethering, end resection, and ATM checkpoint signaling. EMBO J *35*, 791.

Dreier, M.R., Bekier, M.E., 2nd, and Taylor, W.R. (2011). Regulation of sororin by Cdk1-mediated phosphorylation. J Cell Sci *124*, 2976-2987.

Eichinger, C.S., Kurze, A., Oliveira, R.A., and Nasmyth, K. (2013). Disengaging the Smc3/kleisin interface releases cohesin from Drosophila chromosomes during interphase and mitosis. EMBO J *32*, 656-665.

Elbatsh, A.M., Haarhuis, J.H., Petela, N., Chapard, C., Fish, A., Celie, P.H., Stadnik, M., Ristic, D., Wyman, C., Medema, R.H., *et al.* (2016). Cohesin Releases DNA through Asymmetric ATPase-Driven Ring Opening. Mol Cell *61*, 575-588.

Emsley, P., and Cowtan, K. (2004). Coot: model-building tools for molecular graphics. Acta Crystallogr D Biol Crystallogr *60*, 2126-2132.

Emsley, P., Lohkamp, B., Scott, W.G., and Cowtan, K. (2010). Features and development of Coot. Acta Crystallogr D Biol Crystallogr *66*, 486-501.

Errico, A., Cosentino, C., Rivera, T., Losada, A., Schwob, E., Hunt, T., and Costanzo, V. (2009). Tipin/Tim1/And1 protein complex promotes Pol alpha chromatin binding and sister chromatid cohesion. EMBO J *28*, 3681-3692.

Farina, A., Shin, J.H., Kim, D.H., Bermudez, V.P., Kelman, Z., Seo, Y.S., and Hurwitz, J. (2008). Studies with the human cohesin establishment factor, ChlR1. Association of ChlR1 with Ctf18-RFC and Fen1. J Biol Chem *283*, 20925-20936.

Foley, E.A., and Kapoor, T.M. (2013). Microtubule attachment and spindle assembly checkpoint signalling at the kinetochore. Nat Rev Mol Cell Biol *14*, 25-37.

Fragkos, M., Ganier, O., Coulombe, P., and Mechali, M. (2015). DNA replication origin activation in space and time. Nat Rev Mol Cell Biol *16*, 360-374.

Francis, L.I., Randell, J.C., Takara, T.J., Uchima, L., and Bell, S.P. (2009). Incorporation into the prereplicative complex activates the Mcm2-7 helicase for Cdc7-Dbf4 phosphorylation. Genes Dev *23*, 643-654.

Fudenberg, G., Imakaev, M., Lu, C., Goloborodko, A., Abdennur, N., and Mirny, L.A. (2016). Formation of Chromosomal Domains by Loop Extrusion. Cell Rep *15*, 2038-2049.

Gandhi, R., Gillespie, P.J., and Hirano, T. (2006). Human Wapl is a cohesin-binding protein that promotes sister-chromatid resolution in mitotic prophase. Curr Biol *16*, 2406-2417.

Gerlich, D., Koch, B., Dupeux, F., Peters, J.M., and Ellenberg, J. (2006). Live-cell imaging reveals a stable cohesin-chromatin interaction after but not before DNA replication. Curr Biol *16*, 1571-1578.

Gillespie, P.J., and Hirano, T. (2004). Scc2 couples replication licensing to sister chromatid cohesion in Xenopus egg extracts. Curr Biol *14*, 1598-1603.

Gligoris, T.G., Scheinost, J.C., Burmann, F., Petela, N., Chan, K.L., Uluocak, P., Beckouet, F., Gruber, S., Nasmyth, K., and Lowe, J. (2014). Closing the cohesin ring: structure and function of its Smc3-kleisin interface. Science *346*, 963-967.

Goto, Y., Yamagishi, Y., Shintomi-Kawamura, M., Abe, M., Tanno, Y., and Watanabe, Y. (2017). Pds5 Regulates Sister-Chromatid Cohesion and Chromosome Bi-orientation through a Conserved Protein Interaction Module. Curr Biol *27*, 1005-1012.

Gruber, S., Arumugam, P., Katou, Y., Kuglitsch, D., Helmhart, W., Shirahige, K., and Nasmyth, K. (2006). Evidence that loading of cohesin onto chromosomes involves opening of its SMC hinge. Cell *127*, 523-537.

Gruber, S., Haering, C.H., and Nasmyth, K. (2003). Chromosomal cohesin forms a ring. Cell *112*, 765-777.

Guacci, V., Koshland, D., and Strunnikov, A. (1997). A direct link between sister chromatid cohesion and chromosome condensation revealed through the analysis of MCD1 in S. cerevisiae. Cell *91*, 47-57.

Guillou, E., Ibarra, A., Coulon, V., Casado-Vela, J., Rico, D., Casal, I., Schwob, E., Losada, A., and Mendez, J. (2010). Cohesin organizes chromatin loops at DNA replication factories. Genes Dev *24*, 2812-2822.

Haarhuis, J.H., Elbatsh, A.M., and Rowland, B.D. (2014). Cohesin and its regulation: on the logic of X-shaped chromosomes. Dev Cell *31*, 7-18.

Haarhuis, J.H., Elbatsh, A.M., van den Broek, B., Camps, D., Erkan, H., Jalink, K., Medema, R.H., and Rowland, B.D. (2013). WAPL-mediated removal of cohesin protects against segregation errors and aneuploidy. Curr Biol *23*, 2071-2077.

Haarhuis, J.H.I., van der Weide, R.H., Blomen, V.A., Yanez-Cuna, J.O., Amendola, M., van Ruiten, M.S., Krijger, P.H.L., Teunissen, H., Medema, R.H., van Steensel, B., *et al.* (2017). The Cohesin Release Factor WAPL Restricts Chromatin Loop Extension. Cell *169*, 693-707 e614.

Haering, C.H., Farcas, A.M., Arumugam, P., Metson, J., and Nasmyth, K. (2008). The cohesin ring concatenates sister DNA molecules. Nature *454*, 297-301.

Haering, C.H., Schoffnegger, D., Nishino, T., Helmhart, W., Nasmyth, K., and Lowe, J. (2004). Structure and stability of cohesin's Smc1-kleisin interaction. Mol Cell *15*, 951-964.

Hara, K., Zheng, G., Qu, Q., Liu, H., Ouyang, Z., Chen, Z., Tomchick, D.R., and Yu, H. (2014). Structure of cohesin subcomplex pinpoints direct shugoshin-Wapl antagonism in centromeric cohesion. Nat Struct Mol Biol *21*, 864-870.

Hartman, T., Stead, K., Koshland, D., and Guacci, V. (2000). Pds5p is an essential chromosomal protein required for both sister chromatid cohesion and condensation in Saccharomyces cerevisiae. J Cell Biol *151*, 613-626.

Hauf, S., Roitinger, E., Koch, B., Dittrich, C.M., Mechtler, K., and Peters, J.M. (2005). Dissociation of cohesin from chromosome arms and loss of arm cohesion during early mitosis depends on phosphorylation of SA2. PLoS Biol *3*, e69.

Hauf, S., Waizenegger, I.C., and Peters, J.M. (2001). Cohesin cleavage by separase required for anaphase and cytokinesis in human cells. Science *293*, 1320-1323.

Hegemann, B., Hutchins, J.R., Hudecz, O., Novatchkova, M., Rameseder, J., Sykora, M.M., Liu, S., Mazanek, M., Lenart, P., Heriche, J.K., *et al.* (2011). Systematic phosphorylation analysis of human mitotic protein complexes. Sci Signal *4*, rs12.

Heidinger-Pauli, J.M., Onn, I., and Koshland, D. (2010). Genetic evidence that the acetylation of the Smc3p subunit of cohesin modulates its ATP-bound state to promote cohesion establishment in Saccharomyces cerevisiae. Genetics *185*, 1249-1256.

Heller, R.C., Kang, S., Lam, W.M., Chen, S., Chan, C.S., and Bell, S.P. (2011). Eukaryotic origin-dependent DNA replication in vitro reveals sequential action of DDK and S-CDK kinases. Cell *146*, 80-91.

Hellmuth, S., Rata, S., Brown, A., Heidmann, S., Novak, B., and Stemmann, O. (2015). Human chromosome segregation involves multi-layered regulation of separase by the peptidyl-prolyl-isomerase Pin1. Mol Cell *58*, 495-506.

Hinshaw, S.M., Makrantoni, V., Kerr, A., Marston, A.L., and Harrison, S.C. (2015). Structural evidence for Scc4-dependent localization of cohesin loading. Elife *4*, e06057.

Hirano, T. (2006). At the heart of the chromosome: SMC proteins in action. Nat Rev Mol Cell Biol *7*, 311-322.

Hou, F., and Zou, H. (2005). Two human orthologues of Eco1/Ctf7 acetyltransferases are both required for proper sister-chromatid cohesion. Mol Biol Cell *16*, 3908-3918.

Huang, J., Hsu, J.M., and Laurent, B.C. (2004). The RSC nucleosome-remodeling complex is required for Cohesin's association with chromosome arms. Mol Cell *13*, 739-750.

Hughes, S., Elustondo, F., Di Fonzo, A., Leroux, F.G., Wong, A.C., Snijders, A.P., Matthews, S.J., and Cherepanov, P. (2012). Crystal structure of human CDC7 kinase in complex with its activator DBF4. Nat Struct Mol Biol *19*, 1101-1107.

Huis in 't Veld, P.J., Herzog, F., Ladurner, R., Davidson, I.F., Piric, S., Kreidl, E., Bhaskara, V., Aebersold, R., and Peters, J.M. (2014). Characterization of a DNA exit gate in the human cohesin ring. Science *346*, 968-972.

Ilves, I., Petojevic, T., Pesavento, J.J., and Botchan, M.R. (2010). Activation of the MCM2-7 helicase by association with Cdc45 and GINS proteins. Mol Cell *37*, 247-258.

Inoue, A., Li, T., Roby, S.K., Valentine, M.B., Inoue, M., Boyd, K., Kidd, V.J., and Lahti, J.M. (2007). Loss of ChlR1 helicase in mouse causes lethality due to the accumulation of aneuploid cells generated by cohesion defects and placental malformation. Cell Cycle *6*, 1646-1654.

Ivanov, D., and Nasmyth, K. (2005). A topological interaction between cohesin rings and a circular minichromosome. Cell *122*, 849-860.

Ivanov, D., Schleiffer, A., Eisenhaber, F., Mechtler, K., Haering, C.H., and Nasmyth, K. (2002). Eco1 is a novel acetyltransferase that can acetylate proteins involved in cohesion. Curr Biol *12*, 323-328.

Ivanovic, T., Choi, J.L., Whelan, S.P., van Oijen, A.M., and Harrison, S.C. (2013). Influenza-virus membrane fusion by cooperative fold-back of stochastically induced hemagglutinin intermediates. Elife *2*, e00333.

Jia, L., Kim, S., and Yu, H. (2013). Tracking spindle checkpoint signals from kinetochores to APC/C. Trends Biochem Sci *38*, 302-311.

Kagey, M.H., Newman, J.J., Bilodeau, S., Zhan, Y., Orlando, D.A., van Berkum, N.L., Ebmeier, C.C., Goossens, J., Rahl, P.B., Levine, S.S., *et al.* (2010). Mediator and cohesin connect gene expression and chromatin architecture. Nature *467*, 430-435.

Kang, Y.H., Farina, A., Bermudez, V.P., Tappin, I., Du, F., Galal, W.C., and Hurwitz, J. (2013). Interaction between human Ctf4 and the Cdc45/Mcm2-7/GINS (CMG) replicative helicase. Proc Natl Acad Sci U S A *110*, 19760-19765.

Kanke, M., Tahara, E., Huis In't Veld, P.J., and Nishiyama, T. (2016). Cohesin acetylation and Wapl-Pds5 oppositely regulate translocation of cohesin along DNA. EMBO J *35*, 2686-2698.

Katis, V.L., Galova, M., Rabitsch, K.P., Gregan, J., and Nasmyth, K. (2004). Maintenance of cohesin at centromeres after meiosis I in budding yeast requires a kinetochore-associated protein related to MEI-S332. Curr Biol *14*, 560-572.

Kawashima, S.A., Yamagishi, Y., Honda, T., Ishiguro, K., and Watanabe, Y. (2010). Phosphorylation of H2A by Bub1 prevents chromosomal instability through localizing shugoshin. Science *327*, 172-177.

Kikuchi, S., Borek, D.M., Otwinowski, Z., Tomchick, D.R., and Yu, H. (2016). Crystal structure of the cohesin loader Scc2 and insight into cohesinopathy. Proc Natl Acad Sci U S A *113*, 12444-12449.

Kitajima, T.S., Kawashima, S.A., and Watanabe, Y. (2004). The conserved kinetochore protein shugoshin protects centromeric cohesion during meiosis. Nature *427*, 510-517.

Kitajima, T.S., Sakuno, T., Ishiguro, K., Iemura, S., Natsume, T., Kawashima, S.A., and Watanabe, Y. (2006). Shugoshin collaborates with protein phosphatase 2A to protect cohesin. Nature *441*, 46-52.

Krantz, I.D., McCallum, J., DeScipio, C., Kaur, M., Gillis, L.A., Yaeger, D., Jukofsky, L., Wasserman, N., Bottani, A., Morris, C.A., *et al.* (2004). Cornelia de Lange syndrome is caused by mutations in NIPBL, the human homolog of Drosophila melanogaster Nipped-B. Nat Genet *36*, 631-635.

Kueng, S., Hegemann, B., Peters, B.H., Lipp, J.J., Schleiffer, A., Mechtler, K., and Peters, J.M. (2006). Wapl controls the dynamic association of cohesin with chromatin. Cell *127*, 955-967.

Labib, K. (2010). How do Cdc7 and cyclin-dependent kinases trigger the initiation of chromosome replication in eukaryotic cells? Genes Dev *24*, 1208-1219.

Ladurner, R., Bhaskara, V., Huis in 't Veld, P.J., Davidson, I.F., Kreidl, E., Petzold, G., and Peters, J.M. (2014). Cohesin's ATPase activity couples cohesin loading onto DNA with Smc3 acetylation. Curr Biol *24*, 2228-2237.

Ladurner, R., Kreidl, E., Ivanov, M.P., Ekker, H., Idarraga-Amado, M.H., Busslinger, G.A., Wutz, G., Cisneros, D.A., and Peters, J.M. (2016). Sororin actively maintains sister chromatid cohesion. EMBO J *35*, 635-653.

Lafont, A.L., Song, J., and Rankin, S. (2010). Sororin cooperates with the acetyltransferase Eco2 to ensure DNA replication-dependent sister chromatid cohesion. Proc Natl Acad Sci U S A *107*, 20364-20369.

Lammens, K., Bemeleit, D.J., Mockel, C., Clausing, E., Schele, A., Hartung, S., Schiller, C.B., Lucas, M., Angermuller, C., Soding, J., *et al.* (2011). The Mre11:Rad50 structure shows an ATP-dependent molecular clamp in DNA double-strand break repair. Cell *145*, 54-66.

Langmead, B., and Salzberg, S.L. (2012). Fast gapped-read alignment with Bowtie 2. Nat Methods *9*, 357-359.

Lee, B.G., Roig, M.B., Jansma, M., Petela, N., Metson, J., Nasmyth, K., and Lowe, J. (2016). Crystal Structure of the Cohesin Gatekeeper Pds5 and in Complex with Kleisin Scc1. Cell Rep *14*, 2108-2115.

Lee, J., Kitajima, T.S., Tanno, Y., Yoshida, K., Morita, T., Miyano, T., Miyake, M., and Watanabe, Y. (2008). Unified mode of centromeric protection by shugoshin in mammalian oocytes and somatic cells. Nat Cell Biol *10*, 42-52.

Lee, K.Y., Im, J.S., Shibata, E., Park, J., Handa, N., Kowalczykowski, S.C., and Dutta, A. (2015). MCM8-9 complex promotes resection of double-strand break ends by MRE11-RAD50-NBS1 complex. Nat Commun *6*, 7744.

Leman, A.R., Noguchi, C., Lee, C.Y., and Noguchi, E. (2010). Human Timeless and Tipin stabilize replication forks and facilitate sister-chromatid cohesion. J Cell Sci *123*, 660-670.

Leman, A.R., and Noguchi, E. (2014). Linking chromosome duplication and segregation via sister chromatid cohesion. Methods Mol Biol *1170*, 75-98.

Lengronne, A., Katou, Y., Mori, S., Yokobayashi, S., Kelly, G.P., Itoh, T., Watanabe, Y., Shirahige, K., and Uhlmann, F. (2004). Cohesin relocation from sites of chromosomal loading to places of convergent transcription. Nature *430*, 573-578.

Lengronne, A., McIntyre, J., Katou, Y., Kanoh, Y., Hopfner, K.P., Shirahige, K., and Uhlmann, F. (2006). Establishment of sister chromatid cohesion at the S. cerevisiae replication fork. Mol Cell *23*, 787-799.

Lin, Z., Luo, X., and Yu, H. (2016). Structural basis of cohesin cleavage by separase. Nature *532*, 131-134.

Liu, H., Jia, L., and Yu, H. (2013a). Phospho-H2A and cohesin specify distinct tension-regulated Sgo1 pools at kinetochores and inner centromeres. Curr Biol *23*, 1927-1933.

Liu, H., Qu, Q., Warrington, R., Rice, A., Cheng, N., and Yu, H. (2015). Mitotic Transcription Installs Sgo1 at Centromeres to Coordinate Chromosome Segregation. Mol Cell *59*, 426-436.

Liu, H., Rankin, S., and Yu, H. (2013b). Phosphorylation-enabled binding of SGO1-PP2A to cohesin protects sororin and centromeric cohesion during mitosis. Nat Cell Biol *15*, 40-49.

London, N., and Biggins, S. (2014). Signalling dynamics in the spindle checkpoint response. Nat Rev Mol Cell Biol *15*, 736-747.

Losada, A. (2014). Cohesin in cancer: chromosome segregation and beyond. Nat Rev Cancer *14*, 389-393.

Losada, A., Hirano, M., and Hirano, T. (1998). Identification of Xenopus SMC protein complexes required for sister chromatid cohesion. Genes Dev *12*, 1986-1997.

Losada, A., Yokochi, T., and Hirano, T. (2005). Functional contribution of Pds5 to cohesin-mediated cohesion in human cells and Xenopus egg extracts. J Cell Sci *118*, 2133-2141.

Losada, A., Yokochi, T., Kobayashi, R., and Hirano, T. (2000). Identification and characterization of SA/Scc3p subunits in the Xenopus and human cohesin complexes. J Cell Biol *150*, 405-416.

Luo, S., and Tong, L. (2017). Molecular mechanism for the regulation of yeast separase by securin. Nature *542*, 255-259.

MacAlpine, H.K., Gordan, R., Powell, S.K., Hartemink, A.J., and MacAlpine, D.M. (2010). Drosophila ORC localizes to open chromatin and marks sites of cohesin complex loading. Genome Res *20*, 201-211.

Macbeth, M.R., Schubert, H.L., Vandemark, A.P., Lingam, A.T., Hill, C.P., and Bass, B.L. (2005). Inositol hexakisphosphate is bound in the ADAR2 core and required for RNA editing. Science *309*, 1534-1539.

Mannini, L., Cucco, F., Quarantotti, V., Krantz, I.D., and Musio, A. (2013). Mutation spectrum and genotype-phenotype correlation in Cornelia de Lange syndrome. Hum Mutat *34*, 1589-1596.

Masai, H., Matsumoto, S., You, Z., Yoshizawa-Sugata, N., and Oda, M. (2010). Eukaryotic chromosome DNA replication: where, when, and how? Annu Rev Biochem *79*, 89-130.

McGuinness, B.E., Hirota, T., Kudo, N.R., Peters, J.M., and Nasmyth, K. (2005). Shugoshin prevents dissociation of cohesin from centromeres during mitosis in vertebrate cells. PLoS Biol *3*, e86.

Merkenschlager, M., and Odom, D.T. (2013). CTCF and cohesin: linking gene regulatory elements with their targets. Cell *152*, 1285-1297.

Michaelis, C., Ciosk, R., and Nasmyth, K. (1997). Cohesins: chromosomal proteins that prevent premature separation of sister chromatids. Cell *91*, 35-45.

Minamino, M., Ishibashi, M., Nakato, R., Akiyama, K., Tanaka, H., Kato, Y., Negishi, L., Hirota, T., Sutani, T., Bando, M., *et al.* (2015). Esco1 Acetylates Cohesin via a Mechanism Different from That of Esco2. Curr Biol *25*, 1694-1706.

Minor, W., Cymborowski, M., Otwinowski, Z., and Chruszcz, M. (2006). HKL-3000: the integration of data reduction and structure solution--from diffraction images to an initial model in minutes. Acta Crystallogr D Biol Crystallogr *62*, 859-866.

Moldovan, G.L., Pfander, B., and Jentsch, S. (2006). PCNA controls establishment of sister chromatid cohesion during S phase. Mol Cell *23*, 723-732.

Monserrate, J.P., and York, J.D. (2010). Inositol phosphate synthesis and the nuclear processes they affect. Curr Opin Cell Biol *22*, 365-373.

Montpetit, B., Thomsen, N.D., Helmke, K.J., Seeliger, M.A., Berger, J.M., and Weis, K. (2011). A conserved mechanism of DEAD-box ATPase activation by nucleoporins and InsP6 in mRNA export. Nature *472*, 238-242.

Muir, K.W., Kschonsak, M., Li, Y., Metz, J., Haering, C.H., and Panne, D. (2016). Structure of the Pds5-Scc1 Complex and Implications for Cohesin Function. Cell Rep *14*, 2116-2126.

Murayama, Y., and Uhlmann, F. (2014). Biochemical reconstitution of topological DNA binding by the cohesin ring. Nature *505*, 367-371.

Murayama, Y., and Uhlmann, F. (2015). DNA Entry into and Exit out of the Cohesin Ring by an Interlocking Gate Mechanism. Cell *163*, 1628-1640.

Musio, A., Selicorni, A., Focarelli, M.L., Gervasini, C., Milani, D., Russo, S., Vezzoni, P., and Larizza, L. (2006). X-linked Cornelia de Lange syndrome owing to SMC1L1 mutations. Nat Genet *38*, 528-530.

Nasmyth, K. (2011). Cohesin: a catenase with separate entry and exit gates? Nat Cell Biol *13*, 1170-1177.

Nasmyth, K., and Haering, C.H. (2009). Cohesin: its roles and mechanisms. Annu Rev Genet *43*, 525-558.

Nishiyama, T., Ladurner, R., Schmitz, J., Kreidl, E., Schleiffer, A., Bhaskara, V., Bando, M., Shirahige, K., Hyman, A.A., Mechtler, K., *et al.* (2010). Sororin mediates sister chromatid cohesion by antagonizing Wapl. Cell *143*, 737-749.

Nishiyama, T., Sykora, M.M., Huis in 't Veld, P.J., Mechtler, K., and Peters, J.M. (2013). Aurora B and Cdk1 mediate Wapl activation and release of acetylated cohesin from chromosomes by phosphorylating Sororin. Proc Natl Acad Sci U S A *110*, 13404-13409.

Onn, I., Heidinger-Pauli, J.M., Guacci, V., Unal, E., and Koshland, D.E. (2008). Sister chromatid cohesion: a simple concept with a complex reality. Annu Rev Cell Dev Biol *24*, 105-129.

Otwinowski, Z., Borek, D., Majewski, W., and Minor, W. (2003). Multiparametric scaling of diffraction intensities. Acta Crystallogr A *59*, 228-234.

Otwinowski, Z., and Minor, W. (1997). Processing of X-ray diffraction data collected in oscillation mode. Methods Enzymol *276*, 307-326.

Ouyang, Z., and Yu, H. (2017). Releasing the cohesin ring: A rigid scaffold model for opening the DNA exit gate by Pds5 and Wapl. Bioessays *39*.

Ouyang, Z., Zheng, G., Song, J., Borek, D.M., Otwinowski, Z., Brautigam, C.A., Tomchick, D.R., Rankin, S., and Yu, H. (2013). Structure of the human cohesin inhibitor Wapl. Proc Natl Acad Sci U S A *110*, 11355-11360.

Ouyang, Z., Zheng, G., Tomchick, D.R., Luo, X., and Yu, H. (2016). Structural Basis and IP6 Requirement for Pds5-Dependent Cohesin Dynamics. Mol Cell *62*, 248-259.

Panizza, S., Tanaka, T., Hochwagen, A., Eisenhaber, F., and Nasmyth, K. (2000). Pds5 cooperates with cohesin in maintaining sister chromatid cohesion. Curr Biol *10*, 1557-1564.

Parish, J.L., Rosa, J., Wang, X., Lahti, J.M., Doxsey, S.J., and Androphy, E.J. (2006). The DNA helicase ChlR1 is required for sister chromatid cohesion in mammalian cells. J Cell Sci *119*, 4857-4865.

Peters, J.M., and Nishiyama, T. (2012). Sister chromatid cohesion. Cold Spring Harb Perspect Biol *4*.

Peters, J.M., Tedeschi, A., and Schmitz, J. (2008). The cohesin complex and its roles in chromosome biology. Genes Dev *22*, 3089-3114.

Rahman, S., Jones, M.J., and Jallepalli, P.V. (2015). Cohesin recruits the Esco1 acetyltransferase genome wide to repress transcription and promote cohesion in somatic cells. Proc Natl Acad Sci U S A *112*, 11270-11275.

Ramirez, F., Ryan, D.P., Gruning, B., Bhardwaj, V., Kilpert, F., Richter, A.S., Heyne, S., Dundar, F., and Manke, T. (2016). deepTools2: a next generation web server for deep-sequencing data analysis. Nucleic Acids Res *44*, W160-165.

Rankin, S. (2005). Sororin, the cell cycle and sister chromatid cohesion. Cell Cycle *4*, 1039-1042.

Rankin, S., Ayad, N.G., and Kirschner, M.W. (2005). Sororin, a substrate of the anaphase-promoting complex, is required for sister chromatid cohesion in vertebrates. Mol Cell *18*, 185-200.

Rao, S.S., Huntley, M.H., Durand, N.C., Stamenova, E.K., Bochkov, I.D., Robinson, J.T., Sanborn, A.L., Machol, I., Omer, A.D., Lander, E.S., *et al.* (2014). A 3D map of the human genome at kilobase resolution reveals principles of chromatin looping. Cell *159*, 1665-1680.

Remeseiro, S., Cuadrado, A., and Losada, A. (2013). Cohesin in development and disease. Development *140*, 3715-3718.

Ribeiro, A.L., Silva, R.D., Foyn, H., Tiago, M.N., Rathore, O.S., Arnesen, T., and Martinho, R.G. (2016). Naa50/San-dependent N-terminal acetylation of Scc1 is potentially important for sister chromatid cohesion. Sci Rep *6*, 39118.

Riedel, C.G., Katis, V.L., Katou, Y., Mori, S., Itoh, T., Helmhart, W., Galova, M., Petronczki, M., Gregan, J., Cetin, B., *et al.* (2006). Protein phosphatase 2A protects centromeric sister chromatid cohesion during meiosis I. Nature *441*, 53-61.

Roig, M.B., Lowe, J., Chan, K.L., Beckouet, F., Metson, J., and Nasmyth, K. (2014). Structure and function of cohesin's Scc3/SA regulatory subunit. FEBS Lett *588*, 3692-3702.

Rolef Ben-Shahar, T., Heeger, S., Lehane, C., East, P., Flynn, H., Skehel, M., and Uhlmann, F. (2008). Eco1-dependent cohesin acetylation during establishment of sister chromatid cohesion. Science *321*, 563-566.

Rong, Z., Ouyang, Z., Magin, R.S., Marmorstein, R., and Yu, H. (2016). Opposing Functions of the N-terminal Acetyltransferases Naa50 and NatA in Sister-chromatid Cohesion. J Biol Chem *291*, 19079-19091.

Ross-Innes, C.S., Stark, R., Teschendorff, A.E., Holmes, K.A., Ali, H.R., Dunning, M.J., Brown, G.D., Gojis, O., Ellis, I.O., Green, A.R., *et al.* (2012). Differential oestrogen receptor binding is associated with clinical outcome in breast cancer. Nature *481*, 389-393.

Rowland, B.D., Roig, M.B., Nishino, T., Kurze, A., Uluocak, P., Mishra, A., Beckouet, F., Underwood, P., Metson, J., Imre, R., *et al.* (2009). Building sister chromatid cohesion: smc3 acetylation counteracts an antiestablishment activity. Mol Cell *33*, 763-774.

Rubio, E.D., Reiss, D.J., Welcsh, P.L., Disteche, C.M., Filippova, G.N., Baliga, N.S., Aebersold, R., Ranish, J.A., and Krumm, A. (2008). CTCF physically links cohesin to chromatin. Proc Natl Acad Sci U S A *105*, 8309-8314.

Rudra, S., and Skibbens, R.V. (2012). Sister chromatid cohesion establishment occurs in concert with lagging strand synthesis. Cell Cycle *11*, 2114-2121.

Rudra, S., and Skibbens, R.V. (2013). Chl1 DNA helicase regulates Scc2 deposition specifically during DNA-replication in Saccharomyces cerevisiae. PLoS One *8*, e75435.

Samora, C.P., Saksouk, J., Goswami, P., Wade, B.O., Singleton, M.R., Bates, P.A., Lengronne, A., Costa, A., and Uhlmann, F. (2016). Ctf4 Links DNA Replication with Sister Chromatid Cohesion Establishment by Recruiting the Chl1 Helicase to the Replisome. Mol Cell *63*, 371-384.

Sanborn, A.L., Rao, S.S., Huang, S.C., Durand, N.C., Huntley, M.H., Jewett, A.I., Bochkov, I.D., Chinnappan, D., Cutkosky, A., Li, J., *et al.* (2015). Chromatin extrusion explains key features of loop and domain formation in wild-type and engineered genomes. Proc Natl Acad Sci U S A *112*, E6456-6465.

Schmitz, J., Watrin, E., Lenart, P., Mechtler, K., and Peters, J.M. (2007). Sororin is required for stable binding of cohesin to chromatin and for sister chromatid cohesion in interphase. Curr Biol *17*, 630-636.

Schneider, T.R., and Sheldrick, G.M. (2002). Substructure solution with SHELXD. Acta Crystallogr D Biol Crystallogr *58*, 1772-1779.

Schuck, P. (2000). Size-distribution analysis of macromolecules by sedimentation velocity ultracentrifugation and lamm equation modeling. Biophys J *78*, 1606-1619.

Schvartzman, J.M., Sotillo, R., and Benezra, R. (2010). Mitotic chromosomal instability and cancer: mouse modelling of the human disease. Nat Rev Cancer *10*, 102-115.

Seeber, A., Hegnauer, A.M., Hustedt, N., Deshpande, I., Poli, J., Eglinger, J., Pasero, P., Gut, H., Shinohara, M., Hopfner, K.P., *et al.* (2016). RPA Mediates Recruitment of MRX to Forks and Double-Strand Breaks to Hold Sister Chromatids Together. Mol Cell *64*, 951-966.

Sheard, L.B., Tan, X., Mao, H., Withers, J., Ben-Nissan, G., Hinds, T.R., Kobayashi, Y., Hsu, F.F., Sharon, M., Browse, J., *et al.* (2010). Jasmonate perception by inositol-phosphate-potentiated COI1-JAZ co-receptor. Nature *468*, 400-405.

Sheldrick, G.M. (2008). A short history of SHELX. Acta Crystallogr A *64*, 112-122.

Sherwood, R., Takahashi, T.S., and Jallepalli, P.V. (2010). Sister acts: coordinating DNA replication and cohesion establishment. Genes Dev *24*, 2723-2731.

Sheu, Y.J., and Stillman, B. (2006). Cdc7-Dbf4 phosphorylates MCM proteins via a docking site-mediated mechanism to promote S phase progression. Mol Cell *24*, 101-113.

Shintomi, K., and Hirano, T. (2009). Releasing cohesin from chromosome arms in early mitosis: opposing actions of Wapl-Pds5 and Sgo1. Genes Dev *23*, 2224-2236.

Shintomi, K., and Hirano, T. (2010). Sister chromatid resolution: a cohesin releasing network and beyond. Chromosoma *119*, 459-467.

Simon, A.C., Zhou, J.C., Perera, R.L., van Deursen, F., Evrin, C., Ivanova, M.E., Kilkenny, M.L., Renault, L., Kjaer, S., Matak-Vinkovic, D., *et al.* (2014). A Ctf4 trimer couples the CMG helicase to DNA polymerase alpha in the eukaryotic replisome. Nature *510*, 293-297.

Skibbens, R.V. (2009). Establishment of sister chromatid cohesion. Curr Biol *19*, R1126-1132.

Skibbens, R.V., Corson, L.B., Koshland, D., and Hieter, P. (1999). Ctf7p is essential for sister chromatid cohesion and links mitotic chromosome structure to the DNA replication machinery. Genes Dev *13*, 307-319.

Soh, Y.M., Burmann, F., Shin, H.C., Oda, T., Jin, K.S., Toseland, C.P., Kim, C., Lee, H., Kim, S.J., Kong, M.S., *et al.* (2015). Molecular basis for SMC rod formation and its dissolution upon DNA binding. Mol Cell *57*, 290-303.

Solomon, D.A., Kim, T., Diaz-Martinez, L.A., Fair, J., Elkahloun, A.G., Harris, B.T., Toretsky, J.A., Rosenberg, S.A., Shukla, N., Ladanyi, M., *et al.* (2011). Mutational inactivation of STAG2 causes aneuploidy in human cancer. Science *333*, 1039-1043.

Song, J., Lafont, A., Chen, J., Wu, F.M., Shirahige, K., and Rankin, S. (2012). Cohesin acetylation promotes sister chromatid cohesion only in association with the replication machinery. J Biol Chem *287*, 34325-34336.

Stemmann, O., Zou, H., Gerber, S.A., Gygi, S.P., and Kirschner, M.W. (2001). Dual inhibition of sister chromatid separation at metaphase. Cell *107*, 715-726.

Stigler, J., Camdere, G.O., Koshland, D.E., and Greene, E.C. (2016). Single-Molecule Imaging Reveals a Collapsed Conformational State for DNA-Bound Cohesin. Cell Rep *15*, 988-998.

Strom, L., Karlsson, C., Lindroos, H.B., Wedahl, S., Katou, Y., Shirahige, K., and Sjogren, C. (2007). Postreplicative formation of cohesion is required for repair and induced by a single DNA break. Science *317*, 242-245.

Sumara, I., Vorlaufer, E., Gieffers, C., Peters, B.H., and Peters, J.M. (2000). Characterization of vertebrate cohesin complexes and their regulation in prophase. J Cell Biol *151*, 749-762.

Sun, Y., Kucej, M., Fan, H.Y., Yu, H., Sun, Q.Y., and Zou, H. (2009). Separase is recruited to mitotic chromosomes to dissolve sister chromatid cohesion in a DNA-dependent manner. Cell *137*, 123-132.

Sun, Y., Yu, H., and Zou, H. (2006). Nuclear exclusion of separase prevents cohesin cleavage in interphase cells. Cell Cycle *5*, 2537-2542.

Sutani, T., Kawaguchi, T., Kanno, R., Itoh, T., and Shirahige, K. (2009). Budding yeast Wpl1(Rad61)-Pds5 complex counteracts sister chromatid cohesion-establishing reaction. Curr Biol *19*, 492-497.

Takahashi, T.S., Basu, A., Bermudez, V., Hurwitz, J., and Walter, J.C. (2008). Cdc7-Drf1 kinase links chromosome cohesion to the initiation of DNA replication in Xenopus egg extracts. Genes Dev *22*, 1894-1905.

Takahashi, T.S., Yiu, P., Chou, M.F., Gygi, S., and Walter, J.C. (2004). Recruitment of Xenopus Scc2 and cohesin to chromatin requires the pre-replication complex. Nat Cell Biol *6*, 991-996.

Tan, X., Calderon-Villalobos, L.I., Sharon, M., Zheng, C., Robinson, C.V., Estelle, M., and Zheng, N. (2007). Mechanism of auxin perception by the TIR1 ubiquitin ligase. Nature *446*, 640-645.

Tanaka, H., Kubota, Y., Tsujimura, T., Kumano, M., Masai, H., and Takisawa, H. (2009). Replisome progression complex links DNA replication to sister chromatid cohesion in Xenopus egg extracts. Genes Cells *14*, 949-963.

Tanaka, K., Hao, Z., Kai, M., and Okayama, H. (2001). Establishment and maintenance of sister chromatid cohesion in fission yeast by a unique mechanism. EMBO J *20*, 5779-5790.

Tang, Z., Shu, H., Oncel, D., Chen, S., and Yu, H. (2004a). Phosphorylation of Cdc20 by Bub1 provides a catalytic mechanism for APC/C inhibition by the spindle checkpoint. Mol Cell *16*, 387-397.

Tang, Z., Shu, H., Qi, W., Mahmood, N.A., Mumby, M.C., and Yu, H. (2006). PP2A is required for centromeric localization of Sgo1 and proper chromosome segregation. Dev Cell *10*, 575-585.

Tang, Z., Sun, Y., Harley, S.E., Zou, H., and Yu, H. (2004b). Human Bub1 protects centromeric sister-chromatid cohesion through Shugoshin during mitosis. Proc Natl Acad Sci U S A *101*, 18012-18017.

Tedeschi, A., Wutz, G., Huet, S., Jaritz, M., Wuensche, A., Schirghuber, E., Davidson, I.F., Tang, W., Cisneros, D.A., Bhaskara, V., *et al.* (2013). Wapl is an essential regulator of chromatin structure and chromosome segregation. Nature *501*, 564-568.

Terwilliger, T. (2004). SOLVE and RESOLVE: automated structure solution, density modification and model building. J Synchrotron Radiat *11*, 49-52.

Terwilliger, T.C. (2003). SOLVE and RESOLVE: automated structure solution and density modification. Methods Enzymol *374*, 22-37.

Tonkin, E.T., Wang, T.J., Lisgo, S., Bamshad, M.J., and Strachan, T. (2004). NIPBL, encoding a homolog of fungal Scc2-type sister chromatid cohesion proteins and fly Nipped-B, is mutated in Cornelia de Lange syndrome. Nat Genet *36*, 636-641.

Toth, A., Ciosk, R., Uhlmann, F., Galova, M., Schleiffer, A., and Nasmyth, K. (1999). Yeast cohesin complex requires a conserved protein, Eco1p(Ctf7), to establish cohesion between sister chromatids during DNA replication. Genes Dev *13*, 320-333.

Uhlmann, F. (2016). SMC complexes: from DNA to chromosomes. Nat Rev Mol Cell Biol *17*, 399-412.

Uhlmann, F., Lottspeich, F., and Nasmyth, K. (1999). Sister-chromatid separation at anaphase onset is promoted by cleavage of the cohesin subunit Scc1. Nature *400*, 37-42.

Uhlmann, F., and Nasmyth, K. (1998). Cohesion between sister chromatids must be established during DNA replication. Curr Biol *8*, 1095-1101.

Uhlmann, F., Wernic, D., Poupart, M.A., Koonin, E.V., and Nasmyth, K. (2000). Cleavage of cohesin by the CD clan protease separin triggers anaphase in yeast. Cell *103*, 375-386.

Unal, E., Heidinger-Pauli, J.M., Kim, W., Guacci, V., Onn, I., Gygi, S.P., and Koshland, D.E. (2008). A molecular determinant for the establishment of sister chromatid cohesion. Science *321*, 566-569.

van der Lelij, P., Chrzanowska, K.H., Godthelp, B.C., Rooimans, M.A., Oostra, A.B., Stumm, M., Zdzienicka, M.Z., Joenje, H., and de Winter, J.P. (2010). Warsaw breakage syndrome, a cohesinopathy associated with mutations in the XPD helicase family member DDX11/ChlR1. Am J Hum Genet *86*, 262-266.

Vaur, S., Feytout, A., Vazquez, S., and Javerzat, J.P. (2012). Pds5 promotes cohesin acetylation and stable cohesin-chromosome interaction. EMBO Rep *13*, 645-652.

Verni, F., Gandhi, R., Goldberg, M.L., and Gatti, M. (2000). Genetic and molecular analysis of wings apart-like (wapl), a gene controlling heterochromatin organization in Drosophila melanogaster. Genetics *154*, 1693-1710.

Vietri Rudan, M., Barrington, C., Henderson, S., Ernst, C., Odom, D.T., Tanay, A., and Hadjur, S. (2015). Comparative Hi-C reveals that CTCF underlies evolution of chromosomal domain architecture. Cell Rep *10*, 1297-1309.

Villa, F., Simon, A.C., Ortiz Bazan, M.A., Kilkenny, M.L., Wirthensohn, D., Wightman, M., Matak-Vinkovic, D., Pellegrini, L., and Labib, K. (2016). Ctf4 Is a Hub in the Eukaryotic Replisome that Links Multiple CIP-Box Proteins to the CMG Helicase. Mol Cell *63*, 385-396.

Waizenegger, I.C., Hauf, S., Meinke, A., and Peters, J.M. (2000). Two distinct pathways remove mammalian cohesin from chromosome arms in prophase and from centromeres in anaphase. Cell *103*, 399-410.

Watrin, E., Schleiffer, A., Tanaka, K., Eisenhaber, F., Nasmyth, K., and Peters, J.M. (2006). Human Scc4 is required for cohesin binding to chromatin, sister-chromatid cohesion, and mitotic progression. Curr Biol *16*, 863-874.

Wendt, K.S., Yoshida, K., Itoh, T., Bando, M., Koch, B., Schirghuber, E., Tsutsumi, S., Nagae, G., Ishihara, K., Mishiro, T., *et al.* (2008). Cohesin mediates transcriptional insulation by CCCTC-binding factor. Nature *451*, 796-801.

Wu, F.M., Nguyen, J.V., and Rankin, S. (2011). A conserved motif at the C terminus of sororin is required for sister chromatid cohesion. J Biol Chem *286*, 3579-3586.

Wu, N., Kong, X., Ji, Z., Zeng, W., Potts, P.R., Yokomori, K., and Yu, H. (2012). Scc1 sumoylation by Mms21 promotes sister chromatid recombination through counteracting Wapl. Genes Dev *26*, 1473-1485.

Wu, N., and Yu, H. (2012). The Smc complexes in DNA damage response. Cell Biosci *2*, 5.

Xiao, T., Wallace, J., and Felsenfeld, G. (2011). Specific sites in the C terminus of CTCF interact with the SA2 subunit of the cohesin complex and are required for cohesin-dependent insulation activity. Mol Cell Biol *31*, 2174-2183.

Xu, H., Boone, C., and Brown, G.W. (2007). Genetic dissection of parallel sister-chromatid cohesion pathways. Genetics *176*, 1417-1429.

Xu, X., Wang, J.T., Li, M., and Liu, Y. (2016). TIMELESS Suppresses the Accumulation of Aberrant CDC45.MCM2-7.GINS Replicative Helicase Complexes on Human Chromatin. J Biol Chem *291*, 22544-22558.

Xu, Z., Cetin, B., Anger, M., Cho, U.S., Helmhart, W., Nasmyth, K., and Xu, W. (2009). Structure and function of the PP2A-shugoshin interaction. Mol Cell *35*, 426-441.

Yoshizawa-Sugata, N., Ishii, A., Taniyama, C., Matsui, E., Arai, K., and Masai, H. (2005). A second human Dbf4/ASK-related protein, Drf1/ASKL1, is required for efficient progression of S and M phases. J Biol Chem *280*, 13062-13070.

Yu, H. (2013). Chromosome biology: Wapl spreads its wings. Curr Biol *23*, R923-925.

Yu, H. (2016). Magic Acts with the Cohesin Ring. Mol Cell *61*, 489-491.

Zhang, B., Jain, S., Song, H., Fu, M., Heuckeroth, R.O., Erlich, J.M., Jay, P.Y., and Milbrandt, J. (2007). Mice lacking sister chromatid cohesion protein PDS5B exhibit developmental abnormalities reminiscent of Cornelia de Lange syndrome. Development *134*, 3191-3201.

Zhang, J., Shi, X., Li, Y., Kim, B.J., Jia, J., Huang, Z., Yang, T., Fu, X., Jung, S.Y., Wang, Y., *et al.* (2008a). Acetylation of Smc3 by Eco1 is required for S phase sister chromatid cohesion in both human and yeast. Mol Cell *31*, 143-151.

Zhang, N., Panigrahi, A.K., Mao, Q., and Pati, D. (2011). Interaction of Sororin protein with polo-like kinase 1 mediates resolution of chromosomal arm cohesion. J Biol Chem *286*, 41826-41837.

Zhang, Y., Liu, T., Meyer, C.A., Eeckhoute, J., Johnson, D.S., Bernstein, B.E., Nusbaum, C., Myers, R.M., Brown, M., Li, W., *et al.* (2008b). Model-based analysis of ChIP-Seq (MACS). Genome Biol *9*, R137.

Zhou, L., Liang, C., Chen, Q., Zhang, Z., Zhang, B., Yan, H., Qi, F., Zhang, M., Yi, Q., Guan, Y., *et al.* (2017). The N-Terminal Non-Kinase-Domain-Mediated Binding of Haspin to Pds5B Protects Centromeric Cohesion in Mitosis. Curr Biol *27*, 992-1004.

Zou, H., McGarry, T.J., Bernal, T., and Kirschner, M.W. (1999). Identification of a vertebrate sister-chromatid separation inhibitor involved in transformation and tumorigenesis. Science *285*, 418-422.